



Provided by the author(s) and University of Galway in accordance with publisher policies. Please cite the published version when available.

Title	The Optical Signatures of Magnetospheric Phenomena at the End of the Main Sequence and Beyond
Author(s)	Harding, Leon Karl
Publication Date	2012-10-22
Item record	http://hdl.handle.net/10379/3609

Downloaded 2024-03-20T12:24:16Z

Some rights reserved. For more information, please see the item record link above.



The Optical Signatures of Magnetospheric Phenomena at the End of the Main Sequence and Beyond

A DISSERTATION SUBMITTED IN ACCORDANCE WITH
THE REQUIREMENTS FOR THE DEGREE OF
DOCTOR OF PHILOSOPHY
IN THE COLLEGE OF SCIENCE

by

Leon Karl Harding B.Sc. M.Sc.

Supervisors:

Dr. Aaron Golden

Dr. Ray F. Butler

Head of School:

Dr. Mark Lang



Centre for Astronomy
School of Physics,
National University of Ireland, Galway

September 2012

ABSTRACT

In recent years, very low mass stars and brown dwarfs, together known as ultracool dwarfs, have unexpectedly been detected as a radio transient source, where periodic bursts of radio emission were also discovered. Periodicity has subsequently been detected in $H\alpha$ and other photometric data from a number of these objects. It remained unclear whether this periodic behavior was related to the presence of the periodic pulsed radio emission. This thesis investigates this possible connection, and presents multi-epoch periodic photometric variability from a lengthy campaign encompassing six radio detected ultracool dwarfs, spanning the $\sim M8 - L3.5$ spectral range. These include the M tight binary dwarf LP 349-25AB and L tight binary dwarf 2MASS J0746+2000AB, as well as the M8.5 dwarf LSR J1835+3259, the M9 dwarf TVLM 513-46546, the M9.5 dwarf BRI 0021-0214, and the L3.5 dwarf 2MASS J0036+18. Five of these dwarfs exhibit periodic photometric variability, where three of these are newly discovered. One other shows persistent variability, with the possibility of periodicity detected in the data. This work was primarily carried out using the GUFI photometer (Galway Ultra Fast Imager), an instrument commissioned during this campaign to specifically detect optical signatures from these objects, currently stationed on the 1.83 m Vatican Advanced Technology Telescope, on Mt. Graham, Arizona. We sought to investigate the ubiquity of periodic optical variability in both quiescent and time-variable radio detected ultracool dwarfs. The periodic variability is associated with the rotation of the dwarf in all cases and we consider a number of causal photospheric phenomena, including magnetic cool spots and atmospheric dust. An exciting alternative may associate the periodic variability with chromospheric auroral hot spots directly related to the previously discovered periodic radio emission. One dwarf in this study is part of this larger study, and we present the photometric results possibly associated with this phenomenon.

In addition to the search for optical signatures from these ultracool dwarfs, and based on the newly discovered rotation periods for the binary dwarfs, we investigate the orbital

coplanarity of LP 349-25AB and 2MASS J0746+2000AB. We find that in both cases, the inclination angle of the binary spin axes are consistent with being aligned perpendicularly to the system orbital planes to within 10 degrees, as observed for solar-type binary formation. We consider a number of formation mechanisms for such an alignment, including turbulent core fragmentation, disk fragmentation, multiple formation via competitive accretion and dynamical interactions. For 2MASS J0746+2000AB, we have estimated individual component masses and radii based on evolutionary models, which place the binary system at, or just below, the substellar boundary, and at $\sim 1 R_J$. This is the first direct evidence of spin-orbit alignment in the very low mass binary regime.

In supplementary work, we conducted high-speed photometric monitoring of the active M flare stars YZ CMi and AD LEO, in order to investigate the white light flaring emission present in a stellar flare. We present high-speed photometry in B- and V-band, aimed to observe sub-structure in small to large flare events that is inaccessible to spectroscopy (due to slower cadence). For one flaring event in YZ CMi in particular, we report the detection of resolved loop oscillation events in the decay phase of the flare. These data indicate that a periodically repeating structure is being maintained during this phase of the event. Magnetic reconnection has the ability to accelerate non-thermal electrons in to the lower atmospheric regions of these stars - perhaps producing this continuum emission.

Finally, in the later stage of the doctoral work, we built and commissioned a second instrument - the Caltech HIgh-speed Multi-color camERA, or CHIMERA. This photometer has the capability of observing simultaneously in g' and either r' or i' , and does so by using the new innovative technology from Andor - the NEO sCMOS detectors. These are capable of obtaining 100 frames per second full frame, or >1600 frames per second sub-frame. The instrument was commissioned at prime focus of the Palomar 200" telescope, and is stationed as a facility instrument to be used as a Palomar Transient Factory follow-up instrument, as well as being available for a wide range of astronomical observations, such as eclipsing binaries, transiting exoplanets, brown dwarfs, flare stars, and indeed any detected transient source in the sky.

AUTHOR'S NOVEL CONTRIBUTIONS

Harding et al. 2012a, ApJ

Ch. 2, 3, 4, 5

- Discovery of three rotation periods of radio detected dwarfs. Two more were confirmed and their values constrained. Strong case for optical variability being ubiquitous for radio detected ultracool dwarfs.
- Investigated and established levels of amplitude and phase stability over timescales of years for some targets. A baseline of 5 years for TVLM 513-46546 infers that spatial conditions of the surface feature responsible are not greatly changing.
- Instrument scientist for GUFU (Galway Ultra-Fast Imager) photometer - optical design, calibration, commissioning and utilization of instrument for doctorate data.
- Development of routines for data registration, fringe correction, data analysis and post-photometry assessment of lightcurve.

Harding et al. 2012b, ApJL

Ch. 6

- Discovered first direct evidence of spin-orbit alignment in the very low mass binary regime.
- Implications that formation characteristics of solar-type binary stars may hold in the very low mass range (magnetically active (~ 1.7 kG field) close binary (~ 2.7 AU)).
- Inferred individual age, mass and radii, for each component of the system.

Harding et al. 2012d, in prep.

Ch. 7

- Coordinated GUF1 photometric component of flare star campaign.
- Detection of possible resolved periodic loop oscillation events in the decay phase of a flaring event in B-band from the dM4.5Ve flare star YZ CMi.

Harding et al. 2012c, in prep.

Ch. 2, 8; Ap. C

- Instrument scientist for CHIMERA (Caltech High-speed Multi-color camERA) mk.I photometer - optical design, calibration, commissioning and utilization of instrument.
- Optical test design for CHIMERA mk.II at prime focus of Hale 200" - larger field of view of $\sim 10' \times 10'$. Current CHIMERA mk.I field of view of $3' \times 2.7'$.

“ ... Ad astra ... ”

DEDICATION

First and foremost, I would like to thank Gregg Hallinan and Aaron Golden, who, ~4 years ago, identified an enthusiastic would-be astronomer, added him to the ranks of the group, and made it possible for him to complete his graduate studies. To Gregg especially, for the many (!) great and interesting scientific discussions, for being an incredible mentor, and for truly being the catalyst for all of my astronomical endeavors. I cannot express my gratitude enough, and there is no amount of thanks I can ever give. To Aaron for his strong (poetic!) words of encouragement, that always seemed to come at the right time. My sincere thanks to Ray Butler, who was my Masters degree supervisor and became a co-supervisor for my Ph.D. a number of years ago. You supported many trips, and are originally responsible for the 'GUFFI' creation and a large amount of my IRAF skills. Really, thank you for everything Ray. To the original 'old school' crew of The Technodrome, room 139 - John, James, Gary, Ollie, Brendan, Alan and Gregg (the same!). I will always remember the laughs and crazed IRAF-related outbursts in that room - and the many missions in Barn >5pm; it's probably for the best that call signs remain anonymous! Thank you all for your support. To the staff of the VATT telescope - Richard Boyle, Chris Corbally, Dave Harvey, Michael Franz, Ken Duffek, Chris Johnson, as well as all of the VATT and Steward Observatory staff, and to the guys in the VATT house in Arizona. What an incredible experience it was for a Ph.D. student to visit such a facility at ~11,000 feet, and to commission a scientific instrument in 0.7" seeing. My thanks for all of your help since the first VATT 4K CCD run in January 2009, and most importantly, for all of the laughs. To John, who passed the XPS powerhouses down the line - Haydes and Gigantor; and for his unwavering place in the phalanx beside me. Thank you bro - Vires Quod Veneratio. To Mark Lang, who, throughout my entire doctoral studies, was so incredibly accommodating with teaching positions, as well as travel and others. Although always expressing concerns for a

healthy balance of studies and other work, he trusted that I would manage my time. My thanks to you Mark - I very much so appreciate your considerations. To Andy Shearer, for his constant support and words of encouragement, and for making the Centre for Astronomy outreach program a truly enjoyable experience - even on cloudy Wednesday evenings! Thanks also to Matt Redman for giving me the opportunity to demonstrate in his C programming labs which kept my C skills sharp. A special thanks to Tess in the Physics office - I will continue to send postcards! To Conor, PJ, James N. and Stewart, thank you guys for all of your knowledge and technical expertise over the years, and for making tea breaks in the canteen a belly-laughing experience! To friends on a similar journey in the department (some already there!) - Ronan R., Arlene, Gillian, Seán, Ronan H., Elaine, Tuathan, Lisa-Marie, Niall, Branden, Michael, Mags, Aonghus, Susan, Mike Sherry, Paul. For being such an incredible help in the horrible world of statistics - Andrea Cesarini, the Jedi. In the realm of Python (and converting JPG -> EPS [long story!]), thank you Navtej! A big thank you to all of my housemates in 101 Forster Court, 17 Atlanta House and 38 Upper Newcastle road: Dave, SteveO, Rowan, Hassett, Ross, Lillian, John, James, Jodi, Wez - I had an absolute blast. Thanks for putting up with doors closing in the long hours of the a.m. on my return from The Technodrome. To my friends at Caltech - thank you for being so welcoming and for the huge amount of chats; scientific and other. You guys are legends! To the Palomar Observatory and Caltech Optical Observatory staff - Steve, Mike, Kevin, Rich D. and Paul. We made the 'two-headed beast' take a bow! - a special thanks to Gillian for her patience in my assimilation of the subtleties of instrumentation and optics. A special acknowledgment and thanks to Suzanne Hawley, Adam Kowalski and Eric Hilton of UW for being so welcoming and for sharing my enthusiasm for magnetic reconnection events - let the flaring continue! My thanks to Quinn Konopacky and Kaitlin Kratter for their many discussions of very low mass binary alignments and formation mechanisms. To my other friends in life in addition to those above, Rob, Fergal, Mark, Odhrán, Séamus, Ambrose, Rob S., Jason, Mike, et al., thank you for the many G-mail chats, and for your cherished friendships, and encouragement. I'd be lost without ye! Let the fun continue. Finally, last but cer-

tainly not least, to my family. Mom, Dad, Wez and Ailbhe. Mom & Dad: thanks for buying me my first telescope! Quite simply, I would not be where I am without you guys - I love you all very much and thank you (∞) for everything. I'll name a crater after all of you when I make it to the moon!

ACKNOWLEDGEMENTS

This work was largely carried out under the National University of Ireland Traveling Studentship in the Sciences (Physics). I gratefully acknowledges the support of the Science Foundation Ireland (Grant Number 07/RFP/PHYF553) and the Galway Local Authority Grant scheme. On a personal note, I would like to thank my project supervisor, Aaron Golden, for initially taking me on-board, and for his never-ending words of encouragement which made it possible for me to complete my graduate studies.



I would also like to thank the staff of the National Radio Astronomy Observatory (NRAO) for their help and support during my time as a graduate intern in Socorro, NM (August - December 2010). Similarly, as a visiting student researcher, my sincere gratitude to all fellow astronomers at the Cahill Centre for Astronomy and Astrophysics at Caltech, CA (March - August 2012), for the many discussions of astrophysics and of Hollywood.

PHILOSOPHY

Although I am fully convinced of the truth of the views given in this volume, I by no means expect to convince experienced naturalists whose minds are stocked with a multitude of facts all viewed, during a long course of years, from a point of view directly opposite to mine. But I look with confidence to the future to young and rising naturalists, who will be able to view both sides of the question with impartiality.

– *Charles Darwin (1809 - 1882), The Origin of Species.*

Go placidly amid the noise and haste, and remember what peace there may be in silence. As far as possible, without surrender, be on good terms with all persons. Speak your truth quietly and clearly; and listen to others, even the dull and ignorant; they too have their story. Avoid loud and aggressive persons, they are vexations to the spirit. If you compare yourself to others, you may become vain and bitter; for always there will be greater and lesser people than yourself ...

... Be yourself. Especially do not feign affection. Neither be cynical about love; for in the face of all aridity and disenchantment it is perennial as the grass. Take kindly the counsel of the years, gracefully surrendering the things of youth. Nurture strength of spirit to shield you in sudden misfortune. But do not distress yourself with imaginings ... With all its sham, drudgery and broken dreams, it is still a beautiful world. Be careful. Strive to be happy.

– *Excerpt from “DESIDERATA” - Found in Old St. Paul’s Church, Baltimore; 1692.*

PUBLICATIONS

[1] Harding, L. K., Hallinan, G., Boyle, R. P., Golden, A., Sheehan, B., Zavala, R. T. and Butler, R. F., **Periodic Optical Variability of Radio Detected Ultracool Dwarfs**. *Submitted to ApJ*.

[2] Harding, L. K., Hallinan, G., Konopacky, Q., Boyle, R. P., Butler, R. F. and Golden, A., **On the Orbital Coplanarity of the L Tight Binary Dwarf 2MASSW J0746425+200032**. *Submitted to ApJL*.

[3] Harding, L. K., Hallinan, G., Kyne, G., Gardner, P., Baranec, C., Konidaris, N. and Kulkarni, S., **CHIMERA - a Prime Focus PTF Follow-up Instrument on the 200"**. *in preparation*.

[4] Harding, L. K., Kowalski, A. F., Hilton, E. J., Hawley, S. L., Hallinan, G., Boyle, R. P., Golden, A. and Butler, R. F., **An Investigation to Characterize the White Light Flare Emission of YZ CMi using High-Speed Photometry**. *in preparation*.

[5] Hallinan, G. et al. *Under embargo*.

[6] Harding, L. K., Hallinan, G., Boyle, R. P., Butler, R. F., Sheehan, B. and Golden, A., **A Search for Periodic Optical Variability in Radio Detected Ultracool Dwarfs: A Consequence of a Magnetically-Driven Auroral Process?** *ASP Conference Series, Vol. 448, p.219. [2011ASPC..448..219H][‡]*.

[7] Harding, L. K., Butler, R. F., Redfern, R. M., Sheehan, B. J., and McDonald, J., **Op-**

[‡]Awarded the **best poster** prize for the brown dwarf category at Cool Stars 16. This paper was therefore also included in the hard-bound proceedings of the conference, amongst the invited talks and plenary session papers.

timised Post-Exposure Image Sharpening Software for L3-CCD Detectors. *American Institute of Physics Conference Series* **984**, 235-240 (2008).

Public Lectures:

1. Invited speaker for the NUI Galway Astronomy Society public lecture series 2012. Title: “*Discovering Extrasolar Planets, and the Search for Life in our Solar System and Beyond*”. Date: 8th October, 2012.
2. Public lecture for the Centre for Astronomy, NUI, Galway, outreach program, Cairns Lecture Theatre. Title: “*Brown Dwarfs - failed stars ... back on the air!*”. Date: 30th March 2011.
3. Public lecture for the Centre for Astronomy, NUI, Galway, outreach program, McMunn Lecture Theatre. Title: “*Observing Extra-Solar Planets from Space - the key to finding life?*”. Date: 24th February 2011.
4. Public lecture for European Space Agency Summer School, Alpbach, Austria. Space Mission Title: “*DWARFS - Diverse Worlds ARound Faint Stars*”. DATE: 31st July 2009.

Presentations (talks and posters):

1. Poster presentation at the Caltech Palomar Transient Factory (PTF) meeting, Santa Barbara, California, USA. Title: “*CHIMERA: Caltech HIgh-speed Multi-color camERA - a prime focus PTF follow-up instrument on the mighty 200-inch*”. Date: 6th July, 2012.
2. Poster presentation at the 17th Cambridge Workshop “Cool Stars” Conference: Cool Stars, Stellar Systems and the Sun, Barcelona, Spain. Title: “*Periodic Optical Variability from Radio Detected Ultracool Dwarfs*”. Date: 24th - 29th June, 2012.
3. Speaker for Journal Club session at the Cahill Centre for Astronomy and Astrophysics, California Institute of Technology (Caltech). Title: “*Periodic Optical Variability from Radio Detected Ultracool Dwarfs*”. Date: 20th April 2012.
4. Poster presentation at the American Astronomical Meeting, Boston, USA. “*An Investigation into the Periodic Optical Variability from Radio Detected Ultracool Dwarfs using the GUF1 Photometer*”. Date: 22nd - 26th May, 2011.

5. Speaker for Journal Club session at the Astronomy Department, University of Washington, Seattle, Washington, USA. Title: “*A Search for the Optical Counterpart to the Radio Pulses Detected from Ultracool Dwarfs*”. Date: 1st March 2011.
6. Invited speaker for the Galway Astronomy Club, Galway. Title: “*Observing Extra-Solar Planets from Space - the key to finding life?*”. Date: 24th February 2011.
7. Poster presentation at the National Radio Astronomy Observatory Colloquium, NM, USA. “*The Optical Periodic Signals from Ultracool Dwarfs*”. Date: November 2010.
8. Poster presentation at the 16th Cambridge Workshop “Cool Stars” Conference: Cool Stars, Stellar Systems and the Sun, University of Washington, Seattle, Washington, USA. Title: “*A Search for Periodic Optical Variability in Radio Detected Ultracool Dwarfs: A Consequence of a Magnetically-Driven Auroral Process?*”. Date: 28th August - 2nd September, 2010: **Brown Dwarf category poster winner.**
9. Speaker for Journal Club session at the Centre for Astronomy, NUI Galway. Title: “*Radio observations of the cool gas, dust, and star formation in the first galaxies*”. Date: 9th May 2010.
10. Conference presentation at the ASGI meeting, Queen’s University, Belfast. Title: “*Determining the Rotation Periods of Brown Dwarfs via Photometric Monitoring*”. Date: 31st March 2010.
11. Invited speaker for the Galway Astronomy Club. Title: “*The Exotic Universe: Are Brown Dwarfs, Planets, Pulsars or Stars?*”. Date: 25th May 2009.
12. Speaker for Journal Club session at the Centre for Astronomy, NUI Galway. Title: “*Optical variability of the ultracool dwarf TVLM 513-46546: evidence for inhomogeneous dust clouds*”. Date: 12th March 2009.
13. Presentation at the Postgraduate Physics seminar, Physics Department, NUI Galway. Title: “*Optimised Post-Exposure Image Sharpening Software and its application to astronomical data*”. Date: 8th January 2008.
14. Poster presentation at the High Time Resolution Astrophysics (HTRA) conference held in the Royal Observatory of Edinburgh, Scotland. Title: “*Optimised Post-Exposure Image Sharpening Software for L3-CCD Detectors*”. Date: 11th – 13th September, 2007

(<http://www.htra.ie>).

15. Presentation at the Postgraduate Physics seminar, Physics Department, NUI Galway.

Title: “*Post-Exposure Image Sharpening Reduction Techniques*”. Date: 8th May 2007.

16. Speaker for Journal Club session at the Centre for Astronomy, NUI Galway. Title:

“*Discovery of five very low mass close binaries, resolved in the visible with Lucky Imaging*”. Date: 23rd March 2007.

DECLARATIONS

The work in this thesis is based on research carried out at the Centre for Astronomy, National University of Ireland, Galway, Ireland. No part of this thesis has been submitted elsewhere for any other degree or qualification and is all my own work unless referenced to the contrary in the text.



Copyright © 2012 by Leon Karl Harding B.Sc. M.Sc..

All Rights Reserved.

APPROVAL

“The Optical Signatures of Magnetospheric Phenomena at the End of the Main Sequence and Beyond”, a dissertation prepared by Leon Karl Harding B.Sc. M.Sc. and submitted in accordance with the requirements for the Degree of DOCTOR OF PHILOSOPHY in the College of Science has been approved and accepted by:

_____	_____
Dr. Aaron Golden Thesis Supervisor	Date
_____	_____
----- Dr. Stuart Littlefair External Examiner	Date
_____	_____
----- Dr. Matt Redman Internal Examiner	Date

ACRONYMS

$\alpha\omega$-dynamo	Alpha-Omega dynamo
2MASS	Two Micron All Sky Survey
ADU	Analogue to digital unit
AO	Adaptive optics
AOI	Angle of incidence
APO	Apache Point Observatory
ARCSAT	ARC Small Aperture Telescope
bKOM	Broadband kilometric radiation
MMT	Multiple Mirror Telescope
Caltech	California Institute of Technology
CCD	Charge-Coupled Device
CfA	Centre for Astronomy
CHIMERA	Caltech High-speed Multi-color camERA
CIC	Clock induced charge
DAM	Decameter radiation
DBSP	Double Spectrograph
DEC	Declination (angle) *celestial sphere coordinate reference*
DIM	Decimeter radiation
DIS	Double Imaging Spectrograph
DFT	Discrete Fourier transform
ECM	Electron cyclotron maser
EM-CCD	Electron multiplication charge-coupled device
EO	Edmund Optics
FOV	Field of view

fps	Frames per second
FWHM	Full width at half maximum
FR	Focal reducer
FT	Fourier transform
GMOS	Gemini Multi-Object Spectrograph
GPE	Gravitational potential energy
GPS	Global positioning system
GUFI	Galway Ultra-Fast Imager
GUI	Graphic user interface
H-R	Hertzprung-Russell (diagram)
HBMM	Hydrogen burning minimum mass
HJD	Heliocentric Julian Day
HOM	Hectometric radiation
HST	Hubble Space Telescope
IRAF	Image Reduction and Analysis Facility
IR	Infrared
IS	Instrument scientist
JPL	Jet Propulsion Laboratory
KBO	Kuiper Belt Object
KE	Kinetic energy
L3	Low Light Level
LBT	Large Binocular Telescope
LDR	Line depth ratio
LFC	Large Format Camera
LGS	Laser Guide System
LS	Lomb-Scargle
LSF	Least squares fit
MC	Monte Carlo
MGIO	Mount Graham International Observatory

Mpx	Mega pixel
MRE	Magnetic reconnection event
NASA	National Aeronautics and Space Administration
NIR	Near-infrared
NIRSPEC	Near Infrared Spectrograph
NMSU	New Mexico State University
NRAO	National Radio Astronomy Observatory
NTP	Network time protocol
NTT	New Technology Telescope
NSF	National Science Foundation
OS	Operating system
PD	Potential difference
PDM	Phase Dispersion Minimization
PI	Principal Investigator
PTF	Palomar Transient Factory
pp	Proton-proton
PSF	Point Spread Function
QE	Quantum efficiency
RA	Right Ascension (angle) *celestial sphere coordinate reference*
RMS	Root mean square
roAp	Rapidly oscillating [peculiar] A type stars
Robo-AO	Robotic Adaptive Optics
ROI	Region of interest
SFI	Science Foundation Ireland
sCMOS	Scientific complementary metal-oxide-semiconductor
SDSS	Sloan Digital Sky Survey
SED	Spectral energy distribution
SMT	Sub-Millimeter Telescope
SNR	Signal-to-noise ratio

TCP/IP	Transmission Control Protocol (TCP) and Internet Protocol (IP)
TCS	Telescope Control Software
TNG	Telescopio Nazionale Galileo
TOA	Time-of-arrival
TTL	Transistor-Transistor Logic
UCD	Ultracool dwarf
USNO	United States Naval Observatory
UTC	Coordinated Universal Time
UV	Ultra-violet
VATT	Vatican Advanced Technology Telescope
VORG	Vatican Observatory Research Group
(J)(E)VLA	(Jansky) (Expanded) Very Large Array
VLBA	Very Long Baseline Array
VLT	Very Large Telescope
WHT	William Herschel Telescope
WISE	Wide-Field Infrared Survey Explorer
XCF	Cross Correlation Function
ZDI	Zeeman Doppler Imaging
ZTF	Zwicky Transient Factory

CONTENTS

Abstract	i
Author’s Novel Contributions	iii
Dedication	v
Acknowledgements	viii
Philosophy	ix
Publications	x
Declarations	xiv
Approval	xv
Acronyms	xvi
Introduction & Motivation	i
1 Background Theory and Discovery of Ultracool Dwarfs	10
1.1 Introduction	10
1.2 What is an Ultracool Dwarf?	11
1.2.1 The Search for Brown Dwarfs: a Brief History	13
1.2.2 Interior Physics	14
1.2.2.1 Temperatures, Luminosities, Radii and Gravity	17
1.2.3 Atmospheres and Spectral Classification: from M- to Y-Type Dwarfs	21
1.3 Stellar and Substellar Magnetic Activity	26
1.3.1 Radio Emission from the Sun and Stars	27

1.3.2	Radio Emission from Ultracool Dwarfs	28
1.3.3	Magnetic Activity in the Planets, and the Observed Aurorae . . .	32
1.4	The Phenomenon of Optical Periodic Variability from Ultracool Dwarfs .	34
1.4.1	Variability due to Magnetic Cool Spots	35
1.4.2	Variability due to Atmospheric Dust	36
1.4.3	The Exciting Alternative: Variability due to Auroral Hot Spots . .	37
1.5	Summary	39
2	Optical Instrumentation	42
2.1	The GUFi mk.II Photometer - Galway Ultra-Fast Imager	42
2.1.1	L3-CCD Technology and the Andor iXon DV887	44
2.1.2	Optical Setup and Instrument Design	48
2.1.3	Hardware and Software	51
2.1.4	Time Server (NTP) Implementation	51
2.2	CHIMERA - Caltech HIgh-speed Multi-color camERA	52
2.2.1	sCMOS Technology and the Andor NEO	53
2.2.2	CHIMERA at Prime ($f/3.5$) Focus of the 200-inch	55
2.2.3	Optical Setup and Final Instrument Design	56
2.2.4	Hardware and Software	63
2.2.5	GPS Tracked Timestamping and Guiding	64
2.2.6	CHIMERA as a Palomar Transient Factory Instrument	65
2.2.7	“First Light” - Proof of Concept Data	67
2.3	Summary	67
3	Data Reduction & Variability Analysis	70
3.1	Data Reduction and Photometry	70
3.1.1	The ‘L3 GUFi Pipeline’ - Photometric Data Reduction	71
3.1.2	Atmospheric OH Spectral Emission - “Fringing”	74
3.1.3	Correcting for Circular Rotation in the Field	77
3.1.4	Aperture Photometry vs. PSF Fitting	78

3.1.5	Differential Photometry	82
3.1.6	Post-Photometry Assessment of Lightcurve	83
3.1.7	Photometric Error Estimation	86
3.2	Variability Analysis of Photometric Datasets	88
3.2.1	The Fourier Transform and the Lomb-Scargle Periodogram	89
3.2.2	Phase Dispersion Minimization	92
3.2.3	The χ^2 Test, the LSF and Sinusoid Fitting	94
3.2.4	Binary Lightcurve Modelling	97
3.2.5	Period Uncertainty Estimation	99
3.3	Summary	101
4	Periodic Optical Variability in Radio Detected Ultracool Dwarfs	102
4.1	Introduction	102
4.2	Discussion of Binary Systems	104
4.2.1	LP 349-25AB	105
4.2.2	2MASS J0746+2000AB	106
4.3	Discussion of Single Systems	108
4.3.1	LSR J1835+3259	108
4.3.2	TVLM 513-46546	109
4.3.3	BRI 0021-0214	110
4.3.4	2MASS J0036+18	111
4.4	Optical Observations	112
4.4.1	The VATT 4K Imager	112
4.4.2	The USNO Detectors	113
4.4.3	Observations and Data Reduction	113
4.5	General Results	117
4.5.1	Binary Dwarfs	117
4.5.1.1	LP 349-25AB (M8+M9)	117
4.5.1.2	The Unusual Behavior of LP 349-25	123

4.5.1.3	2MASS J0746+2000AB (L0+L1.5)	126
4.5.2	Single Dwarfs	129
4.5.2.1	LSR J1835+3259 (M8.5)	129
4.5.2.2	TVLM 513-46546 (M9)	132
4.5.2.3	BRI 0021-0214 (M9.5)	135
4.5.2.4	2MASS J0036+18 (L3.5)	138
4.6	Source of the Periodicity	138
4.7	Summary	144
5	The Phase and Amplitude Stability of TVLM 513-46546	145
5.1	Introduction	145
5.2	Phase Connecting and Amplitude Analysis of Datasets	146
5.2.1	Phase Connecting the 5 Year Baseline	146
5.2.2	Amplitude Analysis	150
5.3	Cross Correlation (XCF) Analysis	150
5.3.1	The XCF Function	150
5.3.2	Applying the XCF	151
5.4	A Magnetically-Driven Auroral Process	152
5.5	Summary	156
6	On the Orbital Coplanarity of Very Low Mass Binary Stars	158
6.1	Introduction	158
6.1.1	High-Precision Dynamical Mass Measurements	159
6.1.2	<i>Individual</i> Rotational Velocity Measurements	160
6.1.3	Periods of Rotation, Colors and the Presence of Lithium?	160
6.1.3.1	LP 349-25AB	161
6.1.3.2	2MASS J0746+2000AB	161
6.2	The Orbital Coplanarity of Very Low Mass Binaries	162
6.2.1	Estimating Masses and Radii	164
6.2.2	Results	167

6.2.2.1	LP 349-25AB	167
6.2.2.2	2MASS J0746+2000AB	170
6.3	Summary	177
7	Flaring in M Dwarfs and the Associated Loop Oscillation Events	179
7.1	Introduction	179
7.2	Selected targets and Observations	181
7.3	Results	183
7.3.1	YZ CMi (dM4.5e)	184
7.3.2	AD Leo (M3.5Ve)	188
7.4	The Periodic Variations due to Loop Oscillations from YZ CMi	191
7.5	Summary	195
8	Conclusions and Future Work	197
8.1	Discussion and Conclusions	197
8.2	Future work	201
8.2.1	High-Precision <i>Individual</i> Dynamical Mass Measurements of Very Low Mass Tight Binaries	201
8.2.2	Resolving the Radio Detected L Dwarf Tight Binary 2MASS J0746+20AB with Robo-AO	203
8.2.3	UV Ceti and BL Ceti	204
8.2.4	Period of Rotation Search for ZDI	204
8.2.5	CHIMERA mk.II and the search for Kuiper Belt Objects	205
	Appendix	236
A	Observations of GJ 1243	236
B	Observations of GL 51, GJ 2069a, GJ 2069b and GL 1111	238
C	CHIMERA mk.II Conceptual Designs	244

INTRODUCTION & MOTIVATION

Astronomy; **astro** ($\alpha\sigma\tau\epsilon\rho\iota$) = star; **nomos** ($\nu\omicron\mu\omicron\xi$) = law

Greek language

“A man should look for what is, and not for what he thinks should be.”

Albert Einstein

Although originally postulated in the 1960s, it was not until 1995 that the first confirmed detection of a bona fide brown dwarf was achieved (Nakajima et al., 1995). Since this initial detection, the population of detected brown dwarfs has exploded, and we now know brown dwarfs to be one of the most populous classes of objects in our galaxy. Low mass stars and brown dwarfs, together known as ultracool dwarfs, are fully convective objects that occupy the spectral range $\geq M7$ (Kirkpatrick et al., 1997), L, T and Y (temperature < 2500 K). These spectral classifications are elaborated on further in Chapter 1. Although it has not yet been confirmed for all very low mass stars, according to the standard models of Chabrier & Baraffe (2000), it is generally accepted that objects later than spectral type $\sim M3 - M4$, or $\sim 0.3 - 0.4 M_{\odot}$, including ultracool dwarfs, move away from partially convective configurations and become fully convective objects. Whereas stars with higher mass are thought to generate their magnetic fields via the so-called $\alpha\Omega$ -dynamo (Parker, 1975), it is not yet established what dynamo mechanism operates in such fully convective stars and brown dwarfs. Although the dynamo is not well understood, M dwarfs later than M3 are associated with intense magnetic activity, exhibiting large magnetic reconnection events of up to 10^{34} ergs in Johnson U-band (Hawley & Pettersen, 1991; Hilton et al., 2010; Kowalski et al., 2010), and often possessing surface magnetic field strengths of a few kilogauss (kG) and greater, e.g. Saar & Linsky (1985); Johns-Krull & Valenti (1996); Reiners & Basri (2007). Moreover, Donati et al. (2006) reported the presence of large-scale, axisymmetric dipolar fields, via spectroscopic mapping of magnetically-sensitive

lines of the M4 dwarf V374 Peg. Following this work, they subsequently found toroidal and non-axisymmetric dipolar fields in observations encompassing a sample of early M0 - M3 type stars, where their results yield stars lowest in mass to exhibit the large-scale fields of mid-M dwarfs (Donati et al., 2006). Large-scale magnetic topologies of mid- and late-M dwarfs have also been shown via the spectropolarimetric analyses of Morin et al. (2008, 2010) - further evidence of stable magnetic field configurations which can cover a significant fraction of the stellar surface. Similarly, Phan-Bao et al. (2009) have revealed smaller magnetic structures for these configurations, that provide significant magnetic energy in stellar photospheres. An alternate dynamo, possessing the ability to sustain such fields, must therefore be effective and present in low mass, fully convective stars.

Observations have now probed the coolest part of the Hertzsprung-Russell (H-R) diagram, and these studies have yielded surprising results. These ultracool dwarfs have now been shown to produce both thermal and non-thermal radio emission, but at the same luminosities as early to mid-M active dwarfs. Interestingly, for \sim M7 dwarfs and later, $H\alpha$ and X-ray luminosities drop sharply signaling that chromospheric and coronal heating becomes less efficient, despite very rapid rotation (Mohanty & Basri, 2003; West et al., 2004; Reiners & Basri, 2008; West & Basri, 2009). Here lies the ultracool dwarf regime, where reduced levels of ionization in the stellar atmospheres, as well as an increase in resistivity, inhibit the necessary injection of energy required for localized plasma heating. The magnetic fields therefore become decoupled in these atmospheric regions, and the chromosphere and corona are no longer effectively supported. Despite this reduction in quiescent emission, a number of $H\alpha$ and X-ray flares have been detected from ultracool dwarfs, indicating that chromospheric and coronal activity is indeed present (Reid et al., 1999; Gizis et al., 2000; Rutledge et al., 2000; Liebert et al., 2003; Fuhrmeister & Schmitt, 2004; Rockefeller et al., 2006b). Furthermore, Berger et al. (2001) reported persistent radio emission from the M9 brown dwarf LP 944-20 - the first detection of radio emission from a brown dwarf. This result was highly irregular based on the established relationships between the peak X-ray and radio luminosities ($L_X - L_R$) for main sequence stars (Güdel & Benz, 1993; Benz & Güdel, 1994). In fact, this unexpected detection violated the $L_X - L_R$ Güdel-Benz

relationship by many orders of magnitude. More detections followed in the coming years, where all detected sources had high rotational velocity ($v \sin i$) values (up to 60 km s^{-1}) (Berger, 2002; Berger et al., 2005; Burgasser & Putman, 2005; Berger, 2006; Osten et al., 2006; Hallinan et al., 2006, 2007; Antonova et al., 2007; Phan-Bao et al., 2007; Osten et al., 2009; Berger et al., 2009; Route & Wolszczan, 2012). This was perhaps an indication that the rotation-activity relationship held for radio emitting ultracool dwarfs even though this relation seemed to break down for other activity tracers such as $\text{H}\alpha$ or X-ray. More radio discoveries followed the observations of Berger et al. (2001), confirming long-term variability of these objects, and most importantly, confirming active and sustained magnetic field environments. Hallinan et al. (2006) reported rotational modulation due to a coherent emission process for the M9 dwarf TVLM 513-46546. This was subsequently confirmed to be due to the coherent electron cyclotron maser (ECM) instability, after 100% circularly polarized bursts of periodic radio emission were detected from this object, along with two others (Hallinan et al., 2007, 2008). Berger et al. (2009) also detected radio pulsing from an early L dwarf binary. Thus it was clear that these substellar objects were transient sources of radio emission.

Following the initial discovery of Gleise 229B, the first empirically confirmed brown dwarf, many studies followed in an attempt to characterize the transient nature at optical wavelengths of these newly discovered substellar objects. Early searches proved to be fruitful, and variability (both aperiodic and periodic) was soon detected in broadband optical photometry e.g. Tinney & Tolley (1999); Bailer-Jones & Mundt (2001); Clarke et al. (2002) - other studies are outlined in Chapter 1. Two causes were primarily invoked as the cause of this variability - 1) the presence of photospheric spots associated with high strength magnetic fields, or 2) the condensation of the more refractory elements in the cool neutral atmosphere of the dwarf into clouds of dust. An intriguing third possibility of this optical variability may be due to emissions associated with particle precipitation into the photosphere and atmosphere, due to the presence of the persistent magnetic fields responsible for the pulsing radio emission. In effect, the optical variability may be caused by processes very similar to those responsible for aurorae at the magnetic poles of the

planets in our solar system, but much more powerful (Hallinan et al., 2012). This thesis directly investigates this possibility. Indeed, modeling these alternative explanations in the photosphere or atmosphere of an ultracool dwarf informs us about the different temporal variations expected in a spectrum for each case. If a dwarf's magnetic field is large-scale and stable for example, the radio pulsing must therefore be confined to a range of phase of rotation of the dwarf, which is directly related to the magnetic field topology. Similarly at optical wavelengths, the stability of the feature responsible for the periodic and aperiodic variability can be investigated by correlating the phase of the optical periodicity from multiple epoch observations. In order to achieve this phasing however, it is necessary to establish the period of rotation to a high level of accuracy.

To date, four ultracool dwarfs have been found to be producing periodic bursts of radio emission (Hallinan et al., 2007, 2008; Berger et al., 2009), and in two of these cases, these pulsing dwarfs have also been found to be periodically variable in broadband optical photometry where the detected periods match the radio pulses (Lane et al., 2007). We therefore undertook a campaign to investigate the ubiquity of optical periodic variability for known radio detected ultracool dwarfs, using the Galway Ultra Fast Imager (GUFI) photometer and the VATT 4K CCD Imager, on the 1.83 m Vatican Advanced Technology Telescope (VATT)¹, on Mt. Graham, Arizona. GUFI was designed and commissioned by the candidate during this doctoral work, to search specifically for optical signatures from ultracool dwarfs. With this goal in mind, over 250 hours of multiple-band photometric monitoring was obtained. Since a large amount of this campaign was carried out simultaneously to spectroscopic and radio observations, the data presented in this thesis provides an insight into the cause of this optical emission and its possible connection to the radio processes. Furthermore, it enables us to assess whether optical periodic signals are present *only* in radio pulsing dwarfs, or perhaps are also observed for quiescent radio detected dwarfs in the sample. The campaign encompassed multiple epoch observations for six ultracool dwarfs.

¹The Vatican Advanced Technology Telescope (VATT) telescope facility is operated by The Vatican Observatory Research Group (VORG), at the Mount Graham International Observatory (MGIO). Further information regarding detector specifications can be found at: <http://cameras.itl.arizona.edu/VATT>.

All confirmed periodically variable sources were taken over multiple epochs where the periodic variability is categorically present in the data. In this work, we consider a number of astrophysical scenarios (established, hypothetical and speculative) that could account for the reported optical periodic signals from these dwarfs:

- 1. Established:** The detected periodic variability is present in a wide range of low mass objects, where the observed optical periodicity may be unrelated to the reported radio emission/radio periodic pulses.
- 2. Hypothesis:** There is some connection, perhaps magnetic in nature, between the detected periodic variability and the periodic bursts of radio emission, where the optical periodicity is not directly caused by the radio process at work.
- 3. Speculative:** The optical and radio emission are inextricably linked, where the same magnetic process is responsible for the periodic behavior in each regime.

These are discussed at length in the relevant chapters that follow. In addition to the VATT telescope, we also obtained data with the 1.52 m telescope in Loiano², Bologna, Italy, as well as the 1.0 m and 1.55 m telescopes of the United States Naval Observatory (USNO)², for selected targets.

Two of the ultracool dwarf sample are in fact very low mass binary systems. These are the M8 tight binary LP 349-25AB and the L tight binary 2MASS J0746+2000AB. Both of these systems have been the focus in other work over the course of the last decade or so, which have included a number of high-precision dynamical mass measurements (Bouy et al., 2004; Dupuy et al., 2010; Konopacky et al., 2010), and the first resolved rotation velocity study that yielded individual component $v \sin i$ measurements (Konopacky et al.,

²The Loiano Observatory (Observatorio Astronomico di Bologna) is based in Bologna, Italy. Refer to <http://www.bo.astro.it/loiano/>, for more details. Information regarding the United States Naval Observatory (USNO) telescopes and detectors can be found here: <http://www.usno.navy.mil/USNO>.

2012). In this thesis, we present the period of rotation for one component of LP 349-25 (most likely LP 349-25B), and the period of 2MASS J0746+2000A. These periods, in addition to the well established dynamical mass and high-precision photometric and spectroscopic parameters, have allowed us to investigate the orbital coplanarity of each system. Previous observations of solar-type binaries have shown that the inclination angle of the binary component equatorial spin axis was perpendicular to the orbital plane of the system, at separations ≤ 40 AU (Hale, 1994). This work investigates the orbital properties of the low mass binary 2MASS J0746+2000AB, and the results show that each component of this system is indeed in agreement with such an alignment. A number of prominent formation mechanisms have been shown to support coplanar alignments, which include turbulent core fragmentation, disk-driven fragmentation, multiple formation via competitive accretion and dynamical interactions (Kratter, 2011, and references therein). Based on the results in this work, it is not clear which mechanism could be responsible for the orbital coplanarity reported here - we discuss these scenarios in more detail in Chapter 6. This is the first such concrete result in the very low mass binary regime. Since we only detect one rotation period for the LP 349-25 system, it was difficult to properly assess this relationship, however tentative analysis which was based on model-derived radii from the literature (Dupuy et al., 2010), suggests that at least one component is indeed coplanar. This is perhaps an indication that a scaled-down version of the solar-type binary formation model may exist for substellar objects, at much closer separations (e.g. ~ 3 AU), and therefore may be expected to hold for all binary stars.

The final section in this thesis reports on high-cadence observations of a number of mid-M type flare stars. This campaign aimed to observe stellar flaring events. During these impulsive events, non-thermal energetic electrons are accelerated down coronal loops via magnetic reconnection. A sharp increase in the white light emission is observed - the so-called ‘blue continuum emission’. However, the source of the white light remains a mystery. We therefore chose to observe simultaneously to a time-resolved spectroscopic campaign being carried out by colleagues from the University of Washington, on the Apache

Point Observatory (APO)³ 3.5 m telescope, as well as simultaneous u' , g' , and r' photometry, at slower cadence, on the 0.5 m ARCSAT telescope at APO. Photometric monitoring can help to assess the correlation between spectral continuum/line variations and the properties of the photometric lightcurves for stellar flares. GUFi was ideal for the photometric component of this campaign, since its high-cadence capabilities enabled the study of much smaller structure in the lightcurve than a large amount of previous photometric monitoring work. We report on the detection of loop oscillation events in the decay of a large flare detected by GUFi in B-band, from the dM4.5Ve dwarf YZ CMi, clearly identified as a result of observations which were taken at exposure times of ~ 0.1 seconds. Importantly, this is one of the first examples of resolved high-cadence loop oscillations from a flare star.

The subsequent chapters in this thesis outline the individual studies and campaigns that were undertaken to investigate the goals presented above. Throughout the thesis, Chapter 2 is referred to as Harding et al. (2012c), Chapter 4 is referred to as Harding et al. (2012a), Chapter 5 and Chapter 6 are referred to as Harding et al. (2012b), and Chapter 7 is referred to as Harding et al. (2012d). Ongoing and future research is discussed in the final part of the thesis - Chapter 8.

Chapter 1 introduces the background theory and discovery of ultracool dwarfs. We outline the search for these objects, the subsequent spectral classification and the evolutionary models which predict characteristics such as mass-radius, and gravity relations, for a given age. We also discuss magnetic activity in stellar and substellar objects, since the optical photometric campaign for the ultracool dwarfs in our sample was largely motivated by these unexpected radio discoveries. Finally, we detail the phenomenon of periodic emission from ultracool dwarfs, and the associated optical variability campaigns that continued

³The Apache Point Observatory (APO) is operated by New Mexico State University (NMSU) and owned by the Astrophysical Research Consortium (ARC). ARC consists of NMSU, The University of Washington, University of Chicago, and Princeton University. The Institute for Advanced Studies, John Hopkins University, University of Colorado and University of Virginia have also since joined. Further information can be found here: <http://www.apo.nmsu.edu/>.

- even throughout this thesis.

Chapter 2 outlines the two astronomical instruments that were designed, built and commissioned over the course of this doctoral work. The GUF1 photometer was designed and used specifically for the ultracool dwarf campaign. CHIMERA, the Caltech H1gh-speed Multi-color camERA, is a two-color photometer that is now stationed at prime focus of the 200" Hale telescope⁴, on Palomar Mountain. This instrument is a Palomar Transient Factory (PTF)⁴ follow-up instrument, designed specifically for transient source characterization at photometric wavelengths.

Chapter 3 discusses the data reduction techniques and statistical methods used for the assessment of the detected periodic variability and the associated period error, in addition to photometric errors. We briefly explain the functionality of various astronomical software packages and outline pipelines and other routines developed during this work. We also detail the reduction methods used to achieve the high-precision photometry required for ultracool dwarf photometric variability studies. The statistical tools used in this thesis include the Lomb-Scargle (LS) periodogram, Phase Dispersion Minimization, the Chi-squared (χ^2) test, sinusoid fitting algorithms, methods of phase folding datasets and period uncertainty estimation.

Chapter 4 reports on the results of the photometric campaign for six radio detected ultracool dwarfs. Periodic variability was detected for five of these targets, with the possibility of the sixth also exhibiting periodic behavior. Three of these targets are newly discovered. These results established that the dwarfs in our sample exhibit very similar photometric signatures in terms of the stability of the period (and thus features evolving or present on these timescales), and also amplitude, indicating that the thermal conditions were not greatly changing between the feature responsible for the periodicity and the surrounding photosphere.

Chapter 5 outlines the long-term stability of amplitude and phase for TVLM 513-

⁴The Palomar Transient Factory (PTF) is a fully automated wide-field survey, that is dedicated to the search for optical transient and variable sources. The 200" Hale telescope is run and operated by Palomar Observatory staff from Caltech, in addition to other partners who include Cornell University, the University of California and the Jet Propulsion Laboratory (JPL).

46546, over a baseline of ~ 5 years of data. This dwarf is shown to exhibit very stable periodic variability in both amplitude and phase over this time frame. These data were also the photometric component of a larger simultaneous spectroscopic and radio campaign, which was investigating the correlation of periodic variability across a large range of wavelengths. We find high-correlated periodic variability in this respect, which may be due to auroral emissions of the dwarf (Hallinan et al., 2012).

Chapter 6 details an investigation in to the orbital coplanarity of the low mass binaries LP 349-25AB, and 2MASS J0746+2000AB. With the newly discovered rotation periods for one component of each system in this work, along with the previously published dynamical mass measurements, rotation velocity measurements and photometry, we were able to assess the relationship of the inclination angle of the equatorial spin axes with respect to the orbital plane. We find, in the case of 2MASS J0746+2000AB, that the system is consistent with being coplanar. This is the first such direct indication of this alignment for a very low mass binary dwarf. LP 349-25AB was more difficult to assess on account of only one discovered rotation period, but at least one component is likely to be coplanar.

Chapter 7 extends the study in to the mid-M dwarf regime, where we conduct high-speed photometric monitoring of active M-dwarfs in order to investigate the white light flare emission during flaring events. These observations yielded the detection of loop oscillation events by GUF1 in B-band (high cadence, ~ 0.1 seconds) and also simultaneously in u' , g' , and r' by ARCSAT (slower cadence of ~ 30 seconds).

Finally, **Chapter 8** concludes with an overview of this work, and outlines ongoing and future projects.

“When I look down, I just miss all the good stuff. When I look up, I just trip over things.”

Ani Defranco, *As Is*

“I was born not knowing and have had only a little time to change that here and there.”

Richard Feynman

1

Background Theory and Discovery of Ultracool Dwarfs

1.1 Introduction

After years of futile searching, the first confirmed detection of a bona-fide brown dwarf was announced by Nakajima et al. (1995), who discovered the brown dwarf Gleise 229B. We now know that brown dwarfs and low mass stars account for most of the stellar mass in our galaxy. Since the time of the initial discovery, these substellar objects have now been assigned four spectral classes, which were based on the vast accumulation of stellar characteristics, both by theoretical and observational studies. In this chapter, we discuss some of the background material related to the ultracool dwarf field. § 1.2.1 summarizes the initial searches for these elusive objects, and consequently the spectral classification that followed. Progress in understanding the physics that governs the theoretical modeling of these atmospheres, has led to a much greater understanding of the dynamic and thermal properties in these regions. These atmospheres are predicted to be highly dynamic environments due to these convective properties coupled with rapid rotation (Allard et al., 2001). Thus, we also briefly outline the evolutionary models that are used to predict mass, radii, gravity and other photometric parameters, for a given substellar age. § 1.3 outlines the magnetic field environments of stellar and substellar objects, and how the dynamo model responsible for the generation of such fields in partially convective stars, no longer exists in the fully-convective regime ($\geq M3$). We also briefly discuss the magnetic fields in planets and the associated aurora in the giant magnetized planets in our

solar system. As this thesis continues, we will find correlations and similar processes for planets and ultracool dwarfs, with respect to the reported radio emission, and its connection to the observed optical photometric variability presented here. Indeed, the recent detection of coherent radio emission from a mid-T dwarf, confirming the presence of a ~ 1.7 kG magnetic field (Route & Wolszczan, 2012), is a strong indication that similar radio processes are in operation throughout the ultracool dwarf spectral sequence. Finally, § 1.4 details a large amount of the optical work carried out thus far, and describes the various photospheric or atmospheric stellar features thought to be responsible for the variability.

1.2 What is an Ultracool Dwarf?

Brown dwarfs and low mass stars are now collectively dubbed ultracool dwarfs, which is a spectroscopic term identified by spectral types $\geq M7$ (Kirkpatrick et al., 1997). Brown dwarfs occupy the mass range between gas giant planets, and low mass stars; thus they lie just at, or below, the substellar boundary. They are cool objects who reside at the tail-end of the Hertzsprung–Russell (H–R) diagram, and are therefore much cooler than stars like our Sun. Ultracool dwarfs are fully convective, and for temperatures below ~ 2000 K, their atmospheres become increasingly cool and neutral. As their life continues, they cannot maintain stable luminosities and temperatures, and thus get cooler with time; with the current generation of telescopes, it is quite difficult to observe ultracool dwarfs beyond ~ 100 pc. The brown dwarf mass range is generally considered to be between $\sim 13 - 75$ times the mass of Jupiter (M_J), with an upper limit of $\sim 75 - 80 M_J$ (i.e. $\sim 0.0012 - 0.075 M_\odot$). Let us first consider the upper end of this range. As signaled by an upper mass limit, brown dwarfs cannot sustain stable thermonuclear hydrogen-burning in their cores (like stars on the main sequence). Theory predicted that a star’s gravitational collapse would be hindered by the presence of electron degeneracy before hydrogen burning can occur (Kumar, 1963). Therefore, objects at this point with less mass than $\sim 0.07 - 0.08 M_\odot$ can never fuse hydrogen in their cores and undergo the same processes as a main sequence object. Evolutionary models such as those of Burrows et al. (1997) and Chabrier & Baraffe (2000) have been used to define the substellar boundary. They predict a hydrogen burning minimum mass (HBMM) of $0.070 - 0.075 M_\odot$ for solar metallicity. However, Ushomirsky et al. (1998) identify the HBMM to be slightly lower at $\sim 0.068 M_\odot$, with core temperatures of $\sim 3 \times 10^6$ K, surface temperatures of between $\sim 1600 - 1750$ K and luminosities of $6 \times 10^{-5} L_\odot$. We elaborate further on this in § 1.2.2.

By the early 1990s, the work of many groups had established that ultracool dwarfs

were expected to be fully convective objects, harboring high-pressure environments, and slowly losing their luminosities, temperatures, and gravitational potential energies (GPE), over a long life time (e.g. Burrows et al. (1993), and references therein). Although brown dwarfs generally cannot sustain their radiative losses via thermonuclear processes, which is used as an upper limit on their mass (outlined above), they do have some temporary thermonuclear burning. Dwarfs heavier than $\sim 0.0012 M_{\odot}$ ($\sim 13 M_J$) fuse deuterium, and those above $\sim 0.06 M_{\odot}$ ($\sim 65 M_J$) fuse lithium (Basri, 2000). Thus, the so-called ‘lithium test’ was initially used as a strong indicator for the confirmation of a brown dwarf, by the identification of the atomic lithium line at 6708 Å (Rebolo et al., 1992). More specifically, the abundance of this light element was a powerful diagnostic tool for a test of substellarity.

The principle of the lithium test is as follows: fusion enables a star to burn its lithium in ~ 100 Myr due to the associated core temperatures. However, observations of low mass objects by Dantona & Mazzitelli (1985), found that for objects $< 0.06 M_{\odot}$, subject to core degeneracy, the minimum lithium burning temperature could not be achieved. The test can be somewhat ambiguous, however. Consider the following: for a young stellar object, lithium can be depleted. But it can also be depleted for a much older larger mass brown dwarf. In addition to this, in the case of mid to late-T dwarfs, lithium is now in molecular form and thus cannot be detected by the 6708 Å line, although it can be identified at the $\sim 15.5 \mu\text{m}$ band (Burrows et al., 2001). The spectral properties of M to Y dwarfs have since been characterized by a large number of ground and space studies, and therefore the lithium test is no longer relied upon for brown dwarf confirmation. Although the Wide-Field Infrared Survey Explorer (WISE) space telescope has many mission science goals and capabilities, a large portion of its time is dedicated to the search and characterization of ultracool dwarfs, and can provide high-resolution spectra which is ideal for such spectral characterization. We elaborate further on this point in § 1.2.3.

At the lower end of the ultracool dwarf range lies the transition between giant planets and brown dwarfs. Although the deuterium fusion point at $\sim 0.0012 M_{\odot}$, or $\sim 13 M_J$, is generally accepted as the defining characteristic that signals the presence of a brown dwarf, some formation properties can also be used. Burrows et al. (2001) discuss such formation processes as a proxy for this classification - whereas brown dwarfs form by the gravitational collapse of an interstellar cloud, planets form via the presence of protoplanetary disks and require the initial formation of a rocky core. Furthermore, planets do not undergo thermonuclear fusion, and since deuterium fusion occurs at roughly $0.0012 M_{\odot}$, this mass was consequently adopted as the giant planet/brown dwarf boundary.

A brown dwarf is therefore defined as a substellar ($\sim 0.0012 - 0.075 M_{\odot}$), fully convec-

tive object, whose mass is not large enough for hydrogen fusion, but is capable of fusing lithium at $\sim 0.06 M_{\odot}$, and deuterium at $\sim 0.0012 M_{\odot}$. We now discuss the long awaited discovery of a brown dwarf, which was predicted over 30 years before the announcement, in 1995.

1.2.1 The Search for Brown Dwarfs: a Brief History

The earliest dedicated searches for brown dwarfs was a frustrating time for astronomers, where false alarms and upper limit constraints were often reported - likely due to the sensitivity limits of technology that was available at the time. We note that comprehensive reviews can also be found in Oppenheimer et al. (2000) and Basri (2000). The earliest surveys included looking for candidates in clusters, companion searches, deep imaging and radial velocity studies. Three main categories were identified in the brown dwarf population: the first were the oldest, visible dwarfs, whose temperatures and luminosities were much lower due the lack of sustained thermonuclear fusion. The second category included dynamically active brown dwarfs, whose orbital properties allowed tentative estimates of their mass. These studies were conducted by observing the gravitational perturbations of the dwarf's stellar companion. However, any estimates were considered as lower limits only, since the inclination angle of the system's orbit was either poorly constrained, or unknown. The third category were young, luminous dwarfs, and were sometimes difficult to distinguish between the lowest mass stars at a young age. Since brown dwarfs were expected to be very red objects, a large amount of infrared imaging was used for these early searches. One of the first detections was reported by McCarthy et al. (1985), who claimed they located a companion to the flare star VB 8B, via IR speckle imaging. However, subsequent follow-up observations by Perrier & Mariotti (1987) and Skrutskie et al. (1987) failed to detect this source, which was likely an unexpected artifact in the data. More surveys by Skrutskie et al. (1989) and Henry & McCarthy (1990) followed which did yield tentative results, however these detections were later confirmed to be low mass stars. Latham et al. (1989) conducted radial velocity measurements of the star HD 114762, and reported small-scale variations at the very edge of their detection limit. These observations implied a mass of $\sim 11 M_J$ for the companion star. Alas, the poorly constrained inclination of the system hindered a bona fide confirmation.

At this time and in the years that followed, a number of large optical and radio surveys were conducted which yielded interesting, but ultimately unsuccessful results (Krishna Kumar, 1985, 1987; Boeshaar et al., 1986; Skrutskie et al., 1990; Henry & McCarthy,

1990; Shipman, 1986; Beichman, 1987; Winglee et al., 1986). This was once again a time of heightened frustration, and indeed skepticism in the brown dwarf community. Would the detection of a substellar object ever come? Interestingly, another study at this time reported a faint companion to GD 165 in an infrared search of white dwarfs (Becklin & Zuckerman, 1988). Kirkpatrick et al. (1993) identified this object as having a cool spectrum and thus was one of the strongest brown dwarf candidates at that time. However this potential candidate has not yet been confirmed as a substellar object - even today. Other surveys of the Hyades, Taurus and Pleiades clusters were carried out, as well as in ρ Ophiuchus and Lk H α 101, identifying a number of potential candidates, but most were later confirmed to be background or stellar sources, e.g. Leggett & Hawkins (1989); Forrest et al. (1989); Rieke & Rieke (1990); Barsony et al. (1991); Bryja et al. (1994); Marcy et al. (1994). In the 1995 meeting of AAS⁵, G. Basri and his research collaborators announced a substellar candidate that appeared to have passed the lithium test for substellarity (later Basri et al. (1996)). This was the M6.5 dwarf PPl 15, which showed the 6708 Å lithium line. However, at the time, an accurate measure of the age of the Pleiades cluster had not yet been established - the cluster where the brown dwarf lay. This delayed the confirmation of PPl 15 as a bona fide brown dwarf, which was subsequently confirmed to be the case.

It was at the Tenth Cambridge Cool Stars Workshop in Florence in 1995, that Nakajima et al. (1995) announced the undisputed discovery of a brown dwarf. With a mass $\sim 20 - 50 M_J$, Gliese 229B was detected as a faint companion to the nearby red dwarf, Gliese 229. Although the group detected this companion in their data a year previous to this, they waited for proper motion confirmation before announcing the result. The unexpected detection of methane was reported in the atmosphere of Gliese 229B by Oppenheimer et al. (1995) - a signature common in the atmospheres of planets. This session was in fact the same meeting that the first extrasolar planet discovery was announced. More discoveries were announced at a conference two years later, thus the population of ultracool dwarfs began to grow (Basri, 2000). Confirming the presence of substellar objects in our galaxy had been accomplished, and the age of characterization had now begun.

1.2.2 Interior Physics

Here we present a brief summary of the physics associated with ultracool dwarfs. The subtleties of substellar (and stellar) interiors are largely signaled by their equation of state,

⁵American Astronomical Society meeting.

which defines the relationships between an object's pressure, mass and temperature. In the low mass star regime however, consideration of a number of factors (described below) are required in order to effectively derive their equation of state. This review is largely based on the reviews of Burrows et al. (1997), Basri (2000), Chabrier & Baraffe (2000) and Burrows et al. (2001). For a more in-depth analysis of these effects, we refer the reader to these texts, and the references therein.

It has now been well established that stars $\geq M_3$ become fully convective objects. Here lies the realm of low mass stars, where the physics can vary depending on the mass of the object. These interiors exhibit densities of $\rho_c \simeq 10 - 10^3 \text{ g cm}^{-3}$, temperatures of $T_c \leq 10^6 \text{ K}$ and pressures of $P_c \simeq 10^5 \text{ Mbar}$ (Burrows et al., 2001), requiring considerations of pressure partial ionization, and polarized and partially degenerate classical and quantum plasmas. Indeed, the plasmas in M_3 stars and greater still behave classically, whereas the matter for stars at the HBMM is subject to partial degeneracy, described by the degeneracy parameter, $\psi = kT/kT_F$. The electron Fermi temperature⁶, T_F , will indicate the degree of degeneracy, where the Maxwell-Boltzmann (classical) limit is $\psi \rightarrow +\infty$, and in the case of full degeneracy (characterized by Fermi-Dirac statistics), $\psi \rightarrow 0$. We show the relationships between the central temperatures, the densities and the degeneracy parameter with respect to a range of mass for ultracool dwarfs and substellar objects (of both solar metallicity at 5 Gyr, and metallicities of the order of $10^{-2} Z_\odot$ for 10^8 years) in Figure 1.1 (Chabrier & Baraffe, 2000). Let us consider central pressures and densities.

In accordance with the standard model for stellar structure, main sequence stars have a polytrope index of $n = 3$. A measure of the polytrope index is important, since it refers to the Lane-Emden equation which relates the pressure (P_c) to the density (ρ_c), and is given by $P_c = K \rho_c^{((n+1)/n)}$, where K is a constant. Due to an increasing radiative core for stars of $M \geq 0.4 M_\odot$, the polytrope changes from $n = 3/2$ to $n = 3$ as the mass (M) increases. We pointed out before that stars below $M \sim 0.4 M_\odot$ become fully convective (with an associated polytrope index of $n = 3/2$), where $M \propto \text{radius } (R)$, and the $\rho_c \propto M^{-2}$, since the gas still behaves in the classical regime. As a star approaches the HBMM point, the electron degeneracy, ψ , is ≤ 0.1 and thus is approaching complete degeneracy. The properties therefore change again, where $M \propto R^{-3}$, and $\rho_c \propto M^2$, signaling non-monotonic behavior of ρ_c and P_c with respect to mass. These mass-radius relations do not quite apply to objects like Jupiter or brown dwarfs that are subject to partial degeneracy, since all have

⁶The Fermi energy is essentially the energy of the highest quantum state in a system of fermions at absolute zero temperature; Fermions include quarks and leptons. N.B. The Pauli Exclusion Principle states that no two identical particles can occupy the same quantum state simultaneously.

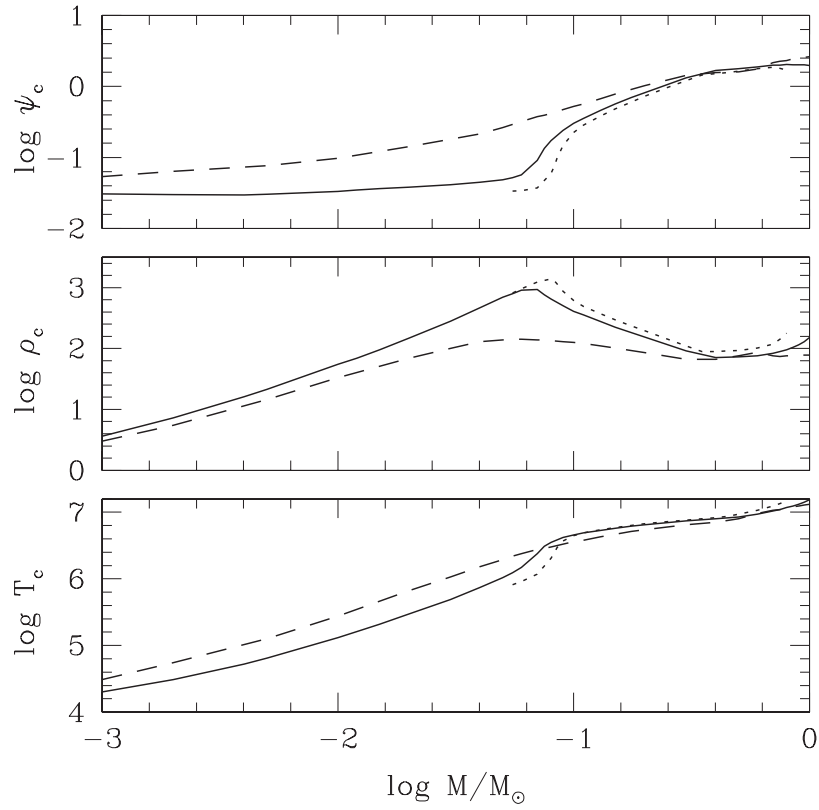


Figure 1.1: We show plots of mass versus central temperature, T_c (in K), central density, ρ_c (in g cm^{-3}), and degeneracy parameter, ψ_c , for low mass stars and substellar objects of both solar metallicity (Z_\odot) at 5 Gyr (*solid line*), and metallicities of the order of $10^{-2} Z_\odot$ for 10^8 years (*dotted line*). This was taken from Chabrier & Baraffe (2000).

similar radii yet can span orders of magnitude in mass. So, strong consideration of these correlated effects must be included in an equation of state derivation.

Finally, regarding the chain reactions that support thermonuclear burning. Ultracool dwarf formation follows standard formation theory via the various fragmentation stages of stellar evolution (e.g. Bodenheimer (1978); Shu et al. (1987)). This includes the collapse of interstellar molecular clouds and thus the gravitational contraction of a protostar (substellar in this case). When contracting protostars, of mass greater than the HBMM, reach core temperatures and pressures high enough to ignite the proton-proton chain (pp-I), these reactions provide $\sim 99\%$ of the energy for substellar objects ($\leq 0.07 M_\odot$), whereas pp-II reactions only contribute $\sim 1\%$. The first branch in the pp-I fusion chain (Equation 1.1 below) defines the thermonuclear burning processes of ultracool dwarfs, and is the most relevant for these objects (Burrows et al., 1993; Chabrier & Baraffe, 1997):

$$p + p \rightarrow d + e^+ + \nu_e \quad (1.1)$$

$$p + d \rightarrow \gamma + {}^3\text{He} \quad (1.2)$$

$${}^3\text{He} + {}^3\text{He} \rightarrow {}^4\text{He} + 2p \quad (1.3)$$

Deuterium burning, although short-lived due to its low abundance, was predicted by Hoxie (1970), for objects above $\sim 0.0012 M_\odot$, and is sustained for $0.1 < \tau < 10$ Myr. During this stage of deuterium burning, $\sim 95\%$ of the total luminosity radiated from the star is given by Equation 1.2, whereas lithium isotopes will burn for stars $\geq 65 M_J$ ($M \geq 0.06 M_\odot$) via the following reactions:

$$p + {}^7\text{Li} \rightarrow 2\alpha \quad \text{and} \quad p + {}^6\text{Li} \rightarrow \alpha + {}^3\text{He} \quad (1.4)$$

where the lithium depletion point is somewhere about 100 Myr (Chabrier & Baraffe, 2000). Lithium burning occurs at this mass of $M \sim 0.06 M_\odot$, as opposed to the HBMM of $\sim 0.07 M_\odot$. It was thus because of the close proximity of the lithium burning point to the HBMM, that the presence of the lithium absorption line at 6708 Å was initially used as a test of substellarity.

1.2.2.1 Temperatures, Luminosities, Radii and Gravity

The evolution of brown dwarfs, which has largely been based on synthetic spectra and other models, has been documented at length by the works of e.g. Chabrier & Baraffe (2000) and Burrows et al. (2001). There is a significant departure in the atmospheric conditions of ultracool dwarfs than earlier M-type dwarfs. The increasingly cooler atmospheres allow for the presence of atmospheric particulates, the collisional excitation (absorbers and emitters) and the formation of various molecular species, depending on the temperature - and other factors such as gravity. Since these substellar objects can never stabilize their temperatures and luminosities, and thus their radiative losses, we observe a slow and steady decrease in their temperature profiles after the initial protostellar contraction phase. We can clearly see this cooling by considering the evolution of the effective temperatures (T_{eff}) for a given mass, as a function of time, in Figure 1.2. Whereas brown dwarfs of $\sim 0.075 M_\odot$ can sustain temperatures of a few thousand Kelvin (up until ~ 300 Myr), after this time

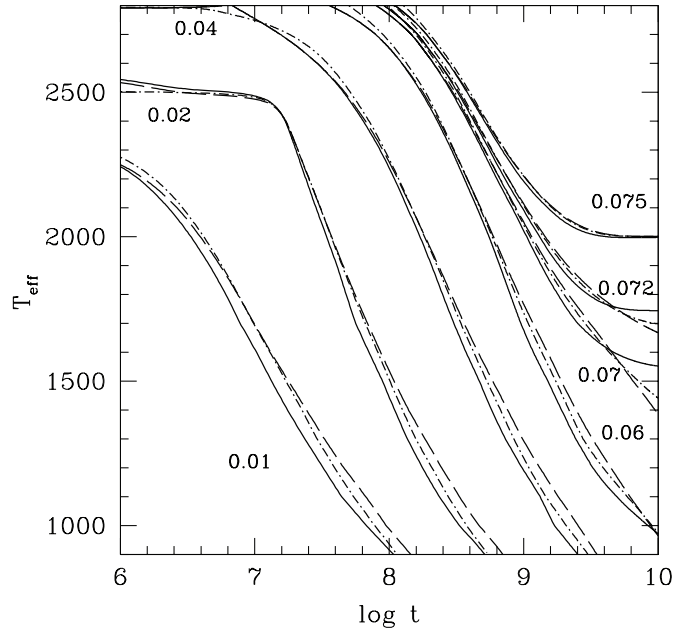


Figure 1.2: Evolution of T_{eff} versus time ($\log \tau$, years). The different masses and evolutionary model sets are shown by the *solid*, *dashed*, and *dash-dotted* isochrones. The *solid lines* correspond to the DUSTY models, which consider turbulent mixing in the atmospheric regions. The *dashed lines* represent the COND models, specific to inefficient atmospheric mixing. And the *dash-dotted lines* show the NextGen models, developed by Allard et al. (1996), which have dust-free environments. We show this plot for the purpose of illustrating the steady decrease in substellar temperature, for a given mass, as a function of time. This plot was taken from the work of Chabrier & Baraffe (2000).

temperatures will never stabilize and will slowly fall for the brown dwarf's life.

Burrows et al. (1997), Chabrier & Baraffe (2000) and Burrows et al. (2001) identify this HBMM point to be $\sim 0.070 - 0.075 M_{\odot}$, and Ushomirsky et al. (1998) infer a HBMM temperature of $\sim 3 \times 10^6$ K, with surface temperatures of between $\sim 1600 - 1750$ K, and luminosities of $6 \times 10^{-5} L_{\odot}$. Similarly, Burrows et al. (2001) identify the minimum stellar luminosity to be $\sim 6 \times 10^{-5} L_{\odot}$. Burrows et al. (2001) also discuss relations which have been used to adequately estimate evolutionary parameters in low mass star formation:

$$T_{\text{eff}} \sim 1550 \text{K} \left(\frac{10^9 \text{yr}}{t} \right)^{0.32} \left(\frac{M}{0.05 M_{\odot}} \right)^{0.83} \left(\frac{\kappa_R}{10^{-2} \text{cm}^2 \text{gm}^{-1}} \right)^{0.088} \quad (1.5)$$

$$L \sim 4 \times 10^{-5} L_{\odot} \left(\frac{10^9 \text{yr}}{t} \right)^{1.3} \left(\frac{M}{0.05 M_{\odot}} \right)^{-2.64} \left(\frac{\kappa_R}{10^{-2} \text{cm}^2 \text{gm}^{-1}} \right)^{0.35} \quad (1.6)$$

where κ_R is the mean opacity. These clearly follow power-laws, however the formulation

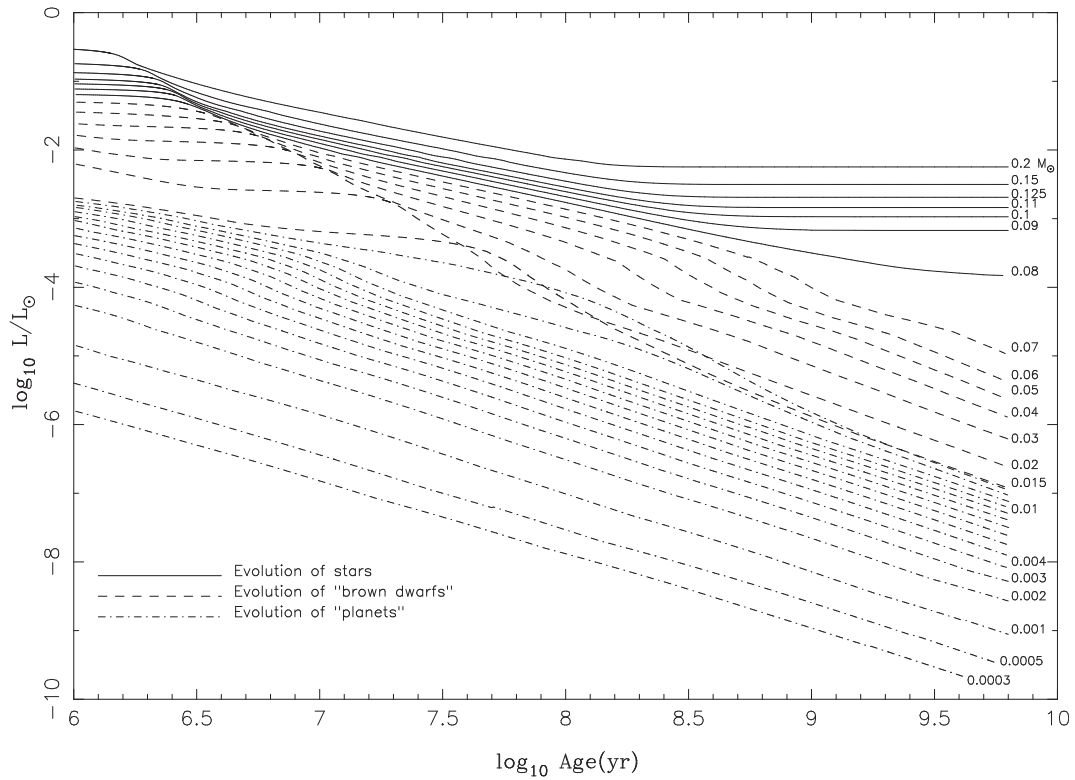


Figure 1.3: Evolution of luminosity (L_{\odot}) of M dwarfs and substellar objects, with solar-metallicity $Z = Z_{\odot}$, as a function of time ($\log \tau$, years). Stars are shown with *solid lines*, whereas brown dwarfs and planets are shown with *dashed* and *dashed-dotted* lines, respectively. This plot was taken from the work of Burrows et al. (1997), where they define a planet as an object that does not achieve deuterium burning (at $\sim 0.0012 M_{\odot}$). The lowest three curves are that of objects with masses equal to Saturn, half the mass of Jupiter and finally one Jupiter mass. The luminosity disconnect for stars and brown dwarfs is clearly shown at ~ 1 Gyr, or $\log \tau 9.0$.

of such relations are based on solar-type metallicities, and this, in addition to other parameters such as the atmospheric opacity, can result in different solutions for equation 1.5 and equation 1.6 above.

Although a brown dwarf's temperature and luminosity changes quite significantly with time, models (Burrows et al., 1997) predict quite a stable evolution of the dwarf's radius over its lifetime. We illustrate this in Figure 1.4 taken from the models of Burrows et al. (1997), where we show evolutionary model-derived plots of T_{eff} vs. R , as a function of time from ~ 300 Myr - 3 Gyr ($\log 6.5 - 9.5$ years). These plots show a steady decrease in the radius, likely due to factors such as compression due to increasing degeneracy over its lifetime (Burrows et al., 1993). Although much larger for a younger object, the radius of

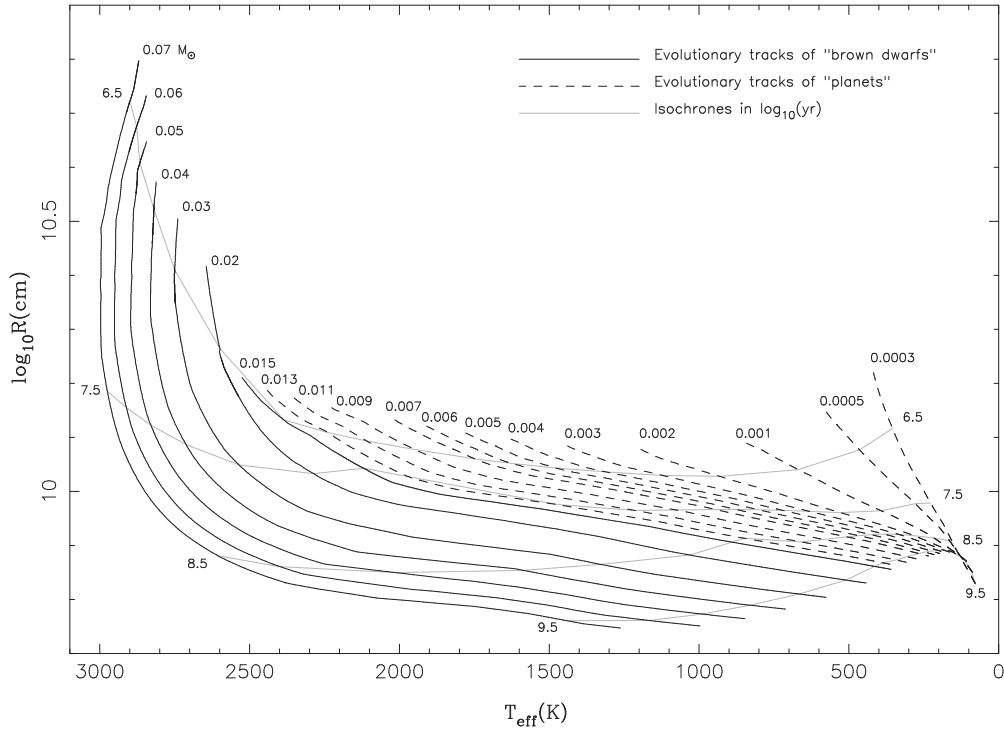


Figure 1.4: Plot of radius (R) vs. effective temperature (T_{eff}), for dwarfs from $0.0003 M_{\odot}$ (i.e. mass of Saturn) to $0.07 M_{\odot}$ (HBMM). This is shown for a range of ~ 300 Myr - 3 Gyr, or $\log 6.5 - 9.5$ years. The *solid lines* represent brown dwarfs, whereas the *dashed-lines* trace the evolution of the lowest mass brown dwarfs, where the upper limit of this range is approximately at, or just above, the deuterium fusion point. Taken from Burrows et al. (1997).

a brown dwarf is usually within $1.0 \pm 0.4 R_J$ over most of their life. Indeed, the models of Chabrier & Baraffe (2000) also follow this relation. Similar to Burrows et al. (1993), Marley et al. (1996) report the following formulas that describe relations of mass and radius for low mass objects:

$$M \sim 36 M_J \left(\frac{g}{1000} \right)^{0.64} \left(\frac{T_{eff}}{1000} \right)^{0.23} \quad (1.7)$$

$$R \sim 67200 \text{ km} \left(\frac{g}{1000} \right)^{-0.18} \left(\frac{T_{eff}}{1000} \right)^{0.11} \quad (1.8)$$

where, again, changes in metallicity and opacity can yield different results.

The surface gravity for low mass and main sequence stars can range from a $\log g \simeq 4.4$ for an object of $\sim 1 M_{\odot}$, a $\log g \simeq 5.5$ at the HBMM for $Z = Z_{\odot}$, to $\log g \simeq 3.4$ for

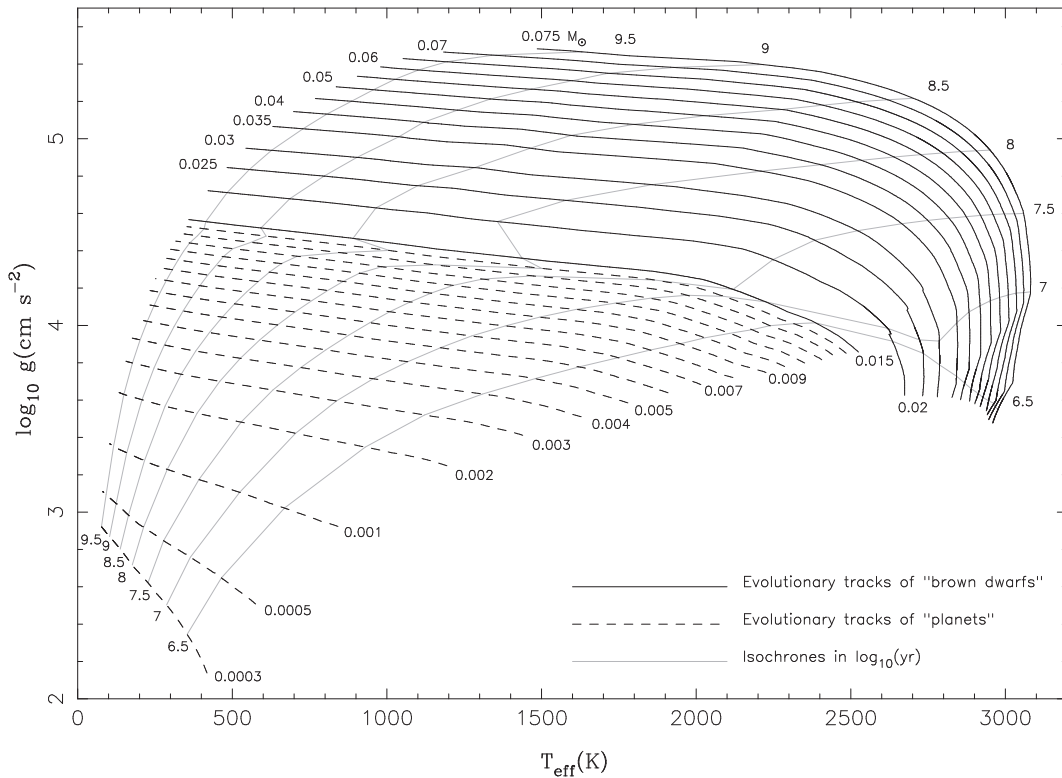


Figure 1.5: Gravity (g , cm s^{-2}) versus effective temperature (T_{eff} , in K) for brown dwarfs and planets, for a range of masses ($0.0003 - 0.075 M_{\odot}$), over a range of ages from 300 Myr - 3 Gyr ($\log 6.5 - 9.5$ years). Note that gravity steadily increases with time for all *solid tracks*, indicating brown dwarfs, and *dashed lines*, representing planets. Taken from Burrows et al. (1997).

objects at the deuterium burning limit and below ($\leq 0.0012 M_{\odot}$). Similar to how the radii evolves for these objects, we show in Figure 1.5 that for relatively flat mass tracks, the gravity remains constant for a given age - except for the highest mass brown dwarfs, who are likely undergoing a period of contraction at higher temperatures and earlier stages of their evolution.

1.2.3 Atmospheres and Spectral Classification: from M- to Y-Type Dwarfs

The atmospheres of ultracool dwarfs are high gravity, high pressure environments, subject to a rich diversity of molecular particulates and thus atmospheric chemistry. It is thought to be at roughly $\sim M3$ that objects move away from partially convective configurations, up to that point possessing both convective and radiative layers, to fully convective stars.

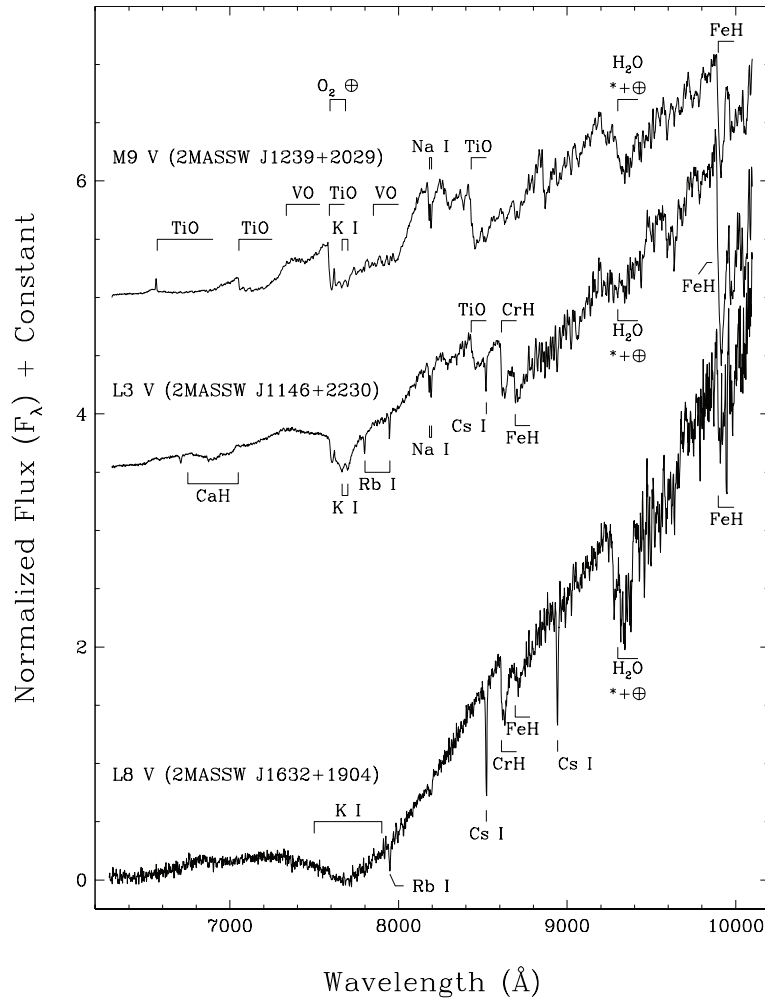


Figure 1.6: Spectra of a late-M, early to mid-L and late-L dwarf, taken from Kirkpatrick et al. (1999). They have marked the prominent metal hydrides, metal oxides, strong absorption lines and neutral alkali and dust grains. It is quite clear that the spectrum of the L-dwarf does *not* contain the oxide absorption features, whereas it is dominated by alkali and hydride bands.

Below this point (≤ 4000 K), hydrogen and carbon are generally found in H_2 and CO form, where other species present such as TiO, VO and H_2O contain oxygen (where there is a less abundance in OH and O molecules) (Fegley & Lodders, 1996). Other metal oxides are also present such as FeH, CaH and MgH, and strong absorption lines of TiO and VO (optical) and H_2O and CO (IR) are prominent. It is at roughly 2000 K that these characteristic TiO and VO bands of M dwarfs condense to form neutral alkalis and iron hydrides. Thus, these band strengths signaled the M dwarf spectral classification (Kirkpatrick et al., 1991, 2000). However, at ~ 2000 K or so, TiO and VO markers become far less dominant, where only a

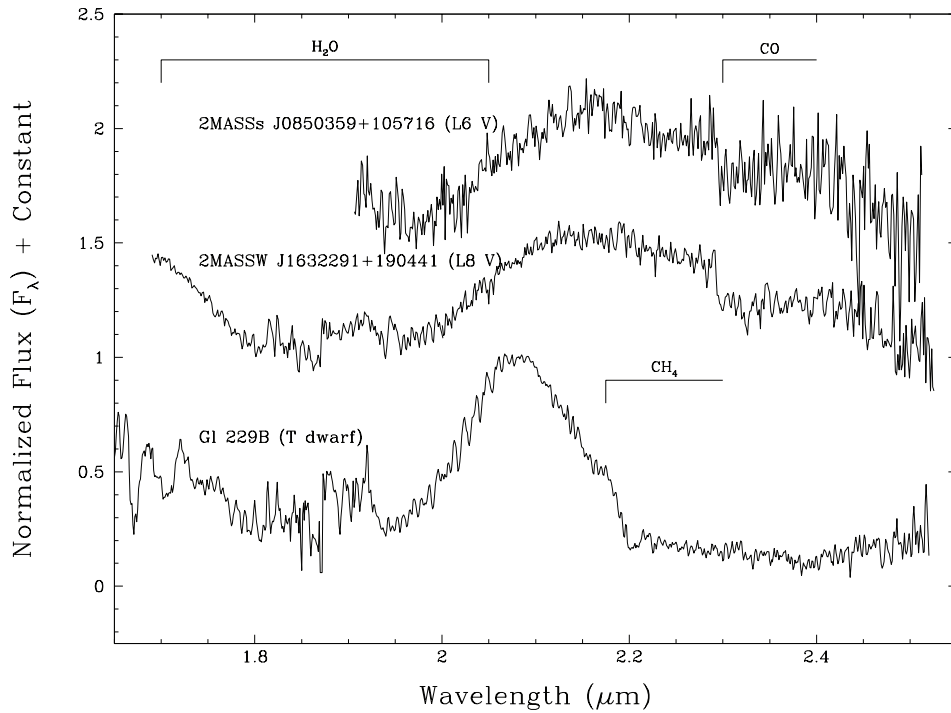


Figure 1.7: Here we show NIR spectra from a mid-L, a late-L and a T dwarf (Gliese 229B), taken from Kirkpatrick et al. (1999). We point out in the spectra above, the absence of methane (CH_4) in the late-L dwarfs, however the CO absorption features are still present.

small amount remains in the spectra.

It has been well established via spectroscopic observations of L dwarfs, that absorption at these wavelengths is due to the presence of metal hydrides (FeH, CrH, CaH, MgH), strong alkali lines (K, Na, Rb, Cs) and CO and H_2O absorption lines. The level of opacity also changes as a result of the existence of chemical particulates (Al, Ca, Fe, Mg, Si) (Kirkpatrick et al., 1999; Martín et al., 1999). We show the difference in spectra between a late-M, early to mid-L and late-L dwarf in Figure 1.6, where we point out the weakening/absence of oxide absorption (TiO) features in the L dwarf spectra, and the dominance of the alkali and hydride bands, e.g. CrH & FeH (Kirkpatrick et al., 1999). In addition to this, the L I, Rb I and Cs I lines strengthen whereas Na I weakens as we move down the spectral sequence. Indeed, ultracool dwarfs are very cool objects and thus are very red in the optical/near infrared (NIR). Furthermore, the increasing slope after $\sim 7500 \text{ \AA}$ also contributes to the color, which is very obvious in Figure 1.6, is caused by the broadening of the K I doublet. Kirkpatrick et al. (1999, 2000) derived an effective temperature range for L dwarfs based on the optical features in the spectra, and defined this to be $2000 \sim 1300$

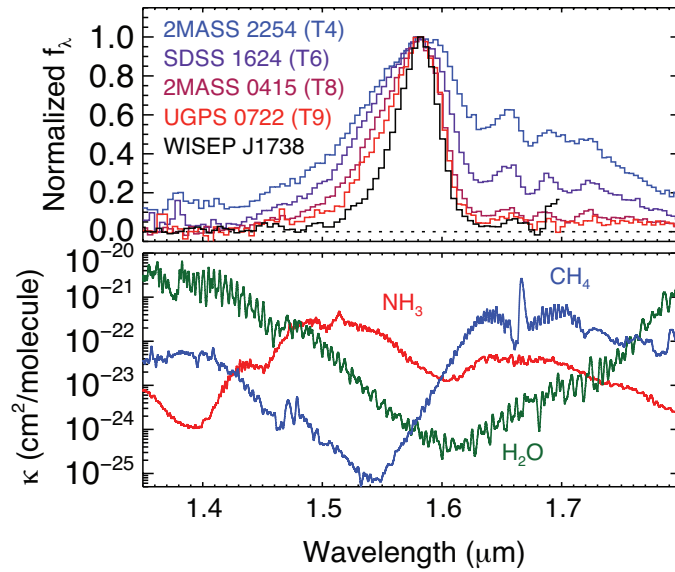


Figure 1.8: *TOP*: Plots from Cushing et al. (2011), who show a H -band spectrum of five ultracool dwarfs, spanning the T4 - Y0 spectral range. The T4, T6 and T8 spectra are the spectral standards of Burgasser et al. (2006), whereas the T9 and Y0 are WISE discoveries. *BOTTOM*: Opacities: NH_3 (Yurchenko et al., 2011), CH_4 (Freedman et al., 2008) and H_2O (Freedman et al., 2008) for $T_{\text{eff}} \sim 600$ K and $P = 1$ bar. Note that the WISEP J1738+2732 dwarf shows excess absorption that correlates to the NH_3 , as shown.

K. Other studies, such as Basri & Martín (1999); Pavlenko et al. (2000); Stephens et al. (2001); Leggett et al. (2001) show consistent predictions for the upper end of this range, but can vary up to +300 K for the lower end.

As we move down the sequence, the L/T transition has largely been identified by a further decrease in condensate opacity, where the effective temperature remains relatively stable (Golimowski et al., 2004; Stephens et al., 2009). Furthermore, the equilibrium form of CO molecules slowly become CH_4 at about 1300 - 1500 K. These dwarfs were initially dubbed the ‘methane dwarf’, and later the T dwarf. In fact, the first bona fide brown dwarf, Gliese 229B, was spectroscopically confirmed to be a T dwarf after methane absorption lines were detected (Oppenheimer et al., 1995). The features of this spectral class are now signaled by the absence of hydride bands, with much more prominent H_2O absorption features than an L dwarf in the optical. Figure 1.7 shows spectra from two late-L dwarfs and a T dwarf, highlighting the transition across the L/T boundary, where the detected CH_4 of the ‘prototype T dwarf’, Gliese 229B, is marked. We can clearly see that in the IR, H_2O and CH_4 also dominate. We refer the reader to Burgasser et al. (2002) and references therein, for an in-depth discussion of T dwarfs, and their spectral classification, and Kirkpatrick

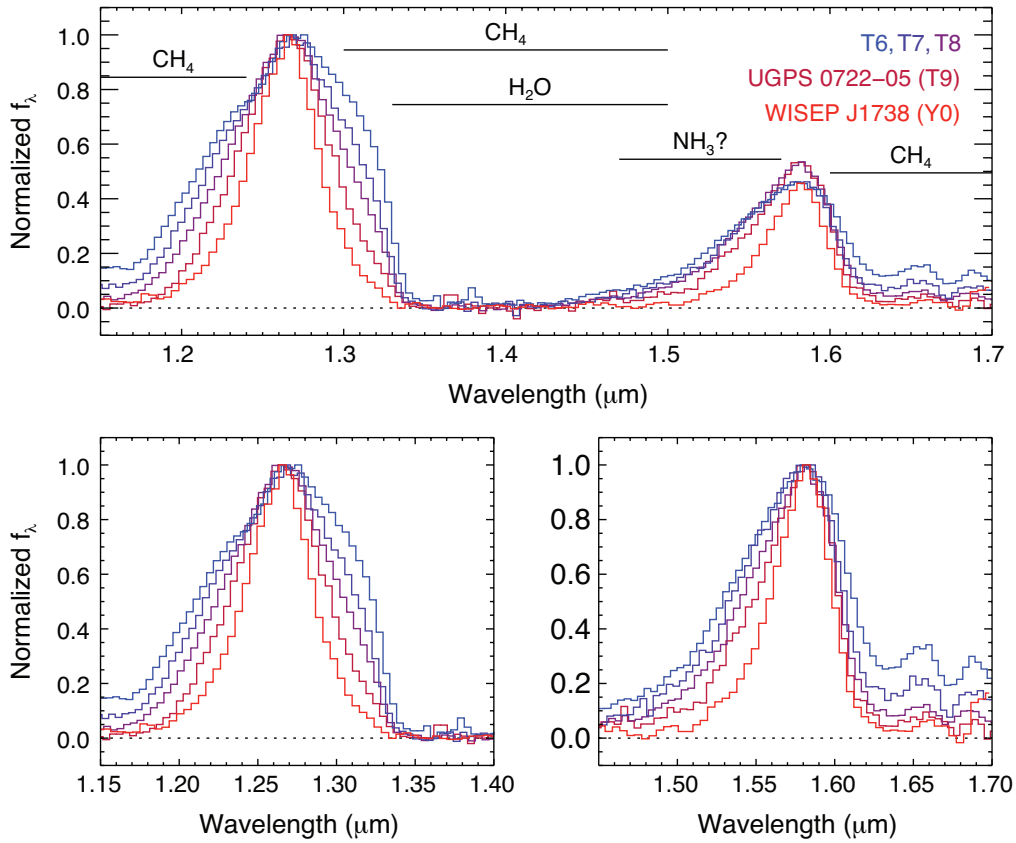


Figure 1.9: Plots from Cushing et al. (2011), that show the spectral standards of a T6, T7 and T8 dwarf Burgasser et al. (2006), as well as a T9 and Y0 dwarf newly discovered by WISE and reported in their paper. Cushing et al. point out that WISEP J1738+2732 exhibits absorption from 1.53 - 1.58 μm , perhaps identifying NH_3 as the feature responsible. They illustrate this further in the *bottom right* plot, where the tentative NH_3 absorption is much more prominent when compared to T6 - T9 standards. They also point out the roughly even change in width of the *J*-band peak (*bottom left*), as opposed to the obvious decline of the blue component of the *H*-band between UGPS 0722-05 (T9) and WISEP J1738+2732 (the now Y0).

(2005) for a detailed overview of the L and T spectral sequence.

In the years that followed the spectral classification of M, L and T dwarfs, some groups proposed the creation of a fourth spectral class - the ‘Y dwarf’, that would follow the T dwarf range (e.g. Burrows et al. (2003); Kirkpatrick (2008)). There were certain properties that were predicted to be quite distinct from T dwarfs, which in turn supported a new spectral range. For example, atmospheric models predicted that the NIR colors of cool dwarf atmospheres (which are much bluer for the hotter T dwarfs due to CH_4 dominated flux in the *H*- and *K*-bands), would move toward the red at roughly 300 - 400 K - effec-

tively at the end of the Wien tail of the SED⁷. The Y spectral class was finally invoked by Cushing et al. (2011), who assigned the Y spectral classification to the Y0 dwarf WISEP J1828+2650, along with five others, with temperature ranges of 300 - 500 K (the coolest brown dwarfs discovered at that point). These were discovered by the WISE space mission and provided a clear morphological spectral transition between the T and Y spectral classes. Although the characteristic T dwarf CH₄ and H₂O bands were also present, Cushing et al. (2011) reported absorption from 1.53 - 1.58 μ m, which tentatively identified NH₃ as the feature responsible. Cushing et al. (2011) illustrate this further in Figure 1.9 (*bottom right*), where the (apparent) NH₃ absorption is much more prominent when compared to T6 - T9 standards. They also point out the roughly even change in width of the *J*-band peak (*bottom left*), as opposed to the obvious decline of the blue component of the *H*-band between UGPS 0722-05 (T9) and WISEP J1738+2732 (the now Y0). Furthermore, they identified a feature from WISEP J1828+2650 that was *not* in any T dwarf. That was that the amplitude of the *J*- and *H*-band intensities, plotted in units of normalized f_λ , were roughly equal. Furthermore, this was the reddest brown dwarf in their sample. We show the spectra from Cushing et al. (2011), of early to mid- and late-T dwarfs, and a newly classified Y0 dwarf, WISEP J1738+2732, in Figure 1.8.

Therefore WISEP J1738+2732 was assigned a Y0 spectral classification. Lastly, the *J-H* colors of the newly discovered Y dwarfs suggest that they are indeed turning toward the red, as predicted by Burrows et al. (2003) and Kirkpatrick (2008), which is consistent with models for objects of $T_{eff} \sim 300 - 400$ K.

1.3 Stellar and Substellar Magnetic Activity

Magnetic activity is an important diagnostic tool in understanding the various structures in regions of a stellar or planetary atmosphere. Radio observations provide the means of assessing such structures at different layers of these atmospheres. The Sun is a strong radio source and consequently was one of the first objects detected by radio telescopes. In fact, J. S. Hey detected a large solar flare from the Sun in 1942 via meter-wavelength radar receivers. Therefore, the various emission mechanisms responsible for quiescent and flaring emission were investigated soon thereafter. In this section, we will briefly discuss the mechanisms responsible for radio emission from the Sun and stars, including the magnetic dynamo that sustains and generates solar magnetic fields. We also give a summary of radio

⁷Spectral Energy Distribution.

discoveries and the associated mechanisms from ultracool dwarfs, and outline the changes in magnetic field configurations and topologies that have been observed down the M spectral sequence, and what proposed dynamo mechanism could be responsible for these manifestations. Finally, aurorae have also been detected at low radio frequencies from some of the magnetized giant planets in our solar system. We briefly discuss the beamed emission responsible for the observed radio bursts, from the planet Jupiter. Indeed, this mechanism is also responsible for the observed periodic bursts of radio emission from ultracool dwarfs (Hallinan et al., 2008). Later in this thesis, Chapter 5 outlines the optical and NIR photometric component of a recent large simultaneous spectroscopic, radio and photometric campaign, that sought to investigate the (correlated) emissions from the M9 dwarf TVLM 513-46546 (Harding et al., 2012a; Hallinan et al., 2012). These photometric observations now appear to be inextricably linked to the radio and spectroscopic emissions, and are auroral in nature. We therefore include the sections that follow, to provide the reader with some context for these connections, in stellar, substellar and planetary regimes.

1.3.1 Radio Emission from the Sun and Stars

This section follows treatments given by Dulk (1985), and we refer the reader to these texts and the references therein for a more in-depth analysis. Many forms of radio emission have been observed in stellar and substellar regimes. The characteristics of these emissions can manifest themselves over a range of radio frequencies, depending on the amount of energy associated with the event. For example, a number of mechanisms thought to be responsible for quiescent or continuum, non-flaring, radio emission have been well characterized (usually attributed to incoherent radiation processes), in addition to more energetic events such as solar flares (detected via bursts of radio emission, and largely associated with coherent radiation). Indeed, many of the radio processes that have been detected in stars were first identified from studies of our Sun.

A large amount of detected radio radiation, is due to collisional excitation where electrons are accelerated or deflected in Coulomb fields and collide with ions, thus causing braking or deceleration or charged particles. This known as bremsstrahlung or ‘free-free’ emission, where the kinetic energy is converted into photons. Alternatively, electrons could also follow spiral paths within a magnetic field, which can often yield much greater accelerations in comparison to particle collisions. These emission processes are called incoherent radiation. For mildly relativistic particles, gyration around these field lines is known as gyro-synchrotron emission, whereas for ultra relativistic particles, it is known as synchrotron

emission. Cyclotron, or gyroresonance emission, is also present, but for nonrelativistic particles. However in some cases, instabilities can occur in the plasma, and can lead to coherent emissions, such as the electron-cyclotron maser (ECM). These particle-wave plasma instabilities are caused by the resonance between gyrating electrons in the magnetic field and the electric field of electromagnetic waves at a given frequency. Plasma radiation is another example of coherent emissions. These are detected at specific frequencies, and can also be generated at the first harmonic in the case of plasma radiation.

We briefly turn to the coherent ECM mechanism, since we will see in the next section that the observed bursts of radio emissions from ultracool dwarfs have now been attributed to the ECM instability - although we note that other processes are likely also present and responsible for the quiescent non-flaring component of the radio emission (see: Hallinan et al. (2008)). The ECM is a non-thermal process that was first investigated by Twiss (1958) and Schneider (1959). However, contrary to these studies that predicted environments that allow for escaping radiation from the plasmas, Wu & Lee (1979) unexpectedly showed that these conditions were not necessarily as extreme, and demonstrated that the radiation could in fact arise from less hostile conditions. The ECM mechanism is a very important emission process, and in some cases is responsible for the coherent radiation detected from magnetized plasmas. These plasmas require instabilities to drive the maser, in addition to strong magnetic fields (see Dulk (1985)). Twiss & Roberts (1958) and Mangeney & Veltri (1976) both investigated the ECM in the context of detected solar radio type I bursts. Others, e.g. Melrose (1976) and Hewitt et al. (1981), showed that it could be used to explain the decametric radio emission from the Jovian magnetosphere. In the same work mentioned above, Wu & Lee (1979) used ECM to interpret the kilometric radiation from Earth - i.e. the aurora. Thus, the ECM has been identified as the mechanism responsible for the Earth's aurorae, Jupiter's decametric emission, and others. Could ECM also be used to interpret emissions from ultracool dwarfs? We discuss this in the following section.

1.3.2 Radio Emission from Ultracool Dwarfs

It has been well established that stars with higher mass generate (and amplify) their magnetic fields via the $\alpha\Omega$ -dynamo (Parker, 1975). The basis for supporting any magnetic field by some effective dynamo is via the motion of a conducting charged fluid; this motion induces an electric field across the magnetic field, in turn producing more electric field which drives current, thus generating a magnetic field and a force (the Lorentz force), and so the loop continues. It is quite clear that a fully operating dynamo requires complex interac-

tions. In the Sun's case, poloidal and toroidal fields are thought to be created where the convective envelope meets the radiative layer - a region occupied by highly turbulent plasmas. It is differential rotation at the base of the convective zone, the so-called 'tachocline', that converts the weaker poloidal fields to large scale toroidal fields. These fields are moved up the zone via magnetic buoyancy and rise through the stellar surface. However, rotation once again generates poloidal fields which are transported to the tachocline thereby starting the process again and maintaining the dynamo. Thus, the ω component of this effect describes the 'stretching' and 'winding' of magnetic field lines, which is caused by stellar differential rotation. By contrast, the α effect 'twists' these lines in to loops, which is thought to be as a result of the upthrust of magnetic tubes from the stellar surface. The magnetic stresses are therefore created through the dragging of magnetic field lines by powerful stellar fluid motions. Indeed, the release of these stresses provide the requisite energy needed to sustain a corona and chromosphere. The coronal and chromospheric X-ray and H α emission, largely used as a measure of magnetic activity, is in fact attributed to the $\alpha\Omega$ -dynamo (thought to hold for $\sim F$ to $\sim M3$ stars), originating from the base of their convective layers.

However, it has not yet been established what dynamo is effectively operating in stars $\geq M3$ ($\sim 0.3 - 0.4 M_{\odot}$), where stars migrate from partially convective configurations, to fully convective. Indeed, stars later than M3 have been shown to exhibit intense magnetic activity, where magnetic field strengths of a few kG and greater have been detected (Saar & Linsky, 1985; Johns-Krull & Valenti, 1996; Reiners & Basri, 2007). Furthermore, since lower mass stars harbor increasingly cooler, neutral atmospheres, and thus higher atmospheric resistivity, dynamo theory predicted the presence of small-scale fields, as well as the presence of a turbulent dynamo, or alternatively large-scale, non-axisymmetric configurations. However, Donati et al. (2006) confirmed the unexpected presence of a strong, large-scale axisymmetric field for the M dwarf, V 374 Peg. They reported this via spectroscopic mapping of magnetically-sensitive lines of the dwarf. They subsequently found toroidal and non-axisymmetric dipolar fields in observations encompassing a sample of early M0 - M3 type stars (Donati et al., 2008). Other groups have also confirmed large-scale magnetic topologies of mid- to late-M dwarfs (Morin et al., 2008, 2010). Thus, stable magnetic field configurations, covering a significant fraction of the stellar surface, must be present.

Chabrier & Küker (2006) have developed a model dynamo based on magnetohydrodynamics simulations which generate large scale magnetic fields for fully convective objects - the α^2 dynamo. In this case, the α effect in field generation essentially refers to the ef-

fects of rotation and stratification of fluid density on the field, with no differential rotation present. Their results yielded large scale, non-axisymmetric fields, where the α^2 effect was successful in generating such fields with kG field strengths for fully convective objects, where faster rotating stars produced larger field strengths.

In the ultracool dwarf regime ($\geq M7$), we observe reduced levels of ionization in the stellar atmospheres, as well as an increase in resistivity. Thus the necessary injection of energy required for localized plasma heating is also reduced. The magnetic fields therefore become decoupled in these atmospheric regions, and the chromosphere and corona are no longer effectively supported. Moreover, current generation becomes even more difficult due to decreasing conductivity (Mohanty et al., 2002), which would suggest that large-scale configurations could not be maintained. Although initial studies identified an obvious reduction in quiescent emission, there were a number of $H\alpha$ and X-ray flares detected, which supported the presence of chromospheric and coronal activity (Reid et al., 1999; Gizis et al., 2000; Rutledge et al., 2000; Liebert et al., 2003; Fuhrmeister & Schmitt, 2004; Rockenfeller et al., 2006b). All the same, these dwarfs were all identified as rapid rotators, possessing rotation velocities of up to 60 km s^{-1} (Basri, 2001). Most importantly, in later chapters in this work, we will show long term optical periodic variability of an M9 dwarf, which exhibits high levels of stability in terms of amplitude and phase over a ~ 5 year baseline. We will also show that the optical and radio emissions are now inextricably linked for this dwarf, where sustained field strengths of $\sim 3 \text{ kG}$ have been detected, suggesting that a stable magnetic dynamo must be present. These results suggest that an alternate dynamo, possessing the ability to sustain such fields, must therefore be effective and operating in low mass, fully convective stars.

Berger et al. (2001) reported persistent and flared radio emission from the M9 brown dwarf LP 944-20, which was the first such detection of radio emission from a brown dwarf, and furthermore was unexpected and highly irregular, based on the established relationships between the peak X-ray and radio luminosities ($L_X - L_R$) for main sequence stars (Güdel & Benz, 1993; Benz & Güdel, 1994). Moreover, this detection violated the ‘Güdel-Benz relationship’ by many orders of magnitude. More detections followed in the coming years (Berger, 2002; Berger et al., 2005; Burgasser & Putman, 2005; Berger, 2006; Antonova et al., 2007; Phan-Bao et al., 2007), where all sources had measured rotational velocities of at least 15 km s^{-1} .

To date, quiescent radio emission has been detected from ten ultracool dwarfs (Berger et al., 2001; Berger, 2002; Berger et al., 2005; Burgasser & Putman, 2005; Osten et al., 2006; Berger, 2006; Phan-Bao et al., 2007; Hallinan et al., 2006, 2007; Antonova et al.,

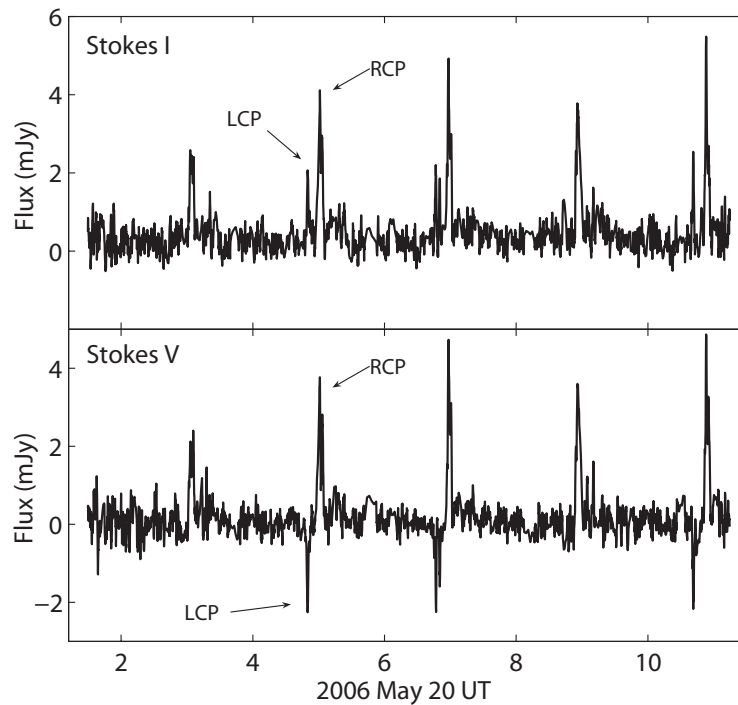


Figure 1.10: We show the radio lightcurves of Hallinan et al. (2007). The top plot contains a lightcurve of total intensity (Stokes I), whereas the bottom lightcurve shows the circularly polarized (Stokes V) emission. These were detected at 8.44 GHz from the M9 dwarf TVLM 513-46546 using the VLA, where the right circularly (RCP), and left circularly (LCP), polarized components are marked on each. These bursts were detected as 100% right and left circularly polarized emission, and were detected to a period of ~ 1.96 hours. These bursts confirmed that ultracool dwarfs can exhibit coherent radio emission, associated with the presence of large-scale, stable, kG magnetic field configurations.

2007; Berger et al., 2009; Route & Wolszczan, 2012), four of which have been found to be producing periodic pulses (Hallinan et al., 2007, 2008; Berger et al., 2009). The mechanisms that appear to drive this radio emission have been attributed to both incoherent and coherent phenomena. Berger (2002) argued that the observed radio emission from the M9 dwarf TVLM 513-46546 was due to incoherent gyrosynchrotron emission, a process responsible for supporting nonthermal populations of mildly relativistic electrons which cause the associated broadly peaked radio emission, beamed perpendicular to the field (Dulk & Marsh, 1982). An alternative mechanism responsible for the radio emission from ultracool dwarfs is the ECM, a process that accounts for the observed periodic behavior (attributed to rotationally modulated emission) from objects containing high-strength, stable magnetic fields such as 2MASS J0036+18 and LSR J1835+3259 (Hallinan et al.,

2008). This emission is generated and detected at the electron cyclotron frequency, $\nu_c \approx 2.8 \times 10^6 B$ Hz. Thus, observations by Hallinan et al. (2007) of TVLM 513-46546, reveal ECM emission as the mechanism responsible for the observed 100% circularly polarized periodic pulses, implying magnetic field strengths of at least 3 kG in the dwarf's magnetosphere (Figure 1.10). Indeed, such a model *requires* kG magnetic field strengths and implies that such fields are large-scale and stable in configuration. Although these observations confirmed the ECM process to be the cause of the polarized periodic emission, it is still unclear as to which mechanism (incoherent or coherent) is driving the quiescent component of the radio emission. kG magnetic field strengths for low mass stars have also been confirmed via Zeeman broadening observations (Reiners & Basri, 2007). Their sample included M2 - M9 spectral types, where field strengths of >3.9 kG were measured, and they find for late M-dwarfs, that the greatest field strengths are generated by the most rapid rotators.

Thus, it was clear that the expected dearth of magnetic activity, including magnetic field strengths, configurations and consequent emission processes, did not hold in the ultracool dwarf regime. Many groups were working along side the above radio studies, who instead were probing the optical transient nature of these objects. We elaborate further on this in § 1.4.

1.3.3 Magnetic Activity in the Planets, and the Observed Aurorae

Here we include a brief discussion of the magnetosphere and auroral emissions from the planet Jupiter, where there are many components of radio emission from various regions of its magnetosphere; these emissions are far higher than any other magnetized planet in our solar system. The Jovian magnetosphere is an extreme environment, harboring an intense quasi-dipolar magnetic field, which acts as a powerful particle accelerator, where electrons can reach kilo-electron-volt (keV; cyclotron radiation from high latitude auroral field lines) and mega-electron-volt (MeV; decimeter synchrotron radiation from particle belts) energies. Various studies have detected a dozen, or so, radio components in the Jovian magnetosphere and the surrounding regions (e.g. Carr et al. (1983); Zarka (1998); Ergun et al. (2000) and references therein). In fact, Jupiter's magnetosphere is responsible for a large magnetic 'well' in the path of the solar wind, occupying a sizable radius of 60 - 120 R_J ; this 'well' consequently aids electron acceleration in the magnetosphere. Jupiter's rapid equatorial rotation velocity (12.6 km s^{-1} ; and $([2 \times \pi \times 1 R_J] / P) \times \sin(i) = P \sim 9.9$ hours), as well as a unique rich supply of plasma from one of its moons (Io), all contribute

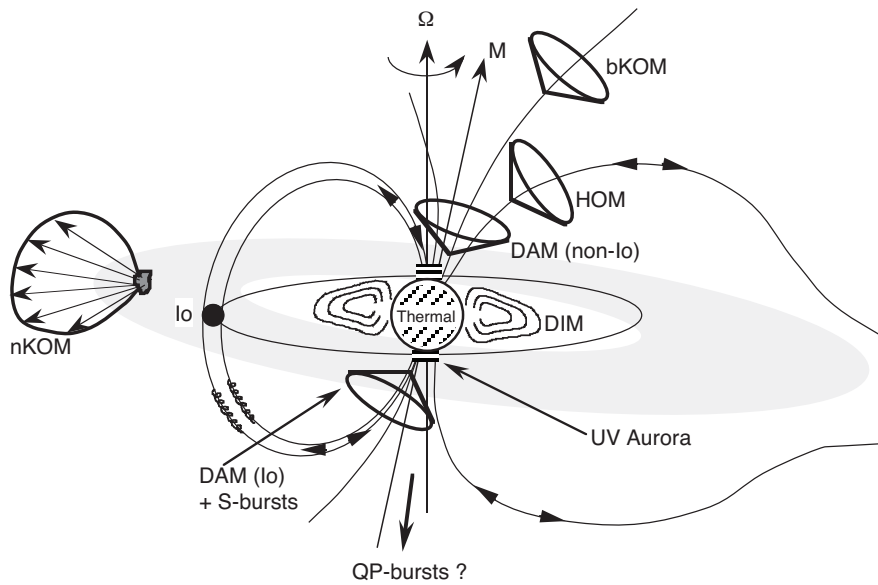


Figure 1.11: This plot shows Jupiter's magnetospheric regions. We highlight sources of decameter radiation (DAM), broadband kilometric radiation (bKOM), narrowband kilometric radiation (nKOM), hectometer radiation (HOM) and decimeter radiation (DIM) in its vicinity. Note the circuit from Io to Jupiter's magnetic field. Taken from Murdin (2001).

to immense particle precipitation in its magnetospheric regions, and thus the production of intense magnetic activity. We refer the reader to e.g. Zarka (1998) and references therein, for a more in-depth discussion of radio emissions from the outer planets.

Similar to Earth's kilometric radiation, it is the decameter, broadband kilometric and hectometer radiations that produce the Jovian auroral emissions. These are generally located at high latitude regions (as shown in Figure 1.11), due to the precipitation of electrons along field lines, although there is a component of decameter radiation from Jupiter's magnetic interaction with its satellite, Io. As previously stated, these emissions can be used as a measure of Jupiter's period of rotation, since they are strongly modulated and beamed in conical configurations where the axes are aligned with the magnetic field lines. These emission cones can therefore be detected by radio telescopes as they sweep Earth due to the geometry of the beaming - thus the observers inclination angle with respect to the beaming angles is very important for such observations. Indeed, it has now been established that the periodic bursts of radio emissions from ultracool dwarfs are analogous to the Jovian conical beams, albeit with much more powerful magnetic fields (Hallinan et al., 2007, 2008), as outlined in § 1.3.2. We point out the significance of these similarities for later sections in this thesis.

1.4 The Phenomenon of Optical Periodic Variability from Ultracool Dwarfs

The successes in characterizing the transient radio emissions from ultracool dwarfs were conducted in parallel with a vast number of studies at other wavelengths. These investigations were undertaken in the last decade, and have found visible and IR variability in this class of object. We have already highlighted the expected composition of ultracool dwarf atmospheres in § 1.2.3, and use this section to specifically discuss optical, NIR and IR variability, where this atmospheric dust has largely been referenced as the cause of these transient detections. The optical characterization of ultracool dwarfs took the following path: 1) ‘the era of discovery’: initial large surveys, outlined in § 1.2.1; 2) identification of physical parameters (e.g. Tinney et al. (1993); Dahn et al. (2002); 3) spectral classification as outlined in § 1.2.3 and finally, 4) the search for variability. § 1.2 to § 1.3 have discussed the first three steps above. We now move on to the optical variability of ultracool dwarfs.

Optical studies have shown that atmospheric dust has a strong effect on the stellar photosphere of low mass objects. Indeed, absorption of elements in their gas phase due to the presence of dust changes important properties of the star, such as the metallicity or the opacity. Allard et al. (2001) have shown that turbulent conditions in these regions are expected, and this, coupled with rapid rotation and the presence of evolving chemical and other atmospheric dynamics, could all be important factors in the classification of stellar transient lightcurves. Moreover, the magnetic properties of low mass stars can be effected by photospheric dust. We have discussed previously, as these atmospheres become increasingly cool and neutral, plasma decoupling can occur from in-situ magnetic field lines, most likely due to increasing electrical resistivity in ultracool dwarf atmospheres after the M/L transition (Mohanty et al., 2002). Similar to the stellar regime, optical variability was expected for low mass objects (due to e.g. magnetic spots after the confirmation of radio emission), however the transitional temperatures from M type to L type dwarfs introduced difficulties when identifying the source of this variability, due to the increasing presence of this atmospheric dust. Indeed, with the recent confirmation of a ~ 1.7 kG magnetic field for a mid-T dwarf (≤ 1300 K) via radio observations (Route & Wolszczan, 2012), it is clear that a combination of stellar magnetic and atmospheric features could potentially drive variability in ultracool dwarfs of lower temperatures. We elaborate further on this matter in later chapters.

As a result of the above, variability has mainly been attributed to magnetic spots on the surface of the dwarf, or the presence of atmospheric dust, or indeed both. Chromospheric

and magnetospheric emission has also been considered in some work (Littlefair et al., 2008). Modulation at the expected rotation period has been found in various studies (Clarke et al., 2002; Koen, 2006; Lane et al., 2007; Littlefair et al., 2008). Similarly, aperiodic variability, or periodic modulations on time-scales not associated with rotation have been inferred (Gelino et al., 2002; Lane et al., 2007; Maiti, 2007). Photometric studies of these objects allow us to investigate the physical nature of their atmospheres; for example, are the features responsible for detected variability stable over long or short timescales? Variability studies have generally been carried out from $\sim 4000 - 25000 \text{ \AA}$, usually using broadband filters such as the Sloan or Johnson filter sets, as well as near infrared $J H K$ filters and $H\alpha$. We briefly outline some variability studies which attribute magnetic spots, and/or atmospheric dust, in the following sections. Table 1.1 shows details from some of these respective campaigns.

1.4.1 Variability due to Magnetic Cool Spots

Magnetic spots are areas of reduced temperature that form on the stellar photosphere, and are created as a result of intense magnetic activity which consequently suppresses convection in these regions. Constrained by the inclination angle relative to the observer's line of sight, this feature could cause optical modulation as the star rotates. A number of methods can be used to assess fluctuations in emitted stellar flux. For example, Zeeman Doppler Imaging (ZDI) is often employed, whereby periodic modulation of Zeeman signatures (magnetically sensitive spectral lines) during stellar rotation, can be identified. However ZDI can generally only be used down to $\sim M7$ dwarfs or so, since these objects get much dimmer and consequently much more difficult for high-resolution spectroscopy - with respect to assessment of a rotation period. Similarly, the Line Depth Ratio (LDR) method can be used where spectral lines sensitive to temperature, are measured. Starspots have a lower temperature than the surrounding photosphere, and thus the profile of temperature sensitive lines can change with respect to depth. This is only effective for slowly rotating stars. Photometry is another method, which measures the flux variations of incoming electromagnetic radiation; this has proven to be very effective with the advent of the newest CCD devices, and has been utilized for the majority of ultracool dwarf variability studies.

The association of magnetic activity with optical variability in ultracool dwarf photometric investigations was prompted as a result of the radio studies in § 1.3.2, which showed the detection of both quiescent and time-variable radio emission in the late-M and L dwarf

range. For higher temperature objects (specifically late-M and early-L dwarfs), the presence of magnetic spots and other magnetic related activity, as seen for earlier M-dwarfs, may also be present (Rockenfeller et al., 2006a; Lane et al., 2007). Lane et al. (2007) reported quasi-sinusoidal periodic variability from the M9 dwarf TVLM 513-46546, with a period of ~ 2 hours. This period of rotation was consistent with results obtained by Hallinan et al. (2006), who found a period of ~ 2 hours via radio observations. Periodic bursts of radio emission was later confirmed to this same period (Hallinan et al., 2007, 2008). In addition to this, Littlefair et al. (2008) reported sinusoidal variability to the same period once again in simultaneous Sloan broadband g' and i' optical photometry. However, most intriguingly, they reported anti-correlated lightcurves in their g' and i' bands, which seemed to refute the proposed model of starspots at that time as the cause for the optical variability. Instead they argue that this anticorrelated signal was likely due to photospheric dust coupled with stellar rotation; however they concede that this explanation was problematic when comparing temperature models for this class of dwarf.

1.4.2 Variability due to Atmospheric Dust

In § 1.2.3, we outlined the spectroscopic properties of M, L, T and Y dwarfs - which is of paramount relevance to this section. The studies that obtained these spectral properties, confirmed the presence of characteristic TiO and VO bands in M dwarfs; metal hydrides (FeH, CrH), strong alkali lines (K, Na, Rb, Cs), CO and H₂O absorption lines, an increased level of opacity and the presence of chemical particulates (Al, Ca, Fe, Mg, Si) for L dwarfs; a decrease in condensate opacity, in addition to the presence of CH₄ for T dwarfs; and prominent NH₃ absorption, as well as a turn to redder colors based on a decline of the blue side of H -band, tentatively defining the Y dwarf (§ 1.2.3 and references therein). Therefore, photospheric clouds of dust are an important consideration in the transient morphology of an ultracool dwarf photometric lightcurve.

Magnetic activity, as signaled by H α , decreases further after the M/L transition (West et al., 2004); therefore in most cases, optical variability has been attributed to the expected presence of dust in the dwarf's atmosphere (Bailer-Jones & Mundt, 2001; Martín et al., 2001; Gelino et al., 2002; Enoch et al., 2003; Maiti, 2007; Littlefair et al., 2008; Goldman et al., 2008; Clarke et al., 2008). These studies were carried out in broadband optical photometry as well as $J H K$ photometry. Indeed, the presence of such clouds of dust existing on timescales longer than a given observation, together with stellar rotation, can lead to periodic and aperiodic time variability. Bailer-Jones & Mundt (2001) suggested

that the dwarf's photometric lightcurve could be affected if the temporal evolution of the dust was on shorter time-scales than the rotation period of the star. Similarly, Artigau et al. (2009) and Radigan et al. (2012) reported the presence of variability in separate photometric IR studies of two early T dwarfs, where both groups attributed this behavior to high-contrast cloud features in these cool stellar atmospheres. We have already pointed out that Littlefair et al. (2008) supported areas of sustained photospheric dust as the cause of their anti-correlated periodic variability of the M9 dwarf TVLM 513-46546. They point out that their Sloan g' band is expected to be dominated by continuum opacity, whereas the Sloan i' by molecular absorption, and thus a cloud in the dwarf's atmosphere could subsequently decrease and increase these bands, respectively.

Whereas late-M dwarfs were originally confirmed to have kG magnetic fields (Hallinan et al., 2007, 2008), we now know that L and T dwarfs also contain high-strength magnetic field environments (Hallinan et al., 2008; Berger et al., 2009; Route & Woloszczan, 2012). Studies of late-M and early L-dwarfs promptly identified magnetic spots as a strong, plausible, explanation for periodic variability due to magnetic activity (Rockefeller et al., 2006a,b; Lane et al., 2007). However, since magnetic activity is clearly present in a wide range of ultracool dwarf spectral classes, even in the regime where dust is thought to dominate, both features (spots and dust) must be considered in variability studies - for all spectral classes.

1.4.3 The Exciting Alternative: Variability due to Auroral Hot Spots

We have outlined above the various features thought to be responsible for variability at optical and NIR wavelengths. Indeed, Table 1.1 shows a large amount of studies that favor the presence of atmospheric dust, as the feature causing this variability. This thesis is different from many of the studies included in the above review sections, since our sample contains *radio detected* ultracool dwarfs - including the four periodic pulsing dwarfs. We are therefore investigating magnetically active dwarfs, where dust may also be prominent for the cooler objects in the study.

In a recently completed large campaign, Hallinan et al. (2012) have obtained multi-wavelength observations of the M9 ultracool dwarf TVLM 513-46546. This campaign utilized many telescopes, and included spectroscopic, photometric and radio observations. The data presented in Chapters 4, and 5, of this thesis, are the photometric component of this study (Harding et al., 2012a). Hallinan et al. (2012) demonstrate that the optical and radio emissions are produced by the same population of electrons in the magnetosphere

Study (1)	Trg/SpT (2)	Band (3)	Variable? (4)	Explanation (5)
Tinney & Tolley (1999)	M(1)/L(1)	TiO	Some	Dust
Bailer-Jones & Mundt (1999)	L(3)	I	Some+PP ^a	RM ^b +H α
Bailer-Jones & Mundt (2001)	M/L(21)	I	Some	Dust+RM
Martín et al. (2001)	BRI 0021(M) ^c	I	Some+PP	Dust+RM
Gelino et al. (2002)	L(18)	I	Some	Dust
Bailer-Jones (2002)	J1145(L) ^d	0.5-2.5 μ m ^e	Some	Dust
Clarke et al. (2002)	Kelu-1(L)	TiO/CrH	Periodic	Dust+RM
Koen (2003)	L(11)/T(1)	I	Some	RM+??
Enoch et al. (2003)	L/T(9)	<i>K</i>	Some	Dust
Bailer-Jones & Lamm (2003)	L(3)	<i>J/K</i>	Some	Dust
Koen et al. (2004)	L/T(18)	<i>J H K</i>	Some	RM
Maiti et al. (2005)	L(3)	R	Some	Dust
Koen (2006)	J0605(L) ^g	R/I	Some	RM/spots/opac ^h
Rockenfeller et al. (2006a)	M(19)	G/R/I	Some+P ⁱ	Spots+RM
Rockenfeller et al. (2006b)	M(19)	U/V/G/R/I	Some+F ^j	Spots+RM
Morales-Calderón et al. (2006)	L(3)	Spitzer(IR) ^k	Some	Dust
Lane et al. (2007)	M(1)/L(1)	I	Periodic	Spots+RM
Maiti (2007)	L(6)	R/I	Some+P	Dust
Littlefair et al. (2008)	TVLM 513(M) ^l	<i>g'/i'</i>	Periodic	Dust+RM
Clarke et al. (2008)	L/T(8)	<i>J</i>	Some+P	RM
Bailer-Jones (2008)	L/T(4)	<i>J H K</i>	Some	Dust
Goldman et al. (2008)	L/T(5)	<i>J H K</i>	Some	Dust+RM?
Artigau et al. (2009)	J0136(T) ^m	<i>J/K</i>	Periodic	Dust+DR ⁿ
Scholz et al. (2009)	VLM(100) ^f	I	Some	RM
Radigan et al. (2012)	J2139(T) ^o	<i>J H K</i>	Periodic	Dust+RM
Harding et al. (2012a)	M(4)/L(2)	R/i'/I	Periodic	Spots+RM +Aurorae^p

Table 1.1: Studies of Optical Variability in Ultracool Dwarfs (1999 - 2012).

DETAILS: Here we show a list of the many ultracool dwarf studies from 1999 - 2012, that have been conducted since the initial discovery of Gliese 229B, in 1995. We refer the reader to the references in these works for other variability studies.

COLUMNS: (1) Reference of study. (2) Target (Trg) or spectral class (SpT). We have abbreviated some targets but elaborate below. We also indicate the number of dwarfs in each study (where applicable). (3) The wave band used in each consecutive study. (4) Here we indicate if variability was detected in the study. Some acronyms are used and are detailed below. (5) The proposed cause of the variability in each study.

ACRONYMS/ABBREVIATIONS: (a) Possible Periodicity. (b) Rotational Modulation. (c) BRI 0021-0214. (d) 2MASS J1145572+231730. (e) IR spectroscopy study. (f) A study of 100 VLM brown dwarfs in the cluster IC4665. (g) 2MASS J06050196-2342270. (h) Opacity. (i) Periodicity. (j) Flaring. (k) Spitzer IRAC observations at 4.5 & 8.0 μ m. (l) TVLM 513-46546. (m) SIMP J013656.5+093347. (n) Differential Rotation. (o) 2MASS J21392676+0220226. (p) Results presented in this thesis.

of the dwarf, and may be *auroral* in nature. Harding et al. (2012a) have also shown that the periodic variability of TVLM 513-46546 is extremely stable in terms of amplitude and phase over a ~ 5 year baseline, suggesting that the feature causing the periodicity is long-lived, and sustained over this time frame. Therefore, perhaps the mechanism responsible for the optical and radio periodicities are no longer mutually exclusive. In fact, the detected ECM emission at 4 and 8 GHz frequencies in their work suggests that such a process in ultracool dwarfs is analogous to the coherent radio emission observed by Zarka (1998), as outlined in § 1.3.2, from the magnetized planets of our solar system. Since ECM emission has now been shown to operate effectively in *all* radio pulsing dwarfs (Hallinan et al., 2007, 2008; Berger et al., 2009), it is quite possible that this mechanism has the ability to provide a sustained bombardment of energy to the stellar surface. Furthermore, it appears that the ECM mechanism is stable on timescales of years in the case of TVLM 513-46546, since it has been observed in many studies (Hallinan et al., 2006, 2007, 2008; Hallinan et al., 2012), and therefore could explain the apparent stability of the causal hot spot detected in our data. We explore this fascinating alternative in Chapters 4 and Chapter 5.

1.5 Summary

In this chapter, we have highlighted some of the important discoveries, and subsequent research that followed, in the ultracool dwarf field. It was these components of study that drove the research carried out in the following chapters. Although Kumar (1963) originally postulated the existence of brown dwarfs, which has been studied for over 50 years now, there were many fundamental questions that needed to be addressed. Our understanding of the internal physics, evolution and characterization of these objects, have answered and confirmed much of the original theoretical predictions. Since the discovery of Gliese 229B by Nakajima et al. (1995), the number of brown dwarfs discovered has grown exponentially, and have been found in many different environments, including clusters, isolated, and in binary and other hierarchical systems. These discoveries subsequently have led to the allocation of four new spectral classes - M-, L-, T- and Y-dwarfs. Although the early era of ultracool dwarf research has yielded a wealth of material to aid our understanding, it also created new fields such as the study of the transient nature of these objects, in the radio, and in the optical regimes.

Following the initial discoveries, ultracool dwarfs were found to be radio active sources, confirming the presence of magnetic activity (Berger et al., 2001). Subsequent observations have confirmed the presence of high-strength, stable magnetic fields, with field strengths

of $\sim 1 - 4$ kG over a wide range of spectral regimes (Hallinan et al., 2007; Reiners & Basri, 2007; Berger et al., 2009; Route & Wolszczan, 2012). Based on the properties of the radio emission, the ECM process was shown to operate effectively in these magnetospheres (Hallinan et al., 2008). Other work has also confirmed the presence of both axisymmetric dipolar field configurations, and non axisymmetric fields (Donati et al., 2006; Morin et al., 2008). The periodic bursts of radio emission, attributed to stellar rotation coupled with the ECM, are analogous to the kilometric radiation in the auroral regions of the Jovian magnetosphere, albeit much more powerful.

Optical variability studies of ultracool dwarfs have also been fruitful, yielding a confirmation that these objects are indeed transient in visible, NIR and IR wavelengths. This variability, which exhibits both periodic and aperiodic variations, has mainly been attributed to the unexpected presence of photospheric dust, or due to magnetically-induced cool spots on the stellar surface. We undertook an optical photometric campaign, which aimed to investigate the ubiquity of optical variability in *radio detected* ultracool dwarfs. In order to do this, we designed and commissioned an optical photometer, the Galway Ultra Fast Imager (GUFI), built specifically to detect variations in the photometric lightcurves of these stars, and have to date obtained over 250 hours of photometric data in this respect. All of these objects have been subject to multi-epoch observations, and some have been part of larger simultaneous campaigns to investigate an exciting alternative to the dust or cool spot explanations - the possibility of auroral emissions from ultracool dwarfs. These optical observations have also yielded interesting results in low mass binary star formation, and in the study of flaring from earlier-type M dwarfs. This thesis therefore describes the research carried out in the ultracool dwarf regime, the astrophysical implications of these results, and the optical instrumentation that was built and commissioned during this time, to do so.

“Leon - the next time you take a break from the observing, and stand outside for a few moments looking at the stars and inhaling all that cool desert air, just remember it’s a privilege to be an astronomer - and that I am as envious as hell, that I’m not out there with you guys ... ”

Dr. Aaron Golden, Ph.D. supervisor, 28/Jan/2009 12:53 (UTC)

*“What a **chimera** then is man! What a novelty! What a monster, what a chaos, what a contradiction, what a prodigy! Judge of all things, feeble earthworm, depository of truth, a sink of uncertainty and error, the glory and the shame of the Universe.”*

Blaise Pascal, French Mathematician, Philosopher and Physicist (1623-1662)

“For the resolving powers of our scientific instruments decide, at a given moment, of the size and the vision of our Universe, and of the image we then make of ourselves.”

Albert Claude



Optical Instrumentation

In this chapter, we outline the optical instrumentation that was developed and used during this doctoral work. Two instruments were designed, built and commissioned, and are currently stationed at telescopes on Mt. Graham, Arizona*, and Palomar Mountain, California†. Section 2.1 and 2.2 discuss the role of each instrument, and their optical design and setup, respectively. All of the instrumentation, the optical setups, the optical designs (Zemax), the hardware designs (Solidworks), and the detector characterization was carried out solely by the author, unless otherwise indicated in the text.

2.1 The GUFi mk.II Photometer - Galway Ultra-Fast Imager

The GUFi instrument was originally commissioned by astronomers in NUI Galway as an optical photometer capable of high-time resolution imaging (Sheehan & Butler, 2008). We modified the GUFi mk.II system to be compatible with the 1.83 m VATT on Mt. Graham, Arizona, where it is currently stationed as a visitor instrument. It saw first light in May 2009, and the MoU⁸ agreement between NUI Galway and VATT has been extended for three consecutive years, based on the research successfully carried out to date (Harding et al., 2012a,b,d).

We designed and commissioned GUFi mk.II (hereafter GUFi) for the sole purpose of detecting the transient signatures from ultracool dwarfs. However, the instrument can

*§ 2.1 - GUFi: optical photometer, brown dwarf science. PI: Dr. Ray Butler.

†§ 2.2 - Chimera: multi-color photometer, PTF follow-up. PI: Prof. Gregg Hallinan.

⁸Memorandum of Understanding.

Parameter (1)	Corresponding Value(s) (2)
Active pixels	512×512
Digitization	14-bit (16-bit available @ 1 MHz)
Pixel size (μm)	16×16
Spectral sensitivity (nm)	~300 - 1000
Field of view (arcminutes)	~3 × 3
Active area well depth (e^-)	200,000
Linear gain register well depth (e^-)	400,000
Readout rates (MHz)	10, 5, 3, 1
Pre-amplifiers	4.6×, 2.4× 1.0×
Readout amplifiers	Conventional (3 & 1 MHz) / EM-CCD
Readnoise	<1 e^- (with EM gain)
Frame rates (fps)	34 (full) - 526 (windowed)
Binning modes	1×1, 2×2, 4×4
Vertical clock speeds (μm)	0.4 - 6.0 (variable)
Peak QE (BV 575 nm)	92.5%
Dark current -70/-90°C ($\text{e}^- \text{pixel}^{-1} \text{sec}^{-1}$)	0.012/0.0035

Table 2.1: **GUFi mk.II Photometer Overview (System Characteristics).**

We show specifications for the Andor iXon DV887 detector, where system parameters are shown in (1), and corresponding values in (2). From: (Data sheet: iXon DV887 Camera Systems. Andor Technology, 2004), and (Data Sheet (issue 3): CCD97-00 Back Illuminated 2-Phase IMO Series, Electron Multiplying CCD Sensor, e2v technologies, 2004), via <http://www.andor-tech.com/> and <http://www.e2vtechnologies.com/>.

also be used over a wide range of astronomical research areas, such as lunar/interplanetary imaging, ‘lucky’ imaging and post exposure image sharpening, transiting exoplanets, AM CVns, flare stars, and any other transient sources in the sky. In fact, we have conducted observations for the purpose of our own research interests, in addition to collaborative efforts, in each of these respective fields. The system uses the Andor iXon DV887 EM-CCD camera (Figure 2.1a), which has a CCD97 thinned back-illuminated sensor from e2v technologies, hosting >90% quantum efficiency (QE) with a native 512 × 512 frame transfer (FT) sensor. The FT option allows for the omission of a mechanical shutter, minimal transfer times (~ 2 ms) and thus is capable of extremely high cadence. Since the CCD97 chip is back illuminated, it has much improved QE over a wide spectral range of $\sim 300 - 1000$ nm (Figure 2.1b) - as compared to a front illuminated sensor. It offers variable readout rates up to 10 MHz and can operate full-frame at 34 frames per second (fps) and up to 526 fps in a windowed configuration, thus producing large data loads. In order to process these

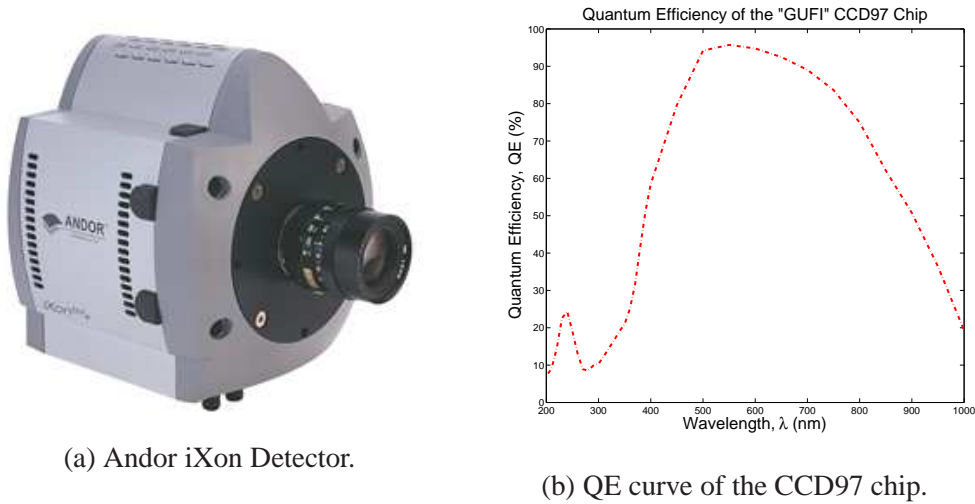


Figure 2.1: Here we show the Andor iXon DV887-BV camera (a), as well as the measured QE curve for the CCD97 chip (b), as used by GUFi. Note the high QE throughout the majority of the visible spectrum and in to the NIR (e.g. Johnson B, R, and I-bands).

excessive data volumes, we modified and utilized the GUFi pipeline (Sheehan & Butler, 2008), that was developed using PyRAF⁹ routines. We elaborate on this further in Chapter 3, § 3.1.1. The pixel size in this sensor is $16 \mu\text{m}$, and the CCD chip is hermetically sealed - providing a dust free vacuum. The chip has on-board cooling via a three-stage thermoelectric cooler, which impressively, can cool the chip to -50°C . It can be cooled further to -90° with the aid of a liquid cooling system which removes any excess heat that is generated from the heat sink to the thermoelectric cooler. The native field of view (FOV) of GUFi at the VATT Cassegrain focus is $\sim 1.7' \times 1.7'$ with a corresponding plate scale of $0.2'' \text{ pixel}^{-1}$. Focal reducer (FR) options for wider fields are limited by the short VATT back focal distance of 50.8 mm, but GUFi provides near-infrared and visible-optimized FRs, offering a FOV of $\sim 3' \times 3'$ and a larger plate scale of $0.35'' \text{ pixel}^{-1}$. The great advantages of GUFi for this study are its 100% observing duty cycle (with a $\sim 2 \text{ ms}$ readout rate), very low readout noise and high QE. A GUFi system overview is shown in Table 2.1.

2.1.1 L3-CCD Technology and the Andor iXon DV887

Charged Couple Devices (CCDs), were first developed by AT&T Bell Laboratories in the 1970's (see: Janesick (2001)). Its silicon wafer chip is composed of many pixels in an array

⁹PyRAF is based on the Python scripting language. It was developed by the Space Telescope Science Institute (STScI): http://www.stsci.edu/institute/software_hardware/pyraf/.

of electrodes, which produces charged packets via the production of electron-hole pairs, and subsequent collection of photoelectrons in wells created by an electric field. These are then read out through a register, and are amplified and digitized. However, this moving charge creates noise in the output signal associated with the rate of the readout. With the advent of L3-CCD devices, known as low-light-level CCDs, images of low intensity can now be obtained at much lower readout noise levels than previous detectors.

An additional feature of L3-CCDs over classical CCD devices is that of the electron multiplication (EM) register, also known as the ‘gain’ register, which consists of a number of stages, each with four electrodes. By applying a voltage (e.g. 40 - 50 V) to these electrodes, the consequent potential difference (PD) produces a process known as ‘avalanche multiplication’, thus amplifying the charge. The gain register has larger depths than other serial registers so that the wells can accommodate this amplification. The EM-register controls the applied voltages in this process, and has no connection to the pixel readout rate - this is an important feature, since the user can operate at fast frame rates without a dramatic increase in readout noise. We refer the reader to Sheehan (2008), for an in-depth discussion of CCD and L3-CCD technology.

The EM process, as outlined by Basden et al. (2003), can produce added noise in the output. Other parameters such as the variance of the output (σ_{op}) and input (σ_{ip}) signals, in addition to the EM-gain level must be considered. This induced noise (Q) can be calculated as follows (Robbins & Hadwen, 2003):

$$Q^2 = \frac{\sigma_{op}^2}{(EM_{gain})^2 \sigma_{ip}^2} \quad \text{where} \quad EM_{gain} = (1 + \alpha)^N \quad (2.1)$$

and α is the probability of multiplication occurring in a given stage (~ 0.01 - 1%), and N is the number of stages. Robbins & Hadwen (2003) explain further that Q will approximate to:

$$Q^2 = \frac{2}{\alpha + 1} \quad (2.2)$$

because $\alpha \ll \text{EM-gain}$. Interestingly, this noise will effectively hinder the QE of the chip because more signal is required to obtain the same SNR as a noiseless scenario. By adopting a value of ~ 0.01 - 1% for the occurrence of EM in Equation 2.2, $\alpha < 1$, thus $Q \sim \sqrt{2} = 1.414$, which is the theoretical limit for the noise factor.

Dark current, and clock induced charge (CIC) are also important considerations when using L3-CCD devices. Essentially, dark current is the result of thermally generated electrons that are trapped in pixel wells. Electron energies follow a Fermi distribution within

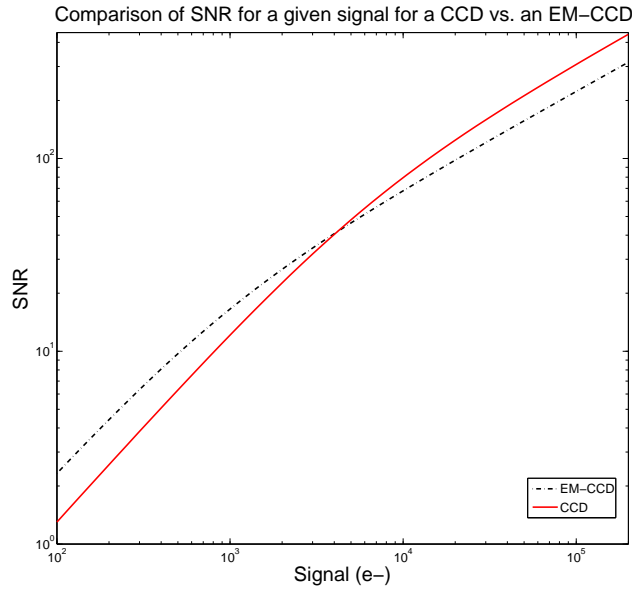


Figure 2.2: We show a plot of an assessment of the SNR of a CCD (red solid line) vs. an EM-CCD (black dashed-dotted line) for a given signal - taken from Sheehan (2008). The plot was computed in this case for object with an angular size of $1''$ and a plate scale of $0.5'' \text{ pixel}^{-1}$. The readout noise was 8 and $1 \text{ e}^- \text{ pixel}^{-1}$ for the CCD and EM-CCD respectively. Note the reduced SNR values at high signal levels with the effect of EM induced noise. This plot highlights the importance of mode and parameter selection for an EM-CCD device. As illustrated here, effective readout noise values for CCDs can be as high as $8 \text{ e}^- \text{ pixel}^{-1}$ (typically $2 - 3 \text{ e}^- \text{ pixel}^{-1}$ for good CCDs), whereas this is factors less for an EM-CCD, at $1 \text{ e}^- \text{ pixel}^{-1}$.

the silicate structures, and therefore at temperatures $> 0 \text{ K}$, some will occupy higher energy states due to this thermal excitation. Some may be captured by the standard registry process outlined above, and thus is registered as extra signal - known as ‘dark current’. Indeed, dark signal non-uniformity can also arise, where a different level of dark current is produced by different pixels. This effect can be countered by acquiring exposures for a given observation that assess this dark current level - which can then be removed (N.B. the same chip temperature, exposure times and mode settings must be used). However, we note the extremely low level of dark current for the iXon DV887 chip, which approximates to $0.0035 \text{ e}^- \text{ pixel}^{-1} \text{ sec}^{-1}$, at -90° . CIC is also an excess effect in the process, whereby extra electrons are created by the clocking out process. This effect can sometimes be a primary source of noise for L3-CCDs operating at these extremely cold temperatures.

For a conventional CCD, the (total) photometric noise (σ_{total}), which includes dark

(1) Readout Amplifier	Pre-amp 1.0×	Pre-amp 2.4×	Pre-amp 4.6×
Conventional	10.08 ± 0.04	4.07 ± 0.01	2.111 ± 0.003
EM-CCD	57.45 ± 0.47	24.20 ± 0.10	12.64 ± 0.04
(2) Readout Rate	Pre-amp 1.0×	Pre-amp 2.4×	Pre-amp 4.6×
1 MHz, Conv	10.88	7.07	6.21
3 MHz, Conv	16.03	10.74	9.45
1 MHz, EM	56.08	31.48	24.38
3 MHz, EM	64.84	40.42	32.98
5 MHz, EM	112.86	63.40	...
10 MHz, EM	185.24	112.72	...

Table 2.2: (1) Measured Sensitivity ($e^- \text{ ADU}^{-1}$), and (2) Readnoise ($e^- \text{ pixel}^{-1} \text{ readout}^{-1}$).

In (1) above, we show the measured sensitivity in $e^- \text{ ADU}^{-1}$, where ADU is ‘Analogue to Digital Unit’, of the iXon DV887, as provided by Andor (Data sheet: iXon DV887 Camera Systems. Andor Technology, 2004). In (2), we show the combinations of readout rates and amplifiers available via the Andor software, and the associated noise levels in $e^- \text{ pixel}^{-1} \text{ readout}^{-1}$. Although EM mode increases nominal readnoise, it decreases effective readnoise to $<1 e^-$.

current (N_{dark}), and readout noise (σ_{RD}), can be characterized as follows (Janesick, 2001):

$$\sigma_{total} = \sqrt{N_{ph} + N_{pix} \cdot (N_{sky} + N_{dark} + \sigma_{RD}^2)} \quad (2.3)$$

where N_{ph} is the photon count, and N_{pix} and N_{sky} are the number of pixels included in a photometric aperture or an area of interest on the chip, and the sky background count in this region, respectively. Since the Andor iXon DV887-BV is an EM-CCD device, we must also consider the effects of EM noise as outlined above. Thus, Robbins & Hadwen (2003) propose that we modify Equation 2.3 to include Q - the induced noise during the EM process. As we will see in Equation 2.4, all components of Equation 2.3 are scaled by Q , with the exception of σ_{RD} , to get:

$$\sigma_{EM\text{total}} = \sqrt{Q^2 \cdot N_{ph} + N_{pix} \cdot (Q^2 \cdot N_{sky} + Q^2 \cdot N_{dark} + \sigma_{RD}^2)} \quad (2.4)$$

During testing of this camera for the GUFi mk.I phase, Sheehan (2008) use Equations 2.3 and 2.4 to investigate the SNR of a CCD device vs. an EM-CCD device, for a range of signals (e^-). We include this plot, in Figure 2.2.

The Andor iXon system has two modes of operation - the electron-multiplication am-

plifier and the conventional amplifier, as well as three pre-amplifier options - $1.0\times$, $2.4\times$, and $4.6\times$. During data acquisition, we use a combination of these settings that provides the desired trade-off between exposure sensitivity, and the effects of readnoise. The conventional and electron multiplication modes have many variable readout rates (10, 5, 3, 1 MHz), but can only be used for certain modes and pre-amplifiers, as shown in Table 2.1. Furthermore, the effective readnoise of the system is $<1\text{ e}^-$ (with EM gain), since the amount of EM-gain used essentially scales the readnoise by: $\sigma_{\text{nogain}} / \sigma_{\text{applied_gain}}$.

Finally, we highlight the importance of the amplifier and pre-amplifier with respect to a balance, or trade off, between instrument sensitivity and read noise, in Table 2.2. Sheehan (2008) and Sheehan & Butler (2008) point out the interdependence of these parameters, and explain that one must be cautious when applying EM-gain, since it reduces the effective well depth of the pixels - which is $400,000\text{ e}^-$ for the CCD97 chip. They show that the peak count and thus the level of EM to be applied can be easily computed, where the peak count (P) is:

$$P = \frac{F \cdot t}{2 \cdot \pi \cdot \xi^2} = \frac{\text{Well depth}}{\text{EM gain}} \quad (2.5)$$

where F is the flux, t is the exposure time, and ξ is the FWHM/2.354 (where FWHM is the Full Width at Half Maximum). Saturation can therefore be avoided by assessing the peak count, and ensuring that the level of EM gain applied (if any) does not cause such an effect in the EM register during the amplification process.

2.1.2 Optical Setup and Instrument Design

We designed the instrument box for GUFi to be light-weight and compact (see Figure 2.3 and Figure 2.4a). We used 0.5" aluminium plates for the main instrument enclosure, which was attached to the Cassegrain focus of VATT via an adaptor flange designed specifically for the telescope mounting pedestal. The instrument flange plate was designed to the precise specifications detailed by the VATT engineers (shown in Figure 2.3), however due to the nature of the telescope's primary $f/1$ mirror, and the virtually non-adjustable secondary mirror (a few mm), the CCD97 chip has to be placed at the back focal distance of 50.8 mm, and even closer when a FR is used. Since we did not include a motorized linear translation stage in the optical design, mechanical spacers were positioned in between the front face of the iXon camera, and the front plate of the instrument; there are three different foci positions depending on whether the NIR or optical FR is used, or if no FR is used. This optical setup provided seeing-limiting image quality at the VATT Cassegrain focus. Furthermore,

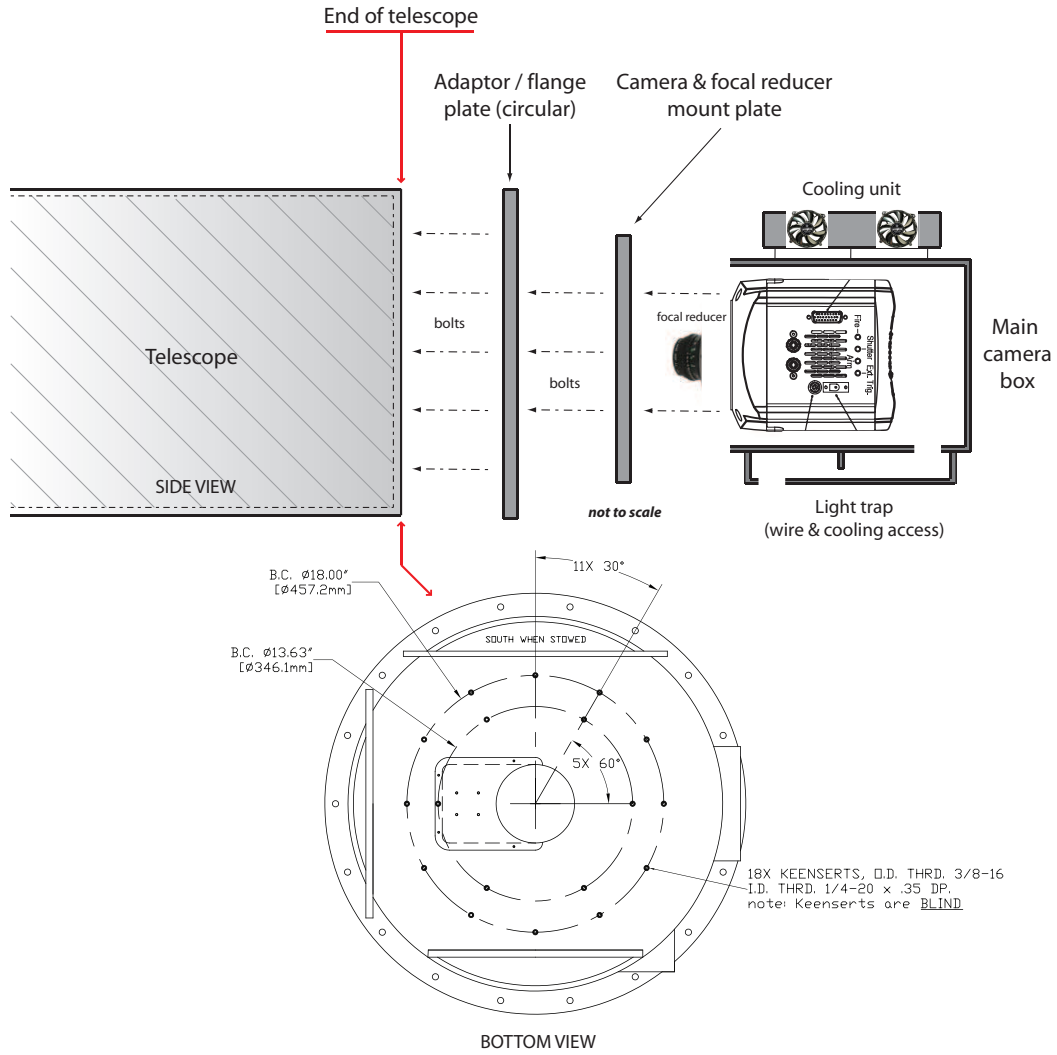


Figure 2.3: GUFi instrument box, and adapter plates/mounts for Cassegrain focus at VATT. We also include the CAD drawing as provided by members of the VATT engineering team, which was used to design the counter-bored hole patterns on the circular adapter plate.

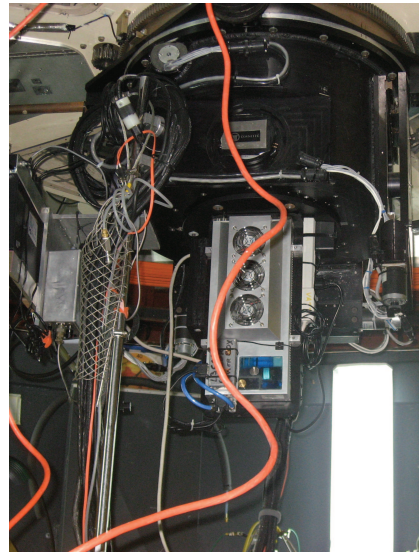
a FOV of $\sim 1.7' \times 1.7'$ was achieved, with a corresponding plate scale of $0.2'' \text{ pixel}^{-1}$ (no FR), or alternatively, a $\sim 3' \times 3'$ FOV and a larger plate scale of $0.35'' \text{ pixel}^{-1}$ (with FR). These FRs were obtained from Edmund Optics¹⁰, and are both achromatic lenses with 25 mm diameters and 60 mm focal lengths. Each have a specific dispersion and coating that optimizes their performance at their respective wavelength ranges.

A light-tight trap, mounted on the left side of the instrument, ensures that no stray light

¹⁰Edmund Optics (EO): <http://www.edmundoptics.com/>.



(a) GUFi during assembly.



(b) Mounted at Cassegrain focus.

Figure 2.4: The GUFi photometer was assembled (a) on site at VATT in May, 2009, after being successfully lab tested at the NUI Galway CfA. It was then mounted at the Cassegrain focus of VATT (b), before its lengthy commissioning observation run in June, and July, of that year.

enters the main enclosure, and communication, power and cooling cables, are run through this passage (Figure 2.3). We did not include a filter wheel internal to the instrument, since VATT provides 2×4 position filter wheels, that are located above the mounting pedestal. These filter positions are controlled via the telescope control software (TCS) in the VATT control room. VATT offers the full Sloan and Johnson photometric ranges, as well as the Vilnius interference filter range, a $H\alpha$ filter, and others. We refer the reader to the VATT website (footnote #1, page iv in the front matter of the thesis) for more information.

VATT is run and operated by the Steward Observatory, based at the University of Arizona, and is part of the Mount Graham International Observatory. VATT saw first light in 1993, and since that time it has been an active telescope which hosts visitor instruments, as well as facility photometers and spectrographs. The seeing at VATT is generally excellent - indeed, we have observed close to $0.7''$ seeing during some observation runs, and typically, observers report sub-arcsecond seeing conditions (with no AO), making it one of the best sites in the world. The primary mirror of VATT is an $f/1$ ‘honeycombed’, borosilicate mirror, which was constructed at the University of Arizona, and was in fact the first spin-cast and stressed-lap built mirror. These techniques were later used to build the 6.5 m Multiple Mirror Telescope (MMT), as well as the mirrors of the Large Binocular Telescope (LBT) - both 8.4 m in diameter.

In the next section, we discuss the hardware and software used to control GUFi. The control computer is located on the main telescope azimuth surface, underneath the primary mirror cell, and close to the instrument. The iXon camera communicates with the control computer via an Andor propriety network cable. However, since GUFi has imaging capabilities of up to 526 fps, the length of this cable is limited to ≤ 10 m, in order to preserve data rates. Thus, the control computer is permanently stationed in the dome, and controlled remotely from the VATT control room by using an Ethernet connection; an Ethernet hub is mounted on the right fork of the alt-az telescope structure.

All of the photometric data presented in this thesis, and submitted for publication, was obtained using GUFi (and the VATT 4K CCD). Therefore we show no proof of concept work in this section, since these data are presented in Chapters 4 - 7 .

2.1.3 Hardware and Software

The GUFi system uses a Dell 1800 server¹¹, that controls the camera and stores the data after acquisition. Data is obtained by using Andor's propriety SOLIS software, and communicates with the control computer by an Andor network card, capable of processing extreme data rates via the onboard camera internal memory. Although Andor designed this software for image acquisition, it also has a large amount of functionality for image analysis during or after an acquisition. It gives the user full control of image properties, including pixel readout rates, horizontal/vertical binning factors, exposure times, automated frame accumulation options, pre-amplifier settings, EM or conventional amplifier selection, triggering mechanisms, vertical shift speeds and dynamic gain settings. Furthermore, the software's region of interest statistics (labeled 'ROI' in the GUI) enables the user to assess the mean and standard deviation of the signal, as well as the maximum and minimum counts and FWHM. 'Spooling' allows direct data storage on hard disks, therefore by-passing memory. Finally, the AndorBasic programming language provides options for scripting. As the software contains many more options and functions, we refer the reader to the Andor website for more details.

2.1.4 Time Server (NTP) Implementation

Since GUFi was designed to be an instrument used for the detection of variable signals from ultracool dwarfs, and other transient sources, the system required a dedicated time

¹¹Basic specs: 2× Xeon 2.8 GHz processors; 2 GB RAM; 5.5 TB storage (RAID-0 config.)

server, in order for the GUFU control computer to be accurately synced with Coordinated Universal Time (UTC). Indeed, this is clearly of paramount importance for any simultaneous observations with other telescopes. The Andor iXon camera has the capability of directly receiving a Transistor-Transistor Logic (TTL) pulse via an external trigger port. However we chose not to install the required GPS antenna to maintain an accurate pulse, and instead implemented a simpler setup via the Network Time Protocol (NTP), which acquires an accurate read of UTC from a receiver on Mt. Graham. The NTP then updates the Windows XP desktop clock, which provides this time to the internal iXon clock. In fact, the NTP identifies five different in situ Mt. Graham receivers - stationed at VATT, the Sub-Millimeter-Telescope (SMT) and LBT, and pings each of these locations every 10 ms, to assess their latency response. The server therefore chooses the receiver with the least amount of latency. SOLIS writes the newly acquired time stamp to each .fits header file, thus preserving UTC accuracy, which is accurate to milli-second time resolutions.

2.2 CHIMERA - Caltech HIgh-speed Multi-color camERA

“The Chimera (χιμύρα) is a monstrous fire-breathing creature of Lycia, depicted as a lion, with the head of a goat, and a tail that takes the form of a snake’s head. It describes a mythological or fictional [instrument] animal with parts taken from various [instruments] animals.”

Greek Mythology

We designed and built CHIMERA as a high-speed, multi-color photometer, for deployment at the prime focus of the Palomar 200-inch telescope. The instrument is optimized for monitoring of targets that vary on timescales from milliseconds to hours, and is positioned to target new classes of short duration transient, and periodic sources, revealed by iPTF¹² and ZTF¹². These sources include compact binaries, flaring stars, transiting planets and eclipsing binaries. The exquisite absolute timing accuracy offered by the instrument ($< 1 \mu\text{s}$) is particularly useful for multi-epoch timing experiments (e.g. AM CVns). At the heart of CHIMERA lie two innovative Andor NEO sCMOS detectors (2560×2160 ; 5.5 Mpx), that outperform the current generation of CCDs and EM-CCDs in many key

¹²The Palomar Transient Factory (PTF, where iPTF is the next phase of PTF with the inclusion of high-throughput spectrographs used for spectral classification) is a wide-field survey used to detect transient sources. Zwicky Transient Factory (ZTF) is due to be commissioned in 2015, and will be used for spectral classification and photometry of crowded host galaxy fields.

Parameter (1)	Corresponding Value(s) (2)
Active pixels	2560×2160 (5.5 Mpx)
Digitization	11-bit and 16-bit
Pixel size (μm)	6.5×6.5
Spectral sensitivity (nm)	$[g'] \sim 300 - 550$; $[r'/i'] \sim 550 - 900$
Field of view (arcminutes)	$\sim 3 \times 2.8$
Pixel well depth (e^-)	30,000 (typical)
Readout rates (MHz)	560, 200
Readnoise	$< 1 e^-$
Readout modes	Rolling/Global shutter
Frame rates (fps)	100 (full), $> 1,600$ (windowed)
Pixel binning	2×2 , 3×3 , 4×4 , 8×8
Peak QE (BV 550 nm)	57%
Dark current -40°C ($e^- \text{pixel}^{-1} \text{sec}^{-1}$)	0.03

Table 2.3: **CHIMERA Photometer Overview (System Characteristics).**

We show specifications for the Andor NEO sCMOS detector, highlighting the main parameters (1) and corresponding values (2). Taken from: (Data sheet: LNeoSS 0412 R1 NEO sCMOS. Andor Technology, 2011), via http://www.andor.com/scientific_cameras/neo_scmos_camera/.

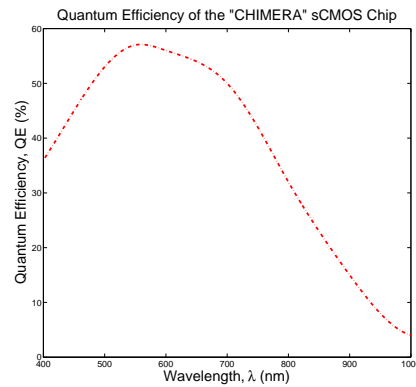
areas. In particular, they can simultaneously deliver ultra-low noise ($< 1 e^-$), rapid frame rates (100 fps full frame, $> 1,600$ fps windowed) over a wide dynamic range ($\sim 30,000:1$). CHIMERA also offers simultaneous observing in the Sloan g' band, and either of the Sloan r' or Sloan i' bands. Indeed, the filter wheel on the (red) transmitted arm can hold up to 9 filters. The instrument currently operates with a field of view of $3' \times 2.8'$, with a future upgrade planned to extend this to 10 square arcminutes (see Appendix C). The instrument saw first light on the Palomar 200-inch on August 1, 2012. In the following sections, we discuss the new sCMOS technology briefly, as well as the optical requirements at prime focus of the 200-inch that were needed to achieve seeing-limited performance, and finally the hardware we use and the science goals intended for the instrument. CHIMERA system properties are shown in Table 2.3.

2.2.1 sCMOS Technology and the Andor NEO

Complementary metal-oxide-semiconductor technology, hereafter ‘CMOS’, was developed in the 1960’s and is used in a wide range of technological applications, such as micro-



(a) Andor NEO Detectors.



(b) QE curve of the sCMOS chip.

Figure 2.5: Here we show the Andor NEO sCMOS detector (a), as well as the measured QE curve (as per the Andor specifications manual outlined in Table 2.3) for the sCMOS chip (b), as used by CHIMERA.

processors, random access memory, imaging sensors, and communications. These circuits are quite complex which can result in a reduction of the available area for light sensitivity. However, since the 1960's, modern CMOS sensors now have much greater sensitivity than their earlier counterparts. Unlike a CCD, each column of pixels in a CMOS sensor contains individual amplifiers, digitization (ADU conversion) and noise reduction circuits. Because of this complex design structure, the pixel area responsible for light capture is reduced, and because conversion is performed for each individual pixel, image uniformity is lower. Nevertheless, CMOS sensors have faster readout capabilities and lower noise. Both CCDs and CMOS images offer unique imaging performance, where CCDs have often been cited for their high QE range and image quality, whereas CMOS sensors have more functions on the chip, and lower power dissipation.

However, the new sCMOS (scientific CMOS) detectors have been specifically designed for scientific imaging, which requires consideration of noise, frame rate, dynamic range, QE, thermal control, and so on. The CHIMERA system uses two Andor NEO sCMOS detectors, to simultaneously image different wavelength ranges. The NEO now offers two readout modes - the global shutter mode, and the rolling shutter mode. In the sCMOS sensor, each column has dual amplifiers and ADU converters, both on the top and bottom of the sensor, thus allowing for split sensor readout. This design reduces readout noise, while maximizing the dynamic range. The architecture of the NEO chip while using the rolling shutter mode provides lower readnoise than the global mode (e.g. 1 e^{-1} vs. 2.3 e^{-1} at 200 MHz). In the rolling mode, each column is read out (by its own amplifier) and

shifted to an electrical bus. The format of the readout is such that each row is individually read out from one side to the other (leading to a temporal latency between beginning and end of readout). One must heavily consider this characteristic if the NEO is being used for variable object science, especially if the time scale of the variations (expected or other) approximate the time scale of the latency. By contrast, the global mode reads the entire chip to the electrical bus, at the expense of greater noise. It is important to note that since the rolling shutter reads different parts of the chip out at different times, the final image could be subject to artifacts such as skew, wobble or partial exposure, due to changing conditions during acquisition. Although the global shutter mode can avoid these effects, if these same conditions change during a global acquisition, artifacts such as image blur can occur. The NEO sensor has 2560×2160 active pixels, with pixel sizes of $6.5 \mu\text{m}$, providing 5.5 Mpx in total. Based on the above sCMOS architecture, the NEO can simultaneously deliver $<1 \text{ e}^{-1}$ of noise, at frame rates of 100 fps full frame, and $>1,600$ fps with a 128×128 pixel region, with rolling shutter enabled, as well as a wide dynamic range of $\sim 30,000:1$. The Andor NEO camera and a plot of QE of the sCMOS chip is shown in Figure 2.5, which reaches a maximum of $\sim 57\%$ at $\sim 550 \text{ nm}$. The overall instrumental response $\leq 400 \text{ nm}$ was poor, therefore we decided to only include the Sloan g' filter on the reflected arm - we discuss this further in the following sections. The NEO camera also contains a spurious noise filter option, capable of reducing the effects of random high-noise ($>5 \text{ e}^{-}$ rms) pixels. For an in-depth discussion of the noise characteristics and associated assessment of these effects for CMOS detectors, we refer the reader to Tian (2000, and references therein).

2.2.2 CHIMERA at Prime ($f/3.5$) Focus of the 200-inch

The optical design of CHIMERA involved overcoming the challenges presented by placing the instrument at prime focus of the 200-inch Hale telescope, the most pertinent being coma aberration¹³. The resolution at focus of a paraboloidal mirror is limited by coma, and is particularly worse for smaller focal ratio (“faster”) mirrors. Other effects such as field curvature¹³ and astigmatism¹³ of the primary mirror must also be considered. These problems were reduced on the 200-inch, by including the existing Wynne corrector (see:

¹³These effects are essentially due to the departure from a flat imaging surface, in this case the curvature of the primary mirror. The resulting shape of the wavefront is different for each effect labeled above, and therefore the points of foci with respect to the image plane are strongly effected, leading to a variety of spot aberrations. We refer the reader to Ross (1933, 1935) for in-depth discussion of these effects.

Wynne (1949, 1965, 1972)) in the optical path for CHIMERA, which provides a 24 arcminute focal plane, with minimal aberration. When the 200-inch was originally being commissioned in the 1930's, a large amount of research was carried out by F. E. Ross, where he worked to characterize and minimize these effects by the inclusion of a correcting lens system between the primary mirror and focus (Ross, 1933). Although the system proved to be effective in removing the primary aberrations via a doublet lens with spherical surfaces, it did introduce spherical aberrations as a result. He later suggested that by using non-spherical surfaces that the effect could be avoided; however later Wynne (1949) showed that this was not the case. Ross (1935) then published a novel three-element corrector, which did in fact take care of the primary and spherical components of aberrations as previously observed in earlier designs. Based on this 'Ross' design, Wynne (1965) outlined a corrector specifically for the 200-inch. Although this system corrected for coma on axis, FOVs of ~ 10 arcminutes were still subject to some coma effects. Wynne (1967) provided another iteration of these paraboloid correctors, this time employing a four-element corrector - this design is currently being used at the 200-inch, and provides a 24 arcminute FOV. We show the optical layout of the Wynne corrector, which is located 4.459" before the prime focus, in Figure 2.6.

Although the Wynne corrector minimizes the inherent coma of the primary mirror, we still needed to carefully consider what optics would best preserve the image quality of the prime $f/3.5$ beam - since lens and mirror properties can all contribute to aberrations at the image plane. These optics were ultimately required in order to shift the prime focal plane to a position where CHIMERA could effectively image a $\sim 3' \times 3'$ field. We found this FOV to be the maximum field size we could achieve, whilst still maintaining seeing-limiting spot sizes (of e.g. $\sim 0.5''$ on axis and $\sim 1.3''$ off axis, where $\sim 1''$ is typical seeing for the Palomar site) in our RMS radius assessments, without the need of custom optic design. We elaborate on this further in the following section.

2.2.3 Optical Setup and Final Instrument Design

A 1:1 relay consisting of a combination of visible achromatic doublet lenses¹⁴ was used to collimate and re-focus the image from this corrected focal plane, on to our two Andor NEO detectors (shown in Figure 2.6). This combination was especially important in minimizing aberrations as the prime beam moved through the system. With a diameter of 2" and a

¹⁴All of the optical lens elements, the optical breadboard, posts and mounts (and other smaller components) were obtained from THORLABS; www.thorlabs.com/.

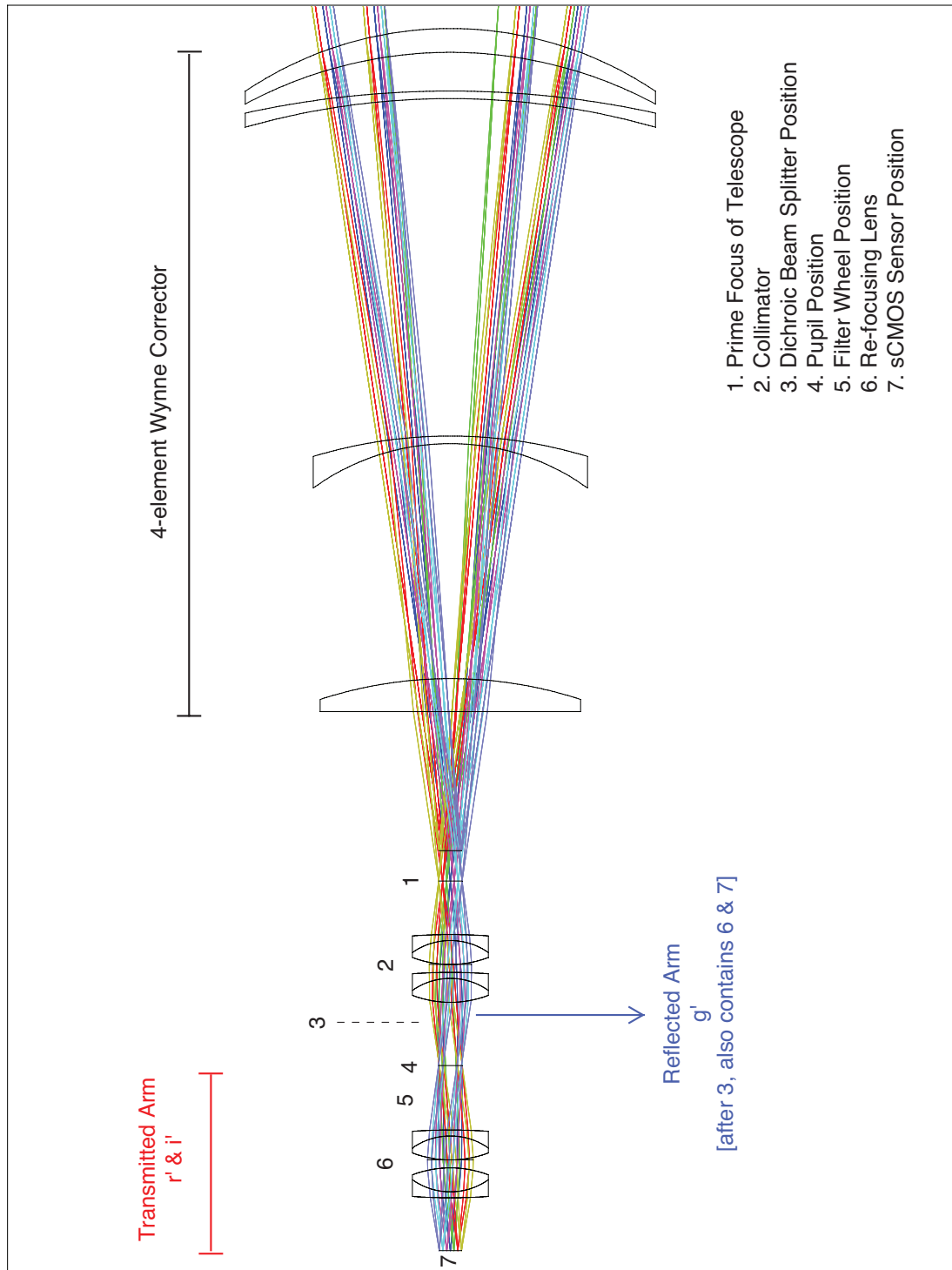


Figure 2.6: Here we show the optical design of CHIMERA, which was assessed using the Zemax optical design software. Since we discussed the Wynne corrector in § 2.2.2, we also include the 4-element Wynne optical system, which is located in the prime focus cage of the 200-inch, 4.459" before prime focus. The transmitted and reflected arms are highlighted; however we opted to omit ray tracing for the reflected arm via the dichroic beam splitter, for clarity in the diagram. Each element, including telescope focus, the pupil position after the collimator, and the filter wheel, is numerically indicated.

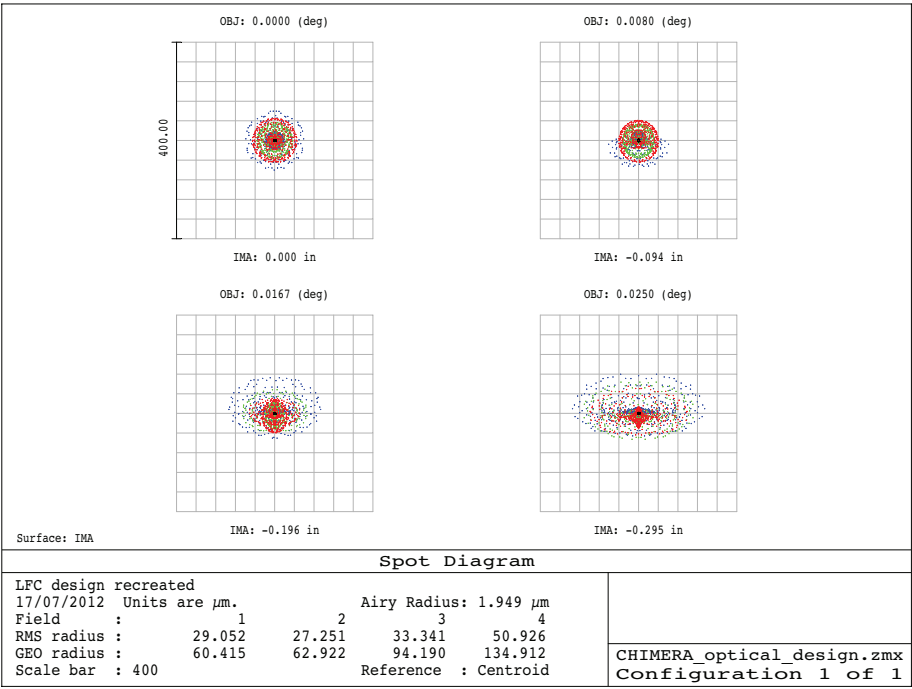
focal length of 4", these doublet lenses were selected because of their visible coatings which are optimized at 400 - 700 nm - the QE range of the sCMOS NEO chip. We split the light along this path via a long pass silica dichroic beam splitter (with an angle of incidence (AOI) of 45°, anti-reflective coatings, and a diameter of 2"). The reflectance and transmittance curves meet at 567 nm, and have >90% throughput for each component. A nine position filter wheel on the 'red arm' houses 1.25" r' and i' filters, whereas the 'blue arm' has an integrated 1.25" g' filter. These filters were acquired from Astrodon¹⁵, and are designed based on the SDSS photometric standards of Fukugita et al. (1996). The pair of achromat doublets used for collimation, were placed at a distance ($d \approx F_{\text{collimating_Lens}}^{\dagger}$) from the focal point of the telescope, in order to collimate the light.

The dichroic beam splitter is located in collimated space, but because of severe space constraints, it was placed $\sim 1.6''$ in front of the optimal pupil position. We were required to move the mirror by this amount, to physically allow for the filter wheel to be placed in the light path (position #5 in Figure 2.6), before the re-focusing lens (position #6 in Figure 2.6), to allow for focus movement. A second pair of achromat doublets is used to re-focus the light after the filter wheel on the transmitted arm, and similarly, the third pair of achromats is used to re-focus the reflected beam. Threaded lens cages and adjustable lens tubes allow for easy adjustment of foci during lab calibration. This combination of achromat lenses in the system provided lab tested diffraction-limiting image quality, and the optical setup provides a FOV of $\sim 3' \times 2.8'$, with a corresponding plate scale of $0.07'' \text{ pixel}^{-1}$. We assessed this quality by simulating a telescope in the lab from two lenses to provide an $f/3.5$ beam. We collimated this beam at infinity with respect to the known telescope focus point by using the collimating doublet element, and then used a $50 \mu\text{m}$ pinhole to focus the system and assess the FWHM of the focused spot. The system will avail of 4×4 pixel binning, in order to sample the PSF over ~ 3 or 4 pixels (optimum seeing conditions). We show Zemax¹⁶ RMS spot radius diagrams in Figure 2.7a, for different points on the image (on axis, out to 3 arcminutes as indicated), which were used to assess the image quality across the full FOV, for a given range of wavelengths. Figure 2.7b shows the same information, where we plot the FOV (x-axis, degrees), against the RMS spot radius (y-axis, μm). Figure 2.7 illustrates this assessment for the integrated flux of the g' , r' and i' filters, where the relative positions of the optical elements in the Zemax analyses were optimized

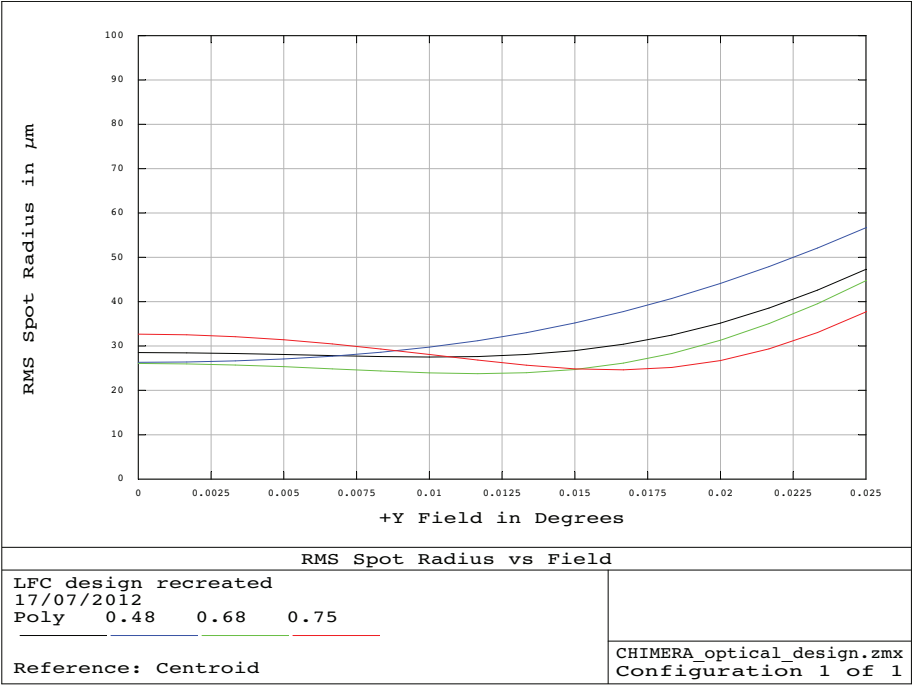
¹⁵Astrodon; Dr. Don Goldman; <http://www.astrodon.com/>.

[†]where d = distance, and F = focal length.

¹⁶Zemax is an optical design program of Radiant Zemax, LLC (Redmond, Washington); www.zemax.com/.



(a) RMS spot radius: on-axis (top left); 0.5' (top right); 1' (bottom left); 1.5' (bottom right). “RMS radius” correspond to $g' + r' + i'$ flux; this differs from Table 2.4 to follow, showing spots for each band separately. Each grid square is 40 μm . Colors indicate central wavelength: blue (480 nm), green (680 nm), red (750 nm).



(b) Plot of RMS spot radius vs. field position. Colors indicate wavelength (nm $\times 10^{-3}$). Seeing-limited PSFs are more or less maintained for all wavelengths until the outer edges of the field ($\sim 2.8'$).

Figure 2.7: Assessment of the image quality of the optical system via Zemax.

Parameter	g' Filter	r' Filter	i' Filter
RMS spot \odot (μm , on-axis)	44	48	50
RMS spot \odot (μm , 1')	42	46	48
RMS spot \odot (μm , 2')	52	60	60
RMS spot \odot (μm , 3')	86	100	102
PSF (arcseconds, on-axis)	1.02	1.06	1.07
PSF (arcseconds, 1')	1.02	1.04	1.06
PSF (arcseconds, 2')	1.08	1.13	1.13
PSF (arcseconds, 3')	1.34	1.46	1.48

Table 2.4: CHIMERA Optical System Image Quality Assessment.

We show the properties of CHIMERA's optical system, in terms of the RMS spot size diameter (\odot) for on-axis beams, and for beam positions at 1', 2' and 3', on the sensor FOV for each SDSS filter. We also show the quality of seeing that the system can produce. We note that average seeing at Palomar mountain is >1 arcsecond. We highlight that we are essentially seeing-limited at all points of the FOV, except at the very edge of the 3 arcminute field, where we lose $\sim 30\%$ of our quality, and are subject to some aberrations (Figure 2.7a, bottom right). These spot radii were assessed using Zemax. Figure 2.7 shows diagrams and a plot of RMS radius vs. field position for all three wavebands summed together. This table reports the individual spot sizes for each filter, assessed independently.

with respect to a range of $\sim 400 - 850$ nm. We also include these analyses in Table 2.4, but for each filter assessed independently.

A filter mount was custom built for the g' filter, which screws directly in to the lens tube on the reflected arm. A baffle is also included after collimation, whose clear aperture (~ 25 mm) is $\sim 50\%$ larger than the beam size at that point (~ 16 mm) - we conservatively selected this aperture to ensure no mechanical vignetting occurred. This baffle acts as a stop for any stray or internally reflected light within the optical system, thus preserving image quality at the image plane. Finally, we custom designed camera mounts, which allowed for re-positioning of each NEO camera in any direction of the x - y plane. These mounts can be seen in the Solidworks¹⁷ drawing in Figure 2.8, and in lab pictures in Figure 2.9b.

The CHIMERA instrument box, like GUF1, was designed to be a light-weight structure, and thus was made of 1/8" aluminium. As shown in Figure 2.8, this allows for easy access to the main instrument, since the enclosure can be easily removed from the instrument

¹⁷Solidworks is a 3D mechanical CAD (computer-aided design) piece of software, that was developed by Dassault Systemes Solidworks Corp., a subsidiary of Dassault Systems, S. A. (Velizy, France); www.solidworks.com/.

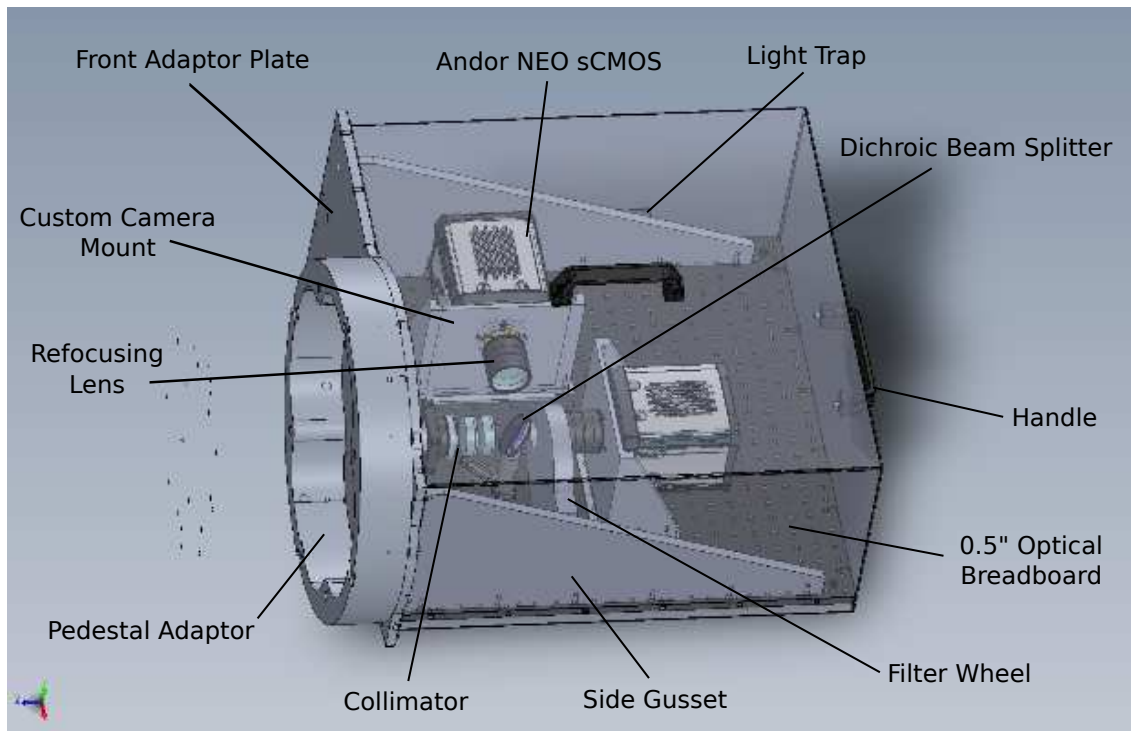
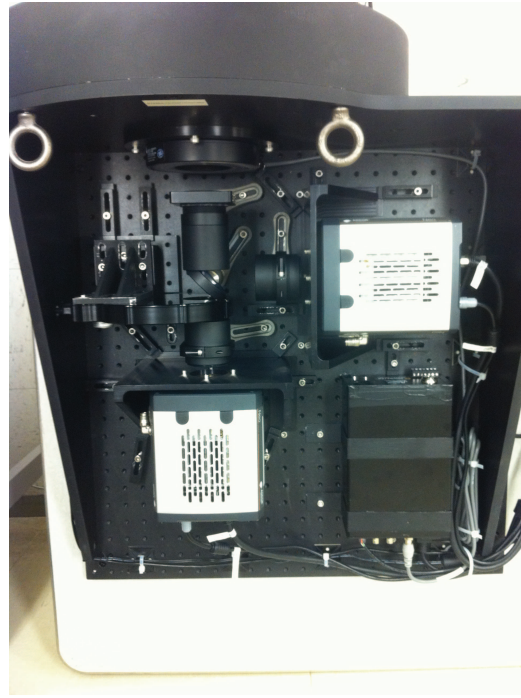


Figure 2.8: Here we show a Solidworks drawing of the CHIMERA instrument. Note that we have removed the lens tube housing on the collimator element, to allow the reader to view the setup in a clearer fashion. Similarly, we removed the posts from the refocusing lenses for the same reason.

structure. All cabling (including power, communication etc.) is connected to the control computer via a light-trap access point on the right of the instrument. In addition to the larger enclosure size, the optical requirements were more complicated (as outlined above), and therefore we had to accommodate many lens elements and mirrors (plus mounts and posts), a filter wheel, two Andor NEO cameras, and a large controller box for the mechanical shutter (shutter and controller described in § 2.2.4). We used a 0.5" optical breadboard, with 1/4"-20 threads on 1" centers, as the main instrument base. The custom front plate of the instrument was designed to be secured to this breadboard, and in order to ensure complete structural support in every plane of motion, we included two large triangular gussets, supporting against stress at the rear of the optical board. As per the mounting requirements of prime focus instruments on the 200-inch, we were required to custom design a pedestal adaptor plate, which attached to the front plate of CHIMERA, and then on to the main prime focus structure. We show labelled SolidWorks drawings of the CHIMERA



(a) Components on the optical breadboard.



(b) CHIMERA fully assembled.

Figure 2.9: (a) CHIMERA at the early stage of assembly. (b) Fully assembled, lab-tested, and ready for commissioning. Components reflect labeling in Figure 2.8.

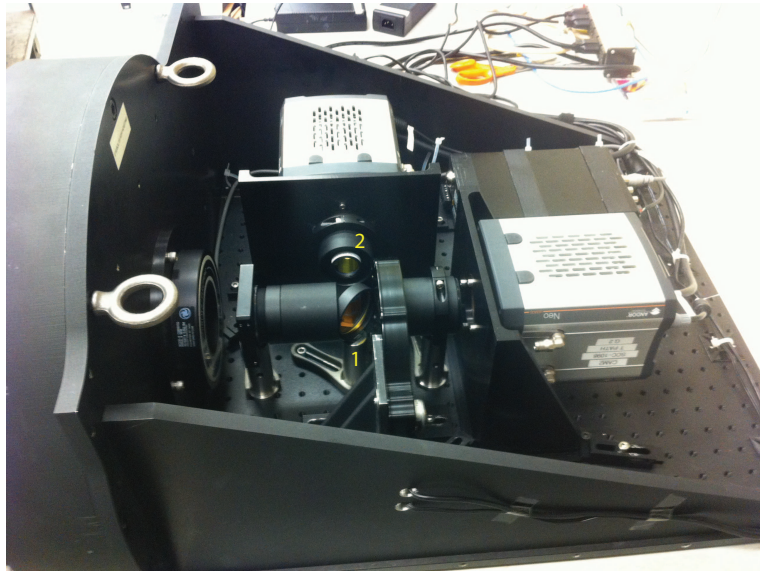


Figure 2.10: Optical setup showing the dichroic beam splitter (1), and the g' filter (2), held at the front end of the focusing tube of the collimating lenses.

design and layout in Figure 2.8, and pictures before and after assembly in Figures 2.9 and 2.10, where optical components that reflect labeling in Figure 2.8 are shown. Finally, a mechanical shutter is mounted at the open aperture of the front mounting plate. A custom mount was built for this purpose. Since the Andor NEO sCMOS camera does not include a physical mechanical shutter on-board, the inclusion of a shutter was important for the acquisition of bias frames. Furthermore, by placing the shutter at the open aperture of the instrument, this was the only way to guarantee a light-tight enclosure.

Briefly, a few words about the 200-inch Hale telescope. It was built by Caltech[†], and is named after George Hale - an astronomer that published an article many years before the commissioning of the 200-inch, detailing his vision of “The Possibilities of Large Telescopes”. The telescope saw first light in 1949, and was in fact the world’s largest telescope for many decades. Indeed, the American astronomer Edwin Powell Hubble was the first astronomer to use the telescope. A great many discoveries have come from this facility, e.g. quasars and hundreds of asteroid detections. Typical seeing at the 200-inch is ~ 1 arcsecond, where < 1 arcsecond is considered to be excellent conditions. The facility hosts a wealth of astronomical instruments, including facility instruments, pseudo-facility instruments and public instruments. As a PTF follow-up instrument, CHIMERA is currently stationed as a facility instrument.

2.2.4 Hardware and Software

CHIMERA is operated by a Supermicro SC825 2U server¹⁸. A RAID-5 configured storage solution offers 8 TB of capacity and allows sustained data rates of 1.4 TB hr^{-1} . The server is mounted in the prime focus cage with CHIMERA. We designed a custom “V-plate” - a $30'' \times 20''$ (L \times W), 0.5'' thick aluminium plate, built specifically as a mount for the server. This V-plate mount is then secured on to one of the many “V-slots”, on the wall of the cage. The computer is remotely controlled from the 200-inch control room, and has a dual-booted OS, including a Windows Server OS, and a Linux Redhat distribution. Andor SOLIS software runs and operates the Andor NEO sCMOS cameras from the Windows partition option. The NEO SOLIS software offers similar functionality to that of the iXon SOLIS versions, and as before, communicates with an on-board network card via a pro-

[†]California Institute of Technology.

¹⁸Intel Xeon 2.40 GHz $2 \times$ quad core E5620 processors, 24 GB DDR3 RAM, 8 TB storage (RAID-10 configured). Full system specs can be found here: <http://www.supermicro.com/products/chassis/2u/825/sc825tqr720u.cfm>.

prierty network cable, as outlined in more detail in § 2.1.3. However, the latest versions of NEO Solis are basic test platforms only, and could not handle data rates ≥ 10 fps, without significant readout times. We highlight that these readout times were software-based bottle-necks, not hardware. Under the Solis operation, files are first stored in the virtual memory section of the selected hard drive. Once the acquisition is complete, this data is then written to disk, which can take longer than acquisition times if spooling ≥ 10 fps, thus reducing the cadence and nullifying the advantage of high readout rates. Therefore, in order to avoid this loss of time on sky, control software was developed[†] in a Linux environment that is capable of controlling both cameras simultaneously, in addition to dealing with any data rate the camera systems offer. It also contains guiding capabilities, as well as auto-focus, PSF assessment and weather assessment, and it can communicate with the Palomar TCS. The software is currently being benchmarked, and is due to be fully launched at the beginning of observing semester 2012B.

As outlined in § 2.2.3, we employed a shutter at the front of the CHIMERA instrument box. We obtained a Uniblitz[‡] CS65 mechanical shutter, with a 65 mm iris aperture. To run and control the shutter mechanism, a VCM-D1 single channel shutter driver was installed, which is mounted inside the instrument enclosure - as shown in Figure 2.9b. The shutter is remotely controlled in the telescope control room via the CHIMERA server by running simple C-code, which provides instructions to open or close the shutter iris.

Finally, in order to accommodate the 1.25" filter size, we obtained a 9-position ATIK¹⁹ EFW2 electronic filter wheel - which can house both 1.25" and 2" filter sizes. On-board drivers allow the wheel to be controlled by a USB connection to the CHIMERA control server, and simple software, such as Astroart or MaxIm DL, communicates directly with the filter wheel.

2.2.5 GPS Tracked Timestamping and Guiding

GPS-assisted timing in CHIMERA provides sub-microsecond absolute timing accuracy, to facilitate multi-epoch timing experiments, as well as coordinated multi-frequency observing campaigns with other telescopes. In order to achieve these timing accuracies, an IRIG-B compatible GPS PCI-e card was installed in the CHIMERA control server. This card connects directly to an RG58/RG59 coaxial cable, running to the prime focus cage of

[†]Credit: Jennifer W. Milburn, Astronomical Instrumentation Software Engineer, Caltech.

[‡]Uniblitz: Vincent Associates; <http://www.uniblitz.com/>.

¹⁹ATIK Instruments; <http://www.atik-cameras.com/>.

the 200-inch from a distribution amplifier. This amplifier is connected to a GPS antenna on the side of the telescope dome, ensuring uninterrupted line-of-sight for satellite communication. The coaxial cable carries an IRIG-B output signal, which synchronizes directly to the GPS receiver. The NEO cameras contain an internal clock with 25 ns accuracy. They are (simultaneously) externally triggered by the Linux control software where a TTL pulse is provided directly to the camera, and maintained during data acquisition. These time stamps are logged and written to the header files of each frame once the data write is complete.

The telescope does not have a stand-alone guiding system; therefore all instruments on-sky are expected to have their own system in place. The TCS accepts communication via a TCP/IP interface. TCS requires two primary instructions to perform correction: 1) a coordinate offset formatted as an ASCII command string with decimal values of right ascension (RA) and declination (DEC), and 2) a slew rate for each axis in units of arcseconds per second. Guiding capabilities have therefore been included in the control software, which provides this information to TCS. The software obtains a frame every n seconds, taken from files already written to disk, and uses *iraf.daofind* routines to locate stars on the frame. It then calculates an x - y coordinate shift which is written to a text file, in the format that the TCS requires to make guiding correction.

2.2.6 CHIMERA as a Palomar Transient Factory Instrument

CHIMERA will commence targeted campaigns of known classes of short duration variables, including those identified by PTF, in semester 2013A. However, as well as carrying out targeted observing campaigns, CHIMERA will be available to PTF to perform early photometric follow-up on candidate PTF transients, to allow quick identification of rapidly varying sources. This mode of operation will commence in semester 2012B. To date, PTF follow-up observations with the Palomar 200-inch involve the use of the Large Format Camera (LFC) at prime focus, and the Double Spectrograph (DBSP) at Cassegrain focus, for photometric and spectroscopic follow-up of candidate transients. The location of these instruments at different foci has allowed these instruments to be used together on individual nights, maximizing the efficiency of PTF observing with the 200-inch.

CHIMERA has been developed as a prime focus instrument to allow it to be used as a direct alternative to the LFC for photometric follow-up of PTF candidate transients. It will exceed the performance of the LFC in producing deep pointings, for example on extragalactic candidate transients, while simultaneously offering the capability to provide

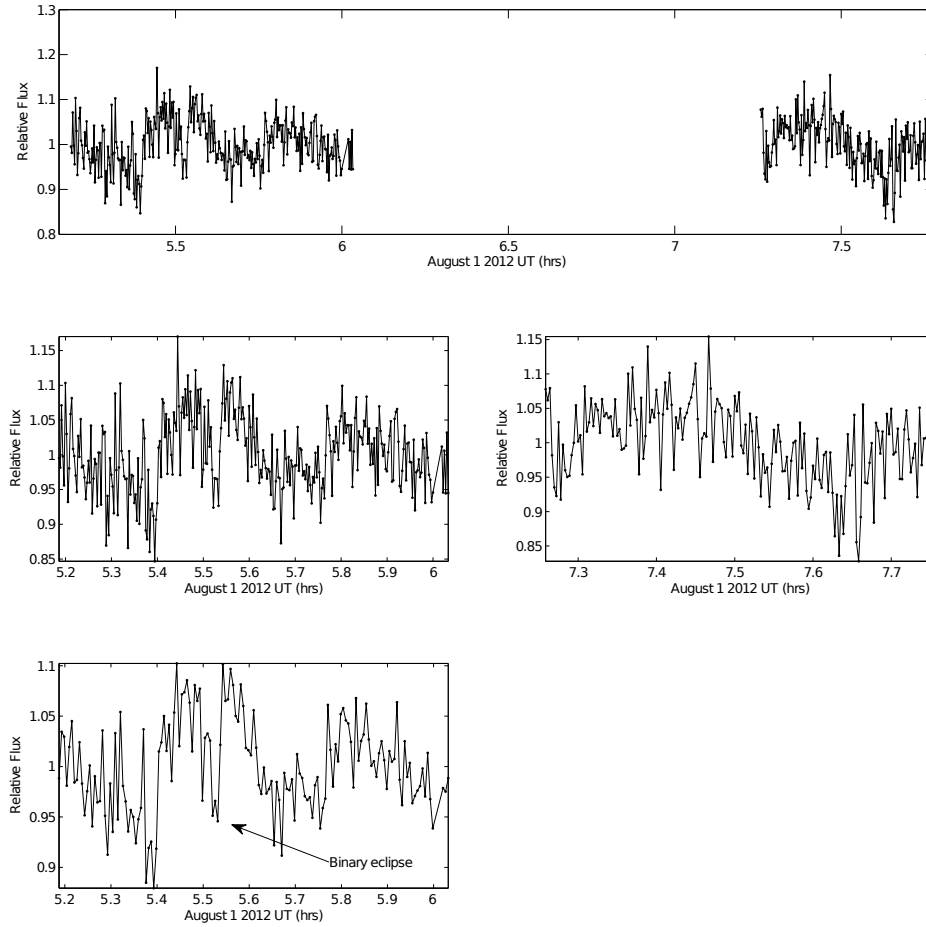


Figure 2.11: We obtained g' and r' data at two different time intervals in the night for an AM CVn target. This is shown here as proof of concept data only to illustrate the commissioned status of CHIMERA. [TOP] We show r' lightcurves taken on August 1, 2012. We were observing another target during the break in the data ($\sim 6.10 - 7.25$ UT). Data were taken with 10 second exposures. [MIDDLE] Individual lightcurves from TOP plotted to show more detail. [BOTTOM LEFT] First lightcurve binned by a factor of 2, where we highlight a detected binary eclipse.

higher time resolution with little impact on sensitivity, to investigate short duration variability. The ability to simultaneously observe in two photometric bands, thereby allowing a rapid color-based preliminary classification, is also particularly useful for PTF transient classification.

The newly commissioned instrument began testing on the Palomar 200-inch on August 1, 2012 and will soon be fully available to fulfill its role for early photometric follow-

up of candidate PTF short duration transients. The instrument will commence targeted campaigns of confirmed targets of interest in 2013A. Proof of concept data from the August 1, 2012, instrument commissioning is shown in the following subsection.

2.2.7 “First Light” - Proof of Concept Data

Here we include ‘proof of concept’ data that was obtained on August 1, 2012, during CHIMERA’s commissioning run. Although the primary goal of this scheduled time was an optical and mechanical test of the instrument, a full science program was prepared for use as test data. The instrument, as well as the control computer and V-plate, were successfully mounted and balanced in the prime focus cage, with no mechanical issues. The weather was excellent ($\sim 0.8''$ seeing); however there were some periods of intermittent cloud throughout.

The optical performance of the instrument was in excellent agreement with the Zemax software tests, and lab tests, prior to commissioning (§ 2.2.3). The system was seeing-limited for on-axis points, where typical FWHM values were measured to be $\sim 7 - 15$ pixels (with a binning factor of 4×4), corresponding to $\sim 1.5''$ seeing - which were in agreement with the seeing estimates from the Palomar in situ weather station. As expected, aberrations were present for stellar PSFs outside field diameters of $\geq 2.8'$. In addition to software, timing, focus and camera performance characterization tests, we observed two eclipsing binary systems, two exoplanet transits (where both ephemerides were known), and a brown dwarf, in multiple bands, simultaneously. We also obtained deep pointings of dense starfields in order to assess stellar PSFs, and optical aberrations, over the field. These data are currently being processed. For the purpose of CHIMERA proof of concept data, we include r' lightcurves from an eclipsing binary in Figure 2.11, taken with 10 second exposure times.

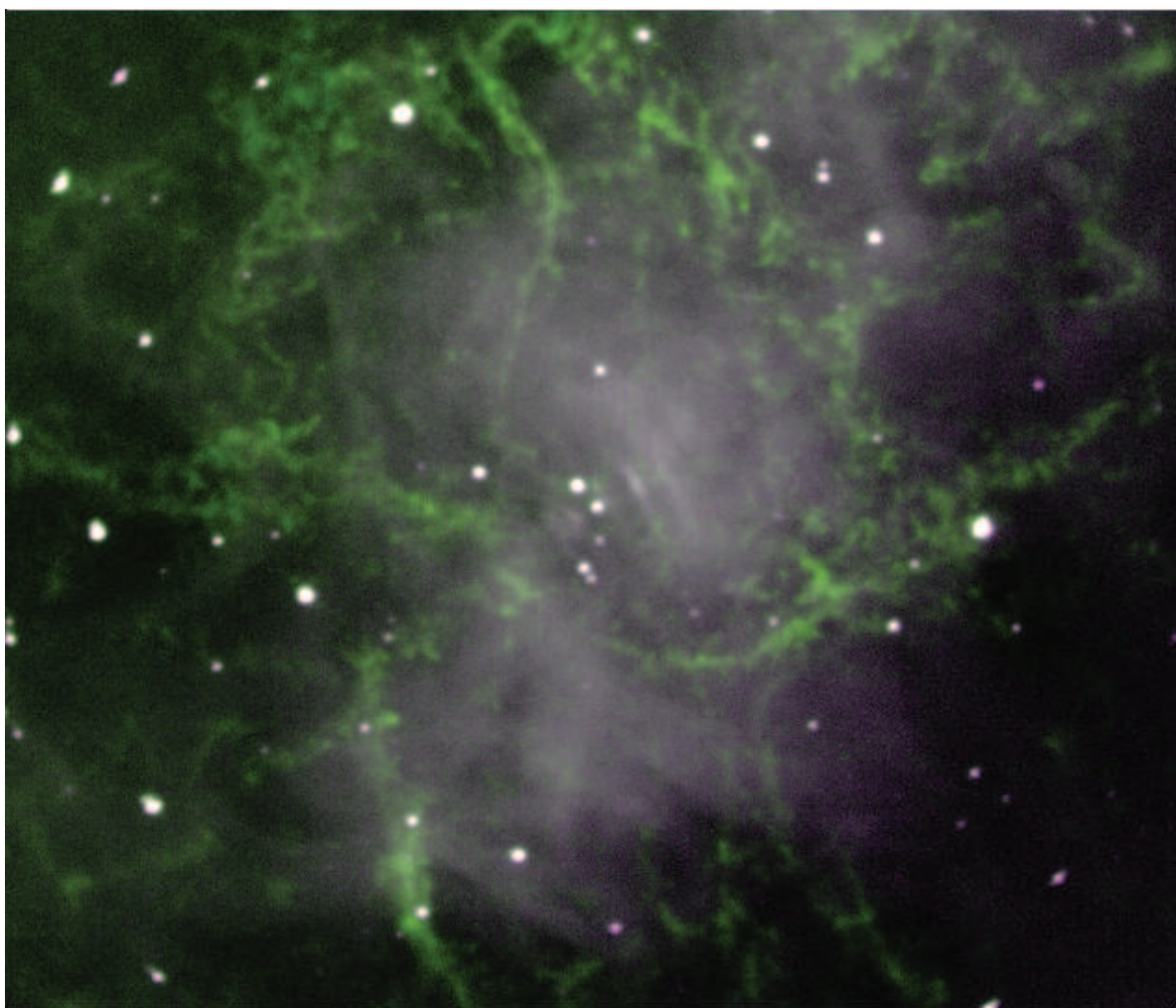
2.3 Summary

In this chapter, we have outlined the optical instrumentation that was developed and used during this work. Two instruments were designed, constructed and commissioned during this time, each with specific capabilities to facilitate their research goals, but also capable of being used for many other observational areas of interest in astronomy.

GUFI, the Galway Ultra Fast Imager photometer, was re-designed from the initial mk.I version, to be deployed on the 1.83 m VATT telescope, on Mt. Graham, Arizona. It was

commissioned on VATT in May 2009, and has been stationed since that time as a visitor instrument. GUFi is a high-speed photometer, which uses the Andor iXon DV887-BV camera, whose primary goal is the search for variability from ultracool dwarfs (Harding et al., 2012a,b). It has also been involved in many flare star campaigns to search for large and small flaring events, obtained with high-cadence imaging (Harding et al., 2012d). The instrument is located at Cassegrain focus of VATT, and offers a native FOV of $\sim 1.7' \times 1.7'$, with a corresponding plate scale of $0.2'' \text{ pixel}^{-1}$. However, GUFi also has options for visible and NIR focal reducers; when installed, the system offers a $\sim 3' \times 3'$, with a corresponding plate scale of $0.35'' \text{ pixel}^{-1}$. The great advantages of GUFi, particularly for observations in transient astronomy, are its 100% observing duty cycle (with a $\sim 2 \text{ ms}$ readout rate) and very low readout noise, while still maintaining high QE.

CHIMERA, the Caltech HIgh-speed Multi-color camERA, was developed as a prime focus instrument on the Palomar 200-inch telescope. The instrument has the capability of providing low-noise, high time resolution images in multiple photometric bands, where users can simultaneously select the SDSS g' filter, with either the r' or i' bands. The system uses the new Andor NEO sCMOS technology, which deliver rapid frame rates (100 fps full frame, $>1,600 \text{ fps}$ windowed) over a wide dynamic range ($\sim 30,000$), with low noise ($<1 \text{ e}^{-}$). CHIMERA also offers absolute timing accuracy ($< 1 \mu\text{s}$), which is extremely useful for multi-epoch timing experiments (e.g. AM CVns, flaring stars, transiting exoplanets). Thus, it is optimized for monitoring of targets that vary on timescales from milliseconds to hours, and indeed, any transient or periodic source, detected by PTF or ZTF. The system offers a FOV of $\sim 3' \times 2.8'$, with a corresponding plate scale of $0.07'' \text{ pixel}^{-1}$, and therefore utilizes software pixel binning options, where the chip is binned to 4×4 to sample the PSF over many pixels. CHIMERA was commissioned and tested on the 200-inch on August 1, 2012, and remains at prime focus as a Caltech/Palomar facility instrument.



The Crab Nebula (M1) as taken by CHIMERA on August 1, 2012, at prime focus of the 200-inch. This is a two-color 10 second exposure. (Observers: Gregg Hallinan, PI; Leon Harding, Inst. Scientist; Gillian Kyne)

“To err is human, but to really foul things up requires a computer.”

Farmers’ Almanac

“Programming today is a race between software engineers striving to build bigger and better idiot-proof programs, and the Universe trying to produce bigger and better idiots. So far, the Universe is winning.”

Rick Cook

3

Data Reduction & Variability Analysis

The primary focus of research in this thesis, is an investigation into the optical signatures from mid M dwarfs, to early L dwarfs. In this chapter, we discuss the data calibration/reduction techniques and time-resolved optical differential photometry that was applied to the data obtained from the instruments commissioned during this work and described in Chapter 2, as well as the subsequent statistical analyses of the detected periodic and aperiodic signals. A number of other telescope facilities and instruments in addition to those described in chapter 2 were also used over the course of this study. In each case, data reduction and differential photometry was also carried out, in order to monitor for such variability. However, different considerations needed to be applied for each data set, since each telescope and instrument inherently contains unique sources of error, different image properties in calibration data, and so on. These considerations are discussed in Chapter 4. We also outline the data reduction pipeline (Sheehan, 2008), that was modified and used for GUF1 mk.II VATT data, and data from other telescopes and instruments. In many of the sections, we give a brief overview of the theory/methods first, followed by descriptions of these methods in more detail in the paragraphs that follow. All of the photometric and statistical routines and scripts in this chapter were developed and implemented by the author unless stated to the contrary in the coming text (some of which utilized well established routines that are cited in the relevant sections).

3.1 Data Reduction and Photometry

In this section, we discuss the pipeline that was largely used to reduce the data in this thesis (§ 3.1.1). Where applicable, other techniques/pipelines were implemented for given

datasets - this is highlighted in the relevant sections. The original pipeline, hereafter ‘L3 pipeline’, was developed by Sheehan (2008), and was used to reduce GUFi mk.I data sets. Like the first iteration of GUFi, the Andor iXon DV887-BV camera (utilized by GUFi mk.II in this thesis) has been used to acquire the data in this work. Therefore we decided to use the existing routines for any GUFi mk.II data, in addition to making modifications to some of the routines for compatibility with other instruments and telescopes. We also developed registration and analysis routines and integrated them into the pipeline. § 3.1.3 briefly outlines some scripts that were written to deal with circular rotation offsets in some data sets. These offsets were due to guiding and derotation errors while using the VATT telescope. § 3.1.2 discusses the effects of OH spectral emission on NIR data - commonly known as “fringing”. We detail the routines that were written to remove these effects. The remaining sections outline the photometric techniques that were used in this work, as well as how reference stars were assessed post-photometry, and finally, how the photometric errors were quantified.

3.1.1 The ‘L3 GUFi Pipeline’ - Photometric Data Reduction

Due to modern imaging technology, far higher frame rates are now possible, allowing for large amounts of data to be collected per given observation. Indeed, the CHIMERA or GUFi systems have the capability of producing Terabytes (TB) of data during an observation. The L3 pipeline was built for the purpose of managing these considerable amounts of data, and accommodating the many operational modes available to the user from the Andor camera systems - as shown in Chapter 2. It uses the Python[†]/PyRAF software language, where all routines are executed as pipeline modules within a PyRAF environment, which has the capability of calling IRAF[‡] tasks. These modules are GUI-based, and use the standard CCD reduction techniques of IRAF. These environments were selected over the ‘IRAF CL’ scripting tools, since the latter do not contain sufficient debugging or error analysis capabilities. Python allows error or exception handling, which was a strong motivation behind this decision.

As data is acquired by the Andor SOLIS software, image information is written to FITS format (.fits) header-files, e.g. acquisition mode, readout rate, amplifier, target RA & DEC,

[†]Python programming language is developed by the Python Software Foundation, and is a general purpose high-level programming language. Details found here: <http://www.python.org/>

[‡]Image Reduction and Analysis Facility. Developed by the National Optical Astronomy Observatory (NOAO), found here: <http://iraf.noao.edu/>.

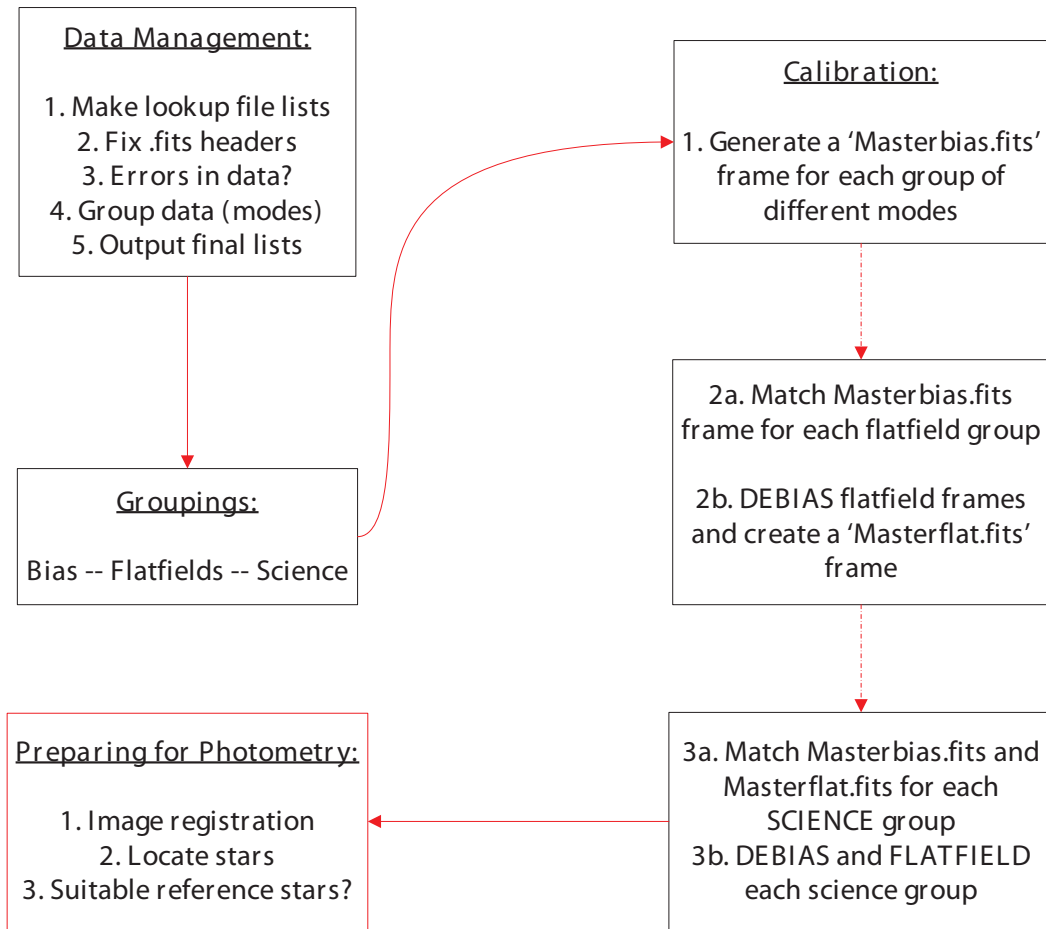


Figure 3.1: Flow-chart of the data management, data calibration/reduction, and pre-photometry steps, of the L3 pipeline. The highlighted red box indicates material that was added to the pipeline by the author in this work. All of the other steps were developed by Sheehan (2008).

image type, UTC, and so on. The pipeline makes use of these metadata in order to begin the data management process. We will break the pipeline up into three categories: **1) Data Management**, **2) Data Calibration/Reduction**, and **3) Preparing for Photometry**. A flow-chart of these steps, internal to the pipeline, is shown in Figure 3.1.

1) Data Management: The pipeline first creates an inventory of each folder type (bias, flatfield, science, focus, test, etc.) via the 'make_folder' routine. Folders are created for an observation night, which contains sub-folders, into which the respective files (classified as 'image types') are placed. Although the pipeline was designed to work with this data management format, it can be made compatible with any layout through appropriate user input,

and thus can be used for detectors other than the Andor cameras. Once these folders are created, a GUI interface allows the user to input file paths which point to these locations ('make_list' routine). The pipeline consequently creates "look-up" files for each image, and an initial data check is executed. This check searches for any inconsistencies in the image headers, such as corrupt filing information ('check_data'). There are also options to check each frame for hot pixels and bad columns; these can subsequently be removed if necessary. Once the pipeline has confirmed non-corrupt look-up lists, the user is required to add calibration data and additional Andor acquisition modes to the header files - these fields are later used to group frames of the same modes together, for the calibration steps that follow. Header information is modified via the 'header_fix' routine, where a GUI allows the user to input information such as: observer information, telescope information, filters, readout rates & modes, detector readnoise, EM-gain values, airmass, and UT and JD time-stamps. Since SOLIS saves the date and time in a single field ("DATE-OBS"), this routine is essential as it creates a stand-alone UT value. Furthermore, SOLIS only saves the *beginning* timestamp of each exposure, and therefore if the user has accumulated a datacube of images, each image will only contain this initial UT value. The 'header_fix' routine saves a time-stamp for each frame (which also takes the 2 ms readout rate into account). Finally, once these requisite fields have been modified and added, a final routine groups common frames, e.g. those of the same filter type, readout rate, amplifier and mode, and creates final look-up group lists ('make_groups'). The data is now ready for the automated data reduction steps.

2) Data Calibration/Reduction: The second stage consists of de-biasing and flatfielding the science frames. 'Bias' is the pixel-to-pixel structure in the positive electronic offset on the image, which prohibits the effects of readout noise from giving negative digitized values during the readout process. A bias frame is acquired by taking a zero second exposure with the shutter closed, and is then subtracted from each flatfield and science frame. Flatfielding is a function of pass-band (filter) and optical setup. This, in addition to the fact that the sensitivities of individual pixels on a CCD are not identical, requires the acquisition of flatfield frames. These are taken by exposing the chip to an evenly illuminated section of the sky or dome. The flatfielding process has the effect of compensating for the shading effect of any object(s) in the light path that can appear on the image as artifacts of optical system, e.g. dust, or other such artifacts, on the lens or filter systems. The flatfield correction is made by dividing the image to be corrected, by the flatfield. Flatfield frames must be corrected for bias and dark effects prior to combining. The data reduction steps of the L3

pipeline are labeled ‘1’ (‘bias_data’ routine), ‘2’ (‘flat_data’ routine) and ‘3’ (‘sci_data’ routine) in Figure 3.1, and are implemented as follows: 1) ‘bias_data’ locates all bias frames of common modes, co-adds these files, and then averages them, to produce a ‘masterbias.fits’ frame. 2a) ‘flat_data’ first assigns one of the masterbias.fits frames to the flatfield sample (based on the modes etc.). 2b) Individual flatfield frames are then de-biased, co-added, and normalized to a mean value of 1, to produce a ‘masterflat.fits’ frame. Finally, 3a) ‘sci_data’ assigns a masterbias.fits and masterflat.fits frame to each science group. 3b) Each science frame is individually de-biased and flatfielded. The data is now reduced.

3) Preparing for Photometry: Once data calibration and reduction has been completed, the pipeline offers various routines to prepare the science data for photometry. These include: breaking up datacubes into individual frames (‘data_ops_breakcube’), data registration (‘data_ops_reg’) - this only accounts for x - y shifts (not rotation), creation of star lists (x - y pixel positions; ‘find_stars’), optimum aperture size for aperture photometry (assessment of aperture radius in pixels vs. SNR; ‘app_size’), reference star evaluation (selection of suitable reference stars for differential photometry - we explain this further in § 3.1.5; ‘ref_stars’), and finally, routines for crowded-field or aperture photometry (‘data_analysis’). For image registration, the pipeline can use either the *iraf.xregister* task, or the *ISIS* C language registration code (Alard & Lupton, 1998; Alard, 2000). However, *ISIS* is generally unsuitable for sparse fields, and thus we opted to use the *iraf.xregister* task on our relatively uncrowded brown dwarf fields. Star lists, aperture selection, reference star evaluation, and photometry are all addressed in the following sections.

3.1.2 Atmospheric OH Spectral Emission - “Fringing”

Fringing is an optical effect in the thinned-substrate of back-illuminated CCDs and is present as a result of spectral emission (e.g. OH) in the atmosphere. Fringing interferes at red/NIR wavelengths much more so than at shorter wavelengths, since shorter wavelengths are absorbed much easier in the CCD silicon material. By contrast, a CCD’s substrate becomes transparent for wavelengths from the redder side of the spectrum (e.g. Johnson I-band), thus suffering from many internal reflections, and so any waveband that approaches the NIR is more susceptible to these fringing effects. We also note that emission lines are more numerous and stronger in the red. The amplitude of the fringing pattern can vary, but not its position. Since the amplitude variations expected in these ultracool dwarf targets are of the order of $\sim 0.2 - 1.20\%$ (waveband depending), it is important to remove these

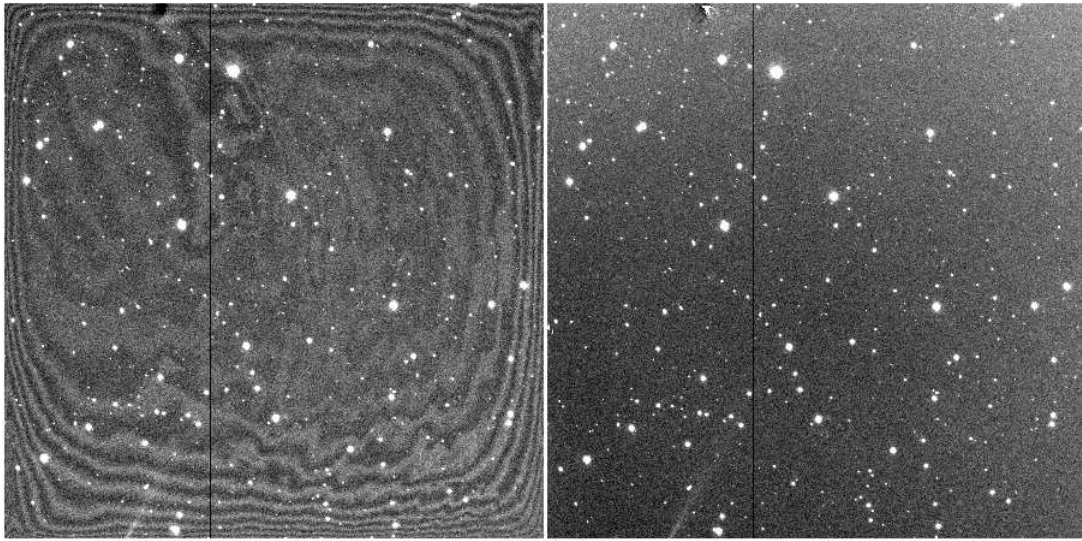


Figure 3.2: An example of a reduced Johnson I-band science frame, from the 2MASS J0746+2000 binary star field, from the $\sim 12' \times 12'$ VATT 4K detector on VATT. The frame on the *left side* clearly contains the fringing pattern, which is noticeably worse at the edges of the chip where the imperfections in the silicate structure, and thus the internal reflections, are worse. We also show the same frame, after fringing removal was applied (*right*). The fringing pattern has been completely removed after running our ‘de-fringing’ routine. A column of bad pixels is still present.

additive effects if the amplitude variations due to fringing are potentially greater than the target star differential lightcurves. We show these effects in Figure 3.2. In order to remove this pattern, we developed a ‘de-fringing.py’ routine, that was scripted in Python, and run in the PyRAF environment. The standard procedure for this correction, and the main steps in this Python script, are as follows:

1. Creation of a fringing template from well sampled dithered/re-pointed median-combined deep sky frames, containing only the fringing pattern.
2. Normalizing this template to each individual frame’s sky background level.
3. Subtracting this normalized pattern out of the science data.
4. Since this subtraction also removes sky background, in the final step we add the original mean sky background value to the frames.

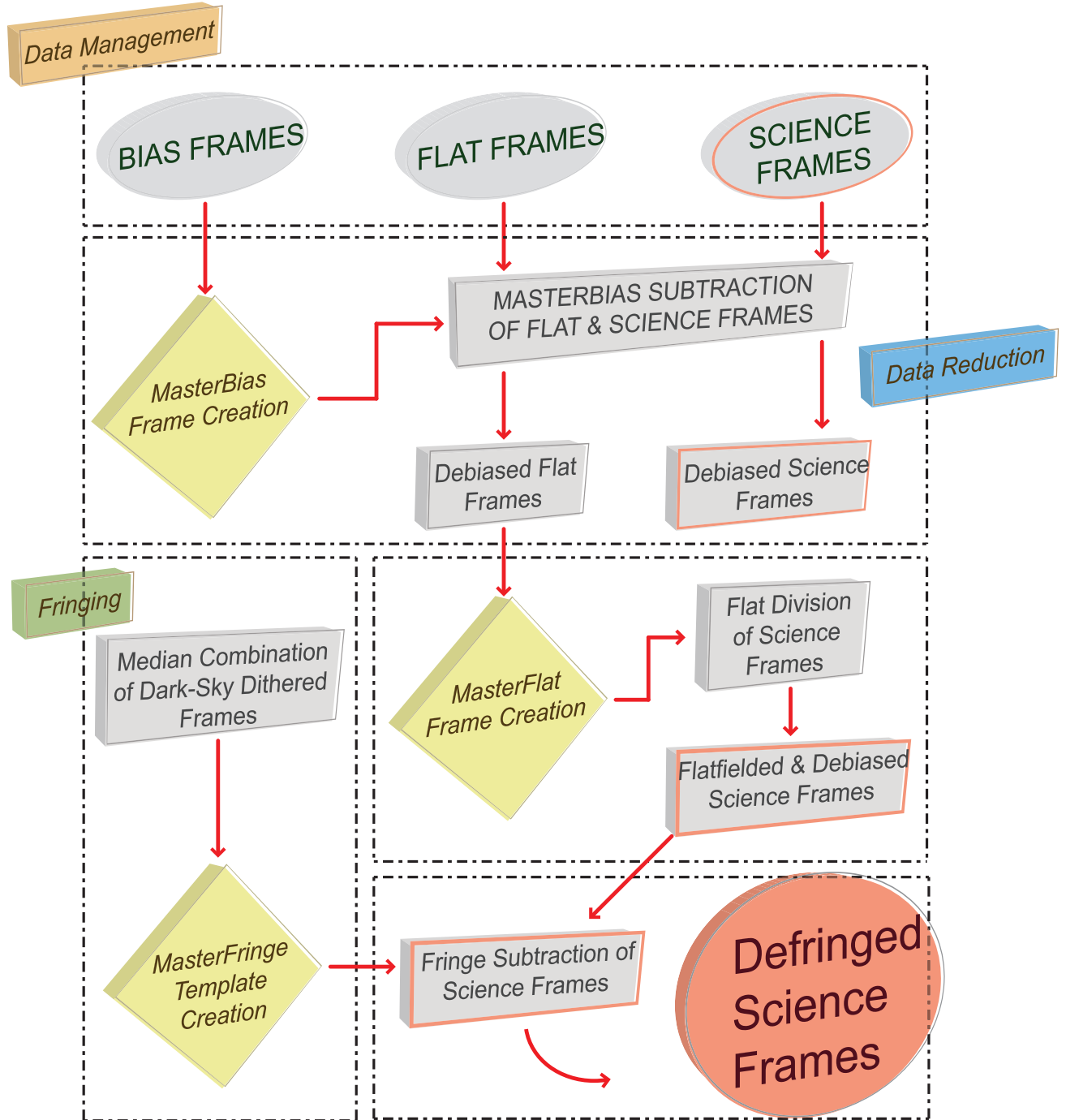


Figure 3.3: Schematic of the data management, data calibration/reduction, de-fringing and final reduced, de-fringed, science frame production. We note that this procedure is specific for each given night, filter and Andor acquisition mode.

We obtained dithered sky frames for all Sloan i' and I-band observations to allow for fringe removal if necessary. We also took dome flatfields which contain none of these atmospheric effects, in addition to twilight flatfields. We conducted tests to investigate the effect of this artifact on each consecutive data set, and if the amplitude of the fringing pattern was varying at a greater level than that of the mean sky background, it was removed. We show the full L3 pipeline procedure, including data management, calibration/reduction, de-fringing and final science frame production, in Figure 3.3. De-fringing was only applied to science data that was fully reduced. It is important to note that the fringing template itself (created in step #1 above), needed to be de-biased and flatfielded. Thus, dome flatfields were used to flatfield these frames, since twilight (sky) flatfields will also contain the fringing artifact in I-band, whereas dome flatfields do not.

3.1.3 Correcting for Circular Rotation in the Field

The VATT guider system uses an off-axis “horse-shoe” mirror, and the TCS contains a catalogue of stars that appear on this mirror, based on the telescope pointing. The guiding software requires focused stars, in the guiding window, with a minimum flux of $\sim 1,000$ counts, where $>65,000$ counts is the saturation point for the guiding camera. Although the guide star is off-axis, telescope tracking with guiding correction maintains a fixed position on the selected star. However, for some observations at VATT, we observed a pixel shift (linear migration) of the field over several arcseconds, and sometimes up to 0.5 arcminutes, over the course of an 8 hour observation. In most cases, this ‘migration’ seemed to be linear across the frame, i.e. moving in one x - y direction. However, some de-rotation tracking errors must also have contributed to this pixel offset from beginning to end of observation. We established this ‘circular rotation’ by blinking frames at the beginning and end of an observation, and identified these trends. Furthermore, the *iraf.xregister* task, which can only deal with translations, not rotations, found it difficult to accurately register stars on the same pixel that were located at the edge of frames - since this rotation was worse off-axis. This was most likely due to guide stars moving toward the edge of the guiding off-axis mirror, where the software found it more difficult to accurately centroid the PSF, thus leading to small guiding errors that accumulated over several hours. Differential flexure between the guiding and imaging systems cannot be discounted either.

Since standard registration tasks were not adequate to deal with this circular drift, we developed a Python script using the IRAF *daofind*, *xyxymatch*, *geomap* and *geotran* tasks. This procedure was implemented via the ‘registration.py’ routine as follows:

1. ***iraf.daofind***: This routine detects stars in an image, once you provide parameters such as the standard deviation of the sky background, the FWHM of the stars, and an upper and lower sigma pixel threshold for a detection. It therefore detects a peak amplitude greater than this threshold value above the local background. The task outputs this new star list in to a user-defined text file, where a range of parameters are included - the most important being the pixel x - y position.

2. ***iraf.xyxy-match***: Once *daofind* has logged all of the stars in each frame, we use *xyxy-match* to match these x - y pixel coordinates. It does so, by referencing every frame's coordinate file to a master reference list (e.g. the first frame in the series) and performs pixel matching via the 'triangles' algorithm. This can deal with linear shifts, axis flips, rotations and scale changes, by applying triangular pattern matching techniques. The user can specify a 'tolerance' (in pixels), and thus the amount of coordinates to be matched. Once this is done, the task writes this information to a 'matched coordinate list', which can be used to register frames via image transformation.

3. ***iraf.geomap***: We can now use the *geomap* task, which computes a transformation that maps two coordinate lists from different coordinate systems, provided by the *xyxy-match* task previously. The task outputs a file containing information regarding the common points in the image of the reference and input lists, as well as the required computed transforms to map these pixels on to one another.

4. ***iraf.geotran***: This is a powerful tool, that corrects for image distortion and misalignment using the geometric information provided by *geomap*. Indeed, it is these geometric transformation capabilities that allowed us to correct for the circular distortions in the images for some of the VATT data. The final images are then stored in a list file, and the data has now been calibrated, reduced, de-fringed and registered.

3.1.4 Aperture Photometry vs. PSF Fitting

Photometry is a technique that is used to measure the level of flux that is being emitted from an astronomical object. Thus, it is very useful in quantifying the behavior of an object's emission, and has been taken advantage of in this work to study the variability of ultracool dwarfs. Aperture photometry was chosen over PSF fitting, and was carried out using the

iraf.phot package. PSF fitting works best for crowded fields, where aperture photometry is less effective. Furthermore, it is also more effective for fainter stars, since the distribution, or standard profile of a star is fitted to all objects in the image, where the amplitude is adjusted for each source accordingly. Indeed, the PSF fitting technique has no risk of an aperture radius getting contaminated by additional flux from close sources. We employed aperture photometry for our fields, since they contained relatively bright, isolated sources on the CCD chip, and were quite sparse. Thus we found that the aperture photometry technique was very effective in treating each star's profile independently by sampling all of the light from each point source, providing an absolute measurement of the star's brightness, and could operate effectively with our data since the chosen aperture radii did not contain stray light from 'wings' of other PSFs. The *phot* task also computes accurate centers for each object, in addition to sky values, which are later used in the magnitude calculations. The L3 pipeline provides a routine to carry out this task - 'data_analysis', which outputs a final photometry file containing file names, date, UT, stellar and reference star flux, magnitudes, errors in flux and magnitude, and a differential photometric calculation, which we outline below.

Before carrying out aperture photometry, we selected a number of suitable reference stars to be used for differential photometry (outlined in the next section). These stars were chosen based on the following guidelines:

1. The reference stars must show near-Gaussian PSFs, and must be point sources.
2. They must be isolated from other reference stars on the chip in order to avoid contamination within annuli of other stars.
3. They must be present on all exposures for continuity.
4. They must not be saturated, *i.e.* linear to within $\sim 75\%$ of the CCD well-depth saturation limit in case of changing photometric conditions.
5. Ideally, if possible, the stars should have the same approximate color/spectral type as the target to minimize the effects of telluric extinction from increasing airmass. This is not always possible if there are unknown stars in the field.

Once suitable, non-variable reference stars are chosen in accordance with the above

guidelines (computed via the ‘*ref_stars*’ routine outlined in S 3.1.1), aperture photometry was performed on the target and reference stars. We provided the task with important initial parameters for these calculations, such as the FWHM of the stars, the standard deviation of the sky background, the aperture to be used, the annulus (radius of the sky aperture) and annulus (width of the sky annulus), and the target and reference star ID numbers (provided from the L3 pipeline’s ‘*find_stars*’ package). The variables that are used to compute the photometric calculations by *phot* are described here, and we define these quantities as: [R , the aperture of the radius in pixels]; [A , the area of the aperture in pixels² where $A = \pi R^2$]; [σ , an estimate of the standard deviation of the sky background, found via the *iraf.imexam.m* task]; [t , the exposure time]; and finally, [$G_{e/ADU}$, the gain in electrons per ADU]. The *phot* task then computes an estimation of the pixel-to-pixel sky background in the sky annulus, M_{sky} , and thus the total number of counts in the aperture, $Flux_{\star}$, excluding the sky values. Finally, it determines the instrumental magnitude, Mag_{\star} , and the associated errors, m_{err} . These computations are determined as follows:

$$Flux_{\star} = \sum(F_{Ap}) - A \cdot M_{sky}, \quad (3.1)$$

$$Mag_{\star} = (zmag) - (2.5 \cdot \log_{10} \cdot Flux_{\star}) + (2.5 \cdot \log_{10} \cdot t), \quad (3.2)$$

where $\sum(F_{Ap})$ is the total number of counts including the annulus in the aperture, and $zmag$ is the zero point of the magnitude scale. The errors are estimated from:

$$Err = \sqrt{\frac{Flux_{\star}}{G_{e/ADU}} + A \cdot \sigma^2 + A^2 \cdot \frac{\sigma^2}{n_{sky}}} \quad (3.3)$$

$$m_{err} = 1.0857 \cdot \frac{Err}{Flux_{\star}}, \quad \text{where } m_{err} \ll 1 \quad (3.4)$$

where Err is a formal photometric error via photon statistics, and n_{sky} is the number of sky pixels used by *phot* for photometry. The L3 pipeline task ‘*app_size*’ provides a calculation of the highest SNR, for a given aperture radius (pixels) via the *phot* routines. The user can select a range of apertures, and *phot* provides a list of formal IRAF errors in the instrumental magnitude for each aperture (σ_{IRAF}), from which the task then computes the corresponding SNR. Equation 3.4 can be modified, where $SNR = Flux_{\star}/Err$, such that:

$$SNR = \frac{1.0857}{\sigma_{IRAF}}, \quad \sigma_{IRAF} \ll 1 \quad (3.5)$$

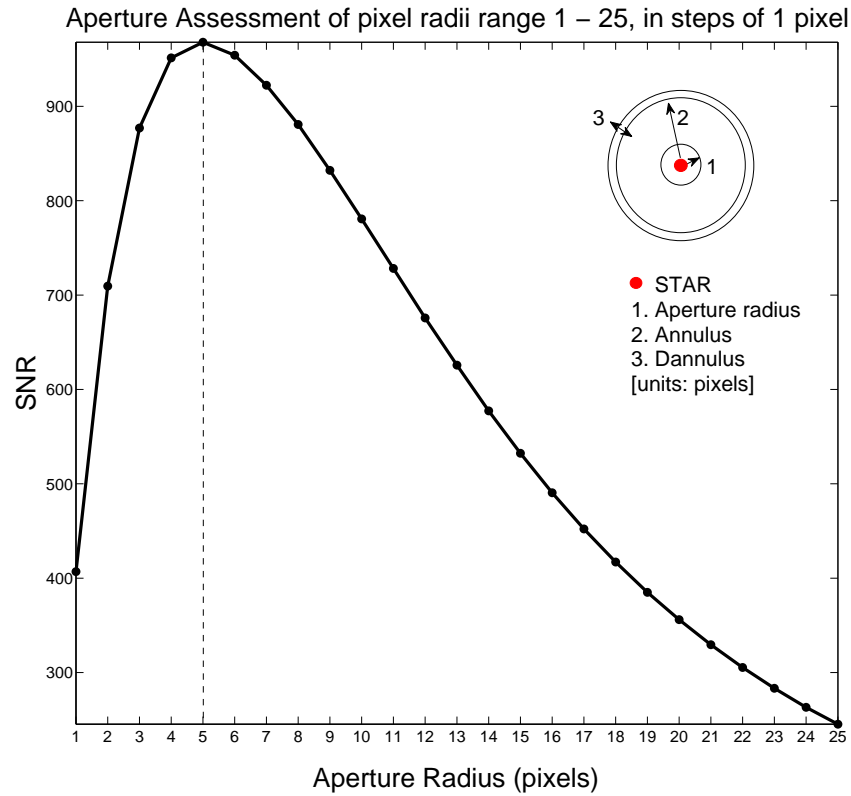


Figure 3.4: We show a plot of an optimum aperture assessment from the ‘app_size’ module. We selected an aperture radii range of 1 - 25 pixels, in steps of 1 pixel. Note how the SNR dramatically decreases for larger apertures, due to increasing noise from sky background. The optimum aperture in this case, with the largest value of SNR, is 5 pixels, as shown. However, the highest SNR value was not *always* chosen, and thus other pixel values in proximity, as indicated by the routine, were sometimes adopted. These variations can depend on factors such as a drastic change in seeing conditions, or the contribution of formal and informal errors (and other systematics) in the data.

Photometric apertures (in pixels) were assessed to establish which provided the highest SNR for the target star. Although this was a good approximation of the best fit aperture radius, we found that other pixel values close to the highest SNR value were sometimes selected for aperture photometry; aperture and sky annulus diameters varied from night to night depending on the average seeing conditions, and also on the contribution of the various systematic errors due to formal and informal errors. We did not compute the optimum aperture for every frame, but rather fixed it per night. An accurate calculation of the optimum aperture can sometimes be difficult, since small apertures only sample a fraction of the total light, whereas larger apertures can be dominated by sky background, or artifacts

from other nearby sources. In this work, we selected an aperture based on the evaluation of pixel vs. SNR values from the *app_size* routine, and we show an example of this assessment in Figure 3.4. Some of the key parameters for this calculation are indicated in the top right corner of the figure.

3.1.5 Differential Photometry

Differential photometry is a technique that is used to assess the change in a star's flux, or magnitude. We applied to it the data in this work to produce differential lightcurves of the target and reference stars. It was chosen over absolute photometry, since this relies heavily on stable atmospheric transparency and careful calibrations for changing airmass. § 3.1.4 outlined the methods used to conduct aperture photometry, which ultimately produces a file containing target and reference star fluxes, magnitudes, the errors in these quantities, and so on. Differential photometry was obtained by dividing the target flux by the mean flux of selected reference stars. However, there are many factors that can contribute to variability in a photometric lightcurve that may not be intrinsic to a target star. These can be quite effectively assessed, and quantified, by investigating instrumental effects for example, or by considering the effects of telluric extinction on stars of different color indices. When carrying out differential photometry, all stars in the field are relatively close together on the sky, and therefore are subject to more or less the same first order effects. For example, their air masses are approximately the same and therefore extinction effects such as $k(X_{\star} - X_c)$ also cancel out, where k is a first order extinction coefficient, X_{\star} is the air mass of the variable star (target) and X_c is the air mass of the comparison star. However, it is worth noting that if a comparison star has a different color to the target, telluric extinction can behave differently for different colors at increasing air mass. The FOV of GUF1 and the VATT 4K photometers capture between 3 - 30 reference stars for a given field. Photometry for all reference stars was also obtained as a measure of their stability, in order to ensure that variability was intrinsic to the target star. As discussed in § 3.1.4, these stars were chosen on the basis of their stability, position, isolation, the properties of their seeing profiles, and being of comparable magnitude (to avoid saturation of much brighter objects for a given exposure time) and color to the target. The L3 pipeline module *data_analysis* calculates relative magnitude (m_{rel}) lightcurves, as a function of UT, via the *iraf.phot* routines. In order to carry this out, it uses F_R , the reference flux in e^-ADU^{-1} for star R , where the number of reference stars in that frame can range from $R = 1 \dots N$. Therefore the reference flux of frame $F_{\bar{R}}$, is the mean value of all chosen reference star fluxes for a given

exposure. Thus:

$$F_R = \frac{1}{N} \sum_R^N F_{\bar{R}} \quad (3.6)$$

A time series of m_{rel} can be found by calculating the difference in relative magnitudes between the target and reference star magnitudes. The reference star magnitude is defined as:

$$m_{\bar{R}} = -2.5 \cdot \log_{10} \cdot F_{\bar{R}}, \quad (3.7)$$

so therefore the relative magnitude of the target is defined as:

$$m_{rel} = m_{\bar{T}} - m_{\bar{R}} = 2.5 \cdot \log_{10} \cdot \left(\frac{F_R}{F_T} \right), \quad (3.8)$$

where F_T and $m_{\bar{T}}$ are the corresponding target flux and target relative magnitude, respectively. $m_{\bar{R}}$ was calculated by averaging fluxes rather than magnitudes, since this gives higher weighting to brighter stars with intrinsically higher SNR, and thus lower photometric errors. Before producing the final differential photometric lightcurve, we move to one final consideration of reference star stability with respect to the target star, and accounting for poor/intermittent changing weather conditions.

3.1.6 Post-Photometry Assessment of Lightcurve

In addition to the calibration, reduction, reference star assessment, and photometric analyses, we developed post-photometry routines which were designed to identify poor quality regions in the lightcurve. Based on the identification of increased rms scatter, this analysis investigates reference star stability, in addition to periods of poor weather conditions (e.g. intermittent cloud, high winds etc.), where the SNR of all, or some, signals has gotten worse), and also identifies erroneous data points in the time series. These routines were written using the MATLAB²⁰ environment. We describe the various steps in this procedure below, and illustrate the steps in Figure 3.5.

²⁰MATLAB has been developed by MathWorks (www.mathworks.com), and is a numerical computing environment capable of matrix manipulation, plotting, the use of algorithms, the creation of user interfaces, and can also accept other computing languages such as C, Java and so on

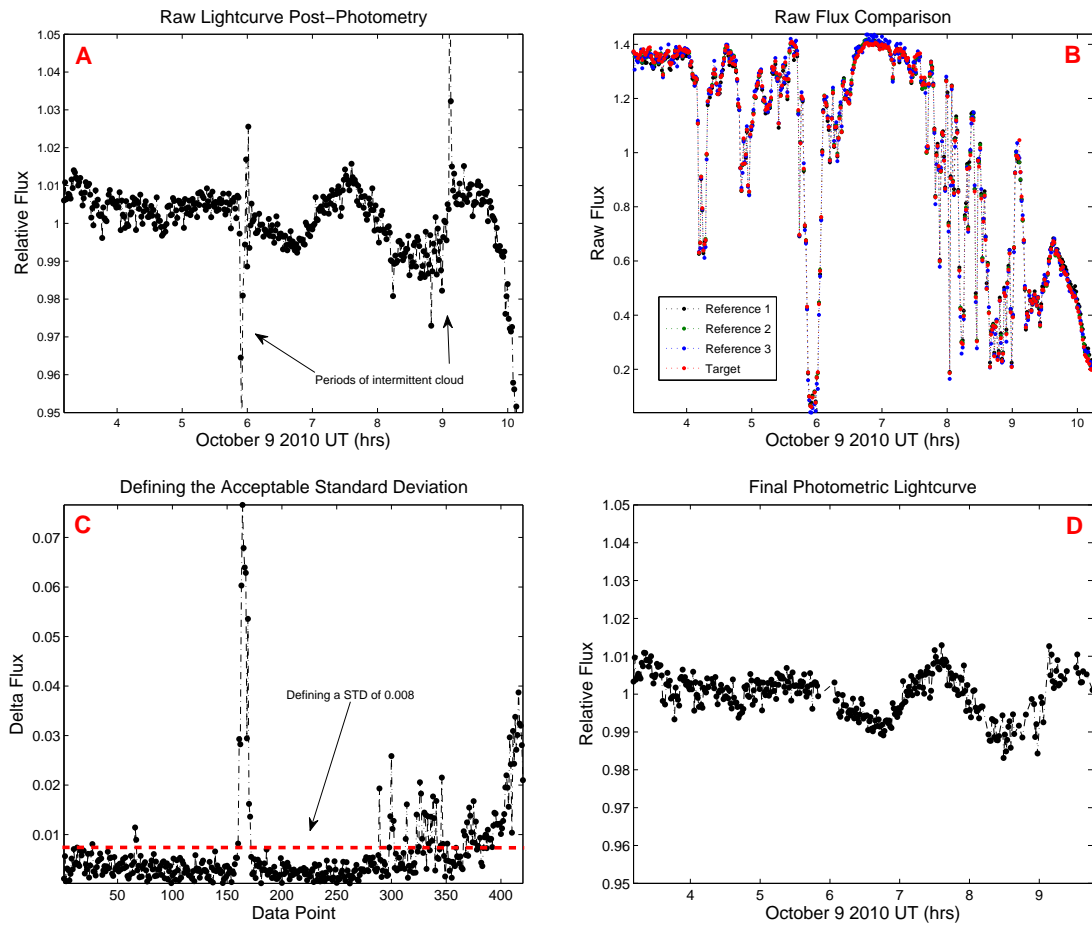


Figure 3.5: Here we show the four main steps in the “quality control” MATLAB routines. We use an observation from October 9 2010 UT, of the M dwarf binary LP 349-25AB. This was selected as an example since the seeing was generally excellent throughout the observation; however there were a number of times when intermittent cloud caused much lower SNR in the data. We highlight the effectiveness of this technique in removing such unwanted artifacts. **A:** Lightcurve from October 9 2010 UT where we show some parts of the night subject to intermittent cloud caused deteriorating transparencies and seeing conditions. This is quite obvious based on the increased rms scatter of the data points. The seeing, as measured by the FWHM of the stars, got worse toward the end of the night as the airmass increased. **B:** We show the raw flux of each reference star (1 - 3; black; green; blue) as well the target (red). The reference stars, as well as the photometric parameters (e.g. apertures) were carefully selected, and therefore each star’s flux was consistent for a given aperture radius throughout the night. Based on the flux in the lightcurve, it is clear at ~ 8 UT, as recorded in our observation logs, that cloud caused a drastic reduction in stellar flux. **C:** Based on the ‘quality’ routine, we select a standard deviation (STD) flux cutoff point of 0.008. We have highlighted this with a red dashed horizontal line. All data points above this will not be used in the final differential photometric calculation. **D:** Lightcurve after example poor weather data points were automatically removed by the routine, where the final lightcurve contains no obviously erroneous data points.

1. Plot the raw target flux, as well as all reference stars' fluxes for a given observation/exposure (marked 'B' in Figure 3.5). Assess the ratio of reference star flux, with respect to the target star. If a reference star has much lower SNR than others in the sample, or if its flux was subject to other effects at some stages in the night (e.g. isolated cloud, hot pixels, cosmic rays, contamination from other stars in its annulus), we do not use the star.

2. Calculate the mean value for each frame of all reference stars, and create one mean flux for all selected reference stars which we call the "superflux" (defined as F_R in Equation 3.8).

3. The value of each *individual* reference star is known from #2, and is divided by F_R to calculate each reference star's departure from the 'superflux'; thus, larger values imply a larger difference between a given reference star and the 'superflux', which suggests that this reference star's flux variations are also behaving differently. We define this difference for each star, of a total number n , as $F_{diff}(n)$.

4. Next, we derive the "quality factor", QF , for reference stars $n = 1 \dots N$, which is:

$$QF = \frac{flux_{ref}(n)}{(F_R - F_{diff}(n))} \quad (3.9)$$

where $flux_{ref}$ is the flux of each reference star, F_R is the 'superflux' and F_{diff} is the ratio of each reference star's mean flux with respect to the 'superflux'. This quality factor, when plotted, allowed us to assess the stability of the reference star fluxes throughout the night in terms of erratic/unusual behavior. We illustrate this in Figure 3.5, marked 'C', where there is clearly a difference at data point ~ 160 and again at around 300 or so.

4. We now assign a standard deviation cutoff point, which is user-defined based on the observed scatter. This point is then used as an absolute constraint on what data points are included for the final differential photometric calculation. Any data point exhibiting an rms scatter above threshold, is not used. This is again shown in Figure 3.5, marked 'C', with the red dashed horizontal line. In this case, we select a standard deviation threshold of 0.008 in units of relative flux.

5. The routines have now logged what data points to exclude based on this newly defined cutoff. These logs include target flux, and reference star fluxes. It also updates the UT data

series, to maintain accurate timestamping throughout (each UT data point was referenced to a corresponding target and reference flux data point at the beginning of the routine). We must re-define F_R at this point which is calculated from this log file, and this is then used for the final differential photometric calculation, along with the target flux values from the same log file. We show an example of this procedure from October 9 2010 UT in Figure 3.5. The final lightcurve is marked ‘D’, and when compared to ‘A’ (the original lightcurve), it is clear that the periods of intermittent cloud during this night have been effectively removed.

We note that we thoroughly checked these erroneous points by visual means in the raw frames, and by their structure in the lightcurve, especially those that were isolated, and exhibited large-amplitude variability. M dwarfs are active stars are thus such objects are commonly subject to flaring events. Since these routines are automated, the potential exists for ‘real’ data values to be identified as erroneous points. We also maintained extremely accurate observation logs during this work, and consequently these could be correlated with the above analyses as well. In order to avoid real data points being incorrectly filtered out, we highlight an alternative whereby the routine is only employed as far as step *B*, thereby flagging all data points below a given relative transparency of e.g. 30 - 50%. This would also account for the erroneous data points that have been removed in this example.

3.1.7 Photometric Error Estimation

Once the final photometric lightcurves have been calculated, we must indicate the photometric errors on each data point of the time series. Magnitude errors in the target and reference star datapoints were initially calculated by the L3 pipeline, in the module *data_analysis*, and were included in the final photometric data file, as outlined in § 3.1.4. Such error estimates are an effective indication of both the formal and informal errors associated with photometric datasets. Formal errors are errors that are derived from photon statistics and known instrumental readnoise by IRAF, whereas informal errors are derived from other sources during the data reduction process, such as flatfielding and defringing. In this respect, by estimating the total photometric error, we can account for formal/informal sources; indeed, this is a powerful diagnostic tool, since flatfielding or fringing errors are quite difficult to assess independently.

The total photometric error in the differential lightcurve (δm_{tot}) can be computed as follows, where we define m_t and m_n to be the magnitude errors in the target, and n^{th}

reference star, respectively:

$$(\delta m_{tot})^2 = (\delta m_t)^2 + \left(\frac{1}{N \cdot F_R} \right)^2 \sum_n^N F_R^2 (\delta m_n)^2, \quad (3.10)$$

where N is the number of reference stars used, F_R is the combined flux of these reference stars and $F_{\bar{R}}$ is the flux of the n^{th} reference star. This is a good measure of the total error in the lightcurve, and can in principal be applied to each data point. However, in order to calculate the *individual* photometric errors of m_t and m_n , we plotted their formal errors as calculated by IRAF (σ_{IRAF}) vs. the rms scatter of their lightcurves. The free parameters a & b , used as first order polynomials to this fit, determined the errors in these magnitudes via:

$$\sigma_{TOTAL} = a + b \cdot \sigma_{IRAF} \quad (3.11)$$

where σ_{TOTAL} is the total rms scatter of the lightcurve. Once we determined these photometric errors in the stellar magnitudes, we used these to estimate the errors in the individual flux data points. These errors can also be applied to a flux calculation. In order to calculate the error on each data point, we must take the target's error, as well as the sum of the errors from n reference stars, in to account. This was done as follows: consider the target star, T, and three references stars, R1, R2 and R3. The magnitude errors as calculated in Equation 3.10 in each of these are δm_T , δm_{R1} , δm_{R2} and δm_{R3} , respectively. Thus, the error in the target magnitude is known. Now consider the flux of these objects, F_T , F_{R1} , F_{R2} and F_{R3} - those of the target, and three reference stars respectively. Since the error in the magnitude is a percentage, we apply this percentage to each flux in the same manner, which we call δF_{R1} , δF_{R2} and δF_{R3} . These flux errors include the contribution of formal errors as calculated by IRAF. The total flux of the reference stars is $F_{R1} + F_{R2} + F_{R3} = F_{TOT}$. Therefore, δF_{TOT} can be found via:

$$\delta F_{TOT} = \sqrt{(\delta F_{R1})^2 + (\delta F_{R2})^2 + (\delta F_{R3})^2} \quad (3.12)$$

Therefore $\delta F_{TOT} / F \equiv \delta m_{ref}$, the magnitude errors of all reference stars. Finally:

$$\delta m_{datapoint} = \sqrt{(\delta m_T)^2 + (\delta m_{ref})^2} \quad (3.13)$$

where $\delta m_{datapoint}$ is the magnitude error for each lightcurve data point. These errors are indicated in all lightcurves in this work, which we will see in Chapters 4 - 8.

3.2 Variability Analysis of Photometric Datasets

In order to detect periodic variability, and assess its significance, we used a variety of statistical tests as a means of measuring the validity of the detected periodic variability and the associated errors. This assessment was carried out in the order of the following procedures, and will be further explained in the sections below:

STEP 1. The Lomb-Scargle (LS) Periodogram - this provided the period range, the statistical significance of detection (false alarm probability, outlined in S 3.2.1 which follows), and the corresponding power of each significant period.

STEP 2. Phase Dispersion Minimization (PDM) - this provided a measure of the period with the highest statistical significance (obtained via 10^4 Monte-Carlo simulated lightcurves) via phase folding based on range input by the user. This value was compared to the solutions obtained from STEP 1.

STEP 3. Sinusoid fitting and the Chi-squared (χ^2) Test - we assessed the periods which have the greatest significance from the steps above, and then performed χ^2 testing for each lightcurve to assess the amplitude and the error in the amplitude of each lightcurve.

STEP 4. Photometric error estimation (outlined in § 3.1.7) and period uncertainty assessment.

The mean amplitude variability (σ_{tar}) of the target lightcurves was established by Step 3, where the phase and amplitude of the sine function were varied, and then a least squares fit (LSF) calculation was performed. We took this amplitude as σ_{tar} . The PDM routines also give an estimate of the lightcurve amplitude. The corresponding reference star variability (σ_{ref}) was found via the standard deviation of its lightcurve - we take this value as the mean of all reference star standard deviations, in each target field. We plotted each reference star flux against all the others, as a test that each selected reference star was non-variable. Although variability can statistically be detected if the standard deviation is only fractionally larger than the error in the lightcurve's relative magnitude, the periodic variability detected in our target data is categorically present in each epoch, where the variability is clearly above the standard deviation of the reference star relative flux. Furthermore, different sets/combinations of reference stars were used as a 'sanity check' to

confirm that the signal was indeed intrinsic to the target star.

3.2.1 The Fourier Transform and the Lomb-Scargle Periodogram

The Fourier Transform is based on Fourier series analysis, which was first outlined by Jean Baptiste Joseph Fourier (1768 - 1830), a French mathematician and physicist. Fourier series analysis essentially fits the sum of an infinite number of sine and cosine functions to a set of data. Therefore this analysis is based on the decomposition of periodic signals into these trigonometric components. In order to do this, the Fourier Transform (FT) carries out a mathematical *transform* of such data from the time domain, to the frequency domain; thus the transform is a frequency domain representation of the original function. The FT can work on several variables or finite groups; however the accuracy of a periodic determination can be largely dependent on the amount of information the FT uses for its computation (e.g. the number of data points in a time series). Let us consider a given frequency (ν), where $\nu=1/\text{period}$, and t is time in seconds. The FT is described as:

$$F(\nu) = \int_{-\infty}^{\infty} f(t) \exp(i2\pi\nu t) dt \quad (3.14)$$

The classical FT is called the Discrete Fourier Transform (DFT), and can be applied to a function with a finite duration. The first method used for the detection of periodic signals in this thesis was the calculation of the Lomb Scargle (LS) Periodogram (Lomb, 1976; Scargle, 1982), a technique which is effective for unevenly spaced data. The ‘periodogram’ was coined by Arthur Schuster in 1898, and was described as the spectral density of a signal. The reader may find descriptions of the periodogram by Press et al. (1992). Specifically, the LS Periodogram utilizes the DFT, which provides power spectra that are analyzed for significant peaks. Importantly, in the context of quasi-periodic time series, FTs have extremely important properties, one of which is that the FT of a sine wave is a delta function in the frequency domain.

The LS periodogram is essentially a modification of the classical periodogram. However, it over comes some of the inherent difficulties with unevenly spaced data and thus provides greater statistical stability. For example, it evaluates the statistical significance of a spectral feature where periodicity may, or may not, be present, e.g. pseudo-periodic behavior due to trends in the noise, where any significant sigma value can be computed by the algorithm. This assessment is very important for such finite datasets, since other features such as spectral leakage, or aliasing, may also be present. We show examples of these effects in Figure 3.6. Although the LS periodogram gives a significant power solution for a

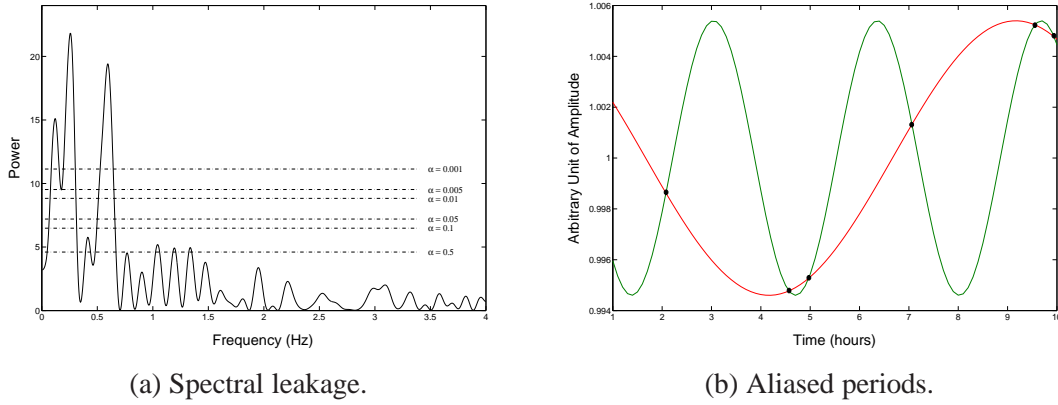


Figure 3.6: (a) We highlight powers of adjacent frequencies, f (e.g. $f \sim$ between 1 - 1.5 Hz) which present themselves as a result of spectral leakage. However, the LS periodogram evaluates the significance of these peaks, where we compute 0.6 - 4σ significance, marked by the horizontal dashed-dotted lines. (b) These data points sample the red sine wave well, but not the green. This undersampled period will therefore be present in the periodogram analysis.

periodic signal, the power in the periodogram can present itself not only at one frequency, but also at adjacent frequencies due to spectral leakage (Figure 3.6a). This can occur at nearby, or distant, frequencies, and is caused by different frequency components being spread in to other DFT bins. This occurs when a window function is applied to the time function, where the window function has a finite duration and therefore frequencies can ‘leak’ in to adjacent bins. Aliasing, or alias periods, arise as a result of sampling whereby periods are undersampled and therefore appear as other periods (Figure 3.6b). Thus, the more data points these analyses use (where e.g. the signal contains a periodic function), the periodogram will yield frequency estimations with much higher significance. Let us now consider the Lomb Scargle periodogram.

In the case of an arbitrary (unevenly) sampled dataset, the LS periodogram is calculated by the following (where the power spectrum P , is a function of angular frequency ω):

$$P(\omega) = \frac{1}{2\sigma_{var}^2} \frac{[\sum_i (h_i - \bar{h}) \cdot \cos \cdot \omega(t_i - \tau)]^2}{\sum_i \cos^2 \cdot \omega(t_i - \tau)} + \frac{[\sum_i (h_i - \bar{h}) \cdot \sin \cdot \omega(t_i - \tau)]^2}{\sum_i \sin^2 \cdot \omega(t_i - \tau)} \quad (3.15)$$

where $\omega = 2\pi f > 0$, $\tau = \tan(2 \cdot \omega \cdot t) = (\sum_i \sin \cdot 2 \cdot \omega t_i / \sum_i \cos \cdot 2 \cdot \omega t_i)$, each consecutive data point is h_i , the mean of the data is \bar{h} and the variance is σ_{var}^2 . The purpose of the Lomb Scargle periodogram is to identify a given signal, despite the presence of noise. In order to do this, the periodogram assigns weighting to the data based on the

individual data points, rather than a per time interval basis. However most importantly, it tests the null hypothesis which is the assumption that the data is described by normally distributed noise. Under this hypothesis, the probability that a measurement at a given peak frequency, ω , with a power of $Z(\omega) > 0$, is $P(> Z) = e^{-Z}$. Therefore, using Figure 3.6a as a reference, in the case of n independent frequencies, the probability that none of these values of f give larger values than Z , is:

$$(1 - e^{-Z})^n \quad (3.16)$$

which was computed by the Lomb-Scargle periodogram routines. The user inputs any number of significance values (Z), and the algorithm also calculates an estimate of the number of independent frequencies (n). There are many ways to calculate n - for example Horne & Baliunas (1986) calculate the number of independent frequencies by applying fitting techniques to empirically generated values of n as a function of N_0 , the number of data points, and found the following formula: $n = -6.362 + 1.193 \cdot N_0 + 0.00098 \cdot N_0^2$. The LS routine that we employ here calculates n as follows: $n = 2 \cdot a/b$, where a is $(0.5 \times \text{the over sampling parameter} \times \text{the input parameters defined as the highest frequency examined divided by the Nyquist frequency} \times \text{the length of the series})$, and b is the oversampling parameter. In this way, the *statistical significance* of all presented peaks in $P(\omega)$ of Equation 3.15 is:

$$P(> Z) = 1 - (1 - e^{-Z})^n \quad (3.17)$$

as shown in Figure 3.6a by the dashed horizontal lines, where we stipulate 0.6 - 4σ significance computations (labeled as $\alpha = 0.5 - 0.001$, where α corresponds to the FAP calculated here as a percentage outside the symmetric interval, $[-\alpha\sigma, \alpha\sigma]$). These σ values can be changed as the user desires in the Lomb Scargle periodogram routines - which were acquired from the Matlab File Exchange²¹ (Press et al., 1992, via Brett Shoelson who coded the routine).

In this work, we selected a range of peaks corresponding to possible periodic solutions (of significance $>5\sigma$) as provided by the techniques above for each target. Let us arbitrarily consider lightcurve 1 and lightcurve 2, where lightcurve 1 was obtained one night previous to lightcurve 2: we shifted lightcurve 2 in time by: $\text{known period} \times \text{number of rotations}$ (corresponding to this period) between lightcurve 1 and 2. By inspecting the correlation of

²¹<http://www.mathworks.com/matlabcentral/fileexchange/>.

the lightcurve peaks, we could further assess which periodic solutions were valid. Finally, we compare the LS power solution for each separate epoch to investigate which powers were in greatest agreement. Despite the effectiveness of the Fourier-based LS method, a number of periodic solutions were identified as strong candidates for each target - due to the various reasons outlined above. Consequently we sought additional techniques to identify which of these solutions were statistically most likely, and a means of assessing the error in this calculation. Finally, we also point out that during this work, we observed a number of mid M dwarf flare stars, where large transient events in the form of stellar flaring were detected in all cases. Periodogram analysis was especially useful during this work. We elaborate further on these events in Chapter 7.

3.2.2 Phase Dispersion Minimization

We employed a PDM technique (Stellingwerf, 1978), in addition to the LS periodogram analysis, as a second statistical tool. Stellingwerf (1978) describes the PDM method as a LSF approach where a fit is calculated by using the mean curve of the data, controlled by the mean of each bin (which can be specified in the algorithm), and the period that produces the least datapoint scatter, or ‘PDM theta statistic’ (Θ), about this computed mean, is the most likely solution.

The characteristics of the PDM approach are defined as follows. Let us consider a discrete observational time series, represented via columns of flux, F and time, t . These data can be phase folded, where the phase, ϕ , is taken as a fraction of a period, P , at a given time. Thus, ϕ can be calculated with respect to an arbitrary reference epoch, t_0 , as follows:

$$\phi = \frac{t - t_0}{P} \quad (3.18)$$

As data is phase folded closer to the correct period solution, the mean scatter about the lightcurve data points will minimize. It is in this way, that the PDM technique indicates the most likely periodic solutions. The n^{th} observation is (F_n, t_n) , where M data points follow $n = 1 \dots M$. Stellingwerf (1978) defines σ^2 as the variance of the individual flux values F , where the mean \bar{F} , is calculated as the $\sum F_n/M$. So:

$$\sigma^2 = \frac{\sum (F_n - \bar{F})^2}{(M - 1)} \quad (3.19)$$

At this point the observation sample variance $v^2 = \sigma^2$; however, we must consider

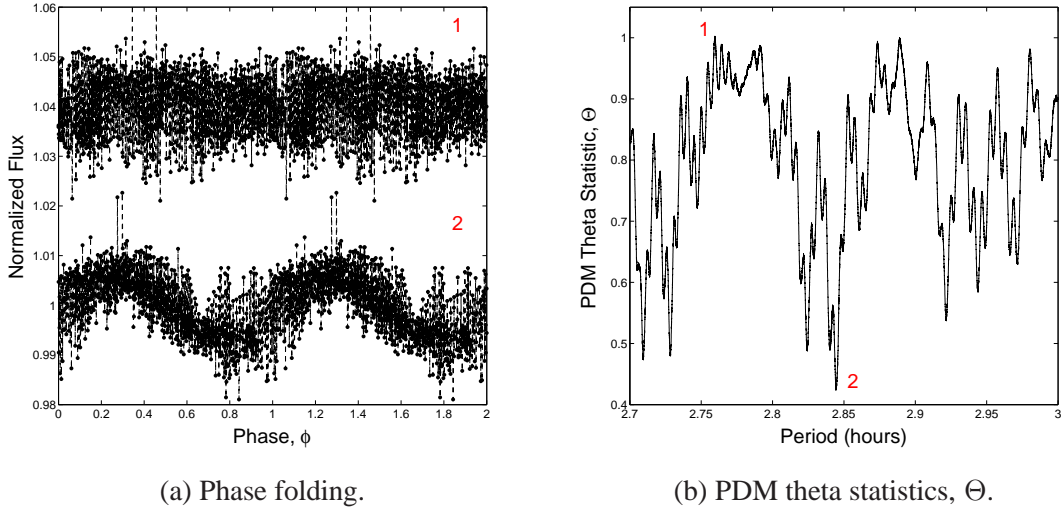


Figure 3.7: (a) Phase folded lightcurves of the M8.5 dwarf LSR J1835+3259, a newly discovered period reported in this work. Lightcurve 1 has been folded to an incorrect period of 2.760 hours that exhibits a large PDM theta statistic, marked with a corresponding ‘1’ in Figure 3.7b, whereas lightcurve 2 has been folded to the correct period of 2.845 hours, marked with a ‘2’ in Figure 3.7b. The scatter in each phase interval/bin in lightcurve 1 is clearly larger than of lightcurve 2. (b) A plot of the output from the PDM routines, highlighting the correct period of 2.845 hours and the corresponding *minimum* theta statistic assessment.

subsets of this discrete series in order to effectively calculate the variance for all samples, where v_i^2 is the variance of each sample within this series. Thus, once again taking M data points for $i = 1 \dots M$, the overall variance, $\sigma_{overall}^2$ for n_i data points is:

$$\sigma_{overall}^2 = \frac{\sum (n_i - 1) \cdot v_i^2}{\sum n_i - M} \quad (3.20)$$

Therefore, the PDM routines seek to minimize the variance in a lightcurve by iterating through different periods. The variance defines the mean scatter of F_n as a function of ϕ (as shown in Figure 3.7). The minimum theta statistics, Θ , is calculated by using Equations 3.19 and 3.20, as follows:

$$\Theta = \frac{\sigma_{overall}^2}{\sigma^2} \quad (3.21)$$

For incorrect periods in the sample, $\sigma_{overall}^2 \approx \sigma^2$, so $\Theta \approx 1$, and for periods ap-

proaching the true value, Θ will approach zero - marked with a '2' in Figure 3.7 for the correct period in the example. In this work, we take the minimum Θ from the PDM analysis, and compare it to the highest peak in the power spectra of the LS. The PDM routine also provides the amplitude of a signal. The period solutions that we found to be in best agreement were then used to set a range of parameters for the χ^2 test, as another statistical confirmation of lightcurve properties, but more specifically, an assessment of the amplitude variability of a target lightcurve.

PDM differs from the DFT approach, whereby the selected lightcurves are phase folded to a given period as defined by the user; the routine can iterate through many different periodic values and independently assess their significance, thus we use a PDM period range obtained from Fourier analysis via the LS power spectra (where peaks have a 5σ significance). The PDM approach is useful for data sets with large gaps and also for time series with a substantial amount of data points. Furthermore, it is insensitive to the lightcurve's shape and therefore makes no assumptions with regard to the morphology. The routine also includes a Monte-Carlo test, used for assessing the statistical significance of the detected Θ minima. Essentially, this test evaluates whether the result at any given Θ level could be a result of noise. It computes this by randomizing the data point order, which removes the signal component. We repeated this for 10^4 trials in order to cover a significant distribution of Θ values due to noise. This distribution of values is then output as Monte-Carlo significance values, which correspond to the best estimate of a given periodic candidate. Similar to the LS technique above, it is possible for many periodic solutions to present themselves due to aliasing - a consequence of gaps in the data. Therefore the Θ statistic can minimize at many different period solutions. For example, Figure 3.7b clearly identifies other Θ minima at ~ 2.72 hours, ~ 2.83 hours and again at ~ 2.92 hours. Therefore strong considerations must be given between the correlation of the LS periodogram solutions and the PDM solutions, in addition to a rigorous visual inspection of raw lightcurve peak correlations throughout the baseline for given period values. For a more indepth discussion of significance treatments, we refer the reader to descriptions by Stellingwerf[†].

3.2.3 The χ^2 Test, the LSF and Sinusoid Fitting

Once the statistical techniques outlined in the previous sections identified a period solution for each target with the greatest statistical significance, we moved to characterize the mean

[†]<http://www.stellingwerf.com/rfs-bin/index.cgi>.

amplitude variability of a given lightcurve. Sinusoid fitting is a very simple approach and proved to be effective for this estimation. It does however, make the assumption that the lightcurve varies in a sinusoidal manner - but this is to be expected in many scenario's of rotational modulation. Furthermore, the confirmed periodic solutions can also be further assessed based on the correlation of a model sinusoidal fit with the real data. The mean amplitude variability (σ_{tar}) of the target lightcurves was found by varying the amplitude, period and phase of a model sinusoidal signal, and then Chi squared (χ^2) and least squares fit (LSF) calculations was performed. We used both techniques since the χ^2 method does not treat each data point equally as does the standard LSF used here, where the error in each data point is also included in the calculation. Although the final result from each technique was very similar, based on the errors included in the χ^2 test, as well as the model fits, it can also provide a good estimation of the error of each varied parameter. At this point, the corresponding reference stars' variability was also found by this means, in order to ensure that the transient signals were intrinsic to the target star (in addition to this, post-photometry analysis of each reference star was carried out, as outlined in § 3.1.6). The model sinusoidal wave, x , was generated simply as follows: $x = a \cdot \sin((2 \cdot \pi \cdot f \cdot t) + \phi)$, where a is the amplitude of the wave, f is the period⁻¹, t is the time and ϕ is the phase offset. We then fit this model to real data, and iterated through a range of amplitudes, periods and phases. We implemented this method by writing a simple Python script, described here:

1. Open the file and read columns of flux, F , and time, t , in to a list file.
2. Create two NumPy²² arrays and populate the arrays with F and t .
3. Fit the input, ready for χ^2 or LSF assessment. Also, provide an initial guess of amplitude, and phase. The period can also be varied and assessed if necessary.
4. Carry out the χ^2 /LSF, where the parameters of the model fit in # 3 above are adjusted to best fit the real data. For the data set containing F and t , where t is an independent variable and F is the dependent variable, for $i = 1 \dots N$, the generated model has the form $z(t, \alpha)$, where α is varied. The LSF, S , identifies the best fit when S is at a minimum:

²²Extension to Python which supports multi-dimensional arrays and matrices. A large volume of high-level mathematical functions are also provided, thus allowing for more efficient computation times.

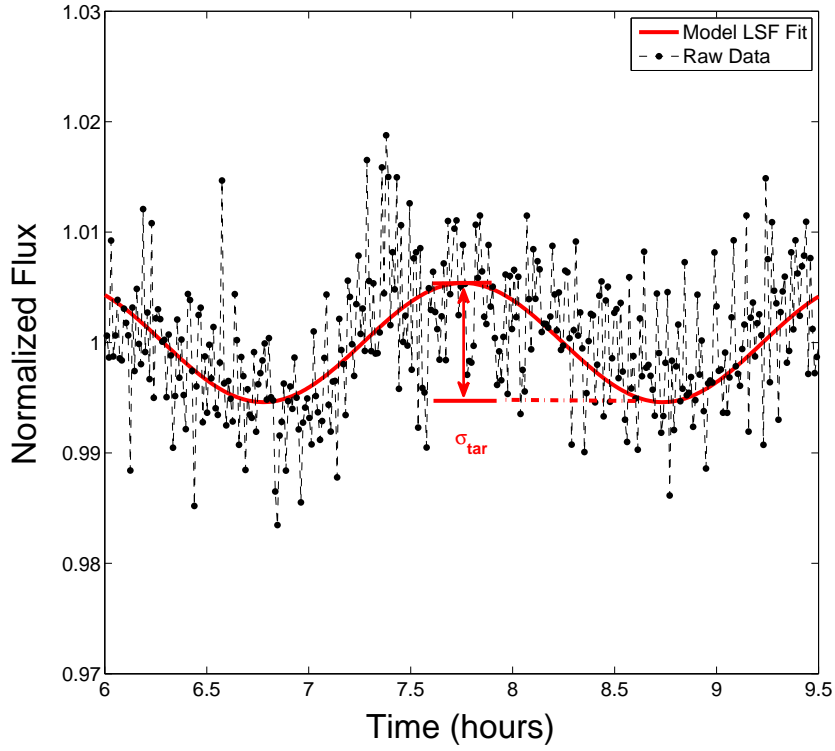


Figure 3.8: Least Squares Fit to a raw lightcurve from the M9 dwarf TVLM 513-46546. The LSF algorithm revealed a σ_{tar} of $\sim 0.54\%$ variability, with a corresponding detected (LS, PDM) period of 1.95958 hours - also identified by the LSF routine as the best fit period solution.

$$S = \sum_{i=1}^N (F_i - z(t_i, \alpha))^2 \quad (3.22)$$

However, as outlined above, the LSF treats all data points with equal weighting, therefore we also carried out a χ^2 minimization, that provided error values for the amplitude variability, period and phase of a given lightcurve. This was calculated as follows:

$$\chi^2 = \sum_{i=1}^N \left(\frac{F_i - z(t_i, \alpha)}{E_i} \right)^2 \quad (3.23)$$

where E_i is the error or standard deviation (calculated by the methods in § 3.1.7) of the i^{th} data element.

5. The results are plotted, where the real data has the best fit model over-plotted. The results are written to an output file and the best fit amplitude and phase are output to the screen.

As a final check of our identified period, we also varied the period of the model wave. In all cases, the best fit period matched those from the LS and PDM analyses described in § 3.2.1 and 3.2.2. In the context of the data in our work that contains some noise component, the mean amplitude variability was therefore not a measure of the peak to peak amplitude of the wave (i.e. from the highest to lowest data points per given rotation), but rather measured from the central points inside the scatter, as shown in Figure 3.8. This amplitude variability assessment was carried out for individual nights of each epoch, of each target. It was important to identify any change in amplitude over the course of our campaign, since the sample of late-M to mid to early-L dwarfs are by nature, very active sources. Thus, these dynamic stellar environments could rapidly evolve causing a change in σ_{tar} over any given timescale. Furthermore, different wavebands such as the Johnson R-band or I-band, were shown to exhibit large differences in amplitude variability. Our method of sinusoid fitting via the χ^2 and LSF minimization techniques were effective in assessing these differences. We discuss this further in the relevant results chapters.

3.2.4 Binary Lightcurve Modelling

The sample of radio detected ultracool dwarfs in this thesis contains two very low mass binaries - the M dwarf tight binary LP 349-25AB, and the L dwarf tight binary 2MASS J0746+2000AB. In each case, the photometry carried out measured the combined flux from both binary members. In a following chapter, we present the photometric results from this campaign. Here we briefly describe the binary lightcurve modeling that was carried out, and why.

The photometric behavior of 2MASS J0746+2000AB was similar to other single targets, where, in addition to a primary periodic signal, some aperiodic variations were also present in epoch lightcurves. However, for LP 349-25AB, the lightcurves exhibited changes in phase and quite significant changes in amplitude over the course of the observation epochs. Amongst other possibilities that we discuss in Chapter 4, we interpreted such characteristics as the possible superposition of two variable sources - i.e. the presence of *both* binary members, varying in phase and amplitude, with different periods (or perhaps a detected period from one and aperiodic variations from the other), over our observation timescales. Thus, similar to § 3.2.3, we developed a Matlab-based script that modeled the

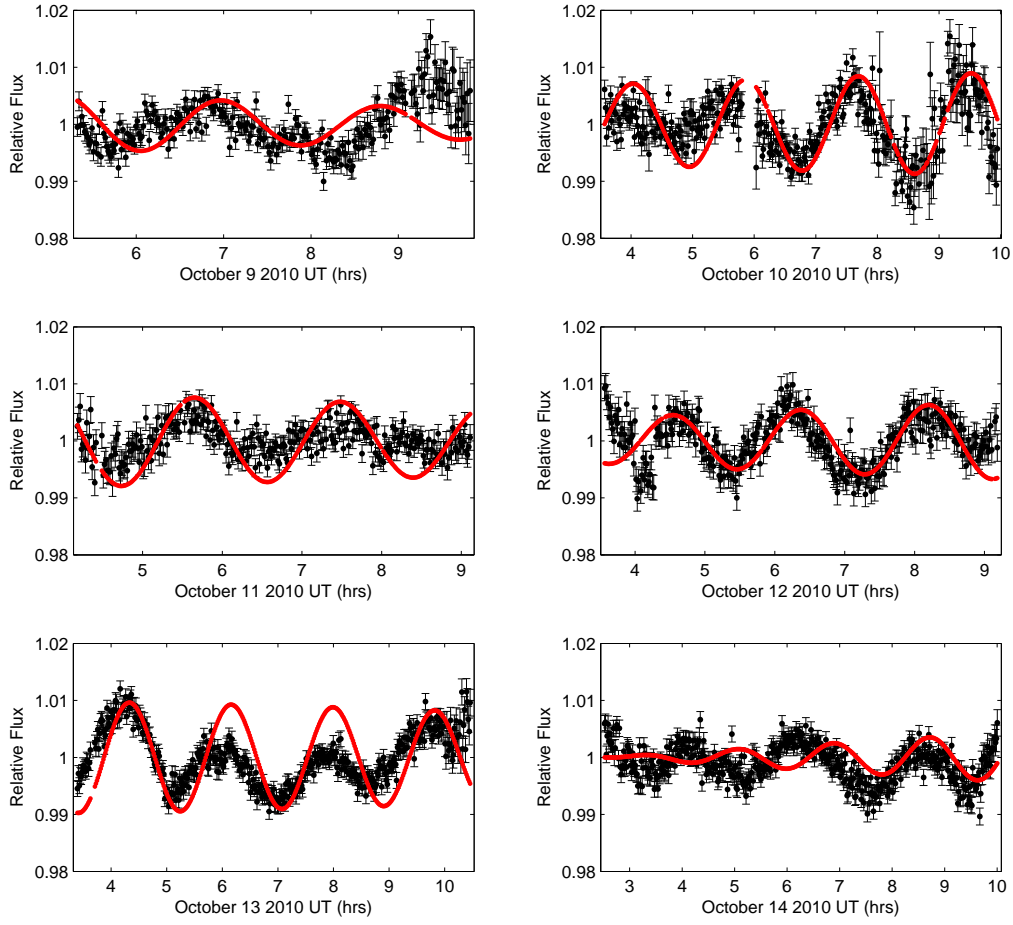


Figure 3.9: Here we show the October 2010 epoch from one of the very low mass binaries in our sample - LP 349-25AB. The red model sinusoid over-plotted is the best fit single sinusoid from our Matlab routines.

superposition of two sinusoidal waves. The function $M(i)$:

$$M(i) = \left[\sin(x(i) + \phi_1) * \left(\frac{2}{P_1} \cdot \pi \right) \cdot a_1 \right] + \left[\sin(x(i) + \phi_2) * \left(\frac{2}{P_2} \cdot \pi \right) \cdot a_2 \right] \quad (3.24)$$

produced a model fit, where for a data set of length $i = 1 \dots N$, the dependent (changing) variables above are the flux values, x , the phase of the first wave, ϕ_1 , the amplitude of the first wave, a_1 , the phase of the second wave, ϕ_2 , and period of the second wave,

P_2 , and the amplitude of the second wave, a_2 . The only independent variable in the above calculation was the period detected in our work, P_1 . We varied the amplitudes, a_1 and a_2 , from 0 - 3% in steps of 0.01%; the period P_2 from 1 - 4 hours in steps of 0.01 hours; and the phases, ϕ_1 and ϕ_2 , from 1 - 360° in steps of 1°. A χ^2 /LSF produced the best fit, which we ran on each epoch dataset independently. We could not run this on the full 2 year baseline, because we did not have an accurate enough period for P_1 to do so. In Chapter 4, we outline the results of this modeling in more detail. Here we show some raw lightcurves from LP 349-25AB and the resulting red model sinusoidal signal overplotted in Figure 3.9.

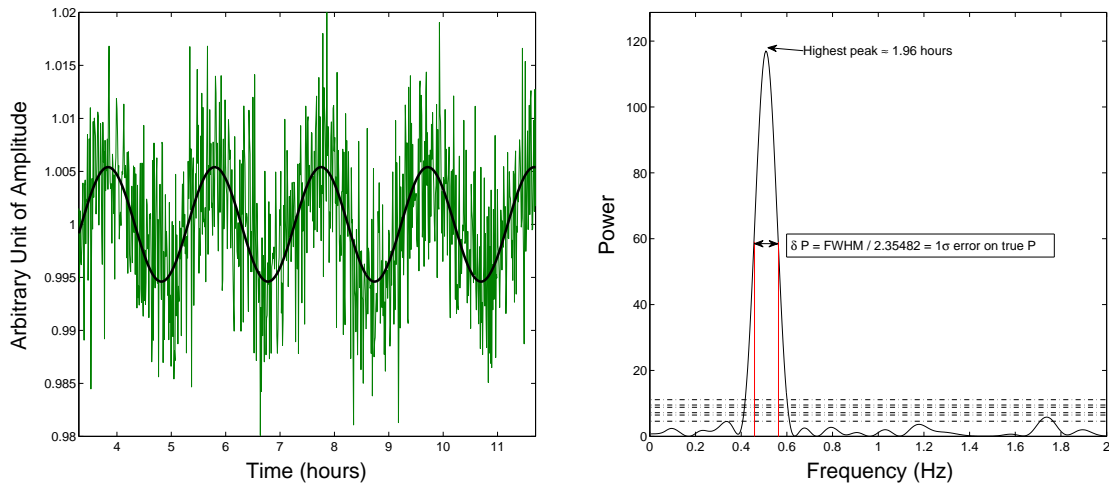
3.2.5 Period Uncertainty Estimation

The periods reported in this work were identified via the methods outlined in the previous sections. We also needed a means of assessing the error on these detections. We assessed the error for two different categories in this work: 1) those targets that could be phase connected, or 2) those that did not have enough periodic accuracy to be phase connected. The potential periods from e.g. the LS periodogram, or PDM routines, were used to investigate which of these solutions allowed us to phase together lightcurves within/between individual epochs. Standard phase connection techniques were employed via Equation 3.18. This allowed us to combine data from two different epochs, if the period from a single epoch could be calculated with sufficient accuracy, such that the rotational phase of the second epoch was unambiguous - in this work we define this threshold to be $\delta\phi < 0.25$. This method can then be continued throughout the entire observation baseline, since each iteration should give a more constrained period solution for epochs that lie n rotations apart, but only if there is one possible solution per given epoch's rotational phase. The initial period accuracy in the first epoch was established via the methods outlined in S 3.2.1 and S 3.2.2.

For targets where phase connection was not possible (or only possible for some of a target's baseline if the period accuracy achieved did not allow for phase connection to other epochs), we overplotted the LS power spectrum period range with a Gaussian profile, and calculated the FWHM. Thus, the width of the FWHM as determined by the Gaussian profile, contained a range of possible period solutions, to some statistical significance. In this way, we estimate 1σ errors on the period uncertainty (δP) for these targets. Since the $FWHM = 2\sqrt{2\ln 2} \sigma = 2.35482\sigma$, δP is therefore defined as:

$$\delta P = \frac{FWHM}{2.35482} \quad (3.25)$$

We find that the uncertainty range calculated for each target for the best-fit period of



(a) Sinusoid model with random noise added.

(b) LS analysis with δP fit assessment.

Figure 3.10: (a) Here we show a model sinusoidal signal (black) with a period of 1.95 hours. Overplotted in green, is the same signal with a random noise component added. (b) We ran a LS periodogram on the green data in (a), and found that the peak of the power spectrum indicated a period of 1.96 hours. By calculating our $\delta P = FWHM / 2.35482$ based on this profile, we find a period and error of 1.96 ± 0.2 hours - a conservative estimate of the error, which brackets the true period by a wide margin.

rotation, allowed other possible solutions within this range to be phased together within epochs. This technique was an effective estimation of δP , since the calculation was based on the same LS power spectrum that was used for period assessment. These estimates are considered upper limits. We show an example of this application in Figure 3.10. On the left in Figure 3.10a, we first plot a model sinusoidal signal with a period of 1.95 hours - shown in black. We then added a random noise component to this signal, which we overplot in green. On the right, we show in Figure 3.10a the LS periodogram analysis, where the highest peak in the spectrum is ~ 1.96 hours. By adopting our method above, and establishing the FWHM of the highest peak, we identify a period and an associated error of 1.96 ± 0.2 hours. This is a conservative error estimate where the true period clearly lies inside the allowed range.

We also used sinusoidal fitting techniques and assessed the error in the best fit period via the χ^2 test, as outlined in a previous section, S 3.2.3. Other authors have established various means of assessing the error in the frequency of a signal, e.g. Schwarzenberg-Czerny (1991) or Akerlof et al. (1994). These techniques utilize parameters such as time span of observations, amplitude of the signal, number of data points, the error in the data

points, and so on. In estimating the error in a given frequency however, these techniques can largely rely on data where the epochs are uniformly sampled in time. Thus, similar to Equation 3.25, they were effective in calculating an error for a single epoch, but not for an unevenly spaced lengthy baseline. Finally, we note that the behavior of the photometric signatures from the very low mass binaries in the sample were somewhat less stable than those of the single targets. Therefore, error estimation by these means proved to be more challenging. We will see this in Chapter 4.

3.3 Summary

In this chapter, we have outlined the various data calibration and reduction techniques that were implemented in this thesis. We have also discussed the time-resolved optical differential photometry, as well as the aperture photometry techniques and photometric error estimation used to produce time series data. In order to carry this out, we used and modified the data reduction and analysis pipeline (Sheehan, 2008). This pipeline provided strong data management functionality, which was essential when dealing with extremely large data sets from the Andor camera systems. Data reduction and data analysis are included in the routines, which utilize IRAF tasks via a Python-based PyRAF environment. We also outlined the various routines that were created during this work, such as de-fringing routines to account for the effects of OH spectral emission at NIR wavebands, post-photometry scripts that were written to assess reference star behavior throughout a given observation, and scripts that were implemented to counter various guiding/tracking errors present during epochs, such as circular rotation errors.

Once data had been calibrated and reduced to produce a time series, we used a variety of signal analysis techniques to assess the periodic variability, or aperiodic variability, as well as other lightcurve properties such as the mean amplitude variability, of our campaign sources. In order to do this, we used the Lomb Scargle periodogram, Phase Dispersion Minimization routines, sinusoid fitting, lightcurve modeling and finally, period uncertainty estimation. Each confirmed period had multiple epochs of observations, where the periodic variability was categorically present in the data - as established by the techniques in this chapter. These statistic tests were useful for other targets in this work, such as mid M dwarf flare stars, where a large amount of data has been acquired to further investigate M dwarf stellar flaring events at high cadence, at photometric wavelengths. These tools provided the means of assessing the variable nature of these objects.

“We will never know how to study by any means the chemical composition (of stars), or their mineralogical composition.”

Auguste Comte (1835)

“Either we are alone in the universe, or we are not. Either thought is frightening.”

Author C. Clarke

4

Periodic Optical Variability in Radio Detected Ultracool Dwarfs

4.1 Introduction

Previous studies of ultracool dwarfs have yielded the detection of periodic bursts of radio emission from four of these objects (Hallinan et al., 2007, 2008; Berger et al., 2009). The extraordinary characteristics of this radio emission, specifically the presence of 100% circularly polarized periodic pulses, have led to these substellar objects being dubbed ‘ultracool dwarf pulsars’. Remarkably, two of these pulsing dwarfs have also been detected as periodically varying optical sources - both in broadband optical photometry (Lane et al., 2007), and one in the $H\alpha$ (Berger et al., 2008a), where in all cases, the detected periods match the radio pulses.

As discussed in Chapter 1, optical periodic and aperiodic variability has largely been associated with the presence of atmospheric dust, and/or the expected presence of magnetic spots on the stellar photosphere. Since all of our targets have been detected as transient radio sources, magnetic activity is clearly present and active, and thus could play an important role in the characteristics of the optically variable nature of such stars. It has been well established that magnetic spots can exist on timescales of many years (Schwabe (1845) observed for 17 years and discovered the ~ 11 year solar cycle). However, we cannot discount the effect of dust in these regions, especially since dwarf photospheres become increasingly cool and neutral after the M/L transition (~ 2000 K). If such clouds of dust could be maintained over comparable timescales, they could also be responsible for the

previously observed optical variability. We note however, that we have not established that stability on timescales of *years* is required for the optical variability discussed here. In this thesis, we present an exciting alternative to the above that may be present during the many epochs of observations and perhaps over baselines of years, that associates particle acceleration in the dwarf's magnetospheric regions with the presence of the same high-strength magnetic fields that are responsible for the pulsed radio emission. By establishing a causal connection to the optical and radio emissions, we have found that the optical variability may be caused by processes very similar to those responsible for aurorae at the magnetic poles of the planets in our solar system, but much more powerful (Hallinan et al., 2012). We present the optical photometric component of this study in this work (Harding et al., 2012a).

In this chapter, we present final results from a lengthy campaign that was undertaken to investigate the ubiquity of optical periodic variability for known radio detected ultracool dwarfs - this work was carried out solely by the author. As outlined in Chapter 2, we constructed and commissioned the GUFi photometer on the 1.83 m VATT telescope, that was built specifically for detecting optical signatures from these stars. Throughout the campaign, we also used the VATT 4K CCD Imager on VATT, as well as the new2k and Tek2k detectors, on the 1.0 m, and 1.55 m telescopes at the USNO, respectively. Data was also obtained using the GUFi mk.I system from the 1.52 m telescope at the Loiano Observatory in Bologna, Italy. These data may provide an insight into the cause of this optical emission and its possible connection to the radio processes. Furthermore, we can assess whether optical periodic signals are present in only some of, or all of, the radio pulsing dwarfs, or perhaps are also observed for the quiescent radio dwarfs in the sample. We present results of periodic variability, from multiple epoch observations for five ultracool dwarfs: the M tight binary dwarf LP 349-25 and L tight binary dwarf 2MASSW J0746425+200032, as well as the M8.5 dwarf LSR J1835+3259, the M9 dwarf TVLM 513-46546, and the L3.5 dwarf 2MASS J00361617+1821104. Each confirmed period has multiple epochs where the periodic variability is categorically present in the data. We have also observed the M9.5 dwarf BRI 0021-0214 and detected variability. There is some evidence of periodicity in this data, and we will discuss this further in this chapter.

The chapter is structured as follows: the next sections, § 4.2 and § 4.3, discuss the stellar properties of each target in order of ascending spectral type, and further outline details of the respective observation campaigns. § 4.4 discusses the optical observations. § 4.5 - 4.5.2 presents the photometric results of optical periodic and aperiodic variability for each source. Finally, § 4.6 discusses the proposed source of the periodicity. The campaign

Parameter	LP 349-25AB	2M J0746AB	LSR J1835	TVLM 513	BRI 0021	2M J0036
SpT	M8+M9	L0+L1.5	M8.5	M9	M9.5	L3.5
Dis (pc)	13.10 ± 0.28	12.20 ± 0.05	~ 0.6	~ 10.5	~ 11.5	~ 8.8
M_I	12.40	15.03	12.90	15.10	15.02	16.05
$\log(L_{bol}/L_{\odot})$	-3.19(A) -3.34(B)	-3.64(A) -3.77(B)	-3.51	-3.65	-3.40	-3.98
$v \sin i$ (km s $^{-1}$)	55 ± 2 (A) 83 ± 3 (B)	19 ± 2 (A) 33 ± 2 (B)	50 ± 5	~ 60	~ 34	~ 37
Lithium?	No	No	?	No	No	No
Est. Mass (M_{\odot})	0.121^{\dagger} ± 0.009	0.151^{\dagger} ± 0.003	$<0.083?$	>0.06	<0.06	$0.06 - 0.074$
Ref.	1-3	2, 4-6	7-9	10-13	11,14-17	4, 5, 18-20
Radio Ref.	21	22	23	24	24	25

Table 4.1: Summary of Campaign Sample Properties.

References: (1) Gatewood & Coban (2009). (2) Konopacky et al. (2010, 2012). (3) Basri & Marcy (1995); Reiners & Basri (2009). (4) Dahn et al. (2002). (5) Vrba et al. (2004). (6) Bouy et al. (2004). (7) Reid et al. (2003). (8) Berger et al. (2008a). (9) Hallinan et al. (2008). (10) Tinney et al. (1993, 1995). (11) Leggett et al. (2001). (12) Basri (2001). (13) Reid et al. (2002). (14) Reid et al. (1999). (15) Mohanty & Basri (2003). (16) Reiners & Basri (2009). (17) Chabrier & Baraffe (2000). (18) Average of Jones et al. (2005) & Zapatero Osorio et al. (2006). (19) Reid et al. (2000). (20) Hallinan et al. (2008) based on work of Reid et al. (2000); Vrba et al. (2004). (21) Phan-Bao et al. (2007). (22) Antonova et al. (2008). (23) Berger (2006). (24) Berger (2002). (25) Berger et al. (2005). \dagger Total system mass.

targets are abbreviated as follows: 2MASSW J0746425+200032 (henceforth 2M J0746); LSR J1835+3259 (henceforth LSR J1835); TVLM 513-46546 (henceforth TVLM 513); BRI 0021-0214 (henceforth BRI 0021) and 2MASS J00361617+1821104 (henceforth 2M J0036). A summary of object properties is shown in Table 4.1 above.

4.2 Discussion of Binary Systems

We selected two very low mass binary stars at the M/L transition for our campaign - LP 349-25AB and 2M J0746AB. These objects were of particular interest, since they are the only binary dwarfs reported thus far to exhibit radio emission in the very low mass binary regime (Phan-Bao et al., 2007; Osten et al., 2009; Antonova et al., 2008; Berger et al., 2009), defined to be $M_{TOT} \leq 0.185 M_{\odot}$ (Close et al., 2003). Furthermore, both objects

were subject to high-precision dynamical mass measurements which were followed up by laser guide star (LGS) adaptive optics (AO) spectroscopy (LP 349-25: Dupuy et al. (2010); Konopacky et al. (2010, 2012), 2M J0746: Konopacky et al. (2010)). These latest $v \sin i$ data are unique, since each *resolved* component of the binary systems provided a measured rotational velocity for each star, and they are consequently the first resolved AO measurements of this kind (Konopacky et al., 2012). Indeed, both LP 349-25AB and 2M J0746AB were cited as the two binaries with the largest differences in component $v \sin i$ in this study. These latest results therefore make the search for periods all the more pertinent. Based on these dynamical mass and rotational velocity measurements, an accurate period of rotation for the system provides the means of assessing the system's orbital and rotational parameters, where the rotational axis of each component with respect to the other and the orbital axis of the system may be further constrained. Moreover, a range of radii can also be estimated. Our method for applying such constraints is explained in Chapter 6.

4.2.1 LP 349-25AB

LP 349-25 is a tight binary that is located at a distance of 13.10 ± 0.28 pc (Gatewood & Coban, 2009). Forveille et al. (2005) reported evidence of the system's binarity via AO observations, where these observations also yielded a separation estimate of 0.125 ± 0.01 arcseconds. The system has an inferred total mass of $0.121 \pm 0.009 M_{\odot}$ and an orbital period of 7.31 ± 0.37 years (Konopacky et al., 2010). Evolutionary models estimate the binary's age to be 140 ± 30 Myr (Dupuy et al., 2010), which infers it should have an abundance of lithium. However, Reiners & Basri (2009) detect no lithium in the binary dwarf's atmosphere, which suggests that the age derived from modeling is perhaps an underestimate of the system's true age. Moreover, based on the color information obtained (companion star in the IR: $M_{K'}=10.46$ and $\Delta m_{K'}=0.26 \pm 0.05$), the spectral type combination of the system is most likely M7.5V+M8.5V or M8V+M9V.

LP 349-25 was reported as the most radio luminous ultracool dwarf yet detected (Phan-Bao et al., 2007); however no radio pulsing similar to other objects such as TVLM 513, 2M J0746 or 2M J0036 (Hallinan et al., 2007, 2008; Berger et al., 2009) was found during the observation. They argued that either gyrosynchrotron or electron cyclotron maser emission could be the mechanism responsible.

Osten et al. (2009) performed multi-frequency follow-up observations to characterize the physical nature of the observed radio emission and to use these properties as a tool for

comparison with other radio detected ultracool dwarfs. They detected broadband, stable radio emission in two additional epochs of observations, found on timescales of 10 s - 10.7 hours, as well as on timescales of 0.6 - 1.6 years. However, they found that the system did not show evidence of large-scale variability as was seen in other studies of radio detected ultracool dwarfs such as those of Hallinan et al. (2006) and Berger et al. (2009), where periodic bursts were observed for example. Due to the lack of variability and the flat spectral index, they argue in favor of incoherent gyrosynchrotron emission. Similarly, more recent radio observations of the system by McLean et al. (2012) also detected the binary at 8.46 GHz, where no radio pulsing was observed.

Konopacky et al. (2012) measured the rotational velocities of individual components of very low mass binaries, including LP 349-25, via NIR AO spectroscopy. Interestingly, they show a $v \sin i$ of $55 \pm 2 \text{ km s}^{-1}$ and $83 \pm 3 \text{ km s}^{-1}$ for LP 349-25A and LP 349-25B, respectively. Under the assumption of a rotational axis which is orthogonal to the orbital plane, the inferred equatorial velocities are $\sim 62 \text{ km s}^{-1}$ and $\sim 95 \text{ km s}^{-1}$, respectively. This would make LP 349-25B the fastest rotating very low mass object ever discovered. There are some discrepancies in the literature with regard to LP 349-25 component radii estimates. Indeed, these estimates have strong implications for the maximum period that can be inferred for each system. We consider this later in Chapter 6.

Thus far, no optical variability has been detected for LP 349-25. We therefore chose to monitor the binary dwarf to investigate the presence of optical variability. We used the VATT I-band and R-band broadband filters for observations with GUF1 mk.II over the course of three separate epochs, for a total of ~ 64 hours, spanning ~ 1.2 years.

4.2.2 2MASS J0746+2000AB

2M J0746 is an L dwarf binary (L0+L1.5) with a separation of $\sim 2.7 \text{ AU}$ (Reid et al., 2001) that is located at a distance of $12.20 \pm 0.05 \text{ pc}$ (Dahn et al., 2002). Based on the measurements of Vrba et al. (2004), it has an effective temperature of between 1900 - 2225 K and an inferred bolometric magnitude of $\log L_{\text{bol}}/L_{\odot} \approx -3.64$. Bouy et al. (2004) initially obtained dynamical mass measurements of the system, estimating the total system mass to be $0.146 \pm_{0.006}^{0.016} M_{\odot}$, which classified the primary star to be low mass but the secondary to be a brown dwarf (individual mass estimates on a model based age estimate, which was found using the DUSTY models by comparing isochrones with luminosity-age, color/magnitude-age, effective temperature-age, and the absence of lithium vs. age). However, Gizis & Reid (2006) argue that the secondary component may not be a brown

dwarf and may in fact be at, or above the sub-stellar limit, thereby classing it as a low mass star. The latest total system mass measurement of the binary is $0.151 \pm 0.003 M_{\odot}$ (Konopacky et al., 2010).

Berger (2006) observed the binary at 8.46 GHz and detected no radio emission above a 3σ limit of $\leq 48 \mu\text{Jy}$. However, the first detection of confirmed radio emission was reported by Antonova et al. (2008), where they detected radio emission at 4.9 GHz with an average flux level of $286 \pm 24 \mu\text{Jy}$ during a 2 hour observation. It was not determined which component of the system was the radio emitter due to the close separation of the stars. They also report the detection of a 100% circularly polarized burst which reached 2.3 mJy; this event followed a rise in quiescent activity to an average flux of $\sim 400 \mu\text{Jy}$, which took place ~ 40 minutes before the burst. They conclude that the burst most likely originated from a small region (\ll radius of the dwarf) of intense magnetic activity, and required coherent ECM emission. This would point toward a magnetic field strength of ~ 1.7 kG for 2M J0746 (based on the electron cyclotron frequency and the observed radio emission at 4.9 GHz) for one component of the system.

Following this observation, Berger et al. (2009) reported periodic radio emission at 4.86 GHz of 2.07 ± 0.002 hours, as well as quiescent radio emission at 8.46 GHz with an average flux of $154 \pm 14 \mu\text{Jy}$. Similar to the pulses found from TVLM 513, LSR J1835 and 2M J0036 (Hallinan et al., 2007, 2008), these 100% circularly polarized period radio bursts were stable, and were therefore attributed to stellar rotation. Based on the similarities of the emission properties in each case, Berger et al. (2009) outline that it is likely that a coherent emission mechanism is responsible for the radio emission. They infer a magnetic field strength of ~ 1.7 kG for the 4.86 GHz detected pulse - a strength consistent with that confirmed by Antonova et al. (2008). In addition to the quiescent and transient radio detections, they report sinusoidal periodic $H\alpha$ emission. The period is the same in the optical and radio, which is attributed to stellar rotation - and is assumed to be coming from the same component of the binary.

A number of rotational velocity studies of 2M J0746 have also been carried out in the past decade. The latest work is that of Konopacky et al. (2012) where they reported the first resolved $v \sin i$ measurements of the system. They measure a $v \sin i$ of $19 \pm 2 \text{ km s}^{-1}$, and $33 \pm 2 \text{ km s}^{-1}$, for 2M J0746A and 2M J0746B, respectively. The same assumptions as for LP 349-25 are adopted, where the member's rotational axes is assumed to be inclined with respect to each other, and with respect to the orbital plane (or at least one component),

To date, in terms of rotation period measurement in optical photometry, there have only been rough estimates where periods of 1.84 - 5.28 hours were inferred from $v \sin$

i and radius estimates (where ‘ v ’, ‘ i ’, ‘ R ’ and ‘ $v \sin i$ ’ were known in the following: $(2 \cdot \pi \cdot R/P) \cdot \sin i = v \sin i$, thus P could be estimated - e.g. Bailer-Jones (2004), as well as some photometric variability which was detected by Clarke et al. (2002b), showing weak evidence of periodicity of ≈ 3 hours.

We obtained multiple epoch I-band observations totaling ~ 62 hours, taken over four separate epochs, spanning ~ 2 years. These observations were taken with the VATT 4K system as well as the GUF1 mk.II photometer.

4.3 Discussion of Single Systems

4.3.1 LSR J1835+3259

The M8.5 dwarf LSR J1835 is located at a distance of ~ 6 pc (Reid et al., 2003) and is a rapid rotator with a $v \sin i$ of 50 ± 5 (Berger et al., 2008a). Reid et al. (2003) show a bolometric luminosity for LSR J1835 of $\log L_{bol}/L_{\odot} = -3.51$. Berger (2006) conducted a large radio survey of 90 dwarf stars and brown dwarfs (M5 - T8) and detected radio emission (0.525 ± 0.015 mJy) from LSR J1835 during a ~ 2 hour observation. The observed emission was assumed to be due to incoherent gyrosynchrotron emission based on the inferred brightness temperature and the physical properties implied in the paper for the source size and magnetic field strength. Berger calculates a field strength of < 30 G from the fraction of polarization ($f_c < 9\%$) and the observed fluxes at 8.5 GHz.

Hallinan et al. (2008) selected this source for observation based on the detection of radio emission discussed above by Berger (2006), because of its close proximity (~ 6 pc), and because of its similar spectral type (M8.5) to the previously detected pulsating dwarf TVLM 513 (M9) (Hallinan et al., 2006). They observed the dwarf for 11 hours at 8.44 GHz, and reported persistent 100% circularly polarized coherent pulses of radio emission with a period of 2.84 ± 0.01 hours, which they attributed to the dwarf’s rotation period. They argue in favor of ECM emission as the dominant source of the pulsed radio emission from LSR J1835. Therefore the detection of ECM emission would require magnetic fields of ~ 3 kG, since the electron cyclotron frequency is found at $\nu_c \approx 2.8 \times 10^6 B$ Hz and based on the fact that the corresponding dwarf’s pulses were detected at 8.44 GHz. Indeed, the detection of a kG magnetic field is in agreement with the previously confirmed magnetic fields for other ultracool dwarfs (Hallinan et al., 2006, 2007; Reiners & Basri, 2007).

Based on the above radio activity of LSR J1835, we decided to further investigate the presence of such variability for the dwarf at optical wavelengths, and whether it was peri-

odic in nature like the optical periodic variability presented by Lane et al. (2007) for the M9 dwarf TVLM 513. We conducted observations over a period of ~ 3 years, encompassing three separate epochs. Initial epochs were taken as test data only for the GUF1 mk.I system in July 2006 in the Johnson I-band, using the 1.52 m telescope in Loiano, Bologna, Italy. We also include Johnson I-band and R-band data from the USNO 1.55 m telescope in Flagstaff, Arizona, obtained by group members in September 2006. Finally, we observed the dwarf in the VATT I-band with the GUF1 mk.II system on the 1.83 m VATT telescope, Mt. Graham, Arizona, to confirm its periodic nature in June 2009. The three epochs contain ~ 33 hours of observations on source.

4.3.2 TVLM 513-46546

TVLM 513 is an M9 ultracool dwarf (≈ 2200 K) which is at a distance of ~ 10.5 pc (Tinney et al., 1993, 1995). It has an inferred mass of $< 0.08 M_{\odot}$ at an age of > 400 Myr, however the fact that no lithium has been detected to date puts constraints on the star's minimum mass, which consequently must be $> 0.06 M_{\odot}$ (Chabrier & Baraffe, 2000; Reid et al., 2002). Therefore, TVLM 513 is categorized as either a high-mass brown dwarf or a very old low mass star. Leggett et al. (2001) show a bolometric magnitude of $\log L_{bol}/L_{\odot} \approx -3.65$ based on 1-2.5 μm spectroscopy. The dwarf is located at the substellar boundary and is one of the most rapidly rotating dwarfs discovered thus far with a $v \sin i$ of $\sim 60 \text{ km s}^{-1}$ (Basri, 2001). All the same, only weak levels of $H\alpha$ have been found in its spectrum (Martín et al., 1994; Reid et al., 2001; Mohanty & Basri, 2003), with no X-ray detections reported so far.

However, Berger (2002) detected transient radio emission at 8.46 GHz from TVLM 513, which also included a highly circularly polarized flare (flux density $\approx 1100 \mu\text{Jy}$) where the fraction of polarization at or near the peak of the flare was $\approx 66 \pm 4\%$. TVLM 513 was also detected during a VLA radio campaign by Osten et al. (2006) at 8.4, 4.8 and 1.4 GHz, however no obvious flaring or circular polarization was found, and only a small level of variability.

Hallinan et al. (2006) observed the dwarf simultaneously at 4.88 and 8.44 GHz using the VLA where they found persistent periodic radio emission at both frequencies with a period of ~ 2 hours. They concluded that this periodic variability was due to stellar rotation, which supported the measured $v \sin i$ of $\sim 60 \text{ km s}^{-1}$ (Basri, 2001). This rotational velocity measurement gives a maximum rotation period of 2.0 ± 0.2 hours, and furthermore would require a high inclination angle of $\geq 65^\circ$. Hallinan et al. (2006) argue that coherent ECM

emission could generate the high levels of observed circular polarization, in addition to the levels of brightness temperatures reported for this observation.

Following this, Hallinan et al. (2007) once again observed TVLM 513 and reported the detection of periodic bursts of radio emission (100% circularly polarized) which enabled them to constrain the period to ~ 1.96 hours. These observations were conducted simultaneously to a photometric monitoring campaign by Lane et al. (2007), who also detected a periodic signal of ~ 1.96 hours in photometric I-band data - these observations established that the periodicity was due to the rotational modulation of the star, as put forward by Hallinan et al. (2006). This radio detection was also confirmation that ultracool dwarfs were capable of producing broadband, coherent radio emission, which is typically associated with the presence of kilogauss magnetic field strengths. In fact, Lane et al. (2007) attribute this periodicity to magnetic spots coupled with stellar rotation. However, Littlefair et al. (2008) reported anti-correlated Sloan g' and i' photometry of the M9 dwarf. They argue against star spots being the cause of the detected periodicity, and instead propose that atmospheric dust is responsible - since the star spot model was inconsistent with this result.

Interestingly, in an observation by Berger et al. (2008a), they detected sinusoidal $H\alpha$ and $H\beta$ periodicity, with a period of ~ 2 hours, matching the periods found by Hallinan et al. (2006, 2007) and Lane et al. (2007). This was an indication that localized heating existed near the surface of the dwarf via a chromospheric hotspot or perhaps some other magnetically-induced structure in the dwarf's chromospheric regions.

We observed TVLM 513 in optical photometric VATT I-band observations with GUF1 mk.II on VATT in June 2009. We also observed the dwarf during three additional I-band epochs in February and April 2011 using GUF1 mk.II once again, and in May 2011 using the the VATT 4K CCD and a Sloan i' filter. In this work, we also include data taken by members of the group using the USNO 1.0 m telescope, from an epoch in 2008, and earlier VATT data, obtained in 2006. This baseline therefore extends for ~ 5 years encompassing ~ 53 hours of data.

4.3.3 BRI 0021-0214

BRI 0021-0214 is a nearby, rapidly rotating M9.5 dwarf, which is located at a distance of ~ 11.5 pc and has a measured $v \sin i \approx 34 \text{ km s}^{-1}$ (Reid et al., 1999; Mohanty & Basri, 2003). Based on the work of Leggett et al. (2001), the dwarf has an effective temperature of 2100 K and a bolometric magnitude of $\log L_{\text{bol}}/L_{\odot} \approx -3.4$. Neuhäuser et al. (1999) show

no detection of X-rays from BRI 0021. Although Reid et al. (1999) reported a weak $H\alpha$ flare of luminosity $\log L_\alpha/L_{bol} \approx 10^{-4.2}$, a level which is a factor of 3 times lower than the mean quiescent emission of early to mid M dwarfs, no persistent $H\alpha$ emission was found during observations by Tinney & Reid (1998).

However, in a campaign investigating magnetic activity in ultracool dwarfs, Berger et al. (2010) found steady and variable $H\alpha$ emission from BRI 0021 on a $\sim 0.5 - 2$ hour time-scale, albeit no detected radio emission, despite previous low-level detections of radio emission ($\sim 40 \pm 13 \mu\text{Jy}$ at 8.46 GHz) with peak flux densities of $\approx 360 \mu\text{Jy}$ reported from the dwarf (Berger, 2002). Other optical variability has also been reported by Martín et al. (2001), who find I-band variability during multi-epoch photometric observations, including strong peaks in periodogram analysis - indicating periods of ~ 20 hours and ~ 4.8 hours. Their baselines included two separate epochs, where 10 nights and 4 nights of observations were obtained, respectively. They argue that since the dwarf appeared to have low levels of magnetic activity, the variability was probably not due to spots on the stellar surface, but rather due to dust clouds in the dwarf's atmosphere - since the presence of silicate and iron clouds are expected based on the dwarf's spectrum (Chabrier & Baraffe, 2000).

Since BRI 0021 was shown to exhibit this chromospheric and radio activity, in addition to some photometric variability, we decided to observe the dwarf in broadband optical photometry with GUF1 mk.II and consequently obtained data for a total of ~ 28 hours over three epochs of ~ 1.2 years of separation, using the VATT I-band filter.

4.3.4 2MASS J0036+18

2M J0036 is a nearby (~ 8.8 pc) L3.5 brown dwarf with an inferred mass of $0.06 - 0.074 M_\odot$ based on a surface gravity measurement of $\log g \approx 5.4$, which places the dwarf right at the sub-stellar boundary (Dahn et al., 2002; Schweitzer et al., 2001). Although Schweitzer et al. (2001) reported a $v \sin i$ of $\sim 15 \text{ km s}^{-1}$, consequent studies by Jones et al. (2005) and Zapatero Osorio et al. (2006) found respective rotation velocities of 38 and 36 km s^{-1} . The L dwarf has an inferred effective temperature of $\approx 1900 \text{ K}$ and a bolometric magnitude of $\log L_{bol}/L_\odot \approx -3.98$ (Vrba et al., 2004). Hallinan et al. (2008) predict a minimum age of $> 800 \text{ Myr}$ based on this bolometric luminosity, and no detection of lithium thus far.

Berger (2002) detected persistent radio emission, including flaring, via 8.46 GHz VLA radio observations. They found the emission to be persistent with the fraction of polarization during flaring to be $\approx -62 \pm 5\%$, indicating left-circularly polarized emission. Berger et al. (2005) then confirmed the presence of highly variable, periodic radio emission, with

a period of ≈ 3 hours, in two separate epochs of observations. This level of radio emission violated the Güdel-Benz relationship (refer to chapter 1, § 1.3.2) by many orders of magnitude. They interpret the emission as incoherent gyrosynchrotron radiation, with a corresponding magnetic field strength of 175 G.

However, Hallinan et al. (2008) reported 2M J0036 to be once again a persistent source of radio emission, including the presence of 100% circularly polarized pulses of extremely bright radio emission. Periodic unpolarized radio emission was also observed. Most importantly, the unpolarized component of this observation exhibited brightness temperature constraints that excluded gyrosynchrotron radiation as a possible mechanism for the observed radio emission (see Hallinan et al. (2008)). This confirmed that ECM emission was the mechanism responsible for the pulsed radio emission, and furthermore that it required a magnetic field strength of at least 1.7 kG, for 2M J0036. In fact, this field strength measure was the first confirmation of kG magnetic field strengths for an L dwarf.

Prior to these observations, Lane et al. (2007) conducted photometric I-band observations of 2M J0036, and found the dwarf to be photometrically variable, with a periodicity of ~ 3 hours. This confirmed that the periodicity was due to the stellar rotation of 2M J0036. They argue that magnetic spots on the surface of the dwarf, coupled with the rotation of the star, were a likely source of the ~ 3 hour periodicity. Some evidence of aperiodic variability was also present, which they attribute to dust clouds in the cooler L dwarf atmosphere.

We chose to observe 2M J0036 in optical photometry at the same wavelength range as Lane et al. (2007) to determine whether the optical periodicity was present over time-scales of years. We used GUPI mk.II on VATT at I-band wavelengths, for two nights in December 2010, for a total of ~ 10 hours.

4.4 Optical Observations

The GUPI instrument and its capabilities was outlined in great detail in Chapter 2. Here we give a brief description of the other instruments that were used during the campaign, as well as an overall summary of the campaign observation details, and data reduction carried out.

4.4.1 The VATT 4K Imager

The VATT 4K CCD camera is the primary in-house photometer stationed at VATT. It houses a back-illuminated STA0500A CCD with a transfer sensor of 4064×4064 pix-

els, a native FOV of $\sim 12.5' \times 12.5'$ and a plate scale of $0.188'' \text{ pixel}^{-1}$. The standard readout rate for the camera is 50 seconds, however faster readout rates can be achieved based on the level of windowing applied to the frame.

4.4.2 The USNO Detectors

Some observations, as outlined in the relevant target details in Table 4.2 and 4.3, were obtained with the USNO 1.0 m and USNO 1.55 m telescopes. The new2k camera on the 1.0 m telescope has a FOV of $23.2' \times 23.2'$ and a pixel scale of $0.68'' \text{ pixel}^{-1}$. We used the Tek2k camera on the 1.55 m, which has a corresponding FOV of $11.3' \times 11.3'$ with a pixel scale of $0.33'' \text{ pixel}^{-1}$.

4.4.3 Observations and Data Reduction

The observation campaigns were carried out between May 2006 - May 2011. We used the Johnson I-band filter ($\sim 7000 - 11000 \text{ \AA}$), the VATT I-Arizona ($\sim 7200-9100 \text{ \AA}$) and R-Harris ($\sim 5600-8800 \text{ \AA}$) broadband filters, as well as the Sloan i' ($\sim 6500-9500 \text{ \AA}$) filter - for selected targets (Table 4.2 and 4.3). Transmission curves for each filter are shown in Figure 4.1. The campaign encompassed observations to search for periodic variability of all radio detected dwarfs listed in Table 4.2, that were visible from the VATT observatory site ($32^\circ 42' 4.78''$ $109^\circ 53' 32.5''$ W). We also obtained data from the 1.52 m telescope, in Loiano, Bologna, Italy, as well as the 1.0 m and 1.55 m USNO telescopes, in Flagstaff, Arizona, as shown in Table 4.2. Figure 4.1 includes spectra of an M8.5, an L0.5 and an L3.5 dwarf, which covers the range of ultracool dwarf spectral types that our observations covered. Typical acquisition parameters are also summarized in Table 4.2 and 4.3.

Data reduction was carried out using the in-house GUFIL L3 Pipeline, as outlined in Chapter 3. Standard data reduction techniques were employed where the data were bias subtracted using zero-integration frames and flat-fielded using twilight flat-fields. Twilight flat-fields for any given observation consisted of >100 median-combined dithered frames taken from a blank part of the sky. Frames were registered and summed in image space to increase the SNR, and differential photometry was carried out on all science data in order to achieve milli-magnitude photometric precision.

The FOVs of the GUFIL, the VATT 4K and the USNO photometers, provide between 1-20 reference stars for a given field. Photometry for all reference stars was also obtained as a measure of their stability in order to ensure that variability was intrinsic to the target star. These stars were chosen on the basis of their stability, position, isolation, the prop-

Source	Epoch (#)	Total Time/Baseline (~hrs; yrs)	Date of Obs. (UT)	Length of Obs. (~hrs)	Exp. Time (s \times coadd)
LP 349-25AB	3	64; 1.2	2009 Sept 22	7.2	5×24
			2009 Sept 26	4.0	5×24
			2010 Oct 9	4.0	5×12
			2010 Oct 10	6.4	5×12
			2010 Oct 11	5.2	5×12
			2010 Oct 12	5.5	5×12
			2010 Oct 13	6.5	5×12
			2010 Oct 14	7.0	5×12
			2010 Oct 15	6.0	5×12
			2010 Nov 16	7.3	5×12
			2010 Nov 27	5.0	5×12
2M J0746AB	4	62; 2	2009 Jan 25	6.0	25×1
			2009 Jan 26	6.8	25×1
			2009 Jan 28	7.4	25×1
			2010 Feb 19	4.5	5×12
			2010 Feb 20	4.0	5×12
			2010 Nov 13	4.6	5×12
			2010 Nov 14	5.5	5×12
			2010 Dec 2	6.0	5×12
			2010 Dec 12	3.0	5×12
			2010 Dec 13	6.8	5×12
			2010 Dec 14	7.0	5×12
LSR J1835 [†]	3	33; 3	2006 Jul 17	7.0	5×12
			2006 Jul 20	6.5	5×12
			2006 Sept 22	3.6	30×2
			2006 Sept 24	3.0	30×2
			2009 Jun 11	2.2	5×12
			2009 Jun 13	4.0	5×12
			2009 Jun 16	4.0	5×12
			2009 Jun 30	3.0	5×12
			2006 May 21	4.8	30×3
			2008 Jun 17	6.0	60×2.5
			2009 Jun 12	3.6	5×12
TVLM 513 [‡]	6	53; 5	2009 Jun 13	4.1	5×12
			2009 Jun 16	4.0	5×12
			2011 Feb 18	3.5	5×12
			2011 Feb 25	4.3	5×12
			2011 Apr 12	7.0	5×12
			2011 May 7	8.0	25×1
			2011 May 8	8.0	25×1
			2009 Sept 14	4.0	5×12
			2009 Sept 16	5.1	5×12
			2010 Nov 13	4.0	5×12
			2010 Nov 14	5.5	5×12
BRI 0021	3	28; 1.2	2010 Dec 2	5.1	5×12
			2010 Dec 3	4.5	5×12
			2010 Dec 1	5.5	5×24
			2010 Dec 13	5.0	5×24
2M J0036	2	10; 0.03			

Table 4.2: Observation Details.

Source	Band	Readout Rate (MHz)	Amplifier	Refs (#)	Telescope/Instrument
LP 349-25AB	I	1	Conv.	5	VATT/GUFI
	I	1	Conv.	5	VATT/GUFI
	I	1	Conv.	5	VATT/GUFI
	I	1	Conv.	5	VATT/GUFI
	I	1	Conv.	5	VATT/GUFI
	I	1	Conv.	5	VATT/GUFI
	I	1	Conv.	5	VATT/GUFI
	I	1	Conv.	5	VATT/GUFI
	R	1	Conv.	4	VATT/GUFI
	I	1	Conv.	5	VATT/GUFI
2M J0746AB	I	1	Conv.	5	VATT/GUFI
	I	...	Conv.	20	VATT/4K
	I	...	Conv.	15	VATT/4K
	I	...	Conv.	19	VATT/4K
	I	1	Conv.	5	VATT/GUFI
	I	1	Conv.	6	VATT/GUFI
	I	1	Conv.	6	VATT/GUFI
	I	1	Conv.	5	VATT/GUFI
	I	1	Conv.	6	VATT/GUFI
	I	1	Conv.	6	VATT/GUFI
LSR J1835 [†]	I	1	Conv.	6	VATT/GUFI
	I	1	Conv.	5	Loiano/GUFI
	I	1	Conv.	5	Loiano/GUFI
	I	10	USNO/Tek2k
	R	10	USNO/Tek2k
	I	1	Conv.	5	VATT/GUFI
	I	1	Conv.	5	VATT/GUFI
	I	1	Conv.	4	VATT/GUFI
	I	1	Conv.	5	VATT/GUFI
	I	1	Conv.	5	VATT/GUFI
TVLM 513 [‡]	I	6	VATT/2K
	I	10	USNO/new2k
	I	1	Conv.	5	VATT/GUFI
	I	1	Conv.	5	VATT/GUFI
	I	1	Conv.	6	VATT/GUFI
	I	1	Conv.	6	VATT/GUFI
	I	1	Conv.	5	VATT/GUFI
	I	1	Conv.	6	VATT/GUFI
	i'	12	VATT/4K
	i'	12	VATT/4K
BRI 0021	I	1	Conv.	1	VATT/GUFI
	I	I	Conv.	1	VATT/GUFI
	I	1	Conv.	1	VATT/GUFI
	I	1	Conv.	1	VATT/GUFI
	I	1	Conv.	1	VATT/GUFI
	I	1	Conv.	1	VATT/GUFI
2M J0036	I	1	Conv.	6	VATT/GUFI
	I	1	Conv.	6	VATT/GUFI

Table 4.3: Observation Details (cont.).

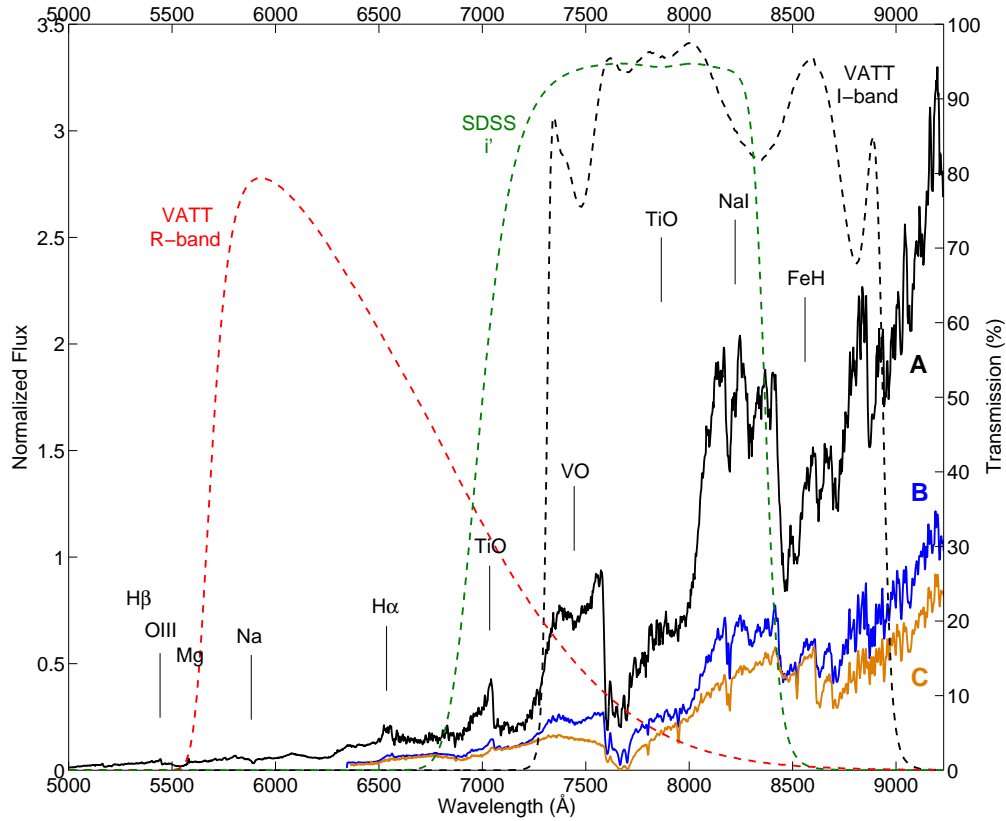


Figure 4.1: Filter transmission curves with over-plotted spectra of an M8 dwarf (A), an L0.5 dwarf (B) and an L3.5 dwarf (C) - the spectral range which encompasses our study. The spectra have been normalized (y-axis left) by the peak flux of the M8 dwarf spectra at 9500 Å, which corresponds to the end of the waveband range. The waveband ranges (x-axes) and % transmission (y-axis right) are indicated by the dashed lines, with the associated band marked beside each curve. [left to right] - Wavebands: VATT R-band (~ 5600 - 8800 Å), Sloan i' (~ 6500 - 9500 Å) and VATT I-band (~ 7200 - 9100 Å).

erties of their seeing profiles, and comparable magnitudes and color to that of the target. Photometric apertures (in pixels) which provided the highest SNR for the target star were selected for aperture photometry; however aperture and sky annulus diameters varied from night to night depending on the average seeing conditions, which typically ranged from 0.7 to 1.6 arcseconds. Differential photometry was obtained by dividing the target flux by the mean flux of selected reference stars. Although changing seeing conditions can ultimately introduce photometric errors, for all observations we ensured that the photometric parameters remained constant for all stars - this allowed the same fraction of total flux to

be observed in the aperture of each source.

4.5 General Results

We report periodic variability for five of the six radio detected dwarfs in the sample, shown in Table 4.4. The properties of this periodicity is generally consistent for all dwarf spectral types, where we detect periodic sinusoidal variability over timescales of years, where there is some evidence of aperiodic variations in lightcurves. We assess the change in levels of amplitude of target lightcurves via the χ^2 test, which provides a measure of the amplitude and the error for a given observation (Table 4.5). This is discussed further in the following sections. The binary dwarfs exhibit significant changes in amplitude during some observations. We investigate the various possibilities that could cause this behavior.

In the following subsections, we outline general results and variability analysis of each target, as well as lightcurve and photometric properties. All confirmed periods in these data were detected to significance values exceeding 5σ via the LS periodogram. In all cases, the periodic variability is associated with the rotation of the dwarf, coupled with an additional feature present in the dwarf photosphere or atmosphere. We discuss these possibilities later in this chapter.

4.5.1 Binary Dwarfs

4.5.1.1 LP 349-25AB (M8+M9)

We detect the binary as a periodically varying source in VATT I-band and R-band, which we report as the first detected optical variability of this system. The primary period of 1.86 ± 0.02 hours is present in each band and varying with a σ_{tar} range of 0.22 - 0.71% in I-band, and $0.98^{+0.22}_{-0.17}\%$ in R-band (single observation), as shown in Figure 4.2. The LS and PDM statistical analysis is shown in Figure 4.3. Mean σ_{ref} were calculated to be $\sim 0.38\%$ and 0.96% in I-band and R-band, respectively. We see larger σ_{ref} in R-band due to intermittently poor seeing. It is difficult to assess the amplitude ratios between each band, since the amplitude level in the I-band is varying to a significant level as shown in Table 4.5. Furthermore, we did obtain simultaneous R-band and I-band data. The significance of this color information is discussed further in § 4.6.

Despite the consistency of the primary periodic component throughout the observations, we observe some aperiodic variations in addition to significant variations in amplitude during some I-band observations (e.g. Oct 10, 11 & 13 2010). We do not image

Parameter	LP 349-25	2M J0746	LSR J1835	TVLM 513	BRI 0021	2M J0036
(1): Period (hrs)	1.86 ± 0.02	3.36 ± 0.12	2.845 ± 0.003	1.95958 ± 0.00005	?	~ 3.0 ± 0.7
(2): New?	Yes	Yes	Yes	No [†]	...	No [‡]
(3): LS P (hrs)	1.86	3.36	2.845	1.95958	...	2.5
(4): PDM P (hrs)	1.86	3.32	2.844	1.95959	...	2.5
(5): $\bar{\sigma}_{tar}$ (%)	I: ~ 0.46 R: $\sim 0.98^a$	I: ~ 0.48	I: ~ 0.63 R: $\sim 0.81^a$	I: ~ 0.41 i' : $\sim 0.47^b$	I: ~ 0.46	I: ~ 1.05
(6): σ_{ref} (%)	~ 0.38 $\sim 0.96^a$	~ 0.36	~ 0.33 $\sim 0.65^a$	~ 0.34 $\sim 0.36^b$	~ 0.37	~ 1.4
(7): $[P]:[v \sin i]$...	0.62:0.57
(8): LS Sign. (σ)	>5	>5	>5	>5	...	>5

Table 4.4: **Confirmed Optical Periodic Variability in Radio Detected Ultracool Dwarf Sample.**

Row (1) Period of rotation and associated error as calculated in Section 1.4. (2) Newly discovered period, or not. Contains references below to those not discovered in this work. (3) Lomb-Scargle Periodogram periods: the quoted periods are those which were determined to be the most likely solution based on the correlation of the highest peaks in all periodograms (all data combined and individual epochs). (4) Phase Dispersion Minimization periods: the PDM periods shown here represent the lowest Θ statistic calculated by the PDM routines, as is shown in Section 4.5. (5) Mean amplitude variability of target lightcurves (mean value of all lightcurves shown for each target for all epochs). Amplitude variability for individual target observations is shown in the following Table, 4.5. (6) Mean amplitude variability of reference star lightcurve in I-band (mean standard deviation of all reference stars used in each case). (7) Konopacky et al. (2012) report individual rotational velocity measurements for 2M J0746AB. These values subsequently yield a $v \sin i$ ratio of ~ 1.7 . We calculate a period ratio of ~ 0.62 based on our reported 3.36 ± 0.12 hour period for 2M J0746A. This ratio was calculated by using the periodic radio pulses of 2.07 ± 0.002 hours of Berger et al. (2009) - the period of rotation of 2M J0746B. Elaborated upon in Chapter 6. (8) LS detection significance for quoted periods. These correspond to a False Alarm Probability (FAP) of 5.733×10^{-7} , or a detected period with a statistical significance of 5σ .

^aMean amplitude variability for R-band data. Similarly for σ_{ref} .

^bMean amplitude variability for Sloan i' . The same for σ_{ref} .

References: [†]Berger et al. (2009). [‡]Lane et al. (2007): TVLM 513 originally published as ~ 1.96 hours, 2M J0036 published as ~ 3 hours.

Source	Date of Obs.	Band	σ_{tar}	$\delta\sigma_{tar}$ χ^2 min.	$\delta\sigma_{tar2.5\%}$ Bootstrap	$\delta\sigma_{tar97.5\%}$ Bootstrap	$\delta\sigma_{tar}$ C.I. 95%
	(UT)		(%)	(S.E. \pm %)	(%)	(%)	(\pm %)
(1)	(2)	(3)	(4)	(5)	(6)	(7)	(8)
LP 349-25AB	2009 Sept 22	I	0.24	± 0.03	0.18	0.30	+0.06 -0.06
	2009 Sept 26	I	0.71	± 0.05	0.63	0.81	+0.10 -0.08
	2010 Oct 9	I	0.52	± 0.04	0.45	0.59	+0.07 -0.07
	2010 Oct 10	I	0.45	± 0.02	0.39	0.52	+0.07 -0.06
	2010 Oct 11	I	0.22	± 0.02	0.18	0.26	+0.04 -0.04
	2010 Oct 12	I	0.47	± 0.02	0.43	0.52	+0.05 -0.04
	2010 Oct 13	I	0.45	± 0.02	0.40	0.50	+0.05 -0.05
	2010 Oct 14	I	0.29	± 0.02	0.25	0.32	+0.03 -0.04
	2010 Oct 15	R	0.98	± 0.08	0.81	1.20	+0.22 -0.17
	2010 Nov 16	I	0.56	± 0.04	0.47	0.66	+0.10 -0.09
2M J0746AB	2010 Nov 27	I	0.42	± 0.02	0.38	0.46	+0.04 -0.04
	2009 Jan 25	I	0.20	± 0.03	0.15	0.26	+0.06 -0.05
	2009 Jan 26	I	0.49	± 0.04	0.40	0.60	+0.11 -0.09
	2009 Jan 28	I	0.39	± 0.03	0.33	0.46	+0.07 -0.06
	2010 Feb 19	I	0.63	± 0.04	0.55	0.70	+0.07 -0.08
	2010 Feb 20	I	0.66	± 0.04	0.59	0.75	+0.09 -0.07
	2010 Nov 13	I	0.59	± 0.03	0.53	0.66	+0.07 -0.06
	2010 Nov 14	I	0.52	± 0.04
	2010 Dec 2	I	0.34	± 0.03	0.29	0.40	+0.06 -0.05
	2010 Dec 12	I	0.69	± 0.03	0.62	0.76	+0.10 -0.07
LSR J1835	2010 Dec 13	I	0.76	± 0.03	0.70	0.82	+0.06 -0.06
	2010 Dec 14	I	0.48	± 0.03	0.42	0.54	+0.06 -0.06
	2006 Jul 17	I	0.54	± 0.05	0.45	0.63	+0.09 -0.09
	2006 Jul 20	I	0.51	± 0.04	0.44	0.59	+0.08 -0.07
	2006 Sept 22	I	0.73	± 0.07	0.62	0.87	+0.14 -0.11
	2006 Sept 24	R	0.81	± 0.26	0.50	1.36	+0.55 -0.31
	2009 Jun 11	I	0.62	± 0.03	0.57	0.67	+0.05 -0.05
	2009 Jun 13	I	0.67	± 0.03	0.55	0.68	+0.01 -0.12
	2009 Jun 16	I	0.66	± 0.02	0.62	0.70	+0.04 -0.04
	2009 Jun 30	I	0.68	± 0.02	0.63	0.75	+0.07 -0.05
TVLM 513	2006 May 21	I	0.41	± 0.06	0.29	0.54	+0.13 -0.12
	2008 Jun 17	I	0.33	± 0.07	0.22	0.49	+0.16 -0.11
	2009 Jun 12	I	0.28	± 0.03	0.22	0.35	+0.07 -0.07
	2009 Jun 13	I	0.36	± 0.03	0.29	0.44	+0.08 -0.07
	2009 Jun 16	I	0.57	± 0.03	0.51	0.64	+0.07 -0.06
	2011 Feb 18	I	0.60	± 0.04	0.53	0.68	+0.08 -0.07
	2011 Feb 25	I	0.35	± 0.04	0.28	0.43	+0.08 -0.07
	2011 Apr 12	I	0.38	± 0.03	0.33	0.44	+0.05 -0.06
	2011 May 7	i'	0.48	± 0.03	0.42	0.55	+0.07 -0.06
	2011 May 8	i'	0.46	± 0.04	0.38	0.55	+0.09 -0.08

Table 4.5: **Amplitude Variability Analysis** (columns explained on next page).

Table continued from previous page							
BRI 0021	2009 Sept 14	I	0.55
	2009 Sept 16	I	0.45
	2010 Nov 13	I	0.36
	2010 Nov 14	I	0.79
	2010 Dec 2	I	0.34
	2010 Dec 3	I	0.26
2M J0036	2010 Dec 1	I	1.10	± 0.09	0.88	1.26	$+0.16$ -0.22
	2010 Dec 13	I	0.99	± 0.11	0.87	1.15	$+0.16$ -0.12

Table 4.6: **Amplitude Variability Analysis (cont.).**

Column (1) Target name. (2) Date of the observation in UT. (3) Photometric band used. R- and I-band correspond to the Johnson system, and i' corresponds to the Sloan system. (4) Amplitude variability as measured by the χ^2 test, outlined in Chapter 3, § 3.2.3. (5) The standard error (S.E. = 1σ) as calculated by the χ^2 routines. (6) Confidence interval (C.I.) by means of the Bootstrapping technique. We Bootstrap the data 1,000 times and obtain two ‘tails’ on either side of the mean value of a 95% C.I. curve. We show one limit of the amplitude range at the first ‘tail’ at 2.5%. (7) The other limit at the second ‘tail’ of the curve at 97.5%, indicating 3σ errors in the amplitude calculation. (8) Errors in the calculated amplitude via the Bootstrap with C.I. of 95% (3σ), as defined by (6) and (7). **Note:** We show example plots of the output from the LSF and χ^2 test, as well as the Bootstrap technique in the following chapter, where we investigate specifically the amplitude stability of TVLM 513-46546.

each component of the binary as a single point source in these observations, therefore the detected sinusoidal periodicity in our data is due to the combined flux of both binary members. We observe fascinating behavior for one night in particular (Oct 14 2010), where the periodic signal appears to move in and out of phase *during* a single observation of ~ 8 hours. We discuss this further in § 4.5.1.2.

It is important to note that in Figure 4.2, the second R-band peak in the signal was an interval of poor weather conditions (thin cloud) shown clearly by an increase in the photometric error measurements. The September 2009 epoch was also subject to poor weather conditions (intermittent cloud & thin cloud throughout), and was therefore binned by a factor of 2 compared to the other data. Photometric error bars are applied as outlined in Chapter 3. The bottom right (red) plot shows a selected reference star that was chosen at random. We plot its raw flux against the mean raw flux of all other reference stars used in the field. This is used as an example of reference star stability compared to target

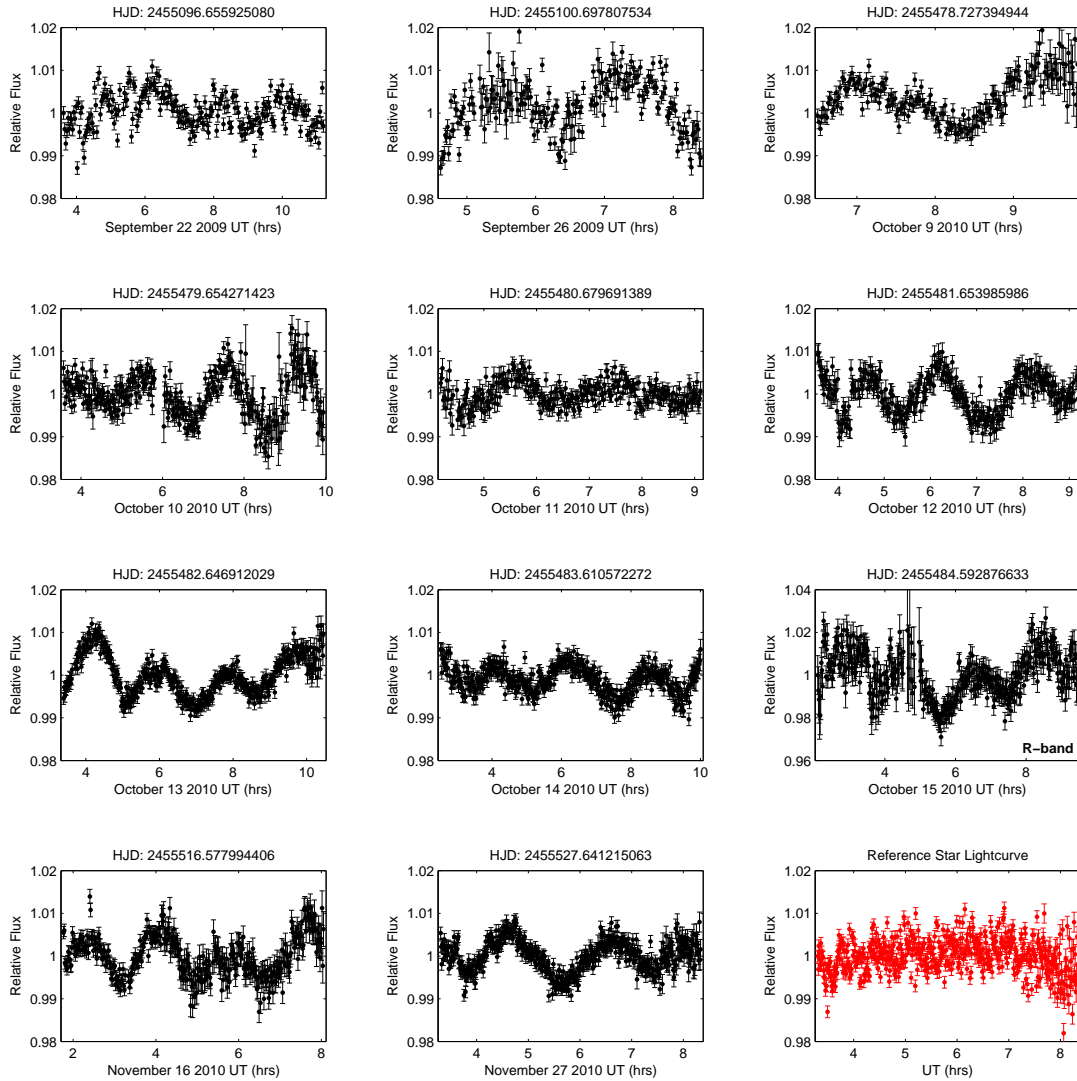


Figure 4.2: LP 349-25: UT dates and times are marked on each lightcurve's x-axis. The HJD time above each figure denotes the start-point of each observation. It is important to note that the x-axis range is not the same for each plot, since observations were of different lengths. All data in this figure was taken in VATT I-band ($\sim 7000 - 11000 \text{ \AA}$), with the exception of October 15 2010 UT which was taken in VATT R-band ($\sim 5600 - 8800 \text{ \AA}$) - this is marked on the relevant lightcurve. Note the difference in scale on the y-axis for the R-band labeled plot. [bottom right] - we selected a reference star at random, and plotted its raw flux against the mean raw flux of all other reference stars used in the field. This is used as an example of reference star stability compared to target variability.

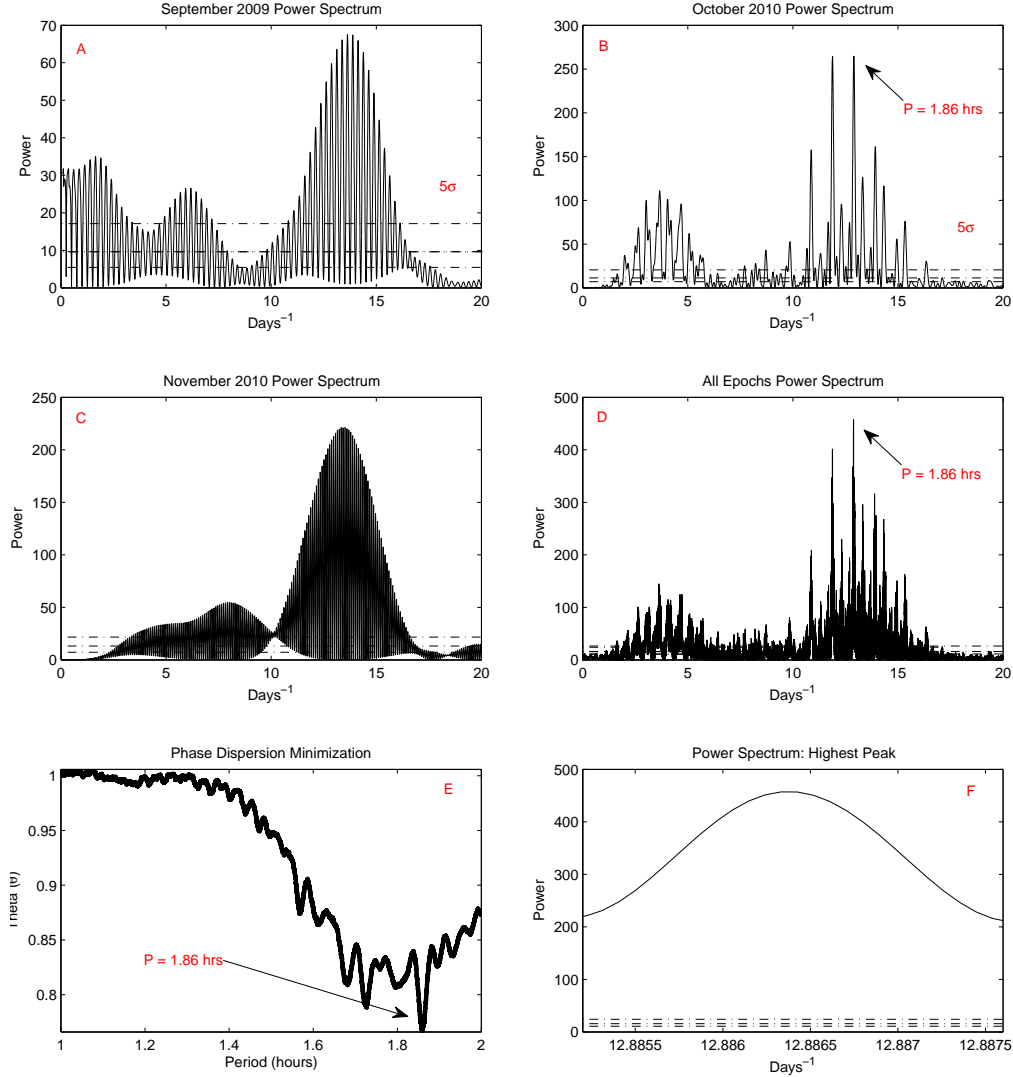


Figure 4.3: LP 349-25: [Figures A - D] Lomb-Scargle Periodograms analysis. *Figure A* shows a periodogram for the binary dwarf for the September 2009 epoch. We include a dashed-dotted line on each plot which represents a 5σ false-alarm probability of the peaks as determined by the Lomb-Scargle algorithm in each case. Similarly, *Figure B* and *Figure C* are the October and November 2010 epochs, and *Figure D* is all data analyzed as one time series. We also indicate the detected period of 1.86 ± 0.02 hours, detected as the highest peak in the periodogram (*Figure F*). *Figure E* shows the Phase Dispersion Minimization plot, of period against the ‘Theta’ (θ) statistic for all of LP 349-25 data. This statistic was determined based on 10^4 Monte-Carlo simulations which randomize the data points and test whether the result at any given Θ level could be as a result of noise.

variability. We note that this lightcurve is an example of one night only, however we used the same reference stars for all epochs in a given band. The mean reference star variability for all reference stars used in this campaign is shown in Table 4.4, row 6, where the different bands are indicated in the table.

Dupuy et al. (2010) obtained dynamical mass measurements of a sample of late-M dwarfs, including LP 349-25AB. Their modeling subsequently yield radii estimates of $\sim 1.30 - 1.44 R_J$ for LP 349-25A and $\sim 1.24 - 1.37 R_J$ for LP 349-25B. However, Konopacky et al. (2010) find much larger radii estimates of $\sim 1.7^{+0.08}_{-0.09} R_J$ (A) and $\sim 1.68^{+0.09}_{-0.08} R_J$ (B). Based on the radii of Dupuy et al. (2010), it is more likely that we detect LP 349-25B as the periodically varying source. If the system's orbital plane is orthogonal to the equatorial axes of each binary member as has been observed in solar-type binary formation (Hale, 1994), this reported period can be used to test this expected alignment. We consider this further in Chapter 6. In § 4.6, we discuss the various possibilities for what may be causing the optical photometric periodic variability of LP 349-25B.

4.5.1.2 The Unusual Behavior of LP 349-25

In this section we discuss the behavior of the lightcurves of the binary LP 349-25AB. As outlined in § 4.5.1.1, we observe significant changes in amplitude in I-band as shown in Table 4.5, as well as changes in phase during single observations, and also during epochs. Due to the close separation of the binary members, the photometric aperture used enclosed the combined flux of both components. Therefore the presence of two periodically varying sources in these data and thus the superposition of these waves is one possible explanation for the varying amplitude we observe here. However, aperiodic variability of a single periodic source could also cause this behavior - in this respect we must also consider other astrophysical phenomena. This is an obvious distinction and one that we investigate below.

We first consider the possibility of the presence of two periodically varying sources by subtracting the main 1.86 hour period out of the raw data. We did this by generating a sinusoidal model wave function with a period of 1.86 hours. We then iterated through a range of amplitude and phase values, and performed a LSF fit to the raw data from the October 2010 epoch. We chose this set of data because we had contiguous observation nights from October 9 - October 15 2010 UT, as shown in Figure 4.2. The best solution which fitted the raw data parameters was subtracted out. Lomb Scargle periodogram analysis was run on the remaining data points, which searched for residual periodic signatures. We observed no obvious evidence in the periodogram of any underlying periodic source. As a follow-up, we modeled the superposition of two sinusoidal sources by setting a period of 1.86 hours

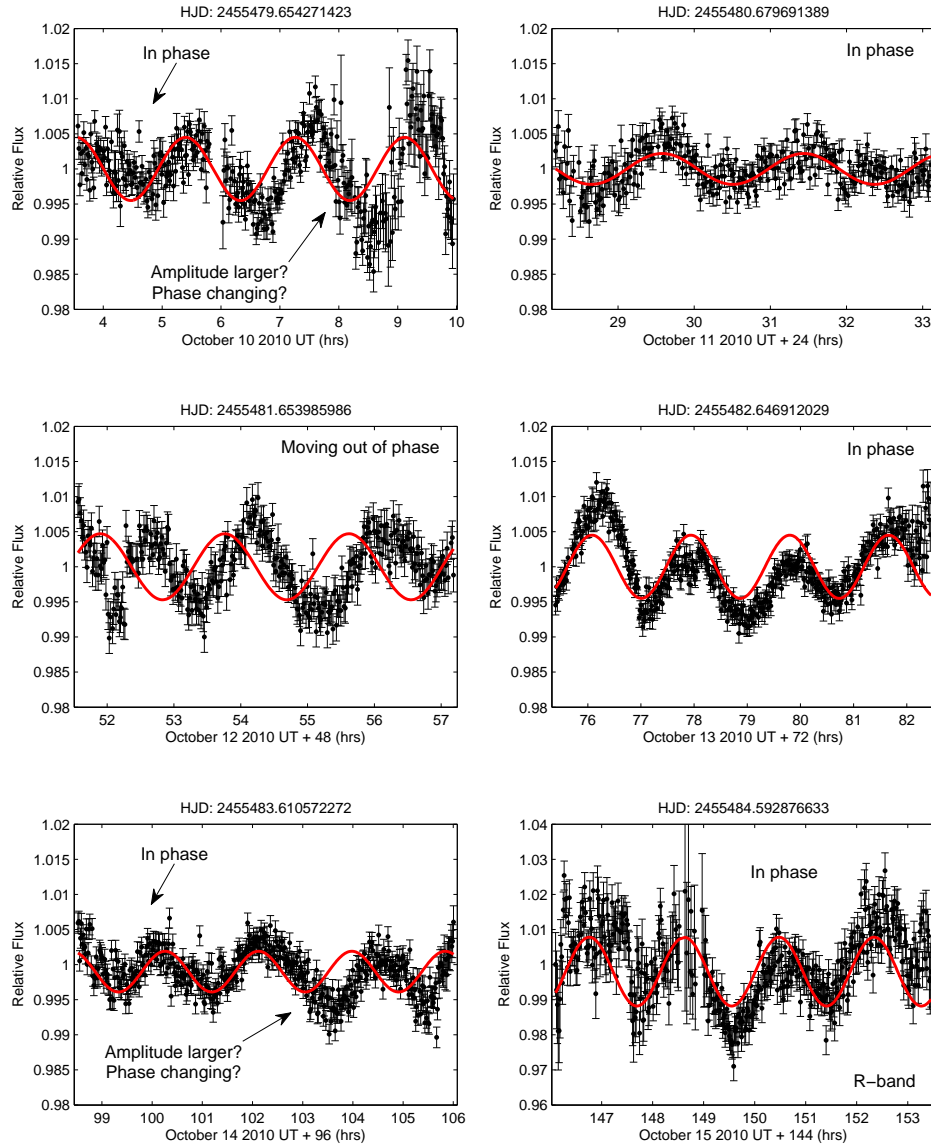


Figure 4.4: LP 349-25: We show lightcurves from October 2010 epoch, with a model sinusoidal fit of $P = 1.86$ hours, the primary periodic component detected in our data. We have scaled the time (x -axis, UT) for each consecutive observation with respect to Oct 10. The lightcurves exhibit most unusual behavior, where we see the model fit move in and out of phase in some cases (e.g. Oct 10, Oct 14). We cite TVLM 513 as an example of a source exhibiting consistent phase stability throughout, as discussed in Chapter 5.

for one source, varying the other period, as well as the amplitude and the phase of both waves, and performed a LSF to our data - as outlined in Chapter 3, § 3.2.4. We note that these models are rudimentary and do not take other systematic error into account. The best

fit to our models yielded a second period of ~ 1.6 hours. It is worth noting that Konopacky et al. (2012) indicate a $v \sin i$ ratio of ~ 1.5 for the system, placing the other period at ~ 1.25 hours or ~ 2.80 hours, assuming coplanarity (Hale, 1994), and adopting the radii estimates of Dupuy et al. (2010). However, the lack of evidence in the periodograms, as well as the inability to clearly detect an underlying source in the residual data after subtracting the main 1.86 hour period out, does not point toward the presence of another period.

Nevertheless, the varying component of amplitude and phase remains in these data, as shown in Figure 4.4. In this plot, we show raw lightcurves from the October 2010 epoch (Oct 10 - Oct 15 UT) with a model sinusoidal wave overplotted (in red). A period of 1.86 hours was used, and corresponding amplitudes from Table 4.5 were adopted for each lightcurve. We use a fixed phase of $\phi_0 = 2.18$ radians (125 degrees) for all nights. As we observe the model wave for each observation, we can see that the wave is in phase for some nights (e.g. Oct 11, Oct 13 and Oct 15). By contrast, the signal appears to have moved out of phase for Oct 12. We can also see, for Oct 10 and Oct 14, that the model is largely in phase for the first half of each observation (although upon closer inspection there is some evidence of trailing and leading peaks and troughs), but then moves partially *out of phase* as the amplitude of the signal increases - we also note changes in lightcurve morphology for these sections.

Although our investigation outlined above did not yield any obvious evidence for the presence of the other component, it does not preclude the possibility of another source - perhaps a more robust modeling technique is required to identify the presence of another period. Alternatively, this behavior could be characteristic of a high-dynamic environment in these regions, where the source of the variability is evolving on these timescales. Perhaps a magnetic feature is not stationary on the stellar photosphere, or alternatively a combination of features could be effecting lightcurve morphology. Moreover, if these features were undergoing changes in size or temperature, this could also have an effect on the sinusoidal shape. However, the presence of dust, coupled with a magnetic spot for example, does not explain this change in phase, where for example the duration of the sinusoidal signal appears to be longer from $\sim 101 - 104$ UT (+ offset) for Oct 14 in Figure 4.4, than at $\sim 99 - 101$ UT (+ offset) in this same observation.

Finally, we briefly mention the phenomenon of pulsations in some main sequence objects, which can result in multiple periods due to the associated oscillations. For example, Kurtz et al. (2011) have reported two pulsation modes for roAp (rapidly oscillating [peculiar] A type stars), where these fascinating stars exhibit pulsations in high overtone, non-radial, pressure modes. However, the internal physics and thus the structural properties of

A type stars are clearly very different to M dwarfs, so this kind of association is premature, albeit very interesting and worth mentioning. Obtaining a contiguous time series of LP 349-25 over many periods of rotation, would allow us to more effectively investigate these interesting changes in lightcurve morphology which could possibly establish such oscillations in the data. Indeed, this is an intriguing development, which made the period constraint of this binary quite difficult. Magnetic spots and photospheric dust as possible sources of the periodicity and aperiodicity are discussed in more detail in § 4.6.

4.5.1.3 2MASS J0746+2000AB (L0+L1.5)

Although we do not resolve each component of the binary as a point source, most intriguingly, we show optical periodic modulation of 3.36 ± 0.12 hours, where the sinusoidal variability exhibits a range of σ_{tar} of $\sim 0.20 - 0.76\%$ in VATT I-band and corresponding σ_{ref} of $\sim 0.36\%$. Therefore, this optical periodic variability originates from the *other* component to that producing the radio emission - reported by Berger et al. (2009) where the binary exhibited periodic bursts of radio emission of 2.07 ± 0.002 hours. By adopting radii of $\sim 0.99 \pm 0.03 R_J$ and $\sim 0.97 \pm 0.06 R_J$, in addition to the $v \sin i$ measurements outlined earlier in this chapter (Konopacky et al., 2012), we derive maximum period values of ~ 4.22 hours and ~ 2.38 hours for 2M J0746A and 2M J0746B, respectively. Therefore this infers that we may have detected the period of rotation of 2M J0746A, the primary component of the system, whereas Berger et al. (2009) found emission from the secondary - 2M J0746B. This optical periodicity is categorically present in the data, thus we propose that the period of rotation of 3.36 ± 0.12 hours is that of the *slower* component of the binary dwarf. The discovery of this period has also allowed us to investigate the orbital coplanarity of the system. We discuss this further in Chapter 6.

Campaign results are shown in Figure 4.5. These data were taken in VATT I-band ($\sim 7000 - 11000 \text{ \AA}$) over a ~ 2 year baseline. We report periodic variability for one component of the binary, with a period of 3.36 ± 0.12 hours. The amplitude variation throughout the observations varies from $\sim 0.20 - 0.76\%$. Photometric error bars are applied to each data point as before. In the bottom right of the figure, we plot an example reference star lightcurve to illustrate the stability of the chosen reference stars as compared to the target star variability. The mean reference star variability for all reference stars used in this campaign for 2M J0746 is shown in Table 4.4. Finally, we show the statistical analysis of the binary in Figure 4.6, where LS periodograms and PDM routines identified the period of 2M J0746A. As shown in the figure, this period was confirmed via the highest peak in the periodogram, and where the PDM Θ statistic minimized. Based on the length of the

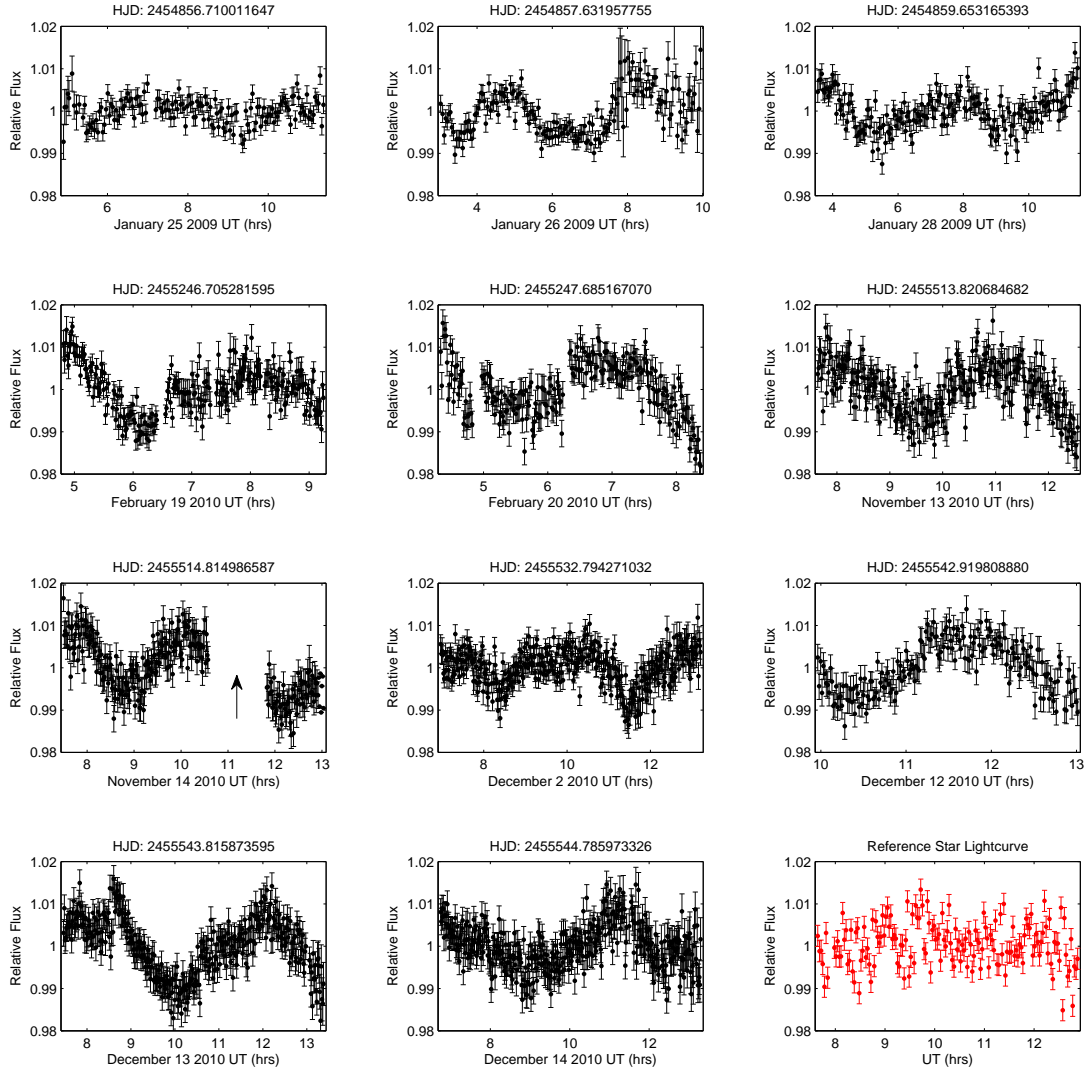


Figure 4.5: 2MASS J0746+2000: UT dates and times are marked on each lightcurve's x-axis along with HJD time above each figure (start-point of each observation). These data were taken in VATT I-band ($\sim 7000 - 11000 \text{ \AA}$) over an ~ 2 year baseline. The amplitude variation throughout the observations varies from $\sim 0.20 - 0.76 \%$. We note that January 25 & 26 2009 were taken during deteriorating weather conditions (thin cloud and high winds) and were therefore binned by a factor of 2 compared to other data. The arrow marked on the November 14 2010 lightcurve points to an interval of complete cloud cover, therefore these data were removed.

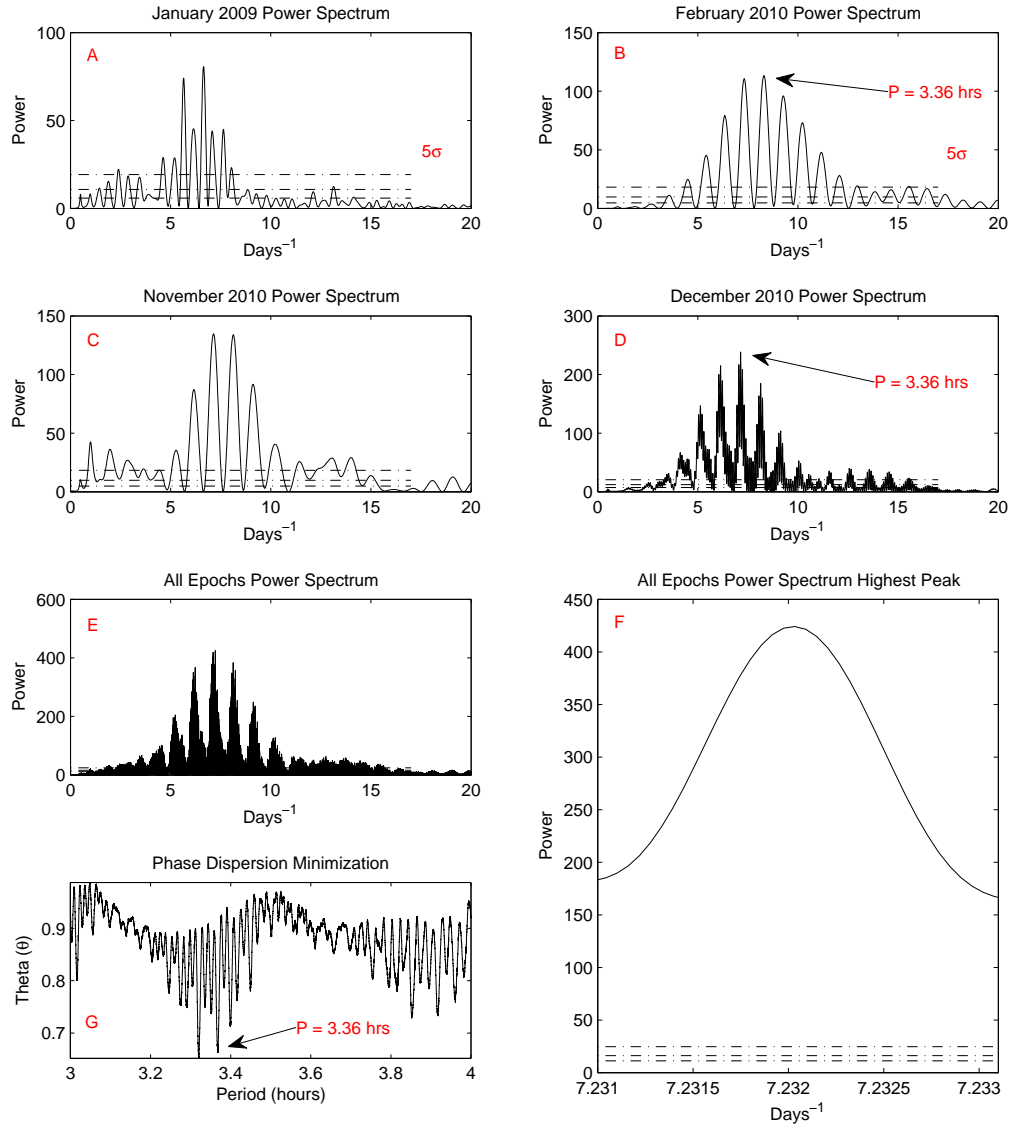


Figure 4.6: 2MASS J0746+2000: [Figures A - E] Lomb-Scargle Periodograms analysis. *Figure A* shows a periodogram for the L binary dwarf for the January 2009 epoch. We include a dashed-dotted line on each plot which represents a 5 σ false-alarm probability of the peaks as determined by the Lomb-Scargle algorithm in each case. Similarly, *Figures B - E* are the February, November and December epochs, as well as LS periodogram that analyzed all of the data as one time series. We also indicate the detected period of 3.36 ± 0.12 hours, detected as the highest peak in the periodogram (*Figure F*). *Figure G* shows the Phase Dispersion Minimization plot of the entire 2M J0746 baseline, of period against the ‘Theta’ (θ) statistic, again, using 10^4 Monte-Carlo simulations.

baseline, and the large amount of data in each epoch, a periodic error of ± 0.12 hours is quite large. However, similar to the lightcurves of the binary LP 349-25AB, 2M J0746A also exhibited some aperiodic behavior - e.g. Jan 26 2009, Dec 2 2010, Dec 13 2010. Thus it was difficult to phase connect the data to the level of accuracy required to connect the ~ 2 year baseline. The error we placed on the period was therefore taken as a 1σ error on the detected period, as outlined in Chapter 3, § 3.2.5. Once again, here we only present the photometric results, and discuss the possible cause of the transient nature of the lightcurves in § 4.6.

4.5.2 Single Dwarfs

4.5.2.1 LSR J1835+3259 (M8.5)

We determined a photometric period of 2.845 ± 0.003 hours in VATT I-band, consistent with the VLA radio observations of Hallinan et al. (2008), who report periodic pulses of 2.84 ± 0.01 hours. This optical period is newly reported in this work, which was conducted between July 2006 and June 2009 with the GUF1 mk.I and mk.II systems. We also find a period of ~ 3 hours in R-band data obtained from the 1.55 m USNO telescope. The weather for this observation was very poor; therefore we do not include the R-band data in the determination of the quoted period of rotation. However, it appears that LSR J1835 has larger R-band amplitude variability than I-band - similar to other targets in the sample. These data exhibit long-term stable periodic sinusoidal variability with mean σ_{tar} and σ_{ref} scatter of 0.63% and $\sim 0.33\%$ in I-band, and $0.81^{+0.55}_{-0.31}\%$ and $\sim 0.65\%$ in R-band. Furthermore, the calculated period supports the rotational velocity estimate of $v \sin i \sim 50 \pm 5 \text{ km s}^{-1}$ (Berger et al., 2008a), which implies a high inclination angle of $\sim 90^\circ$ for the system. These data also appear to be in phase based on this period of 2.845 ± 0.003 hours during constituent epochs. Although we do not achieve a high enough period accuracy in order to phase connect the ~ 3 year temporal baseline, we could phase connect the 2006 July and September data.

Figure 4.7 shows the photometric lightcurve results of LSR J1835 from the ~ 3 year campaign. The 2006 July epoch was taken as test data for the GUF1 mk.I system. We note that R-band ($\sim 5600\text{-}8800 \text{ \AA}$) data obtained via the USNO on September 24 & 25 2006 UT, were subject to poor seeing on both nights. Thus we only present the R-band lightcurve from September 24 2006. As mentioned at the beginning of this section, the period of rotation of 2.845 ± 0.003 hours matches the periodic pulses reported by Hallinan et al. (2008), who attributed this periodicity to the dwarf's rotation. We also attribute the

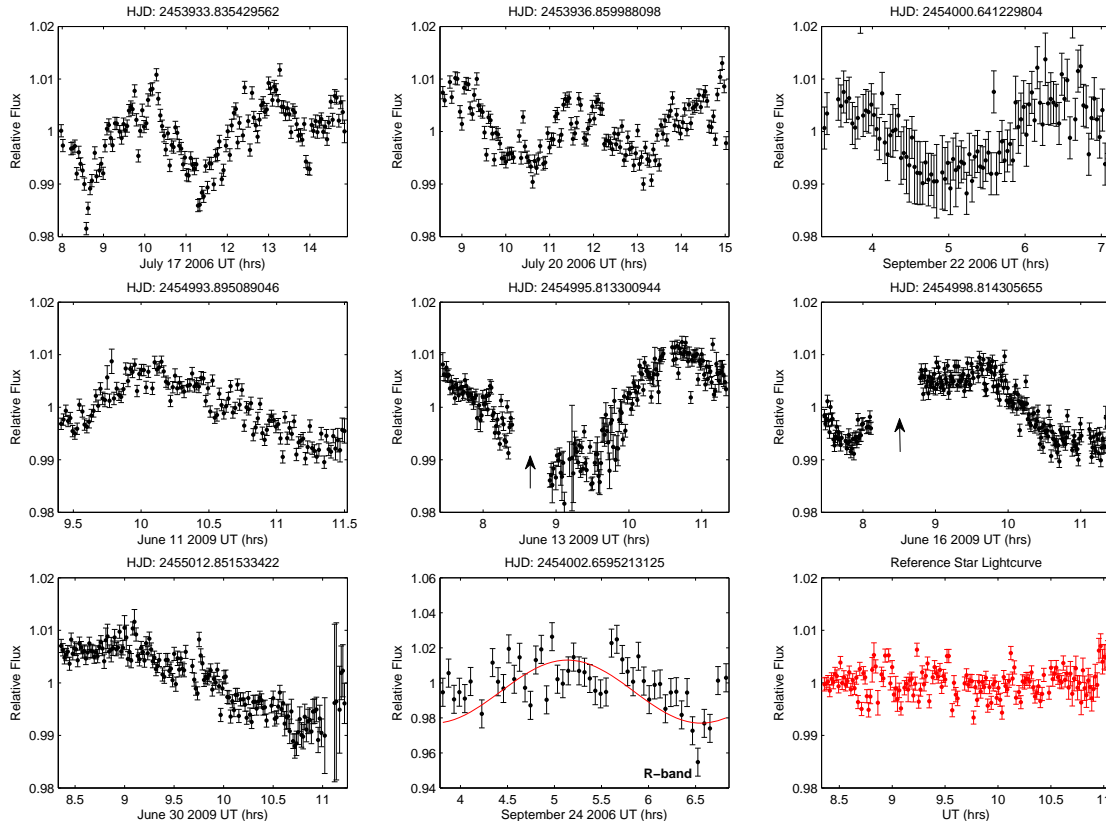


Figure 4.7: LSR J1835+3259: These data were taken over a ~ 3 year baseline at I-band wavelengths ($\sim 7000 - 11000 \text{ \AA}$), where the 2006 July epoch was taken as test data for the GUF1 mk.I system. We also observed the dwarf in R-band ($\sim 5600 - 8800 \text{ \AA}$) using the USNO on September 24 & 25 2006 UT. The seeing on both nights was very poor however. Here we show a binned data set, marked with an R-band label, from September 24 2006 UT. We overplot a model sinusoidal fit (red) to the detected period of 2.845 hours. The arrows shown in June 13 & June 16 mark data gaps due to this object's passing too close to the zenith for the telescope's Alt-Az tracking. Once again we show a reference star lightcurve (bottom right) to illustrate the variability of the target with respect to a non-variable source. Although we have a ~ 3 year baseline, we do not achieve an accurate enough period to phase connect the 2006 and 2009 epochs.

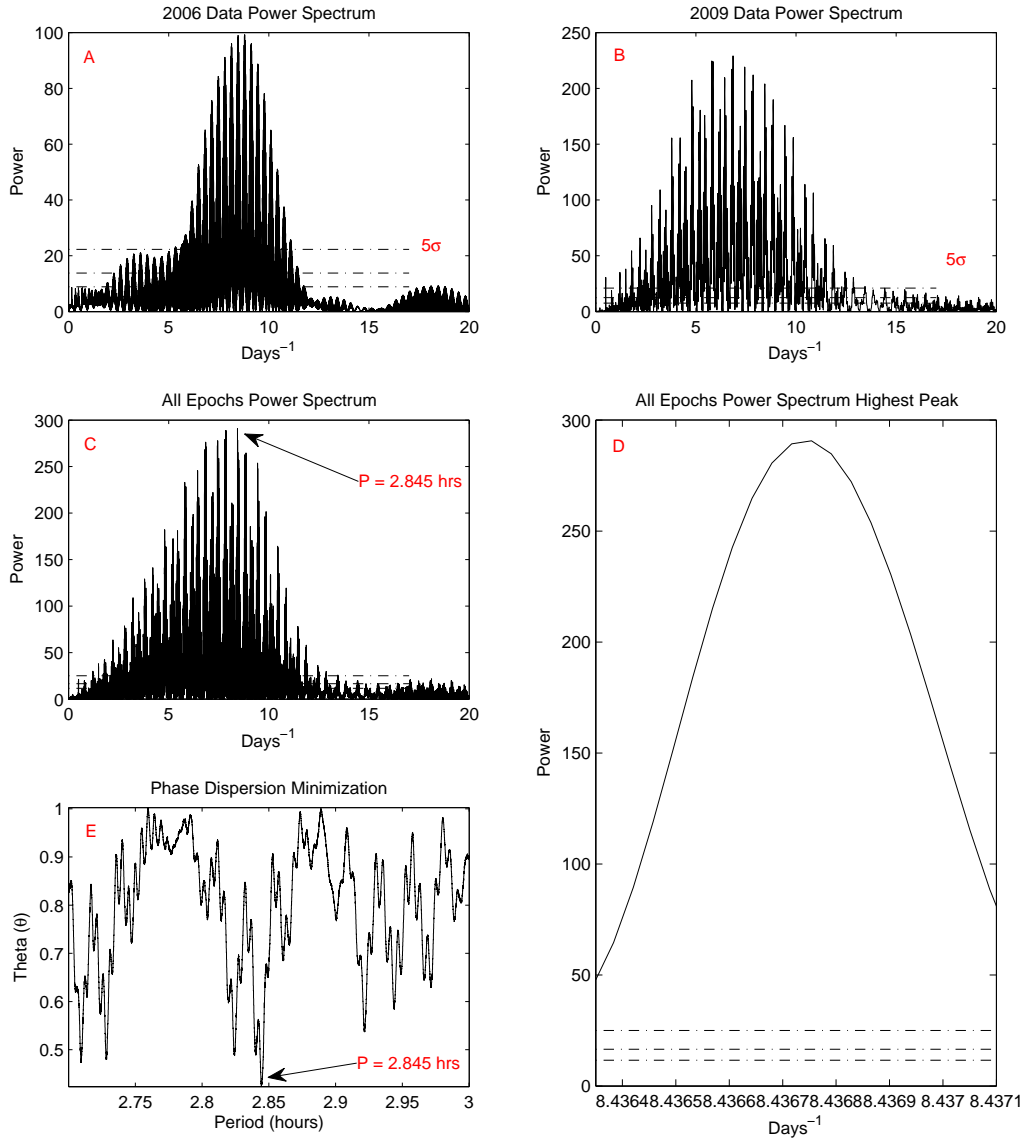


Figure 4.8: LSR J1835+3259: [Figures A - D] Lomb-Scargle Periodograms analysis. *Figure A* shows a periodogram for LSR J1835 for the entire 2006 epoch. We include a dashed-dotted line on each plot which represents a 5 σ false-alarm probability of the peaks as determined by the Lomb-Scargle algorithm in each case. Similarly, *Figures B - D* are the 2009 epochs, all of the epochs together, and the highest peak in the periodogram of *C*. We show the detected period of 2.845 ± 0.003 hours, detected as the highest peak in the periodogram (*Figure D*). *Figure E* shows the Phase Dispersion Minimization plot of all of the LSR J1835 data - period against the ‘Theta’ (θ) statistic (10^4 Monte-Carlo simulations).

periodicity to stellar rotation in this case. The arrows shown in June 13 & June 16 mark data gaps due to this object's passing too close to the zenith for the telescope's Alt-Az tracking. Once again we show a reference star lightcurve (bottom right) to illustrate the variability of the target with respect to a non-variable source. Although we have a ~ 3 year baseline, we do not achieve an accurate enough period to phase connect the 2006 and 2009 epochs. The statistical analysis for LSR J1835 is shown in Figure 4.8, where as before, we include the LS periodogram and PDM plots, and mark the detected period of 2.845 hours.

4.5.2.2 TVLM 513-46546 (M9)

We confirm consistent, stable sinusoidal periodic variability of 1.95958 ± 0.00005 hours, with σ_{tar} of $\sim 0.41\%$ in VATT I-band and $\sim 0.47\%$ in Sloan i' . The morphology and amplitude of the lightcurves are generally consistent for both wavebands throughout the campaign, with a mean σ_{ref} of I: $\sim 0.34\%$ and i' : $\sim 0.36\%$ - we show the variations in amplitude in Table 4.5. This period once again supports previous studies from Hallinan et al. (2006, 2007), Lane et al. (2007), Berger et al. (2008a) and Littlefair et al. (2008), and a clear indication that the photometric I-band periodic variability appears to be stable over time-scales of up to 5 years in this case. It is also consistent with the radius, $v \sin i$ and inclination angle estimates outlined in Hallinan et al. (2008). The calculated σ_{tar} in I-band is in broad agreement with the amplitude variability reported by Lane et al. (2007). However, the i' variability is much higher than that observed by Littlefair et al. (2008), who detect σ_{tar} of only $\sim 0.15\%$ in their data. Lightcurves from each of the six epochs are shown in Figure 4.9 and the LS and PDM analysis is shown in Figure 4.10. In Chapter 5, Figure 5.1 and Figure 5.1, we show phase connected lightcurves over the 5 year baseline in order to investigate the target's phase stability - this study directly investigates the positional stability of the stellar feature responsible for the periodicity. Phase connecting the total baseline of TVLM 513 allowed us to establish a period accuracy much greater than one limited by the minimum time intervals between data points, which we calculate to be ± 0.00005 hours.

This confirmed period greatly constrains the period of ~ 1.96 hours reported by Lane et al. (2007) in I-band, and the period of ~ 2 hours reported by Littlefair et al. (2008) in g' and i' . As always, a randomly selected reference star lightcurve is included and shown as the bottom right plot of Figure 4.9, which was one of the many used in the differential photometric calculation. This level of stability in the phase of this M9 dwarf was remarkable, considering the active nature of such an object. We consider this further in the next chapter.

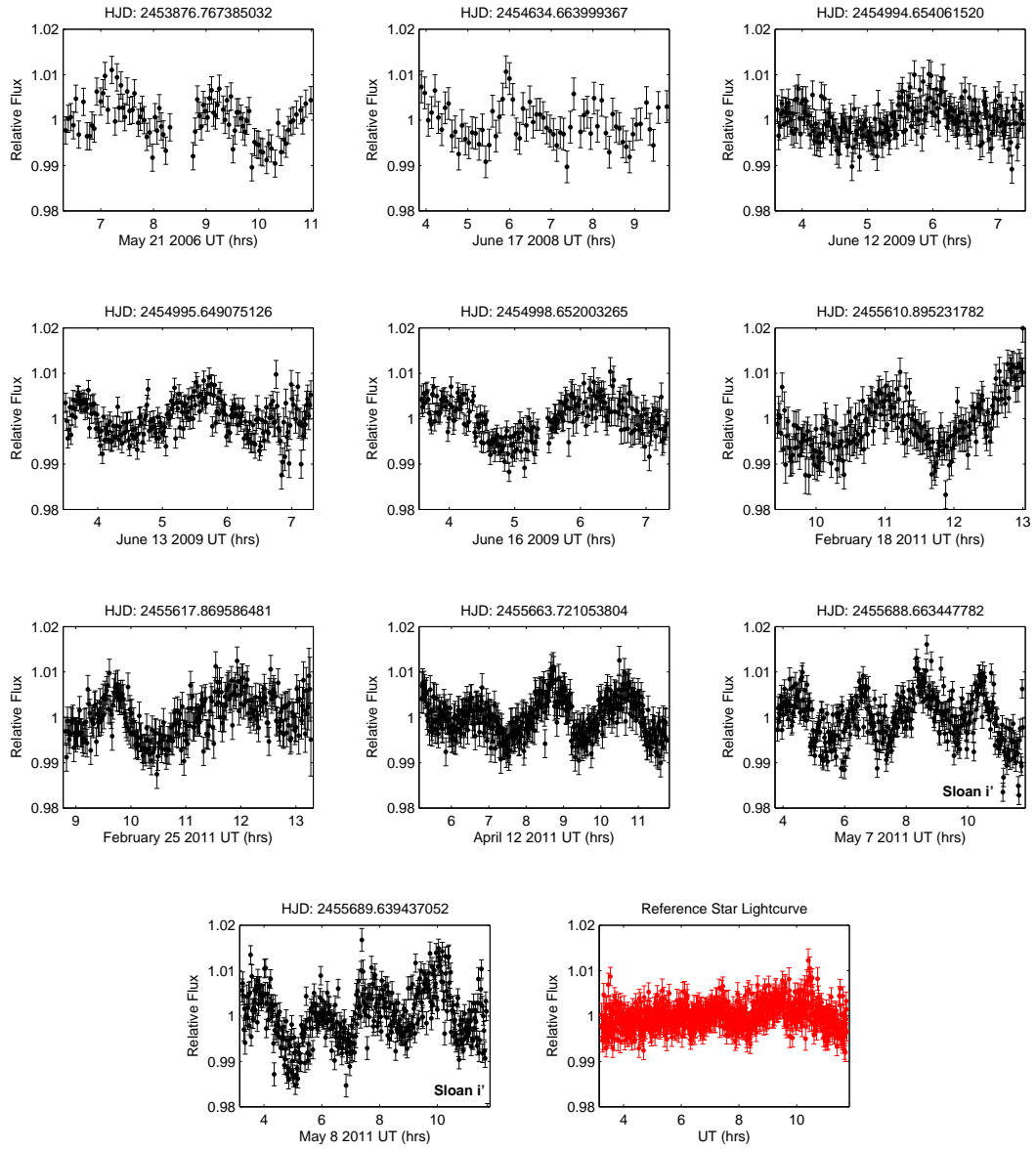


Figure 4.9: TVLM 513-46546: We obtained ~ 53 hours of data, over a ~ 5 year baseline for TVLM 513. Our data shows an extremely stable period of 1.95958 ± 0.00005 hours, which we phase connect over this baseline. The data shown here was taken in I-band ($\sim 7000 - 11000 \text{ \AA}$) and Sloan i' ($\sim 6500 - 9500 \text{ \AA}$), which is marked on the relevant lightcurves (May 7 & May 8 2011 UT).

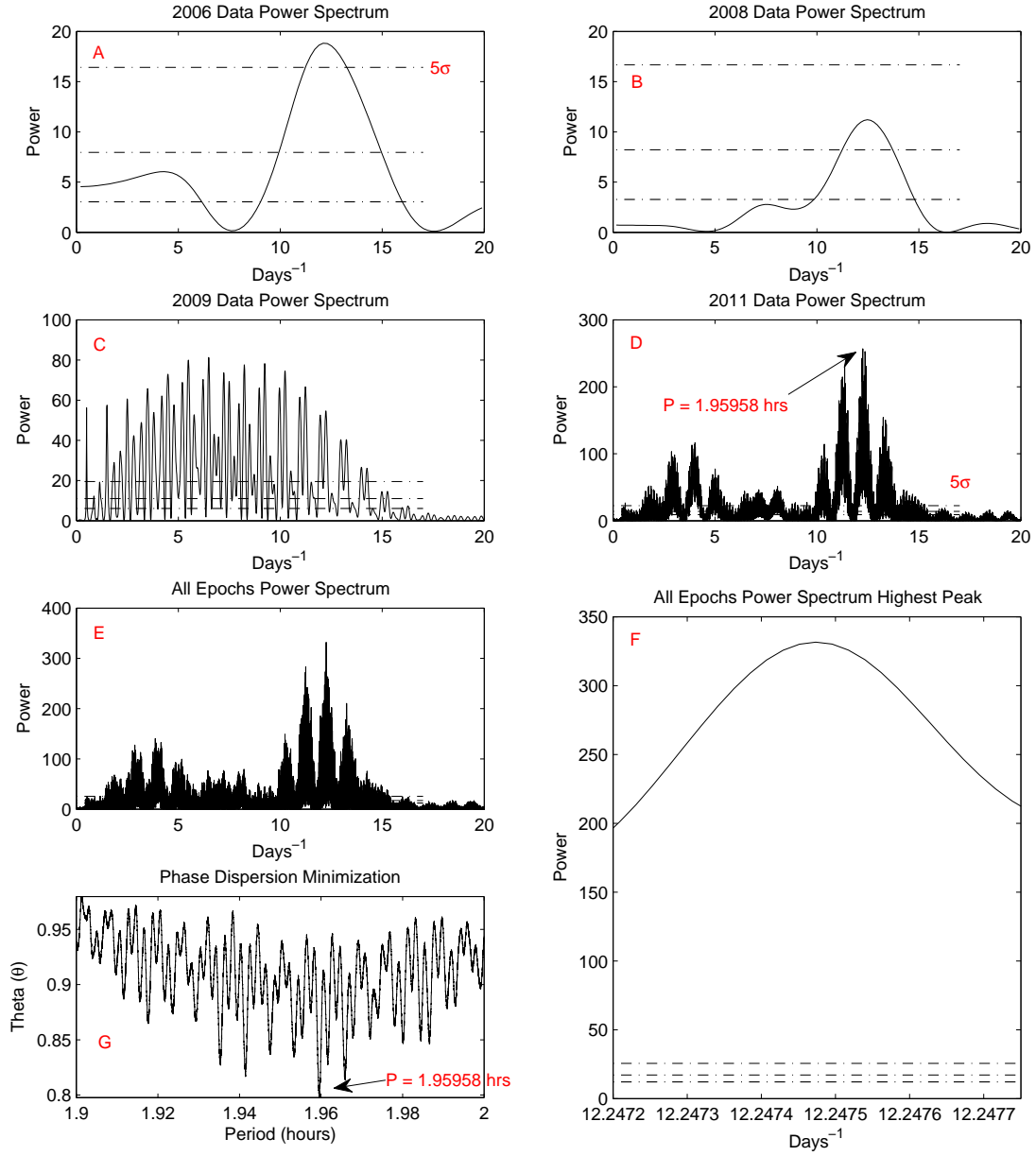


Figure 4.10: TVLM 513-46546: [Figures A - F] Lomb-Scargle Periodograms analysis. *Figure A* shows a periodogram for the M9 dwarf for the entire 2006 epoch. The dashed-dotted line on each plot which represents a 5σ false-alarm probability. *Figures B - F* are the 2008, 2009 and 2011 epochs, as well as all of the epochs together, and the highest peak in the periodogram of *E*. We show the detected period of 1.95958 ± 0.0005 hours, detected as the highest peak in the periodogram (*Figure F*). *Figure G* shows the Phase Dispersion Minimization plot of the entire ~ 5 year baseline, where we plot period against the ‘Theta’ (θ) statistic. As before, this statistic was determined by 10^4 Monte-Carlo simulations.

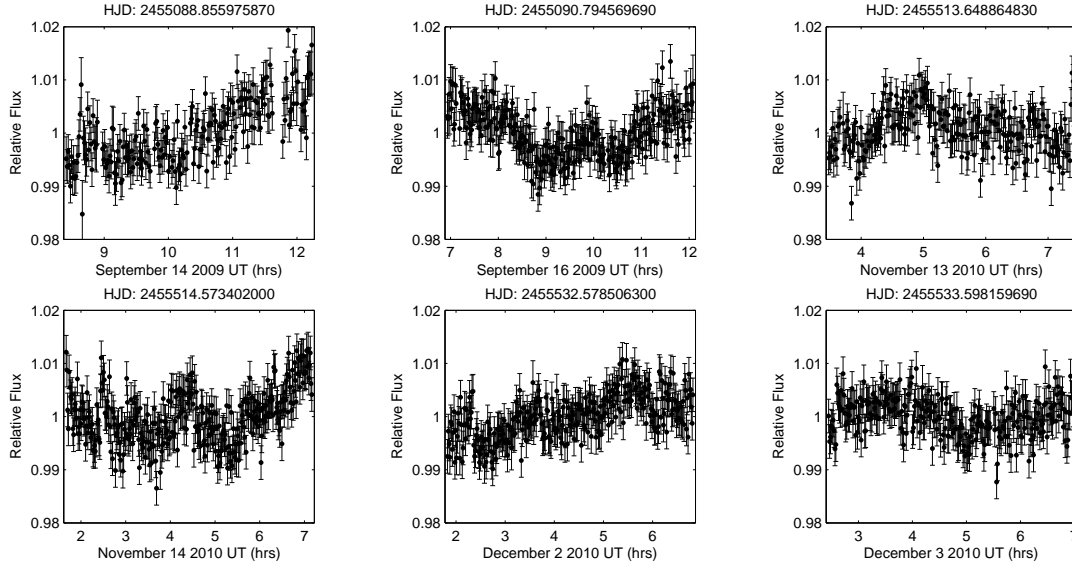
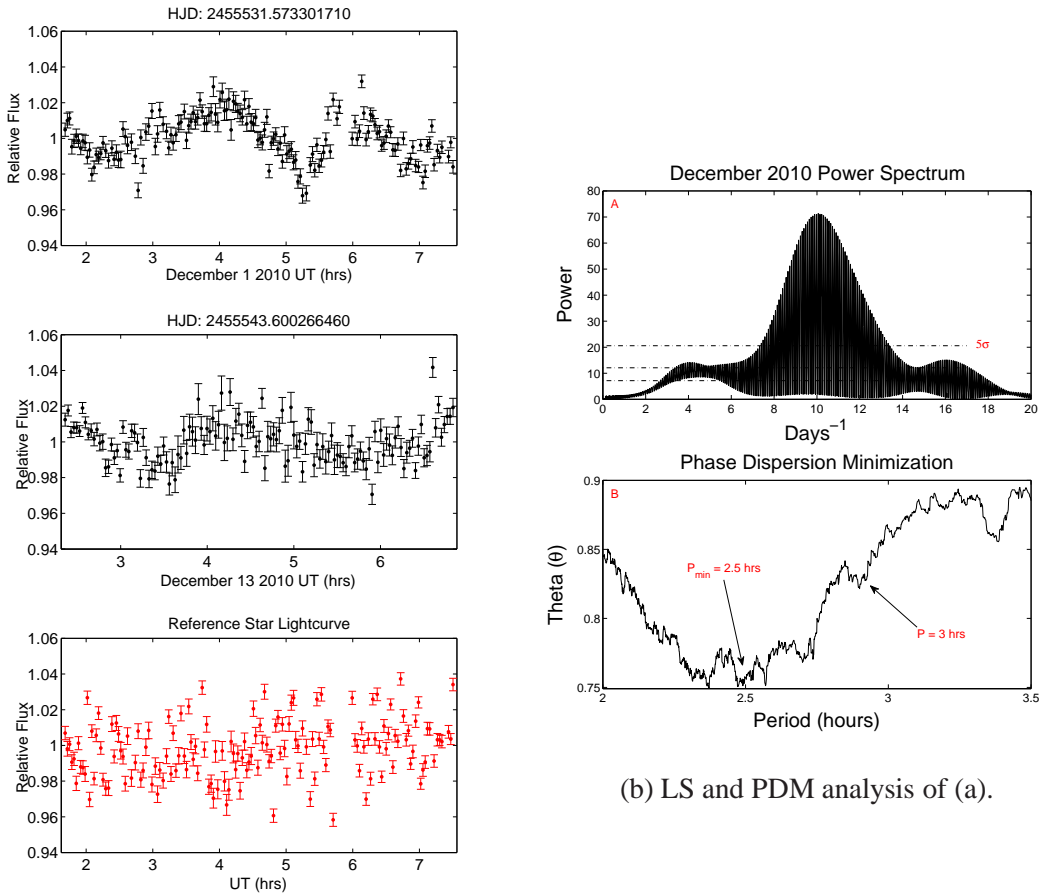


Figure 4.11: BRI 0021-0214: We observed BRI 0021 for a total of 6 nights, over 3 separate epochs. We selected a single reference star based on the basis of its stability which was assessed by Martín et al. (2001). We report aperiodic variability for BRI 0021, with amplitude variations of $\sim 0.46\%$. Although the periodograms show favorable evidence for a period of ~ 5 hours, we take this only as a tentative estimate due to the behavior observed in the lightcurves above; i.e. we could not constrain one likely solution for all epochs without imposing large errors.

4.5.2.3 BRI 0021-0214 (M9.5)

We report photometric VATT I-band aperiodic variability with mean σ_{tar} of $\sim 0.46\%$, and σ_{ref} of $\sim 0.37\%$, which is shown in Figure 4.11. We note that due to $\sim 3' \times 3'$ FOV of GUFI, there was only one suitable reference star used for differential photometry. This star was selected as a suitable candidate on the basis of its observed stability compared to the target star, during the I-band observations of BRI 0021 by Martín et al. (2001). They identify possible periodicity of ~ 20 hours and ~ 4.8 hours, respectively. We do not have sufficient temporal coverage to effectively assess the presence of a ~ 20 hour period. Although there is evidence in our statistical analysis of periods between 4 - 7 hours, we observe substantial aperiodic variations throughout our observations. Upon closer inspection of these possible periodic solutions, we do not observe one definitive solution for a given epoch. Since we only have one reference star as a comparison source ($00^h 24^m 23^s.735, -01^\circ 59' 06.27''$), which cannot be independently assessed in this case, we report aperiodic variations with possible periodic variability. Interestingly, these solutions of $\sim 4 - 7$ hours, are in violation



(a) Photometric results of 2MASS J0036+18.

Figure 4.12: 2MASS J0036+18: (a) We report a period of 3.0 ± 0.7 hours for 2M J0036. Unfortunately, both nights of observation were subject to poor weather conditions (heavy cloud). Nevertheless, our range of periods are in agreement with the observations of Lane et al. (2007), who detect a ~ 3 hour period for this source in the Johnson I-band. Berger et al. (2005); Hallinan et al. (2008) showed this dwarf to be radio pulsing with a period of 3.08 ± 0.05 hours. We note that the lightcurves above were binned to 2 minute frames in order to increase the SNR. (b) The LS periodogram and PDM analysis. Since the weather was so poor, the LS gives a broad range of likely periods, as does the PDM. Since we had the period of rotation from previous work (Lane et al., 2007), we identified the correct solution within our calculated errors.

with the current $v \sin i$ estimates of $\sim 34 \text{ km s}^{-1}$ found by Mohanty & Basri (2003) - which indicate a maximum period for this system of ~ 3.59 hours. Indeed, a periodic signal present and greater than this estimate, could be an indication that the radius of the star has been underestimated. Further observations, with greater coverage on a given night are needed to constrain and qualitatively confirm this result.

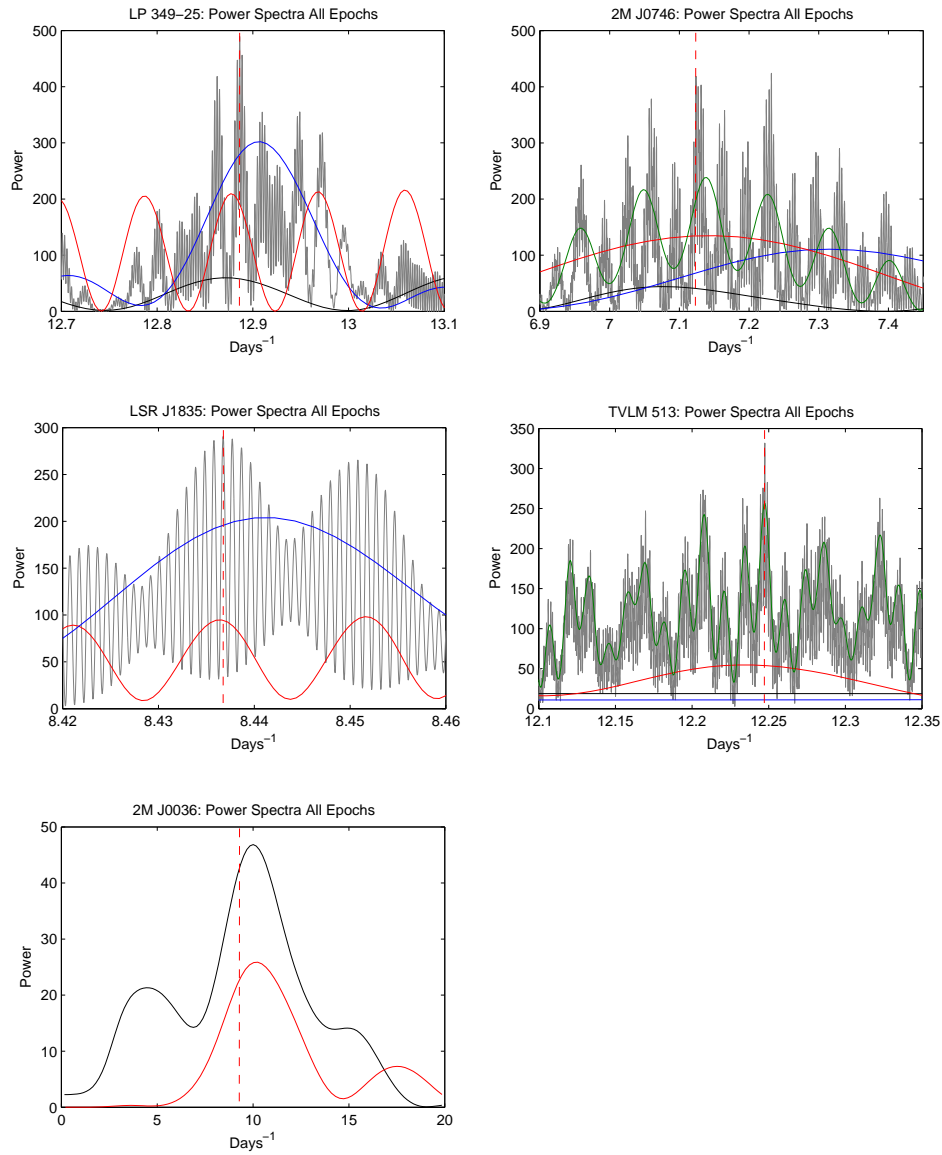


Figure 4.13: **SUMMARY OF SAMPLE STATISTICS:** Lomb-Scargle Periodograms for all periodically detected sources. Each figure shows a periodogram plot for all epochs of each target (grey), as well as periodograms for individual epochs over-plotted to illustrate period correlation between consecutive epochs. Details are as follows: [*LP 349-25*] Black - Sept 2009; Blue - Oct 2010; Red - Nov 2010. [*2M J0746*] Black - Jan 2009; Blue - Feb 2010; Red - Nov 2010; Green - Dec 2010. [*LSR J1835*] Red - 2006 data; Blue - 2009 data. [*TVLM 513*] Black - May 2006; Blue - June 2008; Red - June 2009; Green - 2011 data. [*2M J0036*] Black - Dec 1 2010; Red - Dec 13 2010. The x-axis (Days⁻¹) of each figure is scaled to the approx. period range as calculated by our uncertainty technique, with the exception of 2M J0036 where we show the full range of assessed values due to poorer temporal coverage. We also include a vertical red dashed line corresponding to the quoted period of rotation value.

4.5.2.4 2MASS J0036+18 (L3.5)

We find sinusoidal periodic variability of 3.0 ± 0.7 hours with σ_{tar} of $\sim 1.05\%$ in the optical I-band. However, these data were obtained under extremely poor seeing conditions on both nights of observation. All the same, the range of periods within the calculated error matches the ~ 3 hour periodicity found by the photometric measurements of Lane et al. (2007) and the radio measurements of Berger et al. (2005) and Hallinan et al. (2008). The observed σ_{tar} is larger than that of other I-band data in this work. This is discussed in Section 4.6. We show the differential lightcurves in Figure 4.12, and the analysis of these in Figure 4.12b.

4.6 Source of the Periodicity

In the sample of M8 - L3.5 ultracool dwarfs in this work, where periodic variability was observed, the periodicity has generally been in the form of quasi-sinusoidal modulation, consistent with stellar rotational modulation associated with a surface or atmospheric feature. The sample of ultracool dwarfs in this paper somewhat differs from a large number of previous studies, since these here are all radio detected sources. Hallinan et al. (2007), Hallinan et al. (2008) and Berger et al. (2009) also attribute the observed periodic pulses of radio emission in their work to stellar rotation. We outline three scenarios when considering both the radio emission and optical periodicity in the general case, and then consider if any are applicable in the case of the data reported in this thesis. **Established:** The first is that the detected periodic variability is present in a large percentage of low mass objects, where the optical periodicity is unrelated to any reported radio activity. **Hypotheses:** The second is that there is some connection between the detected periodic variability and the periodic bursts of radio emission, but where the optical periodicity is not directly caused by whatever process is causing the radio detections. **Speculative:** The third is that there is a causal connection between the optical and radio emission, where the same magnetic process responsible for the periodic behavior at radio frequencies is somehow also responsible for the feature causing periodic variability at optical wavelengths.

We first consider a feature due to stellar magnetic activity. Previous studies at the M/L transition have argued that magnetic spots on the stellar surface were responsible for the detected periodic signals (Rockenfeller et al., 2006a; Lane et al., 2007). Rockenfeller et al. (2006a), for example, base this assumption (for magnetic *cool* spots) on model spectra of an M9 dwarf generated by the atmospheric modeling of Allard et al. (2001). Let us consider

the multi-color photometric properties of the lightcurves in this thesis, more specifically addressing the possible presence of a stellar hot or cool spot. Currently, our understanding of starspot temperatures, and thus contrast differences for photometric bands with respect to photospheric and spot temperature differences, is largely based on measurements obtained via modeling of brightness and color variations, Doppler imaging investigations, modeling of molecular bands and atomic LDRs, and so forth. In this work we have observed greater amplitude variations at shorter wavelengths for LP 349-25 (M8+M9; R-band vs. I-band) and LSR J1835 (M8.5; R-band vs. I-band), as shown in Table 4.5. Starspot contrast ratios become more difficult to evaluate for lower temperature objects - for example, studies have shown that the temperature difference between the spot and the surrounding photosphere can be ~ 2000 K for G0 stars, whereas this can fall to ~ 200 K for M4 dwarfs (Berdyugina, 2005). Indeed, Rockenfeller et al. (2006a) estimate a *cool* spot vs. photosphere temperature difference of ~ 100 K for an M9 dwarf in their sample via atmospheric modeling of Allard et al. (2001), which they based on high amplitude variability in G-band, variability to a lesser degree in R-band, and lesser again in I-band. These variability trends are consistent with the results of Littlefair et al. (2008) and with the results in this thesis, in that larger amplitude variability has been detected at shorter wavelengths in all cases. In recent work by Ballerini et al. (2012), they show a range of contrast coefficients as a result of the presence of a magnetic cool spot, by using optical and NIR data and synthetic stellar spectra (see Ballerini et al. (2012)). They infer that spot contrast is larger in blue band-passes for cool stars (M dwarfs), perhaps due to the increasing presence of molecular bands in the IR, which supports the Rockenfeller et al. (2006a) modeling results of an M9 dwarf, mentioned above. Thus, these studies provide evidence that starspots with cooler temperatures than the photosphere can cause larger amplitude variability at shorter wavelengths.

However, in addition to the presence of magnetic cool spots, areas of increased temperature (hotter than the surrounding photosphere) can also manifest themselves at various layers of a star. For example, faculae are bright regions in the stellar photosphere that surround cool spots. Their contrast is generally observed to change from center-to-limb, where their brightness depends on their size and wavelength. In addition to these, photospheric (or chromospheric) hot spots can also be present, and are primarily detected in white light. Most interestingly however, a reduction in their contrast with respect to an unchanging photosphere is expected in the NIR (Solanki & Unruh, 1998; Fröhlich & Lean, 2004), since contrast will depend on λ^{-1} (Chapman & McGuire, 1977). Could another mechanism be responsible for such hot spots in ultracool dwarfs? The confirmation of the ECM as the dominant source of bursting radio emission in these objects was a significant

alternative to broadband incoherent gyrosynchrotron radiation usually thought to be responsible for radio emission in cool stars (Hallinan et al., 2007, 2008; Berger et al., 2009). More recently, Hallinan et al. (2012) demonstrate that the optical and radio emissions are produced by the same population of electrons in the magnetosphere of the late-M dwarf TVLM 513, and may be *auroral* in nature. By considering this model for radio detected ultracool dwarfs, they highlight an intriguing scenario, whereby the possibility exists that the mechanism responsible for the optical and radio periodicities are no longer mutually exclusive. In fact, the detected ECM emission at 4 and 8 GHz frequencies in their work suggests that such a process in ultracool dwarfs is analogous to the coherent radio emission observed by Zarka (1998), from the magnetized planets of our solar system. Since ECM emission has now been shown to operate effectively in *all* radio pulsing dwarfs, it is possible that this mechanism has the ability to provide a sustained bombardment of energy to the stellar surface. These areas could manifest themselves as auroral hot spots, induced by localized heating due to the downward propagating electron beam. So, in contrast to the cool spot scenario outlined above, the higher degree of variability at R-band wavelengths rather than at I-band wavelengths for example, could also support a hot spot in the photosphere, or in the chromosphere. This distinction is most challenging, since the spectrum of a cool spot vs. a hot spot have strong similarities, and in the context of the photometric data presented in this thesis, we cannot definitively associate either feature as the sole cause of the periodic variability in our sample.

We also observe a higher level of variability in I-band for the L3.5 dwarf 2M J0036 than for our other targets. This dwarf's ~ 1900 K photosphere (Vrba et al., 2004) is ~ 200 - 300 K cooler than other late-M dwarfs in our study, and Lane et al. (2007) have previously attributed this periodicity to magnetic spots. Although a higher level of variability compared to other targets would suggest greater contrast between the spot and photosphere, the work mentioned above by (Berdyugina, 2005) provides some evidence that spot contrasts declines monotonically for cooler temperature objects. Perhaps the size of the spot is larger, or alternatively another mechanism could be aiding the level of variability. Our photometric data cannot provide any insight in to these possibilities; however we can conclusively report a higher degree of variability for the coolest object in our sample.

Atmospheric dust must also be considered for other dwarfs at M/L transitional temperatures, since L dwarf atmospheres become increasingly cool and neutral, harboring higher levels of dust opacities. Over the course of each dwarf's observation baseline (spanning M8 - L3.5), we observed a range of amplitude variabilities in the photometric lightcurves. Therefore the temperature contrast, and relative areas, between the stellar photosphere and

the feature responsible for the periodicity must be changing to the levels of variability reported here (Table 4.5). In the case of TVLM 513, Littlefair et al. (2008) is in disagreement with the star spot explanation, instead supporting areas of sustained photospheric dust to account for the periodic variability. Indeed, there is no clear evidence thus far that refutes dust as a feature that could cause this periodicity - or even the long-lived, highly correlated period variability reported in this work. The dynamics of ultracool dwarf atmospheres are not yet completely understood; however Allard et al. (2001) have highlighted that one could expect quite dynamic atmospheric conditions due to convection and rotation. Perhaps for this class of object, the distribution of such clouds of dust would require little turbulence in the associated regions to account for the stability of phase reported here? This line of thought would not be consistent with the stability of the great red spot of Jupiter, which is stable despite the presence of turbulent surroundings in the regions of the Jovian atmosphere (Vasavada & Showman, 2005). Moreover, although the spectrum of TVLM 513 covered by the I-band and Sloan i' band is dominated by molecular absorption, its effective temperature of ~ 2200 K is still quite hot for bands such as TiO and VO to condense and form dust grains. This transition roughly occurs at ~ 2000 K, which would suggest a relatively dust-free photosphere in this case, or perhaps an environment that is unlikely to be dominated by dust. We discuss this target in more detail in the following chapter.

Although we did not achieve accurate enough periods to phase connect all epochs for every other target in the sample, the periods recovered for each target were stable throughout individual epochs, which ranged from weeks to years. In the context of our data, we point out the following:

1. *Pulsing Dwarfs:* We recover the same period of rotation as that reported in previous radio observations, with the exception of the binary 2M J0746 - where we detect the other binary component to that producing the radio emission (discussion to follow in #4). Thus, since all of these targets exhibited radio emission, it is possible that periodic optical variability could be ubiquitous in radio pulsing dwarfs, due to the presence of high-strength kG magnetic fields and consequently the presence of magnetically-induced surface features, such as hot or cool spots. Nevertheless, we cannot discount the presence of dust grains in these regions, especially at cooler temperatures (< 2000 K). Metal hydrides, alkali lines, CO and H₂O absorption lines and dust opacity all become prominent at temperatures < 2000 K. Therefore dust grains could contribute to some aperiodic variations or indeed periodic variability if present on timescales longer than a given observation.

2. *Changes in Amplitude*: As shown in Table 4.5, all targets exhibit changes in amplitude over the course of observation epochs spanning years in some cases. Furthermore, the lightcurve morphology changes quite significantly. These characteristics are not consistent with a stable surface feature. Although it is evident that the feature responsible is not subject to stochastic behavior on a large-scale, the evidence presented here showing changes in amplitude in addition to some aperiodic variability amongst the periodic signals suggests that the thermal conditions are changing to the levels shown in Table 4.5. However, based on the detected periods of rotation in our work, the lightcurves are in phase from night to night within epochs, for all targets (and over the full baseline for TVLM 513). As outlined in #5, this is perhaps evidence that the feature is not moving over these timescales.

3. *LP 349-25*: Although the observed optical periodicity for LP 349-25 does not have supporting data containing radio pulses, it was detected as a relatively strong source of radio emission by Phan-Bao et al. (2007). Therefore magnetic processes are clearly present in this dwarf's magnetosphere, and as outlined above, perhaps the magnetic field alignment of the binary with respect to their spin axes and thus the observer's line of sight, is preventing such a detection where the radio emission is being beamed away.

4. *2MASS J0746+2000AB*: Strong considerations must be given as to why we do not observe optical photometric periodic variability from the radio detected binary component, 2M J0746B ($v \sin i = 33 \text{ km s}^{-1}$) (Berger et al., 2009), or why the slower component, 2M J0746A ($v \sin i = 19 \text{ km s}^{-1}$), does not exhibit radio emission. Indeed, in addition to the periodic bursts of radio emission of 2.07 ± 0.002 hours, Berger et al. (2009) also detected periodic $H\alpha$ emission from 2M J0746B to the same period - signally an active chromosphere. Yet we find periodic variability from the other component. According to model-derived temperature estimates of Konopacky et al. (2010), 2M J0746A has a $T_{eff} \sim 2205 \pm 50 \text{ K}$, whereas 2M J0746B is cooler at $T_{eff} \sim 2060 \pm 70 \text{ K}$. Since our photometry contains the combined flux of both stars, 2M J0746A could be more prominent as a result. If the optical and radio emission are inextricably linked as we put forward as a possibility, why also do we not also observe radio emission from the optically periodic source 2M J0746A? Perhaps the component we detect at optical wavelengths is in fact pulsing at radio frequencies, but is undetectable due to the inclination angle of the system. However, if the binary rotation axes are orthogonally aligned with respect to the system orbital plane as expected (Hale, 1994), and furthermore since the faster component was detected by Berger et al. (2009), the inferred alignment geometry should support detectable beaming from both

stars. This of course assumes that the magnetic field alignment of each member is the same with respect to their rotation axes, which may not be the case. Such a misalignment could mean that the radio emission from 2M J0746A is being beamed away from observer. Alternatively, unlike 2M J0746B, it is also possible that 2M J0746A does not exhibit beamed ECM emission at all, but perhaps only small levels of quiescent radio emission that has not yet been detected by previous studies of the system. The Lomb-Scargle periodogram analysis in this work should extract both signals if they are both present and strong enough, and our data shows strong evidence of variability of the non-radio emitting component. Some aperiodic variability is also present for some observations (e.g. 2009 January 26 & 2010 December 13) - perhaps the second member is effecting the primary periodic signal, or some other photospheric feature could be responsible. Indeed, this is evidence against our discussion of optical variability being ubiquitous in all radio detected sources. However we note that our radio detected sample provides only small statistics for such a claim. Resolved photometry would be an interesting confirmation if the radio-active source is in fact also optically variable.

5. *TVLM 513-46546*: The periodic quasi-sinusoidal variations are in-phase over a ~ 5 year baseline. This suggests that the feature responsible for the optical periodicity is *not moving* and is therefore being generated and sustained by some means within the dwarf's photosphere, or perhaps in the chromosphere if a hot spot outlined above exists. It is interesting that Littlefair et al. (2008) detected much smaller amplitude variations in Sloan i' , in addition to an anti-correlated signal in Sloan g' ; this certainly does not follow the consistency and phase stability we have observed over our ~ 5 year observation baseline, albeit we do have g' data in our work for comparison. We discuss the possibility of an auroral hot spot in the following chapter.

It seems quite possible that either magnetic spots and/or dust could be responsible for periodic variability over a wide range of ultracool dwarf spectral classes. We have also shown that for larger amplitudes in R-band vs. I-band, the variability is perhaps consistent with a hot spot, but not that it cannot be a cool spot. This is an important distinction. Finally, based on the detection of variability for all radio-detected dwarfs in our sample (with one exception outlined above), as well as the recent results of Hallinan et al. (2012), we likely have a case which supports optical variability that is associated in some way with the reported radio emission, and thus is expected to be present in all radio active ultracool dwarfs.

4.7 Summary

We have reported on optical photometric observations of six ultracool dwarfs spanning the \sim M8 - L3.5 spectral range. We detect periodic variability for three of these dwarfs for the first time. Lane et al. (2007) presented a period of rotation for TVLM 513 of \sim 1.96 hours, as well as a period of \sim 3 hours for 2M J0036. We confirm these values in our data and further constrain the period of TVLM 513 to 1.95958 ± 0.00005 hours. We found the M8.5 dwarf LSR J1835 to exhibit I-band periodic modulation of 2.845 ± 0.003 hours, a periodicity that has been established over three separate epochs, from 2006 - 2009. A single R-band observation under poor weather conditions yielded a period of \sim 3 hours for LSR J1835, with higher amplitude variations than that of the I-band observations. Similarly to TVLM 513 and 2M J0036, the optical periodic signals for LSR J1835 are consistent with the radio pulses detected by Hallinan et al. (2007, 2008); Berger et al. (2009), which they argue is due to the rotation of the dwarf.

In the case of the tight binary dwarfs, we present I-band periodic sinusoidal variability of 1.86 ± 0.02 hours and $\sim 3.36 \pm 0.12$ hours for LP 349-25 and 2M J0746A, respectively. We also obtained R-band observations of LP 349-25 and found the same periodic behavior; like LSR J1835, these signals were varying at higher amplitudes than in I-band. We present these data as the first periodically modulated detection from one component of the system - likely LP 349-25B. In addition to this, LP 349-25B exhibits unusual behavior over this campaign, where we observe large changing levels of amplitude and phase shifts. Although we have not completely ruled out the potential presence of the other source, our investigation yields the likely cause of this behavior to be aperiodic variations of a single periodic source. However this morphology could also signal the presence of a dynamic environment where the source region is evolving on these timescales. We find a most intriguing result in the case of 2M J0746. This binary dwarf was observed by Berger et al. (2009) to exhibit periodic radio pulses with a period of 2.07 ± 0.002 hours. However, we report the non-radio detected component to be periodically varying in optical bands with a period of 3.36 ± 0.12 hours, which we infer to be 2M J0746A.

We investigate potential sources of the periodicity, including magnetic cool spots, the presence of photospheric dust, and an alternative explanation related to the previously discovered periodic radio emission. Although we observe stable rotation periods for each target's observation baseline, we cannot discount any of the features above as the sole cause or contributor to this periodicity.

“You can know the name of a bird in all the languages of the world, but when you’re finished, you’ll know absolutely nothing whatever about the bird ... So let’s look at the bird and see what its doing – that’s what counts. I learned very early the difference between knowing the name of something, and knowing something.”

Richard Feynman

“Don’t worry about people stealing an idea. If it’s original, you will have to ram it down their throats!”

Howard Aiken

5

The Phase and Amplitude Stability of TVLM 513-46546

5.1 Introduction

Although some ultracool dwarfs have shown consistent periodic behavior over a number of observations (e.g. Berger et al. (2005); Hallinan et al. (2006, 2007); Lane et al. (2007); Hallinan et al. (2008)), here we investigate whether this stability is long term and stable in phase for the M9 dwarf TVLM 513, and whether this modulation evolves morphologically over these timescales. We achieve an accurate enough period of rotation of 1.95958 hours for the M9 dwarf to phase connect the entire 2006 - 2011 baseline, with an associated error in the period of 0.00005 hours, thereby allowing us to assess its modulated behavior over ~ 5 years. We find long-term, periodic variability which is stable in phase over this time frame. The level of amplitude variability is shown in Chapter 4, Table 4.5, however we discuss this further in this chapter.

The observations of TVLM 513 in this thesis were part of a much larger campaign (Hallinan et al., 2012), which sought to investigate the correlation of periodic variability across many parts of the electromagnetic spectrum. These data are thus the photometric component of this study, which were taken in the Sloan i' and Johnson I wavebands, as shown in Chapter 4. The discovery of periodic radio bursts (Hallinan et al., 2007, 2008), in addition to photometric and spectroscopic periodic variability of ultracool dwarfs (Lane et al., 2007; Berger et al., 2008a) prompted this more detailed investigation. In this chapter, we make a clear distinction between: 1) the work solely carried out by the author: § 5.2

- § 5.3, and 2) the larger campaign carried out by Hallinan et al. (2012) that utilized the TVLM 513 data in this thesis: § 5.4. We note that all of the spectroscopic data (and some photometric data) toward the end of this chapter, are accredited to Hallinan et al. (2012) - which we include for the astrophysical completeness of this work, but more importantly to illustrate the high level of agreement of the GUFi data to these other observations. We will reference these figures accordingly in the following sections.

The chapter is structured as follows: § 5.2 - § 5.3 are a continuation of the results for TVLM 513 presented in Chapter 4, and therefore show results from our investigation in to the phase and amplitude stability of the dwarf. In addition to this, we show some of the techniques used in an attempt to statistically assess the highly correlated nature of the emissions in § 5.3. Finally, we include a short discussion on the results of the Hallinan et al. (2012) campaign which have confirmed auroral emissions for this particular object, in § 5.4. These results are the astrophysical implications of the observed correlation between radio, spectroscopic and photometric wavelengths. For an indepth discussion of all radio and spectroscopic observations, we refer the reader to Hallinan et al. (2012), who have conceived the aurorae hypothesis and are soon due to publish these extraordinary results.

5.2 Phase Connecting and Amplitude Analysis of Datasets

5.2.1 Phase Connecting the 5 Year Baseline

In this section, we use the phase connection techniques explained in Chapter 3, § 3.2.5. Based on these methods, we plot two figures - Figure 5.1 and Figure 5.2, which illustrate the level of stability in phase of TVLM 513 over the ~ 5 year baseline. Lightcurves in each case were selected at random from each of the four epochs in order to investigate this correlation. Indeed, this level of agreement is consistent throughout all target epochs. In each case in Figure 5.1, and in *PLOT 1* of Figure 5.2, lightcurve time stamps were phase folded to the detected period of 1.95958 hours. We sought to illustrate this correlation further in *PLOTS 2 - 5* in Figure 5.2, where we overplot a model sinusoidal signal (red), with the same period of 1.95958 hours, and most importantly - a *fixed* phase solution. It is clear that this dwarf exhibits highly correlated behavior in terms of phase over this baseline, and thus, the stellar feature responsible for such behavior, must exist as a feature equally as stable during these observations. Data were phase folded in *PLOTS 6* and *7* in the same figure. Although it is clear from visually plotting the fixed-phase model to the data, in addition to strong agreement of the phase folded lightcurves, we sought to statistically

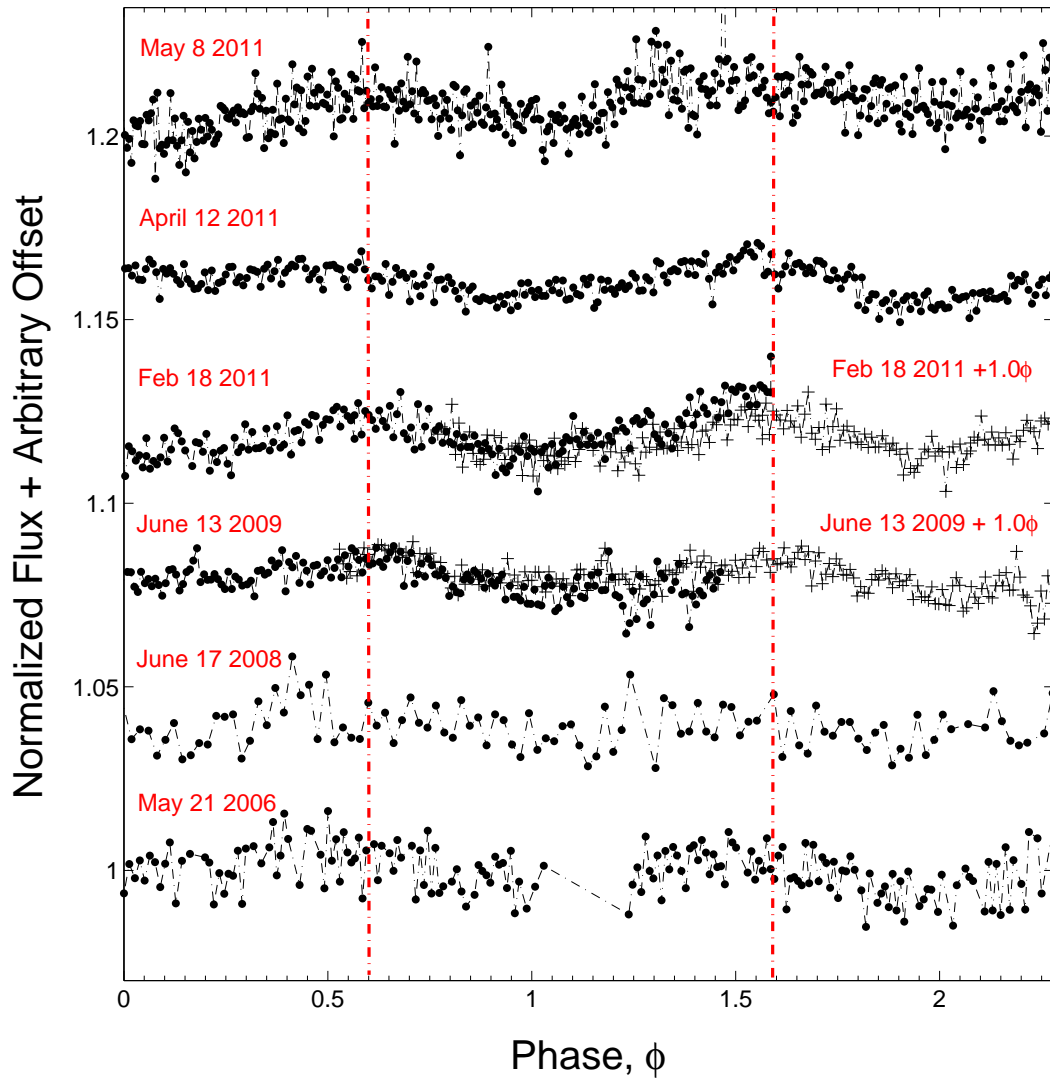


Figure 5.1: This figure illustrates the correlated behavior of TVLM 513 over the ~ 5 year baseline, specifically for the optical photometric data. These raw lightcurves, labeled with the corresponding UT dates, were included in order to assess the correlation of the peak of each lightcurve. We selected lightcurves in this figure from the 2006, 2008, 2009 and 2011 epochs, as shown. This level of agreement is consistent for all lightcurves in the sample. In each case, the time stamps were phase folded to the period of 1.95958 hours. We mark two vertical dash-dotted red lines, which highlight the correlation of the center of each lightcurve peak. We note that the June 13 2009 and February 18 2011 epochs had shorter baselines than the others. Therefore, for continuity on the figure, we plotted each lightcurve again and added a value of $+1.0\phi$ in each case, marked with crosses.

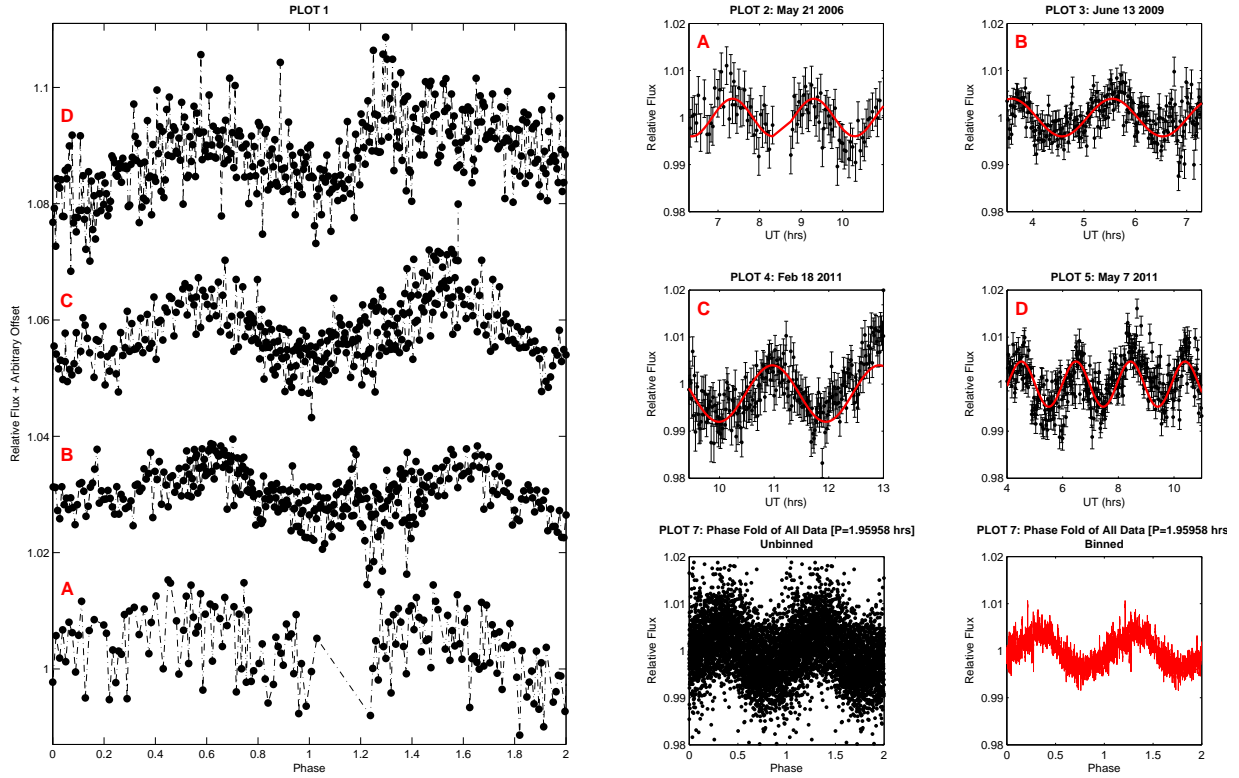


Figure 5.2: [PLOT 1]: This figure illustrates the correlated behavior of TVLM 513 over a ~ 5 year baseline. These raw lightcurves, labeled with red letters A - D (bottom - top), were selected at random from four of the observation epochs (May 2006 - May 2011). As before in each case, the time stamps were phase folded to the period of 1.95958 hours. [PLOTS 2 - 5]: To show this agreement further, the lightcurves A, B, C & D in PLOT 1 correspond to PLOTS 2, 3, 4 & 5, respectively. Each lightcurve contains an overplotted model sinusoidal signal (red), with a period of 1.95958 hours, and a *fixed* phase, which was applied to the full 2006 - 2011 dataset, where we set values between individual observations and epochs to zero. [PLOT 6 & PLOT 7]: We phase fold the entire data set (2006 - 2011, containing $\sim 3,500$ data points) to the detected period of 1.95958 hours. The black phase folded lightcurve in PLOT 6 is raw and has no binning or scaling. The red phase folded lightcurve in PLOT 7, once again of all data, has been binned by a factor of 10.

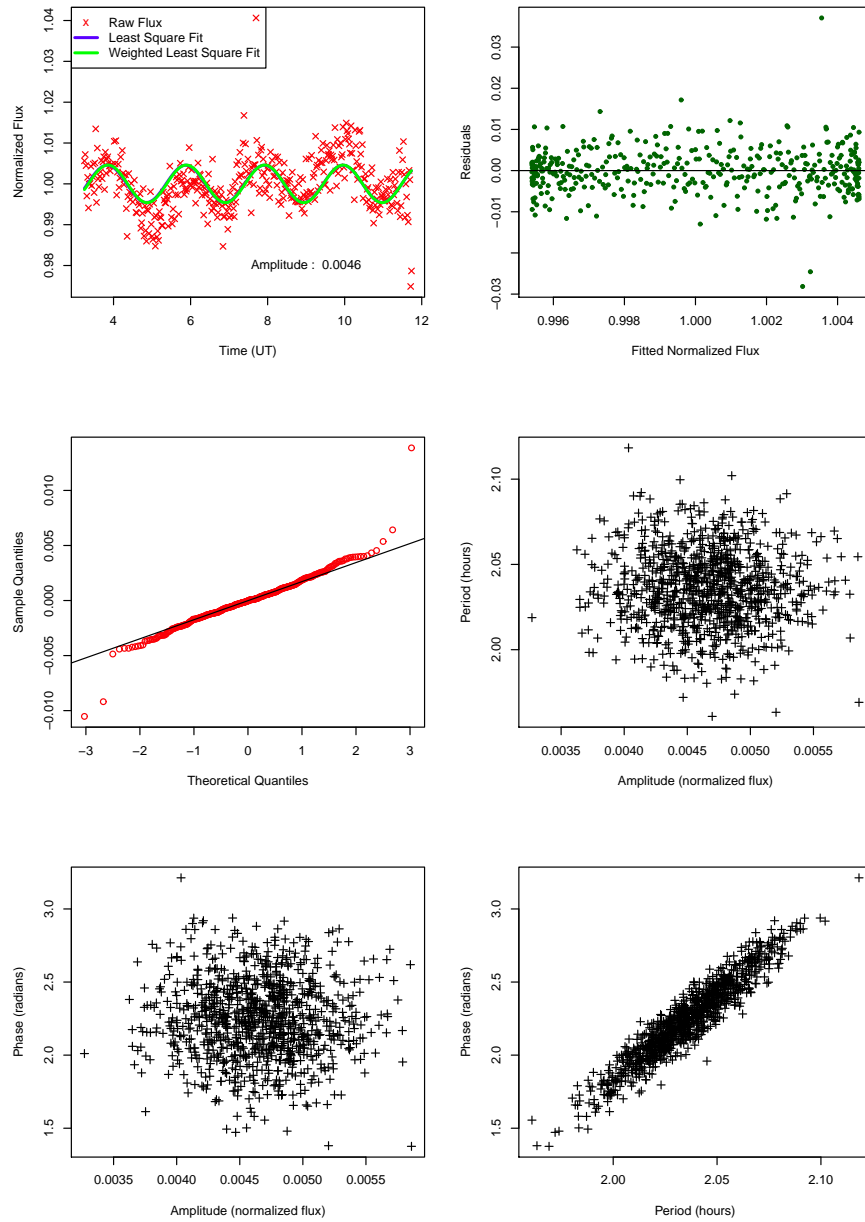


Figure 5.3: Amplitude Variability Analysis: *[TOP LEFT:]* Single night showing the raw flux of May 8 2011 UT. We have overplotted a LSF in blue and a weighted LSF in green. The green model takes errors in each data point into account. *[TOP RIGHT:]* Plot showing residuals from the model fit which validate the fitting. These points should be random as shown, and should not follow any pattern or linear trend. Such features would identify a source of systematic error in the fit. *[MIDDLE LEFT:]* Q-Q plot. This compares the distribution of standardized residuals with respect to a standard normal distribution (plotted as the 45 degree linear regression black line). The red points should lie on this line, where outliers shown here identify erroneous data points in the raw lightcurve; some examples are clearly evident at e.g. ~ 7.5 UT and ~ 11.8 UT. *[MIDDLE RIGHT:]* Distribution of period vs. amplitude carried out by the Bootstrap method. *[BOTTOM LEFT:]* Distribution of phase vs. amplitude carried out by the Bootstrap method. *[BOTTOM RIGHT:]* Distribution of phase vs. period carried out by the Bootstrap method.

investigate any possible phase jitter between the peaks of the lightcurves. We discuss this further in the following section.

5.2.2 Amplitude Analysis

We employ the techniques outlined in Chapter 3 and Chapter 4 to investigate the amplitude variability of TVLM 513, and show an example of this analysis for the May 8 2011 UT observation in Figure 5.3. As outlined in the previous chapter, the Bootstrapping technique was employed which outputs a *C.I.* of 95%, also providing an error in each amplitude value. Previously, we have discussed in great length the various mechanisms that could be responsible for the periodic variability, as well as the significance of the changes in amplitude. In the context of the larger Hallinan et al. (2012) campaign and specifically the author's contribution to this work, we consider the properties of the amplitude variations of TVLM 513 further in § 5.4.

5.3 Cross Correlation (XCF) Analysis

5.3.1 The XCF Function

The Cross Correlation Function (XCF) as described by Edelson & Krolik (1988), is a statistical measure of the correlation between two waveforms. We implemented this technique in an attempt to statistically quantify the difference in the peaks of two different observation nights, as a function of a time lag, τ . This was an effective way of assessing the morphology of the quasi-sinusoidal behavior of TVLM 513 at various epochs, to investigate by other means than a visual inspection, if the peaks of these waves were located at similar points for a known period. If so, this establishes the stability of the lightcurve's spatial peak position, and thus the stability of the feature causing the optical periodic variability - since we would expect the peak of each wave in the lightcurve to change over time if the feature responsible was also spatially changing over these timescales. We used the 'xcorr' function of Matlab, which provides an estimate of the correlation between two sets of data, a and b , as follows:

$$(a \cdot b) = \int_{-\infty}^{\infty} a^*(\tau) b(t + \tau) d\tau \quad (5.1)$$

where a^* is the complex conjugate of a .

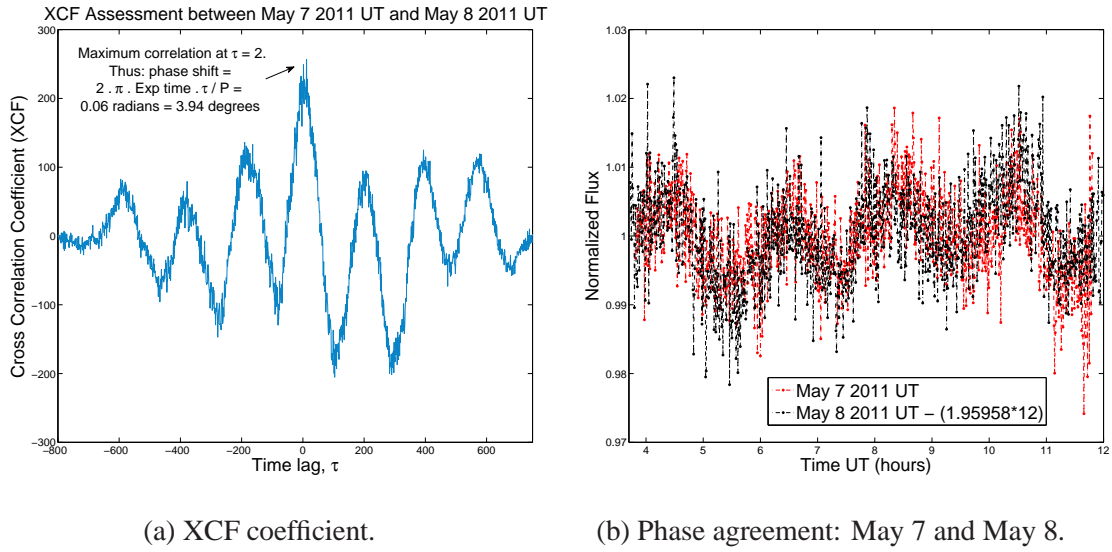


Figure 5.4: (a) Here we include a plot of the XCF between May 7 and May 8 2011 UT. In this case, the two lightcurves (shown in (b)) were phase folded to the period of 1.95958 hours. We then can calculate a time lag, τ , shown here to be 2 between the two data sets. τ represents the integer difference between the peak data points of each data set. Thus, we can calculate the phase shift in radians as follows: $2 \cdot \pi \cdot \text{Exp.time} \cdot \tau / P$, where *Exp. time* is the time interval between data points (which must be the same for both data sets), and P is the period. (b) We include the two lightcurves that the XCF was run on in (a). Here we plot May 7 2011 UT as normal, and then shift May 8 UT as indicated above: May 8 UT - 1.95958×12 , where 12 is the number of rotations between the two observations for a period of 1.95958 hours.

5.3.2 Applying the XCF

We tentatively assessed potential phase jitter between the peaks of the raw lightcurves using the XCF so described, which was calculated for observations between each epoch. However, this technique in the case of our data was not ideal, for a number of reasons. Since the XCF in our Matlab routines relies heavily on evenly spaced data points in the sample, the differences in the peak of each lightcurve were calculated by comparing lightcurves of equal data point spacing; this required further binning for some of the time series datasets since these were taken with different detectors and exposure times. However the technique does not consider sources of error in these data, such as the effect of poor weather at some points of a signal - therefore it was difficult to reconcile this possible phase drift as a true measure of jitter between lightcurve peaks. We show an example of the XCF that we applied to the May 2011 epoch of TVLM 513, between May 7 and May 8 UT in Figure 5.4. In these plots, we show a time lag, τ (an integer difference between data points which is

then scaled by the exposure time), of 2 as provided by the XCF analysis. This corresponds to a phase shift between the lightcurve peaks of ~ 3.94 degrees (where 180 degrees is a completely anti-correlated signal). Ultimately we decided not to use these Matlab XCF routines to identify phase jitter based on the difficulties outlined above.

5.4 A Magnetically-Driven Auroral Process

In this section, we briefly discuss the radio, spectroscopic and photometric results, from the long campaign that investigated the correlated emissions from TVLM 513 (Hallinan et al., 2012), where the GUFU data in this thesis was the photometric component on this work. Our understanding of the magnetic field, and magnetic activity environments, associated with ultracool dwarfs has drastically changed over the past decade or so. Based on the recent detections of radio emissions and the associated optical signatures, it now appears that the ultracool dwarf regime has provided the building-block that bridges the much debated mass range between solar-type stars ($\geq 0.075 M_{\odot}$) that exhibit coronal and chromospheric activity, and giant planets ($\leq 0.0012 M_{\odot}$) such as Jupiter, that possess large-scale magnetic field configurations, as well as cool and neutral atmospheres.

Such discoveries provided an insight in to the characteristic similarities between the lowest mass, low mass stars, and giant planets. However, perhaps the most drastic measure of planet-like behavior was that of the observed radio emissions from ultracool dwarfs. We have previously discussed the periodic optical variability of TVLM 513. The possibility arose that the photometric periodicity and the $H\alpha$ spectral line were related, and furthermore that they were related to the radio pulses of Hallinan et al. (2007). Hallinan et al. (2012) have now confirmed that the correlation between these emissions, in all bands right across the electromagnetic spectrum, are being driven by the presence of high-strength, quasi-stable channels of current (unknown what electric current is being drive by), operating in the magnetospheric regions of the M9 dwarf. Indeed, auroral emissions from Jupiter have previously been observed, where such correlated variability has been observed in the Lyman- α line and in molecular hydrogen (ultra-violet), in $H\alpha$ (optical), in H_3^+ (infrared), and in the radio (Zarka, 1998). Therefore, it appears that this model for the ultracool dwarf TVLM 513, is consistent with the auroral emissions from Jupiter, but many orders of magnitude more powerful. During this campaign, in addition to the ~ 53 hours of photometric GUFU data (and others) encompassing ~ 5 years of an observation baseline reported in this thesis, Hallinan et al. (2012) have conducted simultaneous radio and time-resolved spectroscopic and photometric observations, using the Arecibo and EVLA radio observatories,

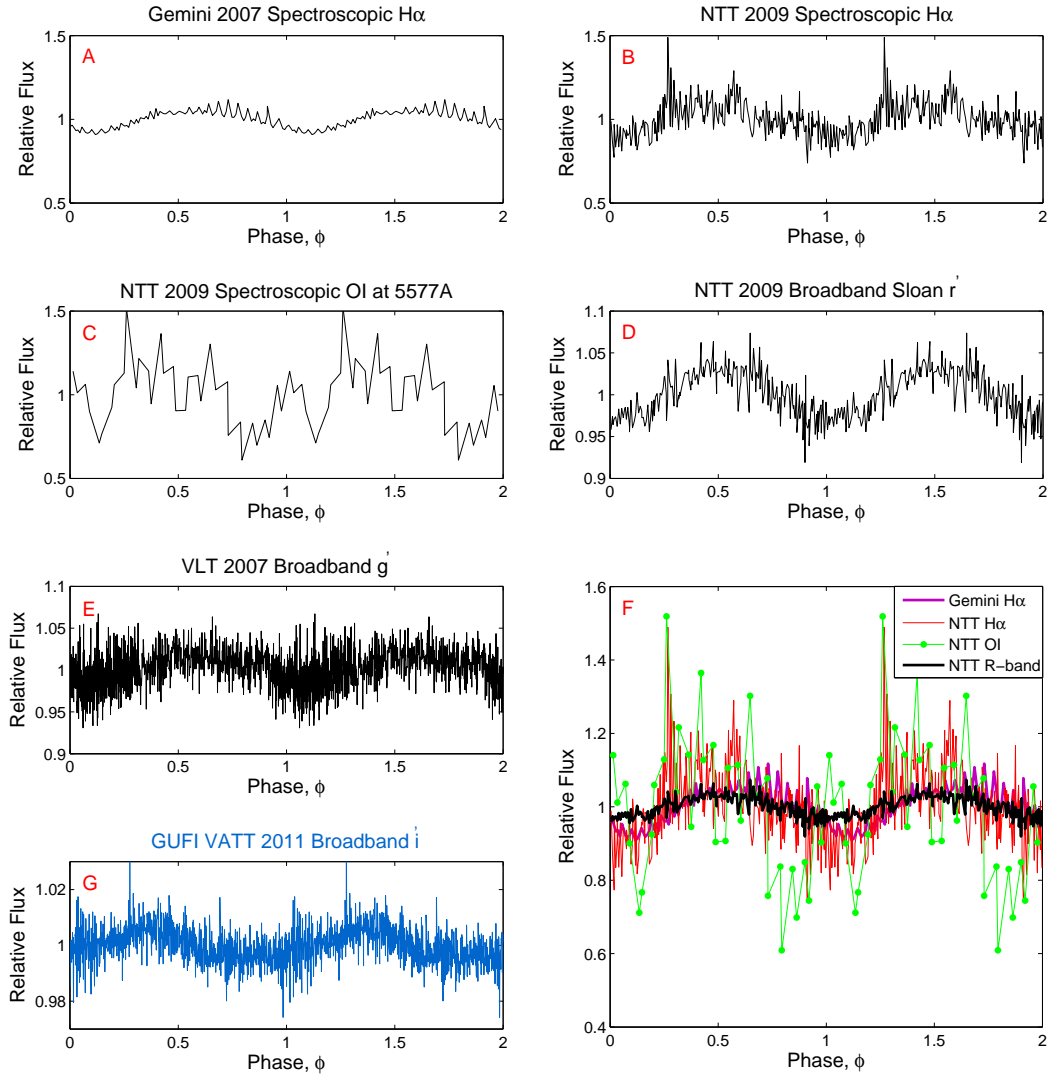


Figure 5.5: **Correlation of GUFi data (BLUE; lightcurve G) with Hallinan et al. (2012) campaign (all other lightcurves A - F):** In this figure we show further examples of the periodic spectroscopic and photometric behavior from TVLM 513, as detected from a large number of telescopes and instruments throughout the campaign (Hallinan et al., 2012; Harding et al., 2012a). All of the lightcurves have been phase folded to the detected period of 1.95958 hours. For the various spectral lines and molecular bands, the continuum was used for the differential calculation. (A) Gemini $H\alpha$; (B) NTT $H\alpha$; (C) NTT OI at 5577\AA ; (D) NTT Sloan r' ; (E) VLT g' ; (F) Overplotted phase folded lightcurves of (A) - (D); finally, (G) GUFi VATT i' in blue, from this work and published in Harding et al. (2012a). The periodic optical variability detected in these data are auroral emissions from an ultracool dwarf (Hallinan et al., 2012).

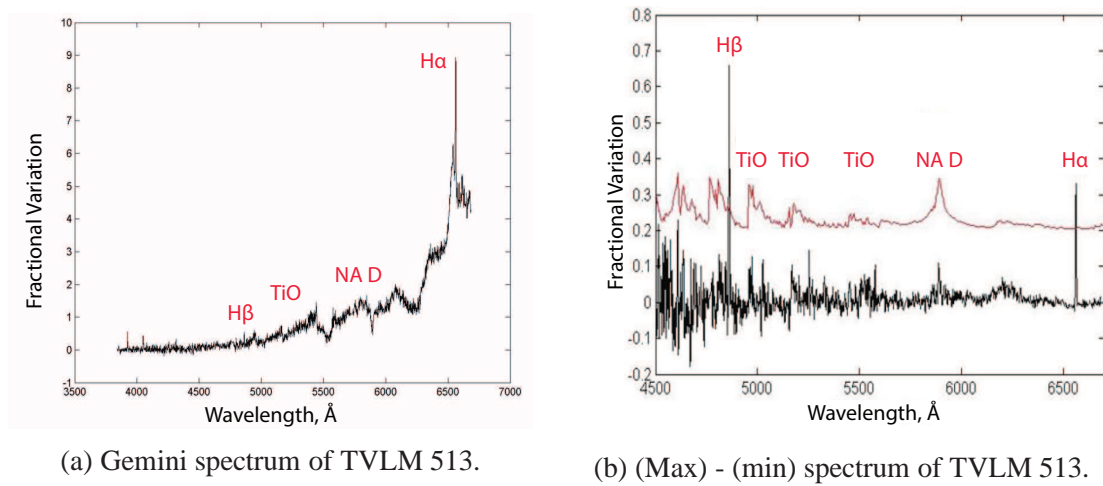


Figure 5.6: **Hallinan et al. (2012)**: Gemini spectrum of TVLM 513 obtained from the Gemini archive by Hallinan et al. (2012) - Program GN-2007A-Q-60. In black, they show the maximum spectrum observed minus the minimum spectrum observed on this night. It is clear that the variability of the individual spectral lines and molecular bands is present. Furthermore, they include the expected spectrum for a hot spot on the surface of an M9 dwarf. This was modeled via the DUSTY atmospheric models of Chabrier & Baraffe (2000), and is shown by the red line.

as well as ULTRASPEC on NTT, and ULTRACAM on the VLT. Spectrographs on the TNG, and on the Gemini and Keck telescopes were also used. As shown in Figures 5.5, these observations yielded the $H\alpha$ line and other continuum waveband ranges to be periodically in phase. Furthermore, the optical continuum was revealed to exhibit a high degree of amplitude variability, showing $\sim 7\%$ amplitude variations (peak to peak), in the Sloan r' (lightcurve *D*) in Figure 5.5). This variability is many times higher than what we report in the Johnson I-band and in the Sloan i' from GUF1 data (Harding et al., 2012a), shown in blue in the same figure. In addition to this, the OI line at 5577\AA was detected as a periodically varying line, also shown in Figure 5.5, lightcurves *C* and *F*, and had the same period of 1.95958 hours. Incredibly, this line is responsible for the green terrestrial aurora, which was once again in phase with the $H\alpha$ and optical continuum, as shown.

After establishing this remarkable degree of correlation, Hallinan et al. (2012) decided to obtain Gemini archival data of TVLM 513 [Program GN-2007A-Q-60] that was previously obtained using the GMOS spectrograph, which covered $3840 - 6680\text{\AA}$. Based on these data, Berger et al. (2008a) had reported $H\alpha$ periodicity of TVLM 513. This spectral range is dominated by many temperature sensitive molecular species, such as TiO. Since auroral hot spots are much hotter regions than the surrounding photosphere, bands such as TiO should be strongly effected by the associated injection of energy required for an auroral

hot spot. Figure 5.6, which was plotted by Hallinan et al. (2012) and inserted here, shows the correlation of these bands in emission to that of a model spectrum of an M9 dwarf from the DUSTY models of Chabrier & Baraffe (2000) (plotted in red in Figure 5.6a), indicating the presence of an auroral hot spot. Importantly, we note here that the spectral signatures of a magnetic cool spot are not too dissimilar to that of a hot spot. However, Hallinan et al. (2012) are putting forward that a *chromospheric* auroral hot spot is more likely based on the correlated emissions in their work.

Thus, these results confirm the presence of an auroral hot spot on the surface of TVLM 513, and are a very significant result in the ultracool dwarf regime. This was the first direct indication that a new kind of magnetic activity existed at the end of the main sequence, based on these magnetospheric phenomena. The GUF1 photometry of TVLM 513 presented in chapter 4 of this thesis, and the phase stability presented in this chapter was the photometric component of this aurora campaign, and provided a key part of the baseline required to assess this correlation across the wide range of wavelengths observed. As outlined before, the high degree of correlation in phase of the GUF1 data suggests the presence of a spatially-stable stellar region that does not appear to move by a significant amount over the entire TVLM 513 baseline. Considering these properties, the phase connected lightcurves presented in this thesis for the optical periodicity, could point towards not only a magnetic mechanism responsible for this behavior, but perhaps a single, sustained feature over these timescales. This would infer that the optical and radio emissions appear inextricably linked - perhaps by an auroral hot spot provided and sustained by the ECM process (discussed previously). This level of photometric phase stability has not been observed before in the ultracool dwarf regime, and carries a large amount of implications with respect to the feature responsible, and the mechanism that is supporting these emissions.

We note however, in the context of the TVLM 513 photometric data in *this* work (Harding et al., 2012a), we have shown that optical variability is consistent with a hot spot - but not that it cannot be consistent with a cool spot. We refer the reader to Hallinan et al. (2012) for a more indepth discussion of aurora in ultracool dwarfs, which include the true (final) spectrum of auroral emission, the temperature differences between the auroral hot spot and the surrounding photosphere, and the amount of energy that is used in these magnetospheric regions to sustain such a spot.

5.5 Summary

We establish an accurate enough period in this work to phase connect the ~ 5 year baseline of TVLM 513, and thus assess the stability of the periodic variability in both amplitude and phase over these epochs. We find that the peaks of the data are in phase for the detected period of 1.95958 ± 0.0005 hours, indicating a stable stellar feature that is long-lived and sustained over this baseline. These photometric data were the photometric component of a much larger campaign (Hallinan et al., 2012), in which simultaneous radio, spectroscopic and photometric observations were obtained, in order to directly investigate the presence of an auroral hot spot on the surface of TVLM 513. These data have confirmed the presence of such a feature on the M9 dwarf TVLM 513, which is a significant departure from the previously associated mechanisms that were thought to cause the optical variability for this dwarf. Furthermore, these discoveries indicate that mechanisms driving magnetic activity at the end of the main sequence may extend all the way down to the giant planet regime - which further bridges the gap between solar-type stars and Jovian-type planets.



Aurorae from the north and south polar regions of the planet Jupiter ...

Credits: John Clarke (University of Michigan), and NASA



“Theories have four stages of acceptance:

- i. this is worthless nonsense;*
- ii. this is interesting, but perverse;*
- iii. this is true, but quite unimportant;*
- iv. I always said so.”*

J. B. S. Haldane, 1963

*“ ... If it be now, 'tis not to come; if it be not to come, it will be now; if it be not now,
yet it will come. **The readiness is all ...**”*

William Shakespeare - Hamlet, V ii, 234-237

6

On the Orbital Coplanarity of Very Low Mass Binary Stars

6.1 Introduction

Studies of solar-type binaries have found coplanarity between the equatorial and orbital planes of systems with <40 AU separation. By comparison, the alignment of the equatorial and orbital axes in the substellar regime and the associated implications for formation theory, are relatively poorly constrained. In Chapter 4, we present measurements of the rotation periods for one component of the tight (1.8 AU) ultracool dwarf binary system, LP 349-25AB (M8 + M9), and for one component of the tight (2.7 AU) binary system, 2MASS J0746+20AB (L0 + L0.5) - the other being previously discovered by Berger et al. (2009). These period of rotation, together with well constrained orbital parameters and rotational velocity measurements, allow us to infer alignment of the equatorial planes of both components with the orbital plane of the systems to within 10 degrees. This result suggests that solar-type binary formation mechanisms may extend down into the brown dwarf mass range, and we consider a number of formation theories that may be applicable in this case. This is the first such observational result in the very low mass binary regime. In obtaining these geometries, we have also estimated masses, radii and ages, for the binary dwarfs, based on the atmospheric models of Chabrier & Baraffe (2000). We adopt the very low mass binary mass boundary to be $M_{TOT} \leq 0.185 M_{\odot}$, from Close et al. (2003).

This chapter is structured as follows: in § 6.1.1 - 6.1.3 we briefly discuss previous

discoveries of system properties, including dynamical mass measurements (Dupuy et al., 2010; Konopacky et al., 2010), individual rotation velocity measurements (Konopacky et al., 2012), and the discoveries of system periods of rotation for each object (Berger et al., 2009; Harding et al., 2012a), as well as colors and spectral features (Bouy et al., 2004; Reiners & Basri, 2009). We decided to include these details as stand-alone sections, since these data provided a significant amount of system property information that was used in constraining binary masses, outlined later in the chapter. Finally, § 6.2 discusses some background theory of previous coplanarity studies of binary systems, and some of the associated formation properties, as well as the results obtained and published during this work (Harding et al., 2012a,b).

6.1.1 High-Precision Dynamical Mass Measurements

The recent high-precision dynamical mass measurements of LP 349-25AB, and 2M J0746AB, have provided astrometric orbital parameters and photometric measurements (Dupuy et al., 2010; Konopacky et al., 2010), as well as important evolutionary model-derived system properties. In these studies, these authors presented estimations of the physical properties of late-M and early L dwarfs in their samples via spectroscopic laser-guiding AO observations. In both cases, they used the DUSTY evolutionary models of Chabrier & Baraffe (2000), as well as the TUCSON models of Burrows et al. (1997), to infer these properties. Both these systems had undergone enough orbital motion in order that their relative orbital parameters, and thus their total system mass, could be derived. However, Konopacky et al. (2010) find inconsistencies between their dynamical mass measurements and those predicted by the evolutionary models, such as TUCSON and DUSTY (Burrows et al., 1997; Chabrier & Baraffe, 2000), where the models over- or under-predict the stellar dynamical mass. These differences suggest that either these atmospheric models are predicting inaccurate temperatures for a given age, or alternatively that the mass-radius relationship as predicted by the models is inaccurate.

Dupuy et al. (2010) express concerns for LP 349-25AB in particular, since the LYON (DUSTY) and TUCSON models predict an age of 140 ± 30 Myr for the system. However, based on the lack of detected lithium in the dwarf's spectrum (Bouy et al., 2004), this age is in disagreement with the empirical lithium depletion point, which implies that the system is older. Thus, similar to Konopacky et al. (2010), the strong possibility exists that the models once again are predicting some of the properties inaccurately, such as the luminosities for example. However, Dupuy et al. (2010) did not adopt the same conclusions as Konopacky

et al. (2010), rather arguing that model atmospheres are at fault, based on their temperature estimates that proved to be ≈ 250 K warmer than DUSTY model predictions (Chabrier & Baraffe, 2000).

The high-precision dynamical mass measurements from the studies above were in close agreement for LP 349-25AB, where Konopacky et al. (2010) measure a total mass of $0.121 \pm 0.009 M_{\odot}$, and Dupuy et al. (2010) measure a total mass of $0.121^{+0.008}_{-0.007} M_{\odot}$. Konopacky et al. (2010) also included 2M J0746AB in their study, and derive a total system mass of $0.151 \pm 0.003 M_{\odot}$, initially measured to be $0.146 \pm^{0.016}_{0.006} M_{\odot}$ by Bouy et al. (2004), placing the dwarf in the very low mass binary regime. As outlined in Chapter 4, § 4.2, Gizis & Reid (2006) instead favored a substellar or low mass star classification. These parameters, in addition to the properties outlined in the below sections, have allowed us to investigate the system's orbital coplanarity.

6.1.2 Individual Rotational Velocity Measurements

As outlined in Chapter 4, the resolved rotational velocity work of Konopacky et al. (2012) has yielded a $v \sin i$ of $55 \pm 2 \text{ km s}^{-1}$ and $83 \pm 3 \text{ km s}^{-1}$ for LP 349-25A and LP 349-25B, respectively. Similarly, they measure a $v \sin i$ of $19 \pm 2 \text{ km s}^{-1}$, and $33 \pm 2 \text{ km s}^{-1}$, for 2M J0746A and 2M J0746B, respectively. They discuss that this difference in the $v \sin i$ measurement is difficult to reconcile based on the closeness of the component's spectral types, whereas they argue that they expect justified intrinsic differences between other targets in their sample due to the different spectral classes. So, it must originate from either an intrinsic difference in the velocities of each object, or else mutually inclined rotation axes. Before this study, only combined system $v \sin i$ estimates were published, and thus could only have been adopted as tentative estimates of the rotation velocities of each component. These individual measurements have provided us with a powerful diagnostic tool in establishing the system's equatorial orientation with respect to the orbital plane. However, in order to truly assess this geometry, system periods of rotation must also be known, since it is a parameter within the calculation of the $v \sin i$, in addition to the system radii. We consider the radii in later sections, and the rotation periods next.

6.1.3 Periods of Rotation, Colors and the Presence of Lithium?

We have already outlined the discoveries of the rotation periods for each of these systems in chapter 4. Since these were critical in the investigation of orbital properties of these

systems, we briefly mention these findings again here, in addition to the color information used, and the question of whether lithium is present in these binary dwarfs.

6.1.3.1 LP 349-25AB

To date, there were no periods of rotation recovered for the M dwarf binary LP 349-25A, or LP 349-25B. Although the system has been shown to exhibit extremely bright radio emission (Phan-Bao et al., 2007; Osten et al., 2009), only levels of quiescent activity has been observed, where no periodic radio bursts, and thus a rotation period measure, have been detected. These were interesting results, since this radio detected binary dwarf was quite similar to another in spectral type (2M J0746, which we discuss in the next sub-section), where both binaries were rapid rotators (as outlined in § 6.1.2) and were magnetically active, but 2M J0746 exhibited periodically pulsed radio emission (Berger et al., 2009). The first period of rotation for one component of this binary system was discovered in this work (Harding et al., 2012a), that of LP 349-25B, with a period of 1.86 ± 0.02 hours. Consequently, in our investigation of the orbital coplanarity of LP 349-25AB, we investigate the alignment of LP 349-25B only.

The color information that we use in this work are that of Konopacky et al. (2012), who reveal well constrained *J H K* photometric measurements of LP 349-25A and LP 349-25B. The colors obtained by Dupuy et al. (2010) are also very close to those of Konopacky et al. (2012). Finally, no lithium was detected in the spectrum of LP 349-25AB in an investigation by Reiners & Basri (2009), which is in disagreement with the model-derived radii and mass estimates of Dupuy et al. (2010), in addition to the estimates presented in this work. We discuss this further later in the chapter.

6.1.3.2 2MASS J0746+2000AB

Berger et al. (2009) reported radio emission with a rotation period of 2.07 ± 0.002 hours, where they also detected periodic $H\alpha$ emission. The period was the same in both instances, and was consistent with stellar rotation. They reported this periodicity to be that of the primary binary member, 2M J0746A. However, the photometric period of rotation discovered in this work of 3.36 ± 0.12 hours, in addition to the individual rotation velocity measurements outlined in § 6.1.2, as well as radii estimates discussed in § 6.2.1, allowed us to infer which binary member was exhibiting the radio bursting, and which was perhaps responsible for the photometric variability. These data infer maximum periods of rotation of ~ 4.20 hours and ~ 2.35 hours for 2M J0746A and 2M J0746B, respectively. Thus, the periodic

bursts of radio emission must have been emanating from the secondary, faster rotating, binary member, with a period of 2.07 ± 0.002 hours, and the period of 3.36 ± 0.12 hours was that of 2M J0746A.

Like LP 349-25AB, we use the color JHK information of Konopacky et al. (2012) for 2M J0746AB, which were obtained during the same campaign. Bouy et al. (2004) have established that no lithium is present in the L tight binary dwarf's spectrum. We show a full list of target properties, including these photometric apparent magnitudes later in this chapter, in Table 6.1. At this point we highlight the fact that both binary dwarfs in our sample are magnetically active based on the reported radio emission above. Could magnetic fields effect the stability of a coplanar orbit in these cases? We describe the various concerns regarding the presence of such fields during stellar formation in § ?? . We first consider previous studies of coplanarity in solar-type binary stars.

6.2 The Orbital Coplanarity of Very Low Mass Binaries

There have been many investigations of the evolution of rotating interstellar clouds, the multiplicity of solar-type stars and their associated formation properties, and the inclination of binary rotation axes (Weis, 1974; Abt & Levy, 1976; Bodenheimer, 1978; Fekel, 1981; Hale, 1994, and references therein). As a result, a large amount of current theory for solar-type binary star formation predicts that the rotation axes of such systems are likely to be perpendicularly aligned to the orbital plane, at all fragmentation stages of their evolutionary track. The formation of our solar system was used as a proxy for these early investigations, since it was an example of a multiple system which formed from a single cloud where planetary axes are roughly coplanar. Furthermore, examples of retrograde rotation only exist in the planets Venus and Uranus, and in the moon Triton, which has a retrograde orbit with its host planet, Neptune. Thus, coplanarity and corotation for short-period multiple systems was expected (and later confirmed for a large number of binaries) based on these observations.

Hale (1994) demonstrated that coplanarity between the equatorial and orbital planes existed for solar-type binaries with separations ≤ 40 AU. Many studies previous to this have also yielded similar results over a range of spectral classes [B - F] (Weis, 1974). Abt & Levy (1976) conducted studies of long-period orbital systems, and concluded that a breakdown in coplanar alignment is expected for systems in their sample with periods > 100 years. They outline that each component could be subject to different gravitationally-bound environments, and therefore by contrast much different rotational momentum vec-

tors. Fekel (1981) investigated coplanarity of hierarchical multiple systems, and found that $\sim 33\%$ of the systems studied did not indicate coplanar alignments between the inner and outer orbits; however he found that orbital periods ≤ 100 years were expected to follow this coplanar prediction. Interestingly, Jensen et al. (2004) and Monin et al. (2006) have reported planar alignment *and* misalignment for wider-separation binaries. Similar to these studies, in the case of very close binaries of semi-major axis ~ 0.3 AU, there have been some examples where systems exhibit both aligned and misaligned axes (Albrecht et al., 2009, 2011). More recently, Wheelwright et al. (2011) have also reported coplanarity between HAe/Be binary systems and circumstellar disks. Thus, it appears that although the binary spin axes have generally been observed to be perpendicular to the orbital plane, there are some exceptions for close, intermediate and wide separation solar-type systems.

In the years following the initial detection of the first brown dwarf Gl 229B by Nakajima et al. (1995), a number of surveys yielded the discovery of ninety-nine low mass star binary and brown dwarf binary systems (hereafter ultracool dwarf binaries), e.g. Burgasser et al. (2007). Following these discoveries, the introduction of LGS AO systems on ground-based telescopes provided the means of assessing the dynamical mass of such systems (Bouy et al., 2004; Dupuy et al., 2010; Konopacky et al., 2010). More recently, Konopacky et al. (2012) obtained resolved LGS AO spectroscopic measurements of individual component rotation velocities for a sample of eleven very low mass dwarf binaries. These data provided additional parameters for intermediately separated sources ($\sim 1 - 10$ AU), but could only be used to tentatively investigate the system orbital properties, since other parameters such as individual component rotation periods, and system properties inferred from evolutionary models, such as radii, were still either unknown or poorly constrained.

Previous studies of binary star formation have highlighted the possible physical effect of magnetic fields during the early stages of binary formation processes (Mestel, 1977; Bodenheimer, 1978; Fekel, 1981; Li et al., 2004, and references therein), whereby the presence of such fields in some cases could potentially hinder the gravitational collapse of the cloud, or indeed contribute to a loss of angular momentum between the spin axis and orbital motion of such systems. Are these concerns of special relevance in the ultracool dwarf regime? M dwarfs later than M3 are now associated with intense magnetic activity, often possessing surface magnetic field strengths of a few kG and greater (Reiners & Basri, 2007; Hallinan et al., 2008; Berger et al., 2009). In this letter, we now have new data to sufficiently investigate the orbital properties for the magnetically-active very low mass L dwarf binary, 2MASS J0746+20AB ($M_{TOT} = 0.151 \pm 0.003 M_{\odot}$). If the system is coplanar, this informs us on the formation of very low mass binary stars, and could signal that a

scaled-down version of evolutionary formation for solar-type binary systems could hold in this regime, despite the possible presence of magnetic fields at the early stages of these object's life. It is clear that characterizing the fundamental properties of very low mass binary star formation is important in establishing a correlation, if any, in the formation and evolution of all types of binary stars.

6.2.1 Estimating Masses and Radii

We used the DUSTY atmospheric models of Chabrier & Baraffe (2000) to estimate the masses and radii of each object. In order to do this, we first identified what parameters we would use as given inputs. These were:

- A.** The established total system mass of each system (Dupuy et al., 2010; Konopacky et al., 2010).
- B.** The well constrained photometric $J H K$ measurements and bolometric luminosity measurements of Konopacky et al. (2010).
- C.** The absence or presence of detected lithium in the binary dwarf's spectrum (Bouy et al., 2004; Reiners & Basri, 2009).

At this point, we were able to place constraints on the evolutionary models of Chabrier & Baraffe (2000) in determining the mass range, and consequently the radii, of each component. We make no initial assumptions for the age of the system, however young ages were ruled out based on this absence of lithium in *both* cases. Thus we had three measured quantities to estimate the mass track (i.e. $J H K$ colors, L_{bol} , and Li). We constrained the mass as follows:

1. Identify a range of ages that did not contain lithium for either component and ignore all others.
2. Interpolate over the range of masses from #1 based on the correlation between the $J H K$ colors of Konopacky et al. (2010), and those of the Chabrier & Baraffe (2000) models.
3. Interpolate over the range of bolometric luminosities with respect to #1 and #2, thus

establishing the best agreement between mass, $J H K$ colors, Li and L_{bol} .

4. Since each binary member must be coeval, the sum of each component's mass must lie within the errors of the estimated total system mass of Konopacky et al. (2010).
5. Steps 1 - 4 above provided a number of ages for the system, thus the individual mass estimates and age range consequently inferred a range of possible radii for each binary component.

Once the range of possible radii were identified, we could then move to assessing the orbital coplanarity of the system. At this point we had all of the system parameters in hand: the periods of rotation of the binary components, the $v \sin i$ of each component, and the radii. The methods expressed above were especially relevant for the 2M J0746AB system analysis. Studies such as Dupuy et al. (2010) had already conducted in-depth model-based estimations of system properties for LP 349-25AB. We found that we also identified the same mass and age values for this M dwarf binary as revealed in previous studies. Having only one period of rotation for one component was helpful in assessing the coplanarity of that specific binary member, however we could not truly evaluate the coplanarity of the system as a whole without the second rotation period. There are also serious problems with the age estimate of this system. We elaborate further in the following section.

In Figure 6.1 we include plots for a given age, of $\log(L/L_{\odot})$, radius (R), M_J , M_H , M_K and gravity vs. mass, for the binary 2M J0746AB, to illustrate the method above. We determine that the three most likely ages are 1 Gyr ($\log 9.0$), 1.25 Gyr ($\log 9.1$) and 1.5 Gyr ($\log 9.2$) [i.e. 1.25 ± 0.25 Gyr], for the L dwarf binary, as indicated by the red, blue and green evolutionary tracks, respectively. We note further that the estimates of gravity were also estimated from the correlation of the Chabrier & Baraffe (2000) evolutionary models and data previously outlined in this chapter, and not by other means such as spectral fitting. Plot B shows the radii estimates of each component that were established based on this process - we discuss these further in § 6.2.2.2 where we show this plot in more detail and also include error bars in the calculation. Although we do not include errors bars in each measurement in Figure 6.1, the mass estimates (x -axis) of each member are in good agreement with the evolutionary tracks of each parameter (y -axis).

Finally, we highlight the dependency of the total system mass, L_{bol} , photometry (and so on), on the parallax measurements of a stellar system. These parameters are therefore positively correlated - this effect between the parameters is not accounted for in this work,

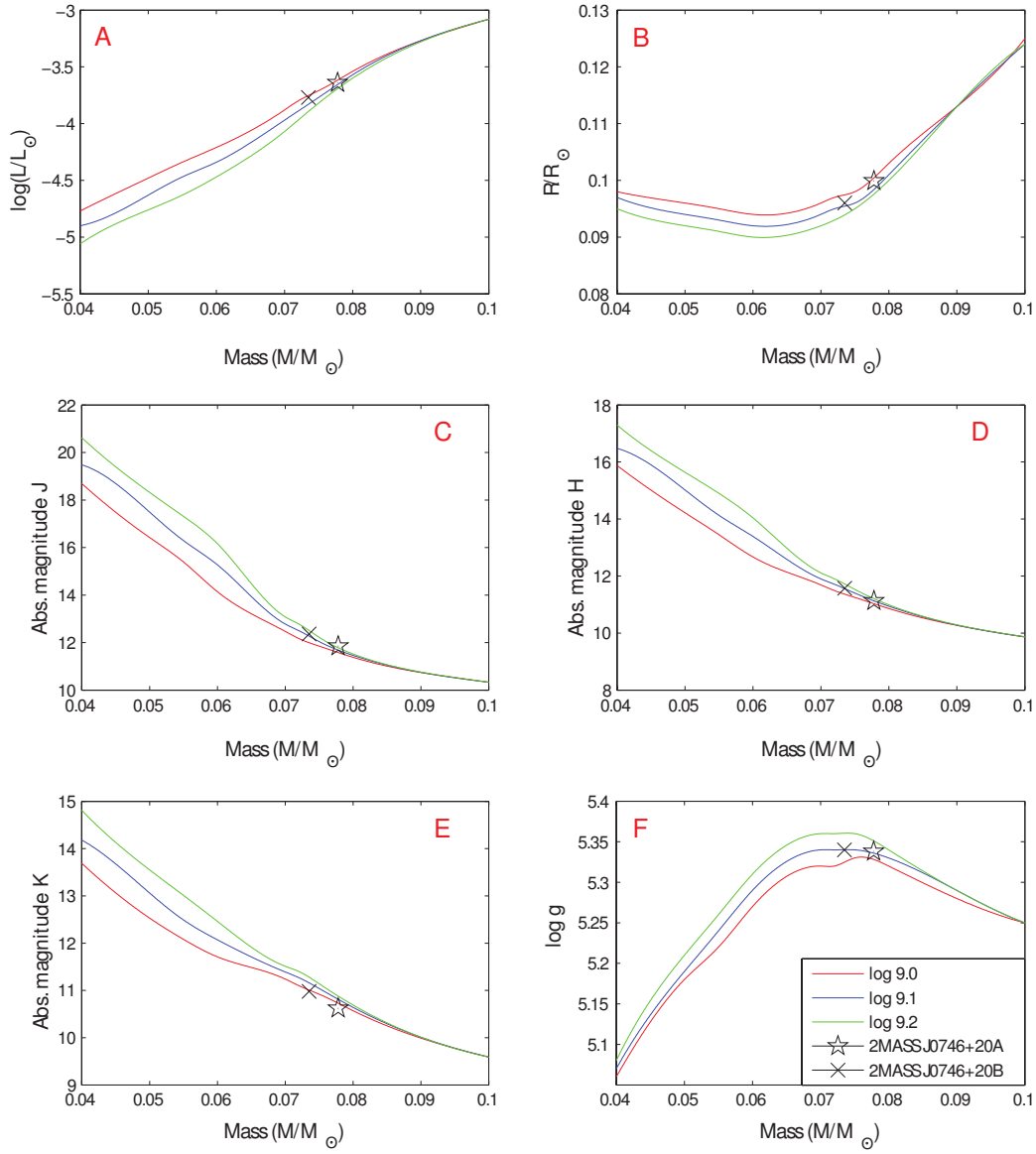


Figure 6.1: Constraining the physical properties of 2M J0746AB. The three most likely ages of 1 Gyr ($\log 9.0$), 1.25 Gyr ($\log 9.1$) and 1.5 Gyr ($\log 9.2$) are indicated with the red, blue and green evolutionary tracks, respectively. A legend for ages and binary members are indicated in figure F.

(A) Bolometric luminosity: $\log(L/L_{\odot})$ vs. mass (M/M_{\odot}). (B) Radius: R/R_{\odot} vs. mass (M/M_{\odot}). (C) J Magnitude: Absolute magnitude, M_J vs. mass (M/M_{\odot}). (D) H magnitude: Absolute magnitude, M_H vs. mass (M/M_{\odot}). (E) K magnitude: Absolute magnitude, M_K vs. mass (M/M_{\odot}). (F) Gravity: $\log g$ vs. mass (M/M_{\odot}).

where again, the fitting is solely based on the evolutionary models of Chabrier & Baraffe (2000).

6.2.2 Results

6.2.2.1 LP 349-25AB

The detected rotation period from LP 349-25B in this work provides an important parameter in assessing whether solar-type binary formation may also apply in the very low mass binary regime. We therefore plot the measured $v \sin i$ of Konopacky et al. (2012) in Figure 6.2, and investigate the case of an expected orthogonal alignment between the binary member's rotational axes and the system's orbital plane ($i \perp \Theta$). We do this by adopting the new period of 1.86 ± 0.02 hours for one or other component of the system. Konopacky et al. (2010) estimate radii of $1.7 \pm_{0.09}^{0.08} R_J$ for LP 349-25A and $1.68 \pm_{0.08}^{0.09} R_J$ for LP 349-25B, both of which are estimated based on evolutionary model-derived parameters from the DUSTY and COND models (Allard et al., 2001). Considering these estimates, as well as an orbital inclination angle of 61.3 ± 1.5 degrees from their work, we derive a maximum period of rotation of ~ 3.77 hours and ~ 2.47 hours for LP 349-25A and LP 349-25B, respectively. Therefore, in this case, it was difficult to assign our detected period to either binary member. Furthermore, these radii appear to be very large when considering the evolutionary models of Chabrier & Baraffe (2000) for a given range of ages, L_{bol} , and total system mass presented in their work, in addition to a lack of detected lithium in the binary spectra (Reiners & Basri, 2009). Contrary to these estimates, Dupuy et al. (2010) estimate smaller radii of $\sim 1.30 - 1.44 R_J$ for LP 349-25A and $\sim 1.24 - 1.37 R_J$ for LP 349-25B, inferring maximum periods of ~ 2.65 hours and ~ 1.67 hours respectively. Similar to Konopacky et al. (2010), they use two different evolutionary model sets to establish these values (Burrows et al., 1997; Chabrier & Baraffe, 2000). This discrepancy could arise from the fact that since Konopacky et al. (2010) use the effective temperature as one of the inputs for model-predicted mass, Dupuy et al. (2010) obtain their temperature estimates via NIR fitting, which is ~ 650 K higher than those of Konopacky et al. (2010), who use only broadband photometry.

We also attempted to estimate the binary radii via the atmospheric models of Chabrier & Baraffe (2000), as per the method outlined in § 6.2.1. We note that LP 349-25 is a magnetically active very low mass binary (Phan-Bao et al., 2007; Osten et al., 2009). There are some difficulties in estimating radii of young magnetically active low mass stars. Although the age and radii of this object are very much so ambiguous as we will see, Dupuy

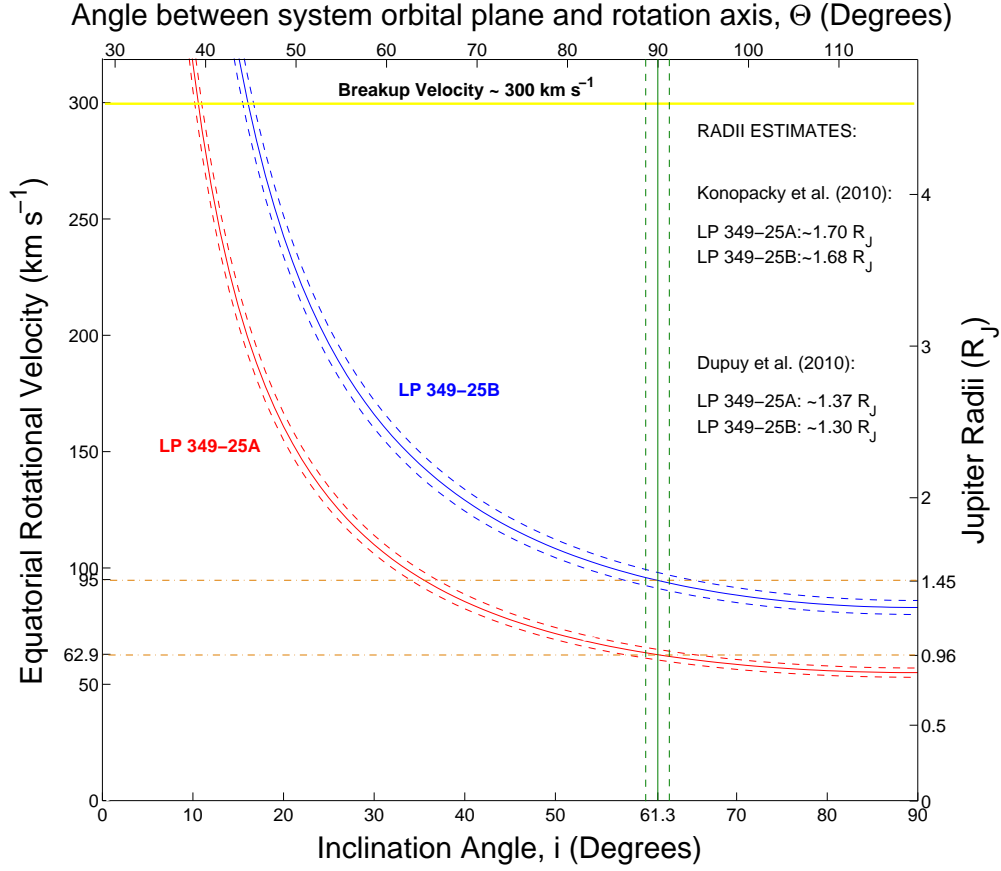


Figure 6.2: Here we plot the $v \sin i$ of LP 349-25A (red) and LP 349-25B (blue) of Konopacky et al. (2012). The dashed red and blue lines correspond to the error in this measurement. This figure investigates the radii estimates of Konopacky et al. (2010) & Dupuy et al. (2010), and whether the binary member's equatorial axes are coplanar with the system's orbital plane (Hale, 1994). We place one explicit constraint here: the presence of a rotation period of 1.86 ± 0.02 hours for one or other of the components. We illustrate this by aligning the measured system inclination angle of 61.3 ± 1.5 degrees, i , x-axis bottom) at 90 degrees to the equatorial axes (x-axis, Θ , top); as shown by the green vertical line and the associated dashed error lines. Konopacky et al. (2012) report equatorial velocities of $\sim 62 \text{ km s}^{-1}$ and $\sim 95 \text{ km s}^{-1}$ for LP 349-25A and B, respectively. It is clear that the radii estimates of Konopacky et al. (2010) are overestimated, based on an orthogonally aligned system. Assuming that the equatorial axes are perpendicular to the orbital plane, a period of 1.86 ± 0.02 hours is inconsistent with that of LP 349-25A, which requires a much smaller radius of $\sim 0.96 R_J$. However, a radius of $\sim 1.45 R_J$ is expected for LP 349-25B, which is in loose agreement with the estimates of Dupuy et al. (2010), by taking errors in the period and $v \sin i$ into account. We therefore have a case to argue for the detection of a 1.86 ± 0.02 hour rotation period for LP 349-25B.

Orbital Coplanarity of LP349-25AB?

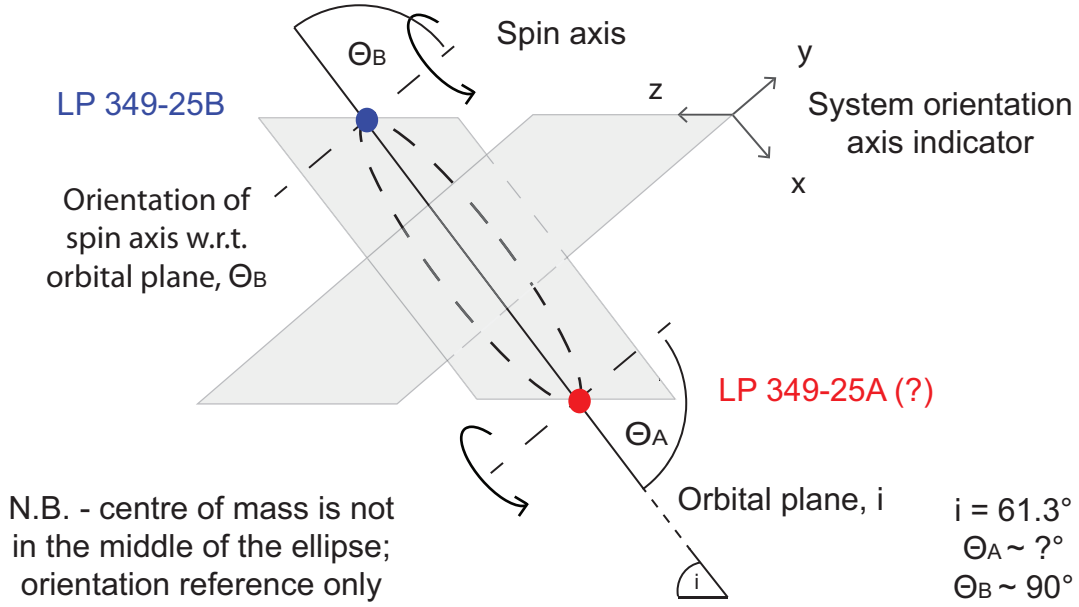


Figure 6.3: Here we sketch the configuration of LP 349-25AB, which loosely illustrates the possible system orientation of LP 349-25B. Based on a radius estimate for LP 349-25B of $\sim 1.37 R_J$ (Dupuy et al., 2010), in addition to the $v \sin i$ of $83 \pm 3 \text{ km s}^{-1}$ (Konopacky et al., 2012), and the period of 1.86 ± 0.2 hours in this work, there is strong indication that the orientation of the equatorial axis of LP 349-25B, Θ_B , is perpendicularly aligned with the inclination angle of the system orbital plane, to within 10 degrees.

et al. (2010) predict an age estimate of $140 \pm 30 \text{ Myr}$ - thus we briefly address this in this paragraph. As outlined in Chapter 1 and Chapter 4, the effects of the presence of convection and magnetic field environments on the interior of stars is not yet fully understood. Nevertheless, it is clear that a magnetic dynamo is effectively operating in the very low mass regime (Donati et al., 2006, 2008; Morin et al., 2008, 2010). However, Chabrier et al. (2007) demonstrate the effect a reduction in convective efficiency can have on the radii of magnetically active, young, low mass objects ($< 0.35 M_\odot$ in their study). Since the adiabatic properties of a star increase with mass, such an environment reduces convection in the outer areas. The end result is a also a reduction in luminosity and core temperatures (since more energy is needed to transport heat), causing the star, and thus the radius, to expand.

However, the calculated total system mass of $0.121 \pm 0.009 M_{\odot}$ classifies LP 349-25AB as a very low mass object, and furthermore it may well be the case the LP 349-25AB is much older than original estimations. Based on the above parameters (mass and photometry) and the absence of lithium, the only ages that mildly agree with these measured parameters suggests that the system has a total mass that far exceeds the total mass above. We find an age consistent with Dupuy et al. (2010) of ~ 140 Myr, however *lithium is present* in this range. Dupuy et al. (2010) have suggested that perhaps the absence of lithium in the spectrum of LP 349-25AB was due to flux domination from the primary member, and given the predicted mass of LP 349-25B in their work, the Li_I doublet is expected since LP 349-25B potentially lies below the theoretically predicted lithium depletion point at $\approx 0.055 - 0.065 M_{\odot}$. This remains to be seen, and requires resolved spectra to investigate if lithium is in fact present. Indeed, based on the discrepancy between the measured luminosities of Dupuy et al. (2010) and Konopacky et al. (2010), perhaps the total system mass is under-estimated, which would place LP 349-25AB at an older age in the models of Chabrier & Baraffe (2000), consequently supporting the observed absence of lithium. Dupuy et al. (2010) also point out this concern.

The equatorial velocity from Konopacky et al. (2012) of $\sim 62 \text{ km s}^{-1}$ for LP 349-25A, requires a radius of $\sim 0.96 R_J$ (lower dash-dotted line in Figure 6.2). Similarly, the equatorial velocity of $\sim 95 \text{ km s}^{-1}$ for LP 349-25B requires a radius of $\sim 1.45 R_J$, shown as the higher dash-dotted line in Figure 6.2. This prediction for LP 349-25B is in good agreement with the estimates of Dupuy et al. (2010), by taking errors in the period and $v \sin i$ into account. We therefore have a case to argue for the detection of LP 349-25B as the periodically varying source in R-band and I-band wavelengths, with a period of rotation of 1.86 ± 0.02 hours. This tentatively supports a coplanar alignment for one component of the system, as shown in Figure 6.3. However, the rotation period of LP 349-25A is required to properly assess this possibility.

6.2.2.2 2MASS J0746+2000AB

We find an age of $\sim 1 - 1.5$ Gyr for the binary based on the model estimates outlined in § 6.2.1, as well as individual mass estimates of $0.078 \pm 0.004 M_{\odot}$ and $0.073 \pm 0.004 M_{\odot}$ for 2MASS J0746+20A and 2MASS J0746+20B, respectively. These mass estimates are consistent with Bouy et al. (2004), Gizis & Reid (2006) and Konopacky et al. (2010), and infer that each component lies at, or just below, the substellar boundary, and furthermore supports the prediction of a low mass star classification for the secondary member (Gizis & Reid, 2006). The difference in rotational velocity between these stars is most intriguing,

Parameter	2MASS J0746+20A	2MASS J0746+20B
Rot. period (hrs)	3.36 ± 0.12^1	2.07 ± 0.002^2
$v \sin i$ (km s $^{-1}$)	19 ± 2^3	33 ± 3^3
Period ratio	$^{10.62}_{-0.03} \pm 0.02$...
$v \sin i$ ratio	$^{30.57}_{-0.10} \pm 0.13$...
Orbital period (yrs)	12.71 ± 0.07	12.71 ± 0.07
Semi-major axis (mas)	$237.3^{+1.5}_{-0.4}$	$237.3^{+1.5}_{-0.4}$
Inc. $_{ORB}$ (deg) ‡	41.8 ± 0.5^3	41.8 ± 0.5^3
Inc. $_{EQ}$ (deg) ‡	$32 \pm 6^\dagger$	$36 \pm 5^\dagger$
Age (log yrs)	$9.1 \pm 0.1^\dagger$	$9.1 \pm 0.1^\dagger$
Mass $_{total}$ (M_\odot)	0.151 ± 0.003^3	0.151 ± 0.003^3
Mass (M_\odot)	$0.078 \pm 0.004^\dagger$	$0.073 \pm 0.004^\dagger$
Lithium?	No 4	No 4
Radius (R_J)	$0.99 \pm 0.03^\dagger$	$0.96 \pm 0.02^\dagger$
Gravity (log g)	$5.34 \pm 0.02^\dagger$	$5.34 \pm 0.02^\dagger$
L_{bol} (log L/L_\odot)	-3.64 ± 0.02^4	-3.77 ± 0.02^4
Abs. mag (J)	11.85 ± 0.04^3	12.36 ± 0.10^3
Abs. mag (H)	11.13 ± 0.02^3	11.54 ± 0.03^3
Abs. mag (K)	10.62 ± 0.02^3	10.98 ± 0.02^3
References	1, 3, 4	2, 3, 4

Table 6.1: **Properties of the L Tight Binary 2MASS J0746+2000AB.**

References. - (1) Harding et al. (2012a). (2) Berger et al. (2009). (3) Konopacky et al. (2012). (4) Bouy et al. (2004). (5) Chabrier & Baraffe (2000)

† Derived in this work from the models of ref. (5) and parameters from (1) - (4).

‡ Inc. $_{ORB}$ is the system orbital inclination as measured by Konopacky et al. (2012), whereas Inc. $_{EQ}$ is the equatorial inclination of each component with respect to the orbital plane, calculated in this work.

considering that each component mass estimate is so similar. However, it is also possible that there is in fact a larger difference in component mass, than what has been estimated by evolutionary models in the above studies.

We have already pointed out that only the faster rotator has been detected as a magnetically active dwarf, and is likely to be 2MASS J0746+20B. This implies that either 1) 2MASS J0746+20A is magnetically active, and the geometry of the magnetic field is such that we cannot detect the emission based on the inclination angle relative to the line of sight, 2) the magnetic activity of 2MASS J0746+20A is not as strong as 2MASS J0746+20B, and thus was not detected during the observations of Berger et al. (2009), or 3) 2MASS

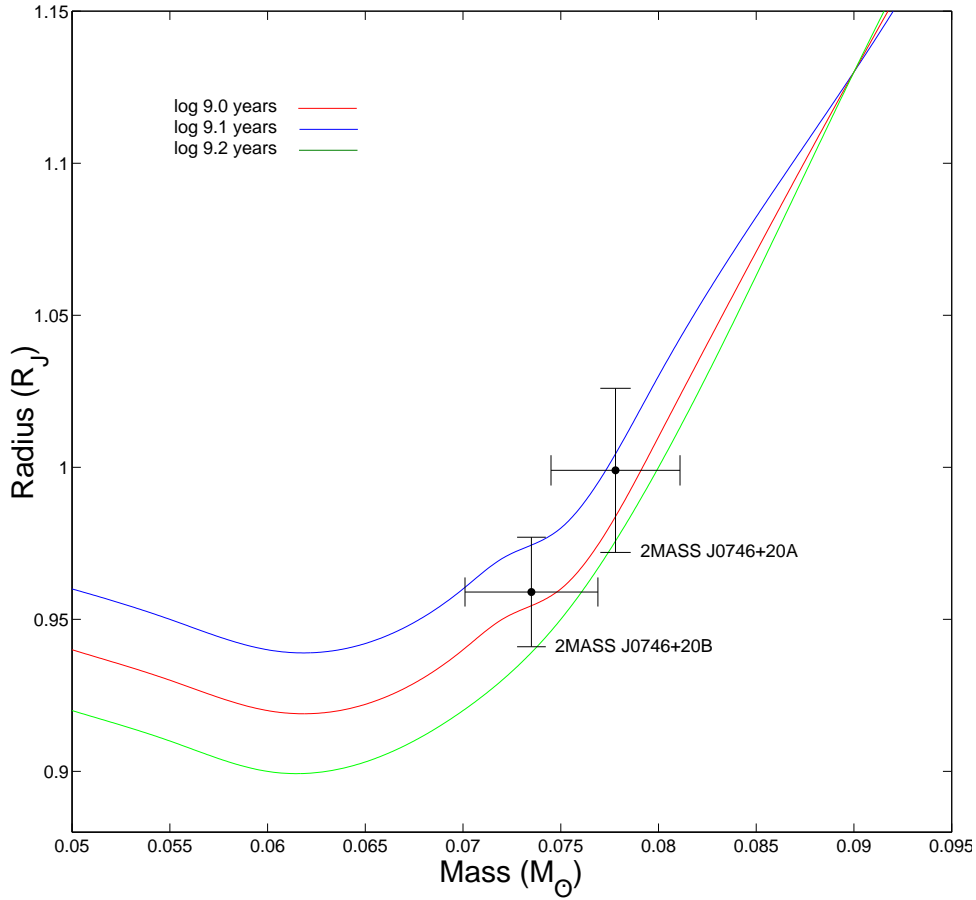


Figure 6.4: We show three low mass star evolutionary tracks of radii (R_J) vs. mass (M_\odot), for ages of ~ 1 (log 9.0), ~ 1.25 (log 9.1) and ~ 1.5 Gyr (log 9.2), derived from the evolutionary models of Chabrier & Baraffe (2000). The measured total system mass of $0.151 \pm 0.003 M_\odot$, in addition to well constrained $J H K$ photometry (Konopacky et al., 2010), was used as a constraint in parameter-space. Furthermore, we highlight that *no* lithium was detected in the binary dwarf’s spectrum by Bouy et al. (2004) - therefore we only considered ages where no lithium is present for the above parameters. We further note, that the errors associate with the individual mass estimates were based on the constraints of the Chabrier & Baraffe (2000) evolutionary models.

J0746+20A is not magnetically active. Assuming the mass estimates above are roughly accurate, and if 2MASS J0746+20A exhibits no or weaker radio emission than its counterpart, would magnetic braking therefore not have a greater effect on 2MASS J0746+20B? Chabrier & Küker (2006) have discussed that magnetic braking can become increasingly inefficient in this mass regime, based on the presence of non-axisymmetric field configurations. Although such a configuration has not been confirmed for 2MASS J0746+20AB,

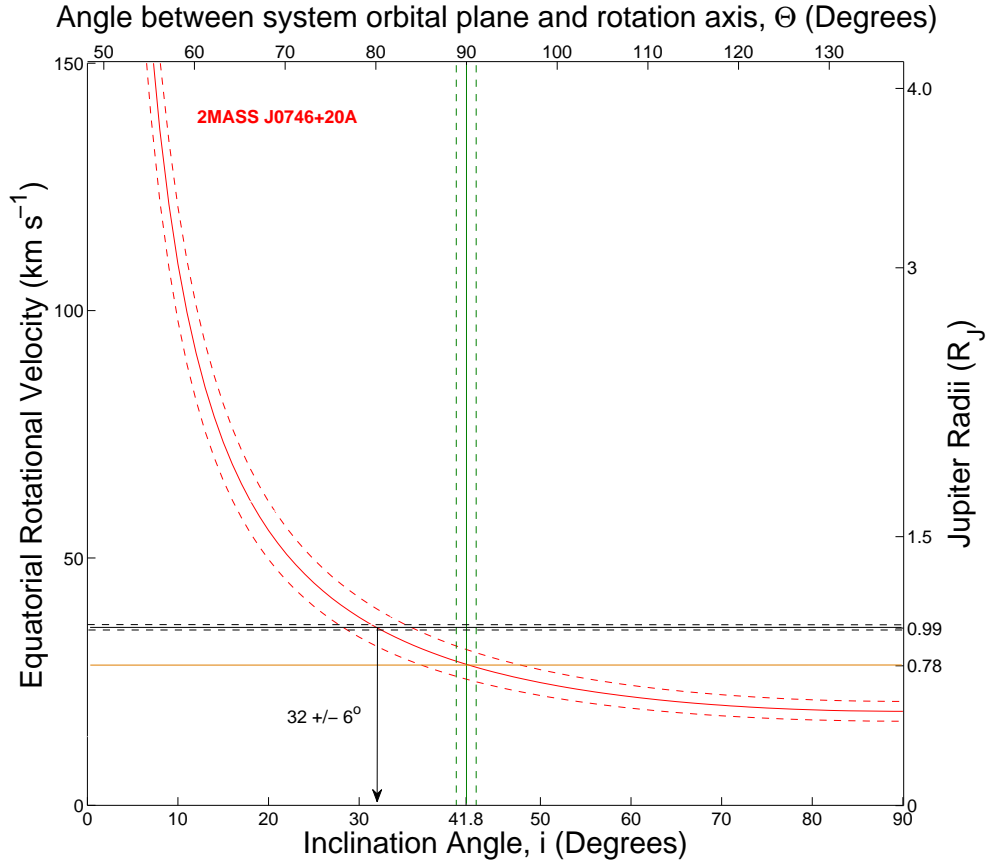


Figure 6.5: We illustrate the rotation velocity of 2MASS J0746+20A, by plotting the equatorial rotational velocity (*y-axis, left*) against the inclination angle of the orbital plane (*x-axis, bottom*). The measured $v \sin i$ of $19 \pm 2 \text{ km s}^{-1}$ is shown by the red solid curve. The dashed lines either side of this are the associated errors. The green vertical solid line and dashed error lines (*x-axis top*) highlight the alignment of the equatorial spin axis with respect to the inclination of the orbital plane of the system, measured to be 41.8 ± 0.5 degrees. *Y-axis, right*, corresponds to the radius of the dwarf, in R_J ($\sim 69550 \text{ km}$). We show our estimated radius of $0.99 \pm 0.03 R_J$ by the black solid horizontal line, as measured by the evolutionary models of Chabrier & Baraffe (2000), outlined in Section 6.2.1. This radius implies that 2MASS J0746+20A has a spin axis inclination angle of $32 \pm 6^\circ$, whereas the orbital plane has an angle of $41.8 \pm 0.5^\circ$, as measured by Konopacky et al. (2012). By plotting the orange horizontal solid line, we illustrate the *required* radius of $\sim 0.78 \pm 0.09 R_J$ in order to satisfy a perfectly coplanar alignment.

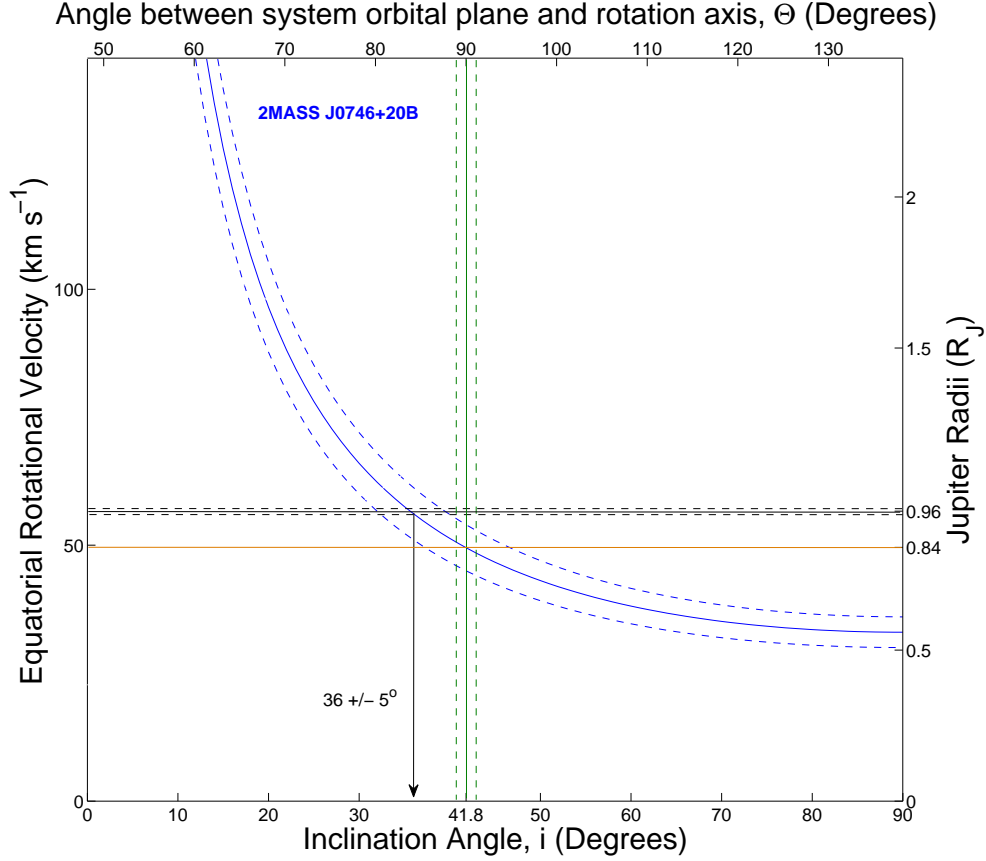


Figure 6.6: Same axis layout and illustration as Figure 6.5, except for the case of 2MASS J0746+20B. Its $v \sin i$ of 33 ± 3 km s⁻¹ is shown by the blue solid line, where the dashed lines represent the errors in this measurement. We highlight our estimated radius of $0.96 \pm 0.02 R_J$ with the green ‘orthogonal’ vertical track, which appears to have a spin axis inclination angle of $36 \pm 5^\circ$. A radius of $\sim 0.84 \pm 0.08 R_J$ (orange line) is required for a perfect alignment.

others have shown that they can operate in this class of object (Donati et al., 2008). A ~ 1.7 kG magnetic field estimated by Berger et al. (2009) for an object of this age, is not unexpected under the assumption of a rotation-activity relationship. If magnetic activity was perhaps playing a role in each member’s rotation rate, by establishing the magnetic properties of 2MASS J0746+20A, one could further investigate this rotational velocity departure. This would be an interesting investigation in to why two objects of such close mass have such different equatorial velocities.

The above mass estimates place each star just below $1 R_J$, as shown in Figure 6.4,

Orbital Coplanarity of 2MASS J0746+20AB?

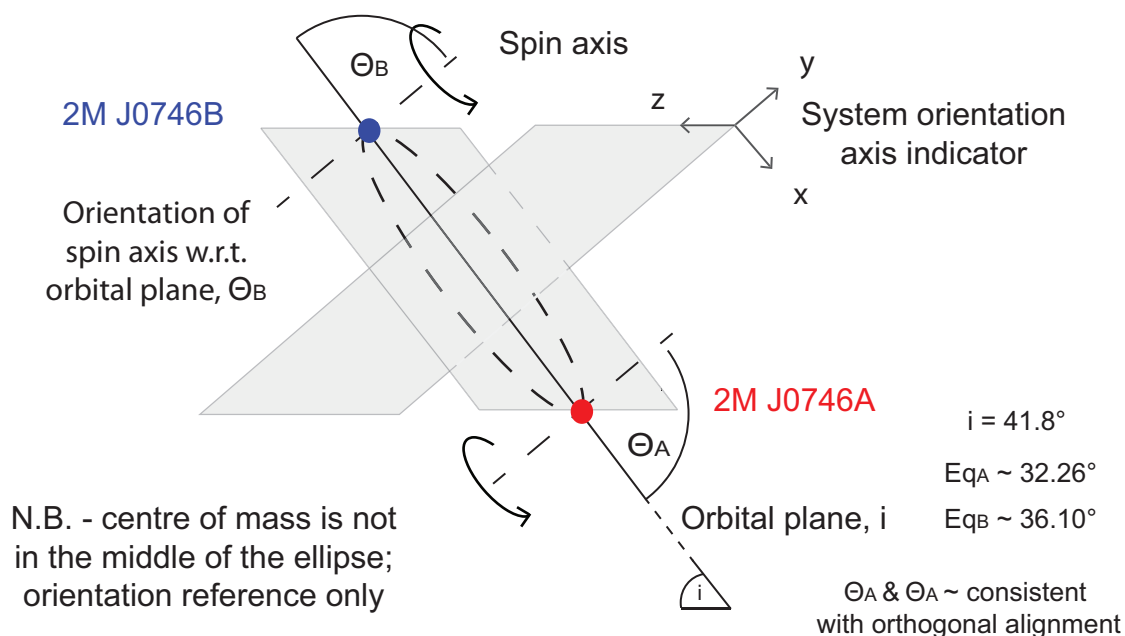


Figure 6.7: Here we sketch the configuration of 2M J0746AB, which illustrates the system orientation of each member. Most importantly, the center of the solid ellipsoidal tracked line connecting the stars is *not* the center of mass of the binary system. We use this only as a reference frame for the orientation of the equatorial spin axis, Θ , with respect to the orbital plane, i.

where we estimate $0.99 \pm 0.03 R_J$ for 2MASS J0746+20A and $0.96 \pm 0.02 R_J$ for 2MASS J0746+20B. Indeed, these predictions are in agreement with those of Konopacky et al. (2010). Furthermore, an age of $\sim 1 - 1.5$ Gyr identifies the system as a much older binary dwarf than originally predicted by Bouy et al. (2004), who found the system to be $\sim 150 - 500$ Myr old. This is a large discrepancy - Bouy et al. (2004) identify this range of ages, despite the *absence of lithium* in each component spectrum, which is expected to be present for stars of this age. This age is also in disagreement with surface gravity estimates of Schweitzer et al. (2001), who compared spectra to the models of Allard et al. (2001). Although their temperature estimates agree with Bouy et al. (2004), the gravity is too high for a 150 - 500 Myr old object. Bouy et al. (2004) put forward that gravity estimates could be effected by the presence of high-strength alkali lines (dust) which would consequently bias a gravity measurement. So, based on the absence of lithium which has been reported

by a number of studies (Reid et al., 2002; Bouy et al., 2004), we have investigated older ages for the dwarf. A summary of system properties is outlined in Table 6.1.

Based on the spectroscopic observations of Konopacky et al. (2012), and the radio and photometric observations of Berger et al. (2009) and Harding et al. (2012a), respectively, we calculate a $v \sin i$ ratio of $0.57 \pm_{0.10}^{0.13}$, and a period ratio of $0.62 \pm_{0.03}^{0.02}$. By adopting these $v \sin i$ and rotation period measurements, the estimated radii in this work indicate that each component in the system is closely aligned with respect to each other's equatorial spin axis, and the system orbital plane, thus supporting a coplanar alignment to within 10° . Alternatively, under the assumption of a perfectly coplanar alignment, the evolutionary models could be over-predicting the radii for a given mass and age. Based on the above discussion, we have shown that the spin axes are inclined at $32 \pm 6^\circ$ and $36 \pm 5^\circ$, respectively, with respect to the observer's line of sight (shown in Figure 6.5 and Figure 6.6). These rotation axes inclinations are in agreement with the inclination angle of the orbital plane, to within a 2σ level. It is not uncommon for small misalignments to exist in these systems, even under the assumption of orbital coplanarity. Indeed, the Sun is misaligned by $\sim 7.25^\circ$ from the ecliptic in our own solar system (Allen, 1973). Furthermore, we point out that any calculated departure from a perfectly perpendicular alignment could be due to an accumulation of measured errors in the $v \sin i$, the periods of rotation, the radii, and the inclination angles of the orbital plane and the equatorial axes. Hale (1994) outlines that objects are likely to be coplanar to within $\pm 10^\circ$, based on such selection effects. Finally, we highlight a geometric effect with respect to system spin axis inclinations. The orientation of the spin axes of each system, could be independently pointed toward our line of sight with respect to the orbital plane, or alternatively be pointed away. Thus, the inclination of each equatorial axes could still be roughly the same, but not necessarily aligned since there is this extra dimension in a 3-D system to consider.

There are numerous binary (and multiple) star system formation theories, the most prominent of which are turbulent core fragmentation, disk fragmentation, multiple formation via competitive accretion, and dynamical interactions (Kratter, 2011, and references therein). This is the first study to assess the orbital alignment properties of a very low mass binary system. Orbit-spin alignment is consistent with multiple formation pathways. Disk fragmentation naturally produces aligned systems, and can also drive components towards equal mass (see Kratter et al. (2010, and references therein)). However, disk fragmentation is more likely for higher mass systems ($> 1 M_\odot$) (Kratter et al., 2008; Offner et al., 2010). Notably, these models have not been extended down to the brown dwarf regime. Stamatellos & Whitworth (2009) proposed an alternative disk fragmentation scenario, where binary

brown dwarfs are born within the disk of a more massive star. This scenario is somewhat inconsistent with 2MASS J0746+20AB, as it produces only very high eccentricity binaries (they predict $e > 0.6$ compared to this system's $e = 0.487$ (Konopacky et al., 2010)).

Both core fragmentation and competitive accretion can also produce aligned systems. In the former scenario, fragments may share the core's net angular momentum vector (Matsumoto & Hanawa, 2003). Recent work by Jumper & Fisher (2012) has shown that a straightforward extrapolation of the turbulent core fragmentation model to lower masses naturally reproduces the separation distribution of brown dwarfs. However, an analysis by Dupuy & Liu (2011), finds that the eccentricity distribution of ultracool dwarf binaries is statistically distinct from that of solar type systems, and more consistent with the clustered, competitive accretion model of Bate (2009, 2012). Even if such systems are born misaligned, tidal torquing between disks can re-align close systems (see Lubow & Ogilvie (2000)). Interaction with a circumbinary disk, as seen in Bate (2012), might also align stars with initially random orientations. As noted above, magnetic interactions, which might be even stronger for fully convective stars, can also alter spin-orbit alignment.

In the case of 2MASS J0746+20AB, alignment cannot be used to distinguish between various formation models. On the contrary, a strongly misaligned system would be more indicative of dynamical processing. Nevertheless, the acquisition of such data for low mass binary systems will place tighter constraints on formation models. Comparing the orbital properties of stars across the mass spectrum will elucidate where different formation pathways dominate.

6.3 Summary

We assessed the rotational and orbital parameters, as well as the radii, of the binary dwarfs LP 349-25AB and 2M J0746AB. We do this by using the recent high-precision dynamical mass measurements of Bouy et al. (2004); Dupuy et al. (2010); Konopacky et al. (2010), the individual rotation velocity measurements of Konopacky et al. (2012), as well as rotation period solutions for each component (Berger et al., 2009; Harding et al., 2012a). From these data, we infer that the binary orbital plane is oriented perpendicular to the stellar spin axes within 10° . Such alignment has previously been observed in studies of solar-type binaries (Hale, 1994), and also more massive stars (Wheelwright et al., 2011). This work is the first direct evidence of spin-orbit alignment in the very low mass binary regime, which informs us on the formation of low mass binary stars.

The newly discovered period of rotation of LP 349-25B in this work (Chapter 4) pro-

vided an additional parameter to assess the system's orbital parameters. We find that the predicted radii of Konopacky et al. (2010) for a period of 1.86 ± 0.02 hours, are inconsistent with this orthogonal relationship. A radius of $\sim 1.45 R_J$ is required for such an alignment for LP 349-25B. This is in close agreement with a radius of $\sim 1.37 R_J$ (Dupuy et al., 2010), tentatively indicating that at least one component, LP 349-25B, of the system is coplanar.

In the case of 2M J0746AB, we find that the rotational and orbital planes of 2MASS J0746+20AB are consistent with a coplanar alignment to within $\leq 10^\circ$. We estimate individual mass estimates of $0.078 \pm 0.004 M_\odot$ and $0.073 \pm 0.004 M_\odot$ for 2MASS J0746+20A and 2MASS J0746+20B, respectively, as well as radii of $0.99 \pm 0.03 R_J$ for 2MASS J0746+20A and $0.96 \pm 0.02 R_J$. We outline the numerous binary formation models that are consistent with the observed alignment. Further theoretical work and a larger sample of very low mass systems will place tighter constraints on the most likely formation pathways.

“The grand aim of all science is to cover the greatest number of empirical facts by logical deduction from the smallest number of hypotheses or axioms.”

Albert Einstein

“Astronomy compels the soul to look upwards and lead us from this world to another.”

Plato



Flaring in M Dwarfs and the Associated Loop Oscillation Events

7.1 Introduction

During a stellar flare event, non-thermal energetic electrons are accelerated down coronal loops via magnetic reconnection events. The electrons follow the associated magnetic field lines which penetrate into the lower regions of the stellar atmosphere, where synchrotron radio emission and hard X-ray emission takes place. At this point of the flare, a sharp increase in white light emission, also called blue continuum emission, is observed. Although this phenomenon has been well characterized with optical spectroscopy, the source of the white light still remains a mystery. Based on the radiative hydrodynamic modeling of M type dwarfs by Allred et al. (2006), the characteristics of the flare spectrum should exhibit a clearly-defined Balmer jump at a wavelength of 3646 Å. However, current optical spectra do not show this expected Balmer jump, but rather exhibit a fascinating $\sim 9000 - 10000$ K blackbody spectrum. Moreover, the models predict that as the electron beam traverses the stellar photosphere, its energy is greatly absorbed and consequently is only heated to 100 - 1000 K, at most (Hawley & Fisher, 1992; Allred et al., 2006). Therefore, fundamental questions have arisen as to nature and cause of the white light, and whether this emission is due to blackbody emission or perhaps the predicted Balmer jump. More recently, Kowalski et al. (2010) observed the dMe4.5 star YZ CMi in U-band optical photometry using the New Mexico State University (NMSU) 1 m telescope, and also using high-cadence spectroscopy with the Apache Point

Observatory (APO) 3.5 m using the Double Imaging Spectrograph (DIS). They observed white light emission during a long lasting flare event, and found that the white light was the sum of a Balmer continuum and a hot $T \sim 10000$ K blackbody, where each component was in anti-correlation. Remarkably, the flare spectrum greatly resembled an A-type star spectrum, with the Balmer continuum in absorption - thereby explaining the observed anti-correlation. Indeed, hydrodynamic models of related spectra do not include such a blackbody component. Therefore, further spectroscopic observations are required in order to assess whether this component of the emission is present during peaks of a flaring event.

Together with colleagues from the University of Washington (UW), we decided to observe the dM4.5e flare star YZ CMi, and the M3.5Ve flare star AD Leo. We also observed the M4 flare star GJ 1243, and include these results in Appendix B. GUFi would provide simultaneous photometric monitoring of AD Leo and YZ CMi with 3.5 m APO spectroscopy. The photometric component presented in this chapter is extremely important for such observations in order to assess the correlation between spectral continuum/line variations, and the properties of the photometric lightcurves for stellar flares. Such simultaneous observations could provide evidence, or lack thereof, of the Balmer jump at bluer wavelengths. The author coordinated and conducted the photometric component of this campaign. This was necessary for the following reasons:

1. To provide high-precision flux calibration in V-band. VATT's 1.8 m mirror, coupled with the observational effectiveness of GUFi, would allow the spectroscopic observations to correct for slit loss.
2. The high-cadence (~ 2 ms readout) capability of GUFi would enable the study of substructure in small, moderate or large flare events inaccessible to spectroscopy. They provide an insight into localized mechanisms that may be aiding or driving the process.
3. The $H\alpha$ line behaves differently than the higher order Balmer lines during flares (Hilton et al., 2010), and is known to vary on short time-scales (Lee et al., 2010). However, $H\alpha$ observations of flare stars are difficult with spectroscopy using the 3.5 m APO, since the $H\alpha$ line saturates quite regularly during moderate flaring. High-cadence $H\alpha$ narrow band observations with GUFi will provide the necessary measurements of $H\alpha$ variability during flaring.

We were awarded time during February 2010 and April 2010 at VATT for photometric monitoring of these flare stars, which would be conducted simultaneously to 3.5 m APO

time-resolved spectroscopic monitoring by our UW collaborators, in April 7 and 8 2010 UT. This campaign aimed to further investigate these white light flare continuum events. In the following sections, we report on the results in a phenomenological manner, and conclude the chapter with a brief discussion of some possible explanations.

7.2 Selected targets and Observations

The targets for the campaign were selected based on those in the sample of Kowalski et al. (2010) and Hilton et al. (2010). AD Leo is a very active M3.5Ve dwarf (Montes et al., 2001), which has been studied extensively by many authors (Rodono' et al., 1989; Hawley & Pettersen, 1991; Bookbinder et al., 1992; Hawley et al., 1995; Mauas & Falchi, 1996; Cully et al., 1997; Hawley et al., 2003; Hilton et al., 2010, and references therein). During these studies, many flares have been observed that are similar to those observed in the Sun, exhibiting properties such as impulsive continuum emission, as well as long-lived chromospheric emission. The dwarf is located at a distance of ~ 4.9 pc, and has an M_V of 9.43 (Høg et al., 2000) and is the brightest very active flare star that is visible from the northern hemisphere. YZ CMi is an dM4.5e flare star (Jenkins et al., 2009), located at a distance of ~ 6 pc, and has an M_V of 11.1 (Perryman et al., 1997; Koen et al., 2010). Like AD Leo, this has also been a much observed flare star, e.g. (Moffett, 1974; Kahler et al., 1982; Worden et al., 1984; van den Oord et al., 1996; Hawley et al., 2007; Kowalski et al., 2010), as a results of its close proximity and strong flaring activity. In order to maximize our chance of observing flaring events, these targets were chosen for this campaign.

Observations were conducted as follows: YZ CMi was observed between February 22 2011 UT - February 26 2011 UT, in the Johnson B- (3510 - 6270 Å) and V-bands (4810 - 6820 Å) using GUF1 on the 1.8 m VATT telescope. Exposure times of < 0.2 seconds were used in order to sample the lightcurves at high-time resolution, and thus detect sub-structure in any flaring events on time-scales ≤ 0.2 seconds. We obtained ~ 22 hours of photometric data and ~ 500000 frames, and detected 20 flaring events over these observations. Some observations were subject to poor weather conditions (heavy and intermittent cloud throughout). Frames were windowed to sub-frame formats of 80×200 pixels from the native resolution of 512×512 , which allowed for a reference star in the field that was suitable for differential photometry.

AD Leo was observed from February 18 2011 UT - February 26 2011 UT, and again on April 8 2011 UT - April 13 2011 UT, in the Johnson B- and V-bands, and in a narrow H α band (6560 - 6610 Å, centered on 6585 Å). Again, frames were windowed to 60×280

Source	Total Time (~hrs)	Date of Obs. (UT)	Length of Obs./# frames (~hrs/#)	Exp. Time (s)	Flares #
YZ CMi	22	2011 Feb 22	4.32/64497	0.28746	3
		2011 Feb 23	5.52/82500	0.23704	2
		2011 Feb 24	3.01/62400	0.087	0
		2011 Feb 25	4.58/136000	0.11759	10
		2011 Feb 26	4.33/128607	0.11759	5
AD Leo	27	2011 Feb 18	2.89/97200	0.28746	2
		2011 Feb 22	4.13/90000	0.15917	0
		2011 Feb 23	4.52/99000	0.15917	1
		2011 Feb 26	2.85/84634	0.11759	0
		2011 Apr 08	1.81/16292	0.11759	0
		2011 Apr 09
		2011 Apr 11	2.68/80000	0.11710	1
		2011 Apr 12	2.42/72000	0.11759	1
		2011 Apr 13	5.56/165430	0.11759	1
Source	Band	Readout Rate (MHz)	Amplifier	Window (pixels)	Instruments
YZ CMi	V	1	Conv.	80 × 200	GUF/NMSU/ARCSAT
	V	1	Conv.	80 × 200	GUF/NMSU/ARCSAT
	V	1	Conv.	80 × 200	GUF/NMSU/ARCSAT
	V	1	Conv.	80 × 200	GUF/NMSU/ARCSAT
	B	1	Conv.	80 × 200	GUF/NMSU/ARCSAT
AD Leo	V	1	Conv.	60 × 280	GUF/NMSU/ARCSAT
	V	1	Conv.	60 × 280	GUF/NMSU/ARCSAT
	V	1	Conv.	60 × 280	GUF/NMSU/ARCSAT
	B	1	Conv.	60 × 280	GUF/NMSU/ARCSAT
	B		Conv.	60 × 280	GUF/NMSU/ARCSAT/DIS

	B	1	Conv.	60 × 280	GUF/NMSU/ARCSAT
	B	1	Conv.	60 × 280	GUF/NMSU/ARCSAT
	H α	1	Conv.	60 × 280	GUF/NMSU/ARCSAT

Table 7.1: Flare Star Observation Details.

Here we show the observation details of the flare star campaign, that was carried out using the GUF photometer on VATT. These were taken simultaneously to the NMSU 1 m telescope and 0.5 m ARCSAT telescopes at APO, which provided Sloan u' - g' photometry, albeit at much slower cadence than GUF. Finally, time-resolved optical spectra from 3400 - 9000 Å was due to be obtained using the DIS spectrometer on the 3.5 m APO on April 8 2011 and April 9 2011 UT, as indicated above. However, both telescopes were shut on April 9 2011 UT due to poor weather, and only VATT was open April 8 2011 UT - APO could not open, again, as a result of weather conditions (snow).

pixels in order to achieve frame rates of ~ 9 Hz. We obtained ~ 27 hours of data, including ~ 705000 frames, and we detected 6 flares during these observations. Unfortunately, we could not obtain data on all of these nights due to poor weather (cloud (Feb) and snow (Apr) conditions).

GUFi was well suited for these observations, since the photometer incorporates an L3-CCD system, has low readout noise, high-cadence imaging capabilities, and is ideal to successfully resolve sub-structure in small/large stellar flare events as we will see in the following sections. We show observation details in Table 7.1. The simultaneous component of the campaign was carried out on April 8 and April 9 2011 UT. While the GUFi photometer obtained high-cadence data in the Johnson B-band, V-band and $H\alpha$ on VATT, the NMSU 1 m telescope and 0.5 m ARCSAT telescopes at APO provided Sloan u' , g' and r' photometry (~ 10 seconds with a ~ 27 second readout), albeit at much slower cadence than GUFi. Finally, time-resolved optical spectra from 3400 - 9000 Å was due to be obtained using the DIS spectrometer on the 3.5 m APO. However, both telescopes were shut on April 9 2011 UT due to poor weather, and only VATT was open April 8 2011 UT - APO could not open, again, as a result of weather conditions (snow).

These events were unfortunate, since the original campaign proposal relied on the simultaneous monitoring of flaring from YZ CMi and AD Leo in both time-resolved photometry *and* spectroscopy, in order to investigate the correlation in the large and small structure of stellar flares from M dwarfs. We plan to pursue this simultaneous campaign in the coming 2013A semester. Nevertheless, VATT, NMSU and ARCSAT did obtain simultaneous monitoring data over the course of the observations outlined in Table 7.1. Therefore, in this chapter we present the optical photometric component of this campaign, where we highlight the effectiveness of high-cadence data from GUFi (B-, V-band and $H\alpha$) in detecting sub-structure in M dwarf flares, and compare the lightcurves of NMSU and ARCSAT in the bluer wavelength ($u' - r'$) regimes.

7.3 Results

In this section we present the photometric results from the flare campaign to observe flaring events in the mid-M dwarfs YZ CMi and AD Leo. In each of the sections included here, we show individual flaring events that were detected on a given observation night. For those that we detect sub-structure in the rise and decay of events, we also show binning factors. In the case of YZ CMi, we include some photometric lightcurve examples of Sloan $u' - g'$ flaring that were observed by ARCSAT simultaneous to the VATT (GUFi) B-, V- or $H\alpha$

observations. Based on the detections in these lightcurves, we can consider the following main points in this work:

1. Investigate sub-structure in the flaring events as a result of high-time resolution imaging.
2. For larger flares, establish periods of possible coronal loop oscillation events.
3. Flare statistics.

In each target's case, we highlight the flares that were detected during the campaign, but we chose to focus on the largest of these events, and how they evolved morphologically before, during and after, the flare.

7.3.1 YZ CMi (dM4.5e)

We report 20 flaring events for the flare star YZ CMi, which were detected over ~ 22 hours of observations encompassing ~ 500000 frames. We used the Johnson B- and V-band, and exposure times of < 0.2 seconds. We observe erratic behavior in the YZ CMi data, specifically for February 25 2011 UT, where we highlight remarkable micro-structure in the flares, as shown in Figure 7.1. We note the repeating structure in the lightcurves, where flaring events occur with subsequent activity thereafter. These lightcurves show an arcade of flares, with perhaps sequential brightening at the footprints of the loops, which then continues. Could these re-occurring events be connected to the energies provided in the flaring that came before - post hoc ergo propter hoc? Indeed, this is something has not yet been characterized, where flaring can manifest itself as stochastic events, with some or no correlation to other bursts in close proximity. These precursor flares have been seen prior to larger events in other studies (Moffett, 1974; Kowalski et al., 2010).

The largest flare that we detect was from February 26 2011, at ~ 3.30 UT, where we find a relative delta magnitude of ~ 1 magnitude. We show this flare, amongst other events, in Figure 7.2 (lightcurve C) - we have binned these data by a factor of 8 to illustrate the smaller structure that has been detected, in the bottom half of Figure 7.2. The possible presence of loop oscillations are the structures following the decay in the first two flares, which we discuss further in § 7.4. There is clearly a precursor flaring event at ~ 3.18 UT as shown in lightcurve A, and zoomed in on in lightcurve B, which increases the B-band flux by $\sim 70\%$ and occurs prior to the larger flare. The impulsive rise to flare peak occurs in ~ 1.2 minutes, where the B-band value in this case is $\sim 220\%$ greater than the flux in

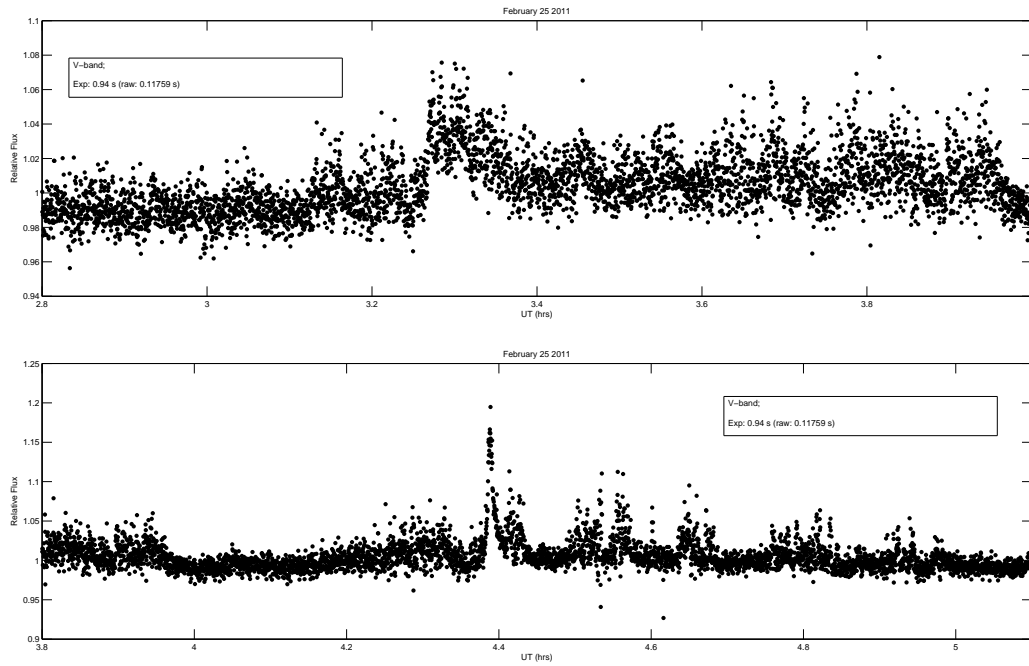


Figure 7.1: Impulsive flaring from YZCMi on February 25 2011 UT. We observe fascinating sub-structure in the lightcurve of the dwarf, highlighting the possibility of a complex series of flaring events, supporting previous observations of e.g. Moffett (1974); Kowalski et al. (2010), who identify such precursor flares as the onset of larger events to follow.

quiescence. The decay phase, containing many possible loop oscillation events, takes ~ 8 minutes, and the B-band flux remains at a higher state of quiescence until returning to almost the original quiescent state at ~ 3.38 UT. We also show the simultaneous $u' - g'$ ARCSAT lightcurves in Figure 7.3.

The advantage of GUFi's high-time resolution is quite obvious in this lightcurve. For example, the precursor flare was sampled by 5 data points in u' by ARCSAT, whereas GUFi sampled the flare with >1200 frames. These data rate comparisons are even more important for sub-structure within the event, as we will see in § 7.4. However, the QE of the GUFi Andor iXon DV-887 chip is virtually not usable ≤ 4000 Å based on the low percentage transmission at these wavelengths, as shown in Chapter 2, Figure 2.1b. By contrast, the ARCSAT detector's QE peaks in the UV wavelength range. Therefore, simultaneous observations using these two photometers proved to be quite effective during this campaign, since we essentially had an operational QE range from $\sim 1000 - 10000$ Å, thus each instrument complemented the other and could provide high quality data in a given wavelength

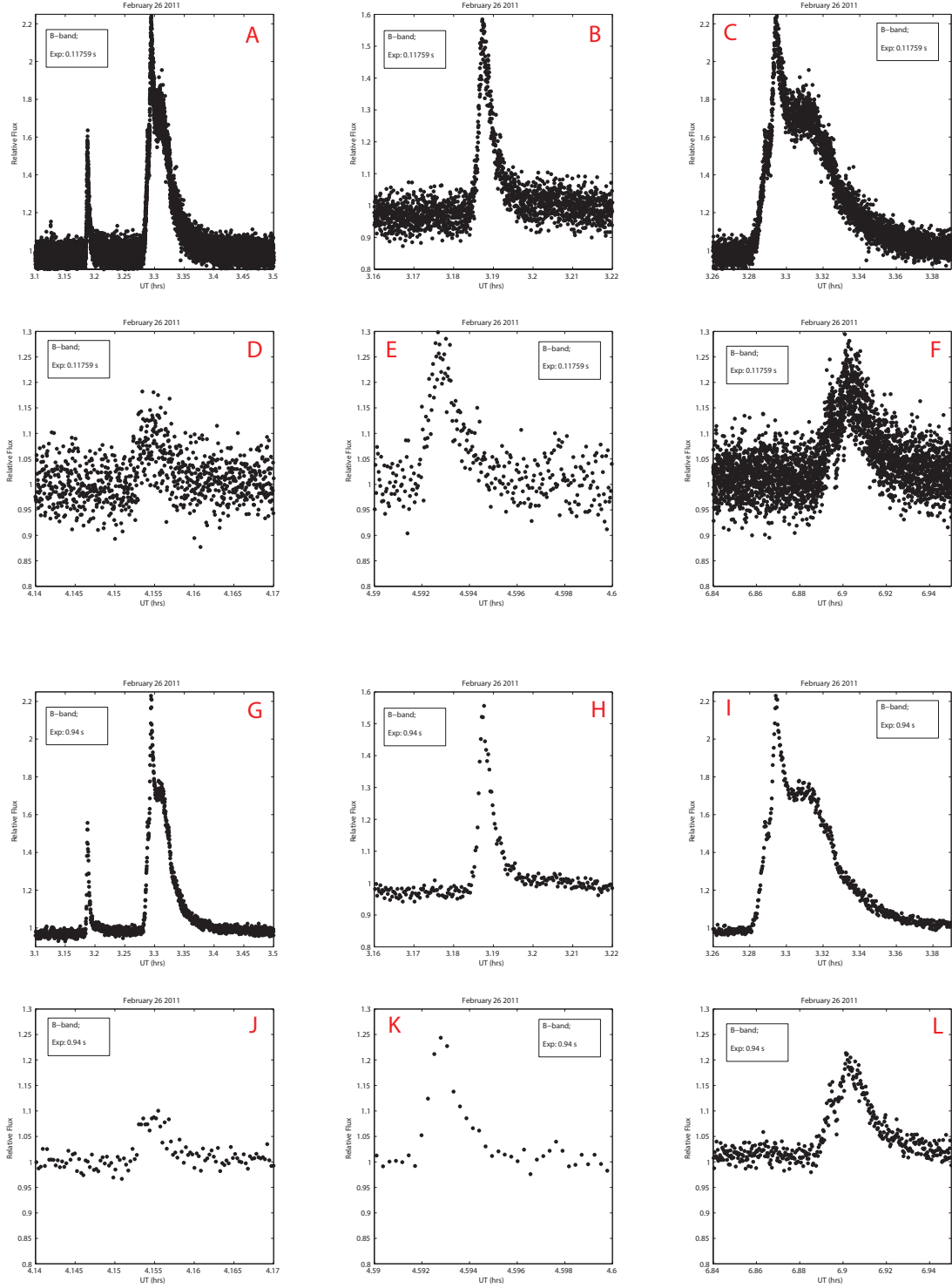


Figure 7.2: Flaring from YZ CMi in B-band from February 26 2011 UT. Lightcurves (top) A - F show the raw data, taken at 0.11759 seconds. We present the lightcurves sequentially as the flaring happened throughout the observation. Similarly, lightcurves (bottom) G - L show the same flares, but binned by a factor of 8, to 0.94 seconds. We highlight the precursor flare and largest flare event, shown in the first and third rows.

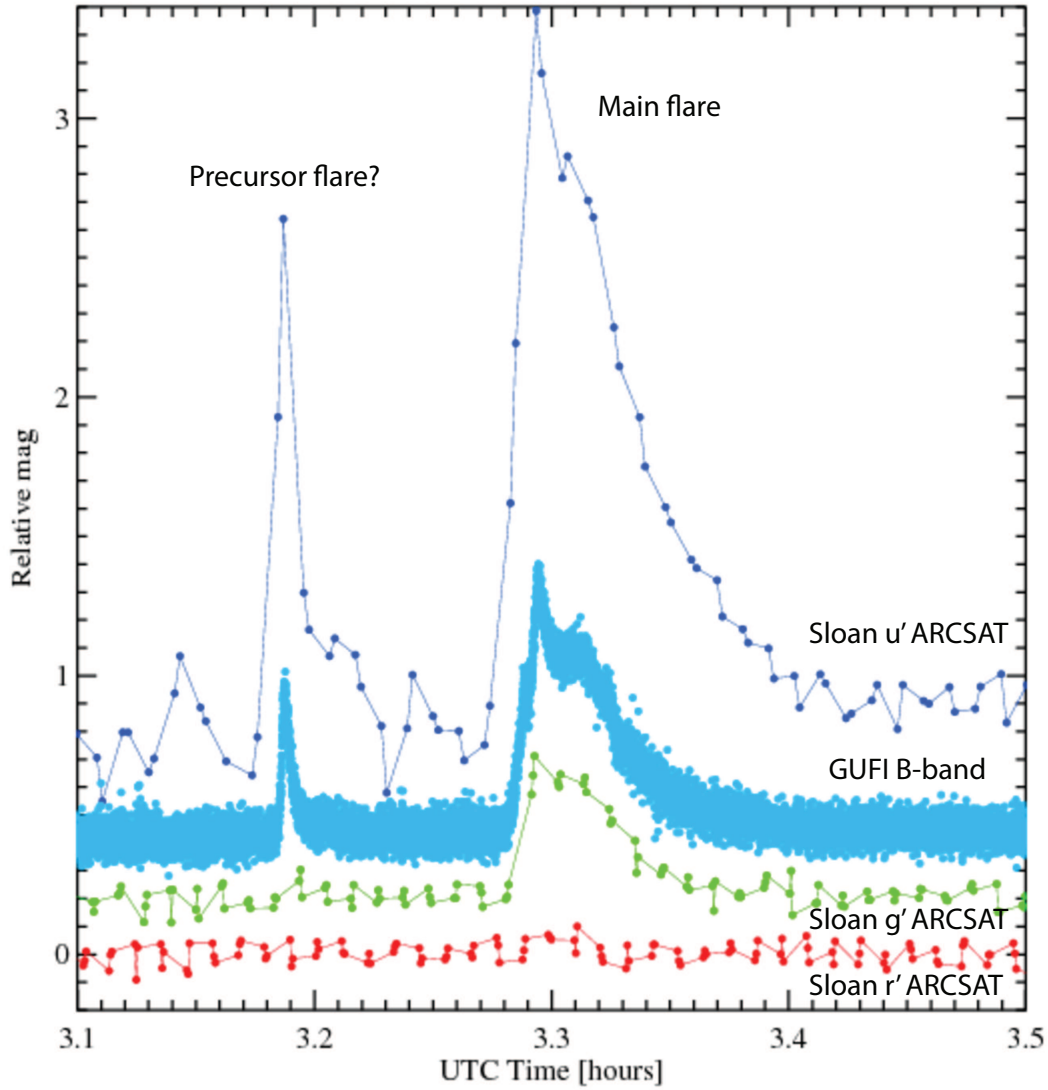


Figure 7.3: Simultaneous observations of YZ CMi on February 26 2011 UT, by ARCSAT using u' , g' and r' , and GUFi using B-band, as indicated above. The precursor flare at ~ 3.18 UT detected by ARCSAT u' was sampled with 5 data points, whereas GUFi obtains >1200 frames. We note however, that the QE of GUFi is virtually not usable ≤ 4000 Å. By contrast, the ARCSAT detector's QE peaks at UV wavelengths.

range. We refer the reader to the APO website here²³, which contains detailed descriptions of the ARCSAT and NMSU observatories, and in-situ instruments. We discuss the causal mechanisms for the observed flaring of YZ CMi in § 7.4.

7.3.2 AD Leo (M3.5Ve)

We obtained ~ 27 hours of data on the M3.5Ve flare star AD Leo. These data were taken over two separate epochs - in February and April 2011, in the Johnson B- and V-bands, and in the $H\alpha$ narrow band filter, where ~ 705000 frames at rates of ~ 9 Hz. We detected 6 flares in total during these observations, as shown in Figure 7.4 above. Although we observed the dwarf for ~ 5 more hours than YZ CMi, we only saw ~ 30 % of the flaring rate, indicating that YZ CMi was in a much more active state over this timescale. The flaring that we detect by GUFi were mostly small events in B- and V-band (up to ~ 10 % amplitude variability i V-band, e.g. lightcurve A in Figure 7.4).

However, like YZ CMi, although we did not have simultaneous DIS spectroscopy via the 3.5 m APO, we did have simultaneous ARCSAT u' , g' and r' photometry, as shown in Figure 7.5. Interestingly, another precursor flare was detected at ~ 9.42 UT, just before the onset of the flare rise phase of the main flare at ~ 9.8 UT, which lasted for ~ 12 minutes. It is quite clear in Figure 7.5 that the ARCSAT u' has sampled this event to much greater detail than other wavebands. This is, of course, is not unexpected since flaring will have higher amplitude variations at shorter wavelengths. The decay of the flare continues for another ~ 30 minutes, and again, u' flux levels are in a much higher state of quiescence thereafter (\sim difference of 0.1 of a magnitude), and until the end of the observation, as shown. In figure 7.6, we show the 0.11759 second (~ 2 ms readout) observations of GUFi in V-band (yellow), and the ~ 10 seconds (~ 27 second readout) observations of ARCSAT in r' (red). Since the V-band and Sloan r' filters overlap in their waveband ranges (V: 4810 - 6820 Å; r' : 5200 - 7600 Å), this figure was included to highlight the effectiveness of high-time resolution flare star imaging. GUFi clearly detects a flare at ~ 9.8 UT, whereas it would be difficult to establish the presence of this same event in the r' lightcurve. We note however, that the QE of GUFi is at its strongest at these wavelengths, whereas the QE of the ARCSAT detector is quite weak in visible, as opposed to the UV. In Figure 7.5 we highlight the effectiveness of ARCSAT in the UV, in detecting the precursor to the large flare, as well as the main flare structure, that GUFi could not in the V-band.

²³www.apo.nmsu.edu

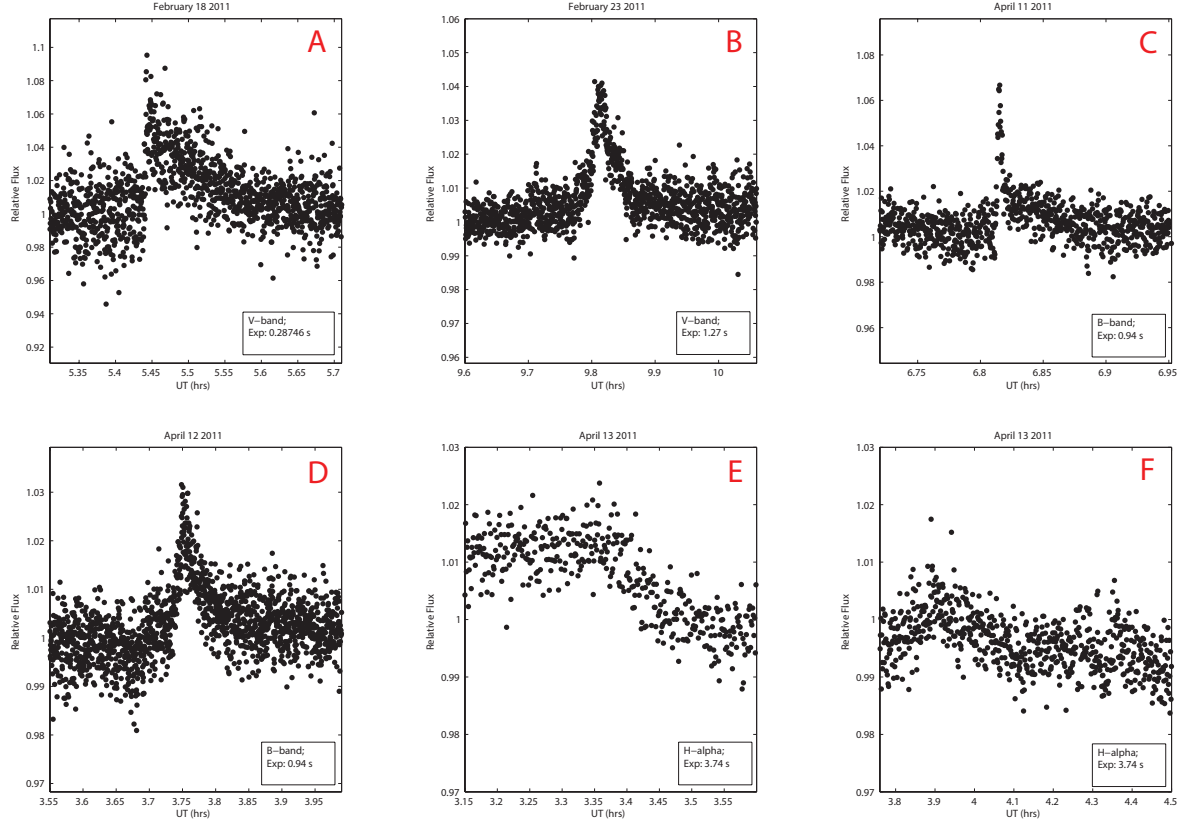


Figure 7.4: Flaring events from AD Leo over the course of our two separate epochs of observations in February and April 2011. Data were taken at ~ 9 Hz (0.11759 seconds) in order to sample sub-structure in the detected flaring events. As before, the flares in lightcurves A - F are shown sequentially as they happened over the course of the observation epochs. The bands and exposure times used are marked in each figure in the bottom left. We note that the $H\alpha$ band was a narrow band filter (6560 - 6610 Å, centered on 6585 Å), and therefore the levels of transmitted flux were not as high. To increase the SNR in the lightcurves, we binned the data by a factor of ~ 30 , to exposure times of 3.74 seconds.

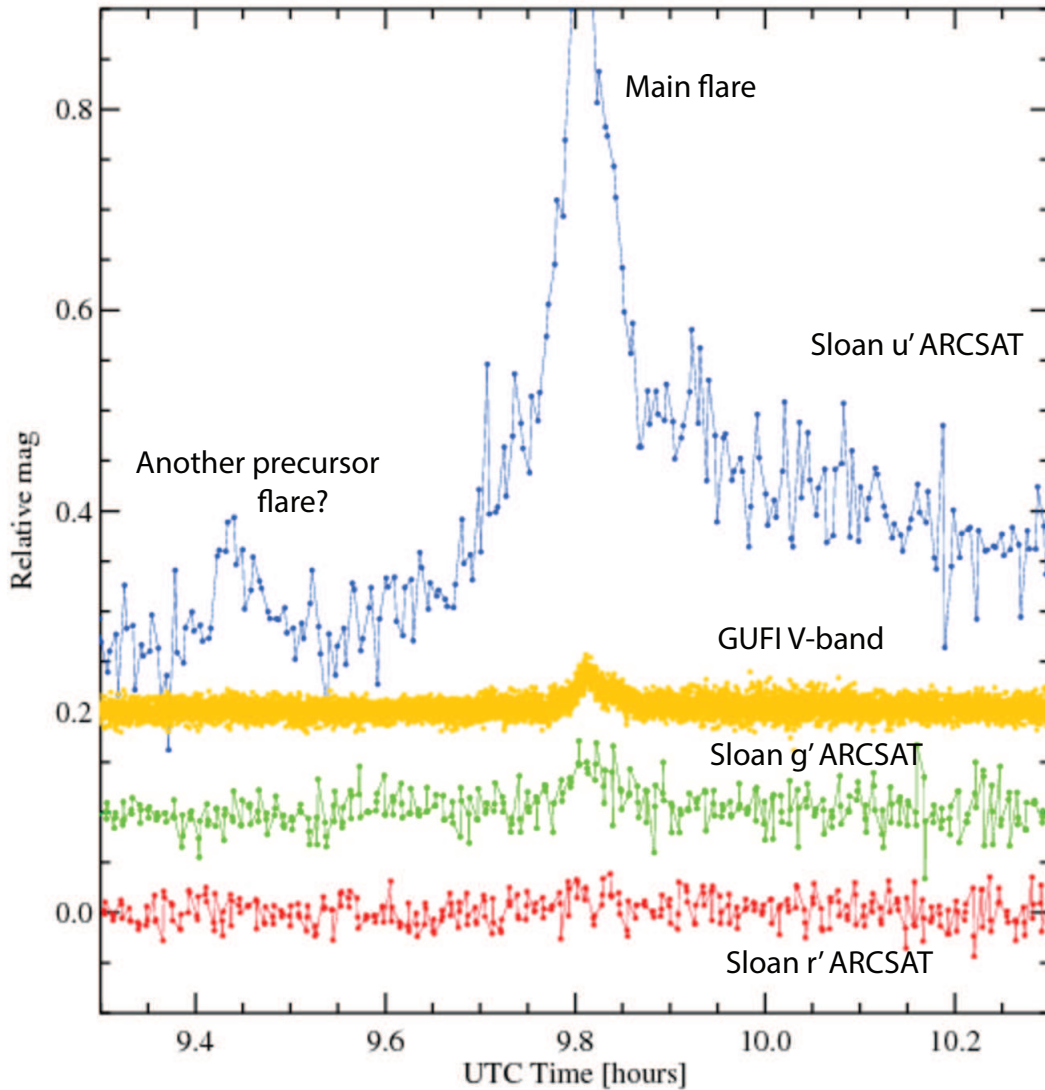


Figure 7.5: Here we show simultaneous observations of a detected flare from AD Leo on February 26 2011 UT. Observations were obtained in V-band by the GUFi photometer on VATT (0.11759 seconds), as well as the Sloan u' , g' and r' range (10 seconds; with a 27 second readout), as labeled above. Again, we highlight a precursor flare, as detected on the YZ CMi flare of February 26 2011 UT (Figure 7.3, ~ 3.18 UT).

We discuss the possible detection of loop oscillation events in the YZ CMi flare of February 26 2011 UT, ~ 3.18 UT, in the following section. Indeed, similar structure could be argued in one of the largest of the AD Leo flares during the slow decay phase, as shown in the u' lightcurves in Figure 7.5, and to a lesser extent in the V-band GUFi lightcurves, where some scatter is clearly present during these possible oscillations. Although simul-

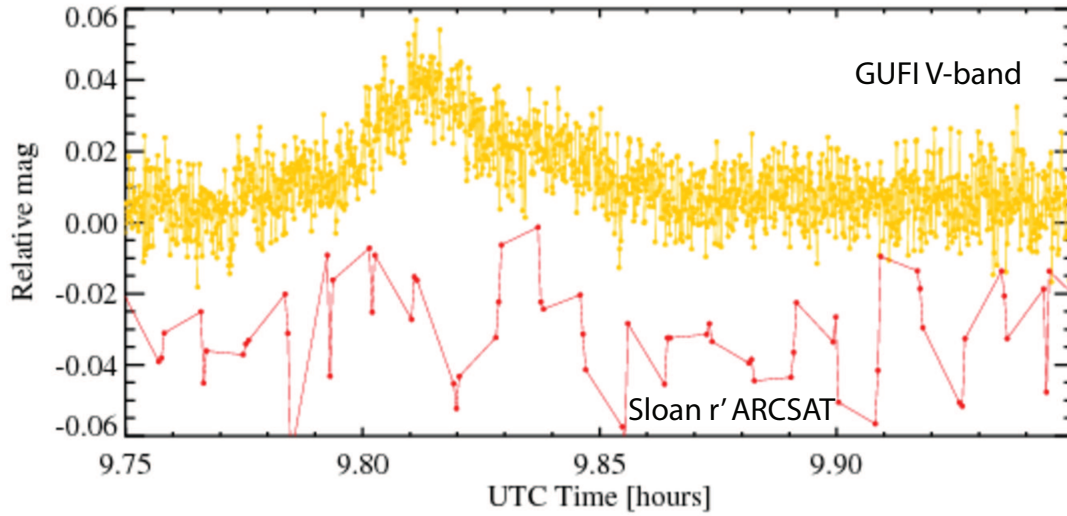


Figure 7.6: We show the 0.11759 second (~ 2 ms readout) observations of GUVI in V-band (yellow), and the ~ 10 seconds (~ 27 second readout) observations of ARCSAT in r' (red). We include this figure as an example of the effectiveness of high-time resolution flare star imaging.

taneous spectra are required to establish what correlated morphologies may be linking the behavior of spectral lines and the photometric oscillations, we can still consider what mechanisms may be at work in the eruptive regions of these stars. We consider this in § 7.4.

7.4 The Periodic Variations due to Loop Oscillations from YZ CMi

In this section we discuss the YZ CMi flare of February 26 2011 UT, that occurred at ~ 3.28 UT. We consider this flare in terms of the periodic variations that we detect in the slow decay phase of the event. We detect these variations with a period of $\sim 10 - 15$ seconds, where the oscillations appear to smooth out toward the end of the decay. These results are quite similar to those detected from the active star EQ PegB by Mathioudakis et al. (2006), who reveal periodic variations of a white light flare that was observed with ULTRACAM on the William Herschel Telescope (WHT). Intriguingly, they also detect variations of about 10 seconds in their data, and do so via Wavelet analysis. They consider a number of causal phenomena for these detected intensity variations. First, the presence of acoustic waves in the region of the event, which are impulsive-driven within a loop. Second, they consider a

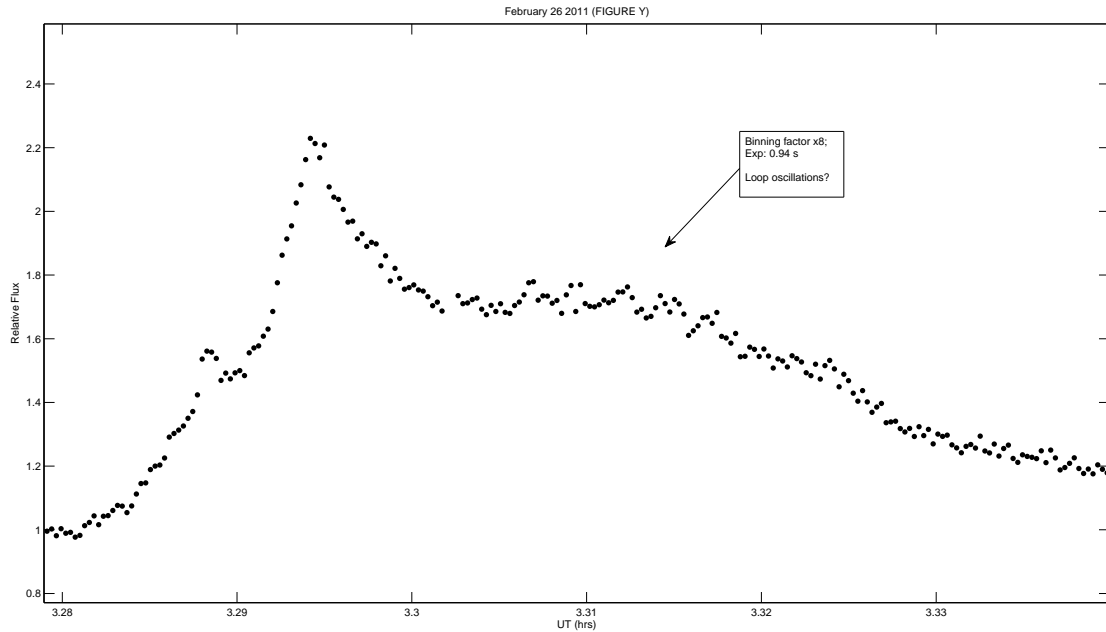
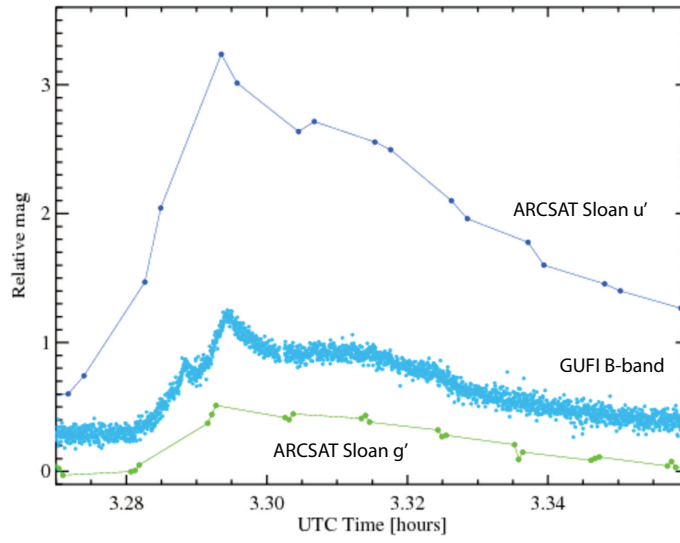


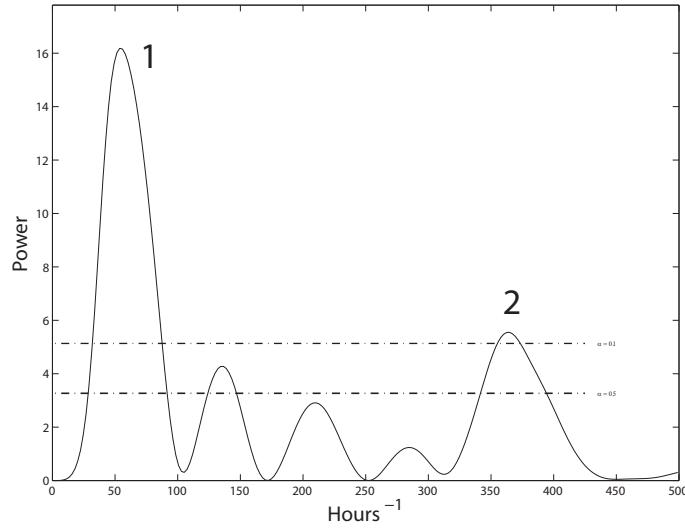
Figure 7.7: We show the B-band lightcurve of the flare containing loop oscillations from YZ CMi, February 26 2011 UT. The impulsive rise to flare peak occurs in ~ 1.2 minutes, where the B-band value in this case is $\sim 220\%$ greater than the flux in quiescence. The decay phase, containing many possible loop oscillation events, takes ~ 8 minutes, and the B-band flux remains at a higher state of quiescence until the end of the observation, as is clearly evident above. Periodic variations, indicated by the arrow in the figure, were detected via the Lomb Scargle periodogram, to $\sim 10 - 15$ seconds.

magnetohydrodynamic wave and its associated interaction with the presence of magnetic field lines, presumably the induced perpendicular perturbations with modulations to this period. And finally, magnetic reconnection events during a flare due to the reconnecting of flare loops during the main flaring event.

Previous studies have also detected periodic oscillations in stellar flares and other energetic events in flare stars. For example, McKenzie & Mullan (1997) have revealed modulations of 10 - 60 second from non-flaring solar corona, whereas Kane et al. (1983) reported 8 second oscillations of hard X-ray and microwave solar flare bursts. Kowalski et al. (2010) have also highlighted this modulated behavior in a large flare of YZ CMi that they detect, and consider reconnecting loops as a possible cause of this behavior. Similarly, flares within coronal loops have been reported, as well as short duration transient detections from flaring, and flare oscillations in the X-ray have also been discovered (Rodonò, 1976; Mullan et al., 1992; Mathioudakis et al., 2003; Mitra-Kraev et al., 2005). Quite often the smallest



(a) Simultaneous UV and optical photometry.



(b) Lomb Scargle periodogram analysis.

Figure 7.8: YZ CMi: (a) We show simultaneous observations of VATT (GUFi) and ARCSAT which cover UV and optical wavelengths. We note that in the GUFi B-band lightcurve in this figure is the raw lightcurve with exposure times of 0.11759 seconds, whereas previously in Figure 7.7 we show the binned 0.94 second frames. Note the difference in sampling of the ARCSAT and GUFi lightcurves, where GUFi obtains ~ 2000 frames during this flare event. The oscillations are undetectable in the g' , with only some indication of some change in structure in u' . (b) The Lomb Scargle analysis of the oscillations (conservatively defined between $\sim 3.3 - 3.34$ UT). We label two peaks in the power spectrum. '1' corresponds to the over all trend in the data for that part, which yields a period in the spectrum of ~ 1.5 minutes. '2' indicates what we have identified as the oscillation events in the decay of the flare, of $\sim 10 - 15$ second modulation.

detections of flares can be skeptical confirmations of such events, since instrumental noise and the effects of sky background (scintillation and so on) can severely effect such signals. It was therefore quite useful in this work to have the ARCSAT and NMSU telescopes of APO at our disposal to simultaneously observe these events. However, as outlined in previous sections, GUFi's much higher cadence meant that it was sensitive to much smaller flaring events than the other instruments, where cadences were up to 40 seconds. Real loop oscillation events are expected to be periodic, or at least quasi-periodic in nature. The ARCSAT photometry indicates that there is some structure present, but the only evidence for periodicity in this case is from GUFi. Thus we cannot claim oscillation events from the ARCSAT component of the observation - although the detection of such events is possible if they are on longer timescales than the ARCSAT cadence.

In figure 7.7, we present possible periodic oscillations in the decay of a flare from YZ CMi. The analysis of the event, and period of $\sim 10 - 15$ seconds was established via the Lomb-Scargle periodogram. These variations were quite difficult to evaluate because of the morphology of the lightcurve. These variations are sitting on top of the larger flaring event, and thus the periodogram yields periodic solutions for many shorter, and longer trends in the data. In Figure 7.8b we show this analysis, and conservatively define the period where the oscillations took place as being between $\sim 3.3 - 3.34$ UT. We label two peaks in the power spectrum. '1' corresponds to the over all trend in the data for that part, which yields a period in the spectrum of ~ 1.5 minutes, as expected. '2' indicates what we have identified as the oscillation events in the decay of the flare, of $\sim 10 - 15$ second modulation. In Figure 7.8a, we show simultaneous observations of VATT (GUFi) and ARCSAT which cover UV and optical wavelengths. We note that in the GUFi B-band lightcurve in this figure is the raw lightcurve with exposure times of 0.11759 seconds, whereas previously in Figure 7.7 we show the binned 0.94 second frames. Note the difference in sampling of the ARCSAT and GUFi lightcurves, where GUFi obtains ~ 2000 frames during this flare event. The oscillations are undetectable in the g' , with only some indication of some change in structure in u' .

Although we do not have simultaneous spectroscopic observations of this event, we can speculate as to what may be causing these flaring oscillations in the flaring region of YZ CMi. Perhaps these are white light flare events. Indeed, the Johnson B-band includes a lot of Balmer emission lines - thus the question arises whether this variability is due to continuum emissions, or due to Balmer lines or Ca II, for example? Perhaps the fact that the level of agreement over a range of broadband filters is strong, indicating continuum emission (e.g. Figure 7.3 - although we have pointed out that these are very tentative variations for

the redder ARCSAT bands). The amplitude of the oscillations seem to be consistent during the decay of the flare, until they appear to cease at ~ 3.34 UT. Upon inspection of other similar flaring events from YZ CMi in the U-band, and in optical spectroscopy (Kowalski, private communication), the structure and temporal morphology of the flare seems to be consistent. Of course there are many types of flaring events which can cause a wide range of lightcurve shapes and trends. Particularly, what is causing the ‘flat’ part of the decay that contains the oscillations in these events? And what does this imply for flare physics? The spectral properties of the models in terms of the widths and profiles of the lines are reproduced quite well for the chromosphere (e.g. Balmer lines). The models also predict levels of continuum emission, but they predict far too much Balmer continuum - thus they are not effectively reproducing the heating distribution of the atmosphere; perhaps the problems lie in the difficulties in predicting more heating at higher particle densities, or at lower regions of the atmosphere (see Kowalski et al. (2010, and references therein)) - how is energy being transported at lower altitudes? The properties of the lightcurves in this section could imply a complex group of reconnecting loops, perhaps occurring in a sequential manner. Furthermore, similar to the processes discussed in earlier chapters, these magnetic reconnection events have the ability to accelerate non-thermal electron beams to the lower atmosphere of such stars, which in turn could produce the optical continuum emission observed here. Although reconnection is a dynamical process, and cannot be easily predicted, a chain reaction of events in these emitting regions could sustain the flaring reported here, if the flaring persists. Further observations, this time simultaneously taken to high-resolution time-resolved spectroscopy could yield interesting results in to the investigation in to this blue continuum emission. We aim to resume this work in the semester starting 2013A.

7.5 Summary

We report on high-time resolution photometric observations of the dM4.5e flare star YZ CMi, and the M3.5Ve flare star AD Leo. These were taken with the GUFi photometer, simultaneously to the ARCSAT and NMSU telescopes of APO, who provided UV and optical simultaneous photometric monitoring. Although two nights of observations were also awarded using the DIS spectrometer on the 3.5 m APO, poor weather prevented these observations. Nevertheless, we report on ~ 22 hours of flare star monitoring from YZ CMi, and ~ 27 hours from AD Leo. 20 flares were detected from the former, and 6 from the latter, implying that YZ CMi was in a much more active state over these timescales. ARCSAT provided ~ 40 second cadence $u' - r'$ monitoring for all observations. GUFi was ideal

for the photometric component of this campaign, since its high-cadence capabilities enabled the study of much smaller structure in the lightcurve than a large amount of previous photometric monitoring work.

Specifically, for YZ CMi, we report on the possible detection of loop oscillation events in the decay of a large flare detected by GUVI in B-band, which we identify as a result of observations which were taken at exposure times of ~ 0.1 seconds. These observations aimed to observe these sub-structures in small to large flare events that are inaccessible to spectroscopy (due to the slower cadence). We detect periodic variations in the oscillations of $\sim 10 - 15$ seconds, based on Lomb Scargle periodogram analysis. These oscillations could be due to a number of causal mechanisms, however without simultaneous spectroscopy, it is difficult to conclusively assess the contribution of e.g. spectral lines or continuum emission, or others. One possibility is that magnetic reconnection events have the capability of providing a bombardment of non-thermal electrons from these intense magnetic regions to the lower regions of the stellar atmosphere, which could produce emissions of this kind.

“The most exciting phrase to hear in science, the one that heralds new discoveries, is not ‘Eureka!’ (I found it!) but ‘That’s funny’ ... ”

Isaac Asimov

“To suppose that the eye with all its inimitable contrivances for adjusting the focus to different distances, for admitting different amounts of light, and for the correction of spherical and chromatic aberration, could have been formed by natural selection, seems, I confess, absurd in the highest degree.”

Charles Darwin, *The Origin of Species*



Conclusions and Future Work

8.1 Discussion and Conclusions

In this thesis, we have presented photometric data that has investigated the possible optical signatures from magnetospheric phenomena from stars at the end of the main sequence, and for stars below the sub-stellar boundary. Amongst other features present in the atmospheres of these objects, powerful magnetic mechanisms could also be responsible for the photometric periodic and aperiodic variability, as well as the impulsive events, detected in this work. In order to carry out these observations and obtain these data, we designed, built and constructed, two instruments during this work, both capable of high-time resolution imaging, each designed specifically with high sensitivity and cadence in order to detect transient events from the active sample of M and L dwarfs in this thesis. In saying this, as outlined in the relevant chapters, both instruments can be used over a wide range of astronomical fields, and are now stationed as facility instruments on 2 meter- and 5 meter-class telescopes in Arizona and California, respectively. These will be used in the on-going projects currently being pursued by the candidate and co-workers, as discussed in the sections that follow.

The Galway Ultra Fast Imager (GUFI) photometer was commissioned on the 1.8 m Vatican Advanced Technology Telescope (VATT), on Mt. Graham, Arizona, in May 2009. Once commissioned and successfully tested, we commenced the photometric campaign to establish the above correlation, if any, between the optical and radio regimes, for six radio detected ultracool dwarfs that were visible from the VATT Site. In this work, we report optical photometric periodic variability from five of these dwarfs - the M dwarf tight bi-

nary LP 349-25B, the L dwarf binary 2MASS J0746A, the M8.5 dwarf LSR J1835, the M9 dwarf TVLM 513, and the L3.5 dwarf 2M J0036. One other dwarf, the M9.5 dwarf BRI 0021, shows persistent variability with the possibility of periodicity being detected in the data. All dwarfs are rapid rotators ($>15 \text{ km s}^{-1}$), and exhibit the optical periodicity in the form of quasi-sinusoidal periodic variations, that are sustained on timescales of up to ~ 5 years in the case of some targets. The amplitude variability of the targets in the sample was detected to be varying at levels between $\sim 0.2 - 1.1\%$ in the I-band, and $\sim 0.8 - 1.0\%$ in the R-band. LP 349-25B reveals changes in phase and amplitude over given epochs ($\sim 0.22 - 0.71\%$), which is likely due to aperiodic variations with periodic variations from one member, or perhaps the effect of the other member via the superposition of two variable signals. 2M J0746, the second binary in the sample, also shows amplitude variability to this level ($\sim 0.20 - 0.76\%$). In all cases, the periodic variability is associated with the rotation of the dwarf. Coupled with this rotational modulation, we consider a number of causal phenomena for the variability. These include atmospheric dust, magnetic cool spots, or the presence of photospheric or chromospheric (auroral) hot spots. We conclude that, although magnetically active, dust cannot be discounted as a feature that could be responsible for, or perhaps effect the morphology of the lightcurves in our sample. We can show however, that three out of four radio pulsing dwarfs also exhibit optical variability, and in these three cases, the same detected period as that of the radio bursting. Furthermore, these periodic variations are consistent on timescales of years for all dwarfs. The fourth pulsing dwarf, 2M J0746A, was detected as the periodically varying optical sources, despite the presence of radio pulsing from the other member. This could be due to a number of scenarios, including the orientation of the dwarf's magnetic field alignment with respect to the equatorial axis, or alternatively that the primary member is exhibiting stronger optical emissions.

For one target in particular, the M9 dwarf TVLM 513, we report stable periodic variability in terms of phase over a ~ 5 year baseline, with a period of 1.95958 ± 0.00005 hours. This data sought to investigate the spatial and thermal stability of the feature responsible for the periodic variability. It showed stable phase, indicating that the feature is not moving. This photometric data was also part of a larger campaign, which included simultaneous radio and spectroscopic monitoring of the dwarf (Hallinan et al., 2012). These data have revealed a high degree of correlation between all signals, right across the electromagnetic spectrum. We have shown in this work, that the photometric Sloan i' and Johnson I-band GUGI data is also in phase with the radio and spectroscopic data, including $H\alpha$, $H\beta$, TiO, NA D, OI 5577, R-band, and g' . The feature, or features, could therefore occupy the

same approximate physical location on the dwarf's surface. As put forward by Hallinan et al. (2012), perhaps these data are all being driven by one process in the magnetosphere of the dwarf? The established electron cyclotron maser instability, responsible for the periodic bursts of radio emission, is also responsible for accelerating high-energy electrons on to the stellar photosphere, and it is via this propagating electron beam that the photometric and spectroscopic periodicity originates. This has been interpreted as auroral emissions from an ultracool dwarf - the same nature of emissions as has been observed in Jupiter for example, albeit many orders of magnitude more powerful. These results yield an entirely different manifestation of magnetic activity at the end of the main sequence, and highlight the similarities of the processes at work in giant planets, and those in low mass stars.

Based on the discovery of rotation periods from the tight binaries in our sample, LP 349-25B and 2M J0746A, we were able to investigate the orbital properties of each binary system. Specifically, our data, in addition to other parameters available in the literature, have allowed us to investigate the orientation of the binary equatorial axes with respect to the system orbital plane, thus investigating the orbital coplanarity of these very low mass binary systems. Indeed, this is the first such empirical study of coplanarity in the very low mass binary regime. In the case of LP 349-25B, based on model predicted radii, dynamical mass measurements, and individual rotation velocity measurements, the period of 1.86 ± 0.02 hours discovered in this work points toward a likely perpendicular alignment of the equatorial axis of LP 349-25B, and the orbital plane of the system. Our study, or others before this, have not yet found the rotation period of LP 349-25A, making such an assessment of the full system difficult. However, in the case of 2M J0746AB, the period of 2.07 ± 0.002 hours for the secondary component, 2M J0746B, had already been reported via radio observations. In this work, we reveal the period of the primary member, 2M J0746A, to be 3.36 ± 0.12 hours. These, together with a well constrained total system mass, bolometric luminosity, and IR photometry measurements, have allowed us to estimate individual component masses and radii via evolutionary models, which support the mass-radius relation $\leq 0.1 M_{\odot}$. Therefore, with all of the above parameters, we have been able to fully investigate the system's orbital coplanarity. We find, based on the above information at our disposal, in addition to the agreement of the period and $v \sin i$ ratios, that the equatorial axis of each component of the binary system is indeed aligned perpendicularly to the orbital plane, to within 10 degrees. This implies that solar-type binary formation may also hold in the very low mass binary regime, supporting disk driven fragmentation as the formation mechanism of binary systems at lower masses. We published these findings in Harding et al. (2012b).

In addition to the transient events of ultracool dwarfs, we have also investigated the flaring in mid M dwarfs, specifically that of the dM4.5e flare star YZ CMi, and the M3.5Ve flare star AD Leo. This campaign originally sought to obtain GUFi photometric data, simultaneously to high-resolution time-resolved spectroscopy, from the 3.5 m telescope of the Apache Point Observatory. However, poor weather prevented us from obtaining simultaneous data for the awarded nights. Nevertheless, we did obtain simultaneous photometric data from the ARCSAT and NMSU telescopes of APO. Although of slower cadence than GUFi, the detector's QE was at its greatest at blue wavelengths. By contrast, GUFi's QE peaks in the visible. We obtained ~ 49 hours of data between these two targets, all of which were simultaneous to the photometric observations at APO. We report 26 flaring events detected above the noise of the data, and in one case for the flare star YZ CMi, we likely have a case for the detection of periodic loop oscillations in the decay phase of a flare from February 26 2011 UT. We calculate a period of $\sim 10 - 15$ seconds for these oscillations, which occur at a flat part of the decay of the flare. Based on the lack of simultaneous spectroscopic data, it is difficult to establish the cause of these variations - perhaps they originate from an active state in the Balmer lines, which are present in the Johnson B-band that these events were detected in. Alternatively, they could be as a result of continuum emissions. A number of causal phenomena, magnetic in nature, could be responsible, but it is clear that a systematic and sequential group of loops are occurring during the flare event.

In the final stage of the doctoral program, we built and commissioned the second instrument in this thesis. This was the Caltech High-speed Multi-color camERA (CHIMERA) photometer (Harding et al., 2012c). Capable of observing simultaneously in the g' , currently with either r' or i' , the photometer utilizes two Andor NEO sCMOS cameras - the new innovative technology, as compared to conventional EM-CCDS (of GUFi for example). These sCMOS detectors are capable of extreme frame rates (up to 1600 fps), with low noise ($< 1 \text{ e}^- \text{ pixel}^{-1} \text{ readout}^{-1}$), making them ideal for the study of transient events and can be applied across a wide range of astronomical applications. First light of the instrument was August 1 2012 UT. This night was a commissioning night, where we confirmed the mechanical and optical working nature of the instrument. In addition to this, we prepared a science program to be carried out, which included two AM CVns, two exoplanet transits (of known ephemeris), a brown dwarf, the M1 nebula, and many Kuiper Belt Object (KBO) fields. Proof of concept data was shown in this thesis, confirming the working status of the instrument. CHIMERA is a Palomar Transient Factory follow up instrument, and is scheduled to be stationed as a facility instrument at prime focus of the 200-inch telescope from the 2012B semester, and for semesters thereafter.

In conclusion, the characteristics of the magnetic mechanisms at work in the surrounding regions of stars at the end of the main sequence, have manifested themselves in many different exciting and exotic ways. The evolutionary relationships in the low mass star regime, including age, rotation, activity, luminosity, radii, gravity (and so on), have been shown to behave in different ways when compared to larger mass stars on the main sequence. With this in mind, the data in this thesis has directly investigated the causal effects of magnetic activity at optical and infrared wavelengths. Specifically, the radio emission from these objects has provided a novel framework within which to identify that the magnetic properties of ultracool dwarfs exhibit behavior that is more like the magnetospheres of giant planets, rather than solar-type stars. Consequently, we have shown a strong link between the optical and radio emissions, and based on other work by Hallinan et al. (2012), the possibility exists whereby auroral emissions may also be present in ultracool dwarfs, as they are in planets. It is now quite clear that low mass stars and brown dwarfs have displayed a significant departure from the magnetic activity observed in larger mass stars. Although a range that was initially plagued by false detections and heightened frustration within the community, ultracool dwarfs now appear to truly bridge the gap between low mass stars and planets, in terms of magnetic activity and the associated optical signatures.

8.2 Future work

In the following sections, we briefly discuss the future work, some of which has already commenced, where both the GUF1 and CHIMERA photometers will be used.

8.2.1 High-Precision *Individual* Dynamical Mass Measurements of Very Low Mass Tight Binaries

Characterizing the fundamental properties of brown dwarfs is an important step in unlocking the physics of substellar objects, and mass is the most fundamental parameter in determining the properties and evolution of a brown dwarf. Since brown dwarfs have no sustainable source of internal energy, they follow a mass-luminosity-age relation, rather than the simpler mass-luminosity relation for main-sequence stars, and thus direct mass measurement of brown dwarfs is critical for empirically constraining substellar evolutionary models. This discrepancy in the mass estimates at a given luminosity and temperature has been highlighted between the evolutionary models of Burrows et al. (1997) and Chabrier & Baraffe (2000). In fact, in a large section of the H-R diagram, it is greater

than 30%. Precise mass measurements ($<10\%$) especially at the low mass end of the BD sequence are essential for constraining the physics and refining the evolutionary models.

Dynamical mass measurement campaigns are on-going and involve AO-assisted astrometric observations with 8 - 10 m class telescopes and the HST (Konopacky et al., 2010, and references therein). Astrometric data is used to determine the relative orbital parameters and hence total mass for the system. However, AO correction is performed over a small field of view (typically $\sim 10 \times 10$ arcsec), which significantly reduces the chances of finding background reference stars to anchor the center of mass motion of the brown dwarf binary. This precludes establishing the masses of the individual components of the system. Supplementary spectroscopic observations can measure radial velocities which can then be used to constrain individual component masses, but L and T dwarfs have too high rotational velocities for this technique to be applied. Thus, the masses of individual components remains very poorly constrained, severely hampering the ability to use these measurements to constrain evolutionary models for brown dwarfs.

Robo-AO²⁴, a new robotic system developed at Caltech, has the advantage of having low observing overheads (~ 1 minute), the ability to get 120 - 150 mas resolution in the SDSS i' and z' bands and with its low noise Andor DV-888 EM-CCD camera, image 20th absolute magnitude targets with an SNR > 20 in 3 minutes of observations. The current field of view of its visible camera (47×47 arcsec) is larger than most AO systems and the anisoplanatism (decorrelation of AO correction moving away from the laser pointing) is less severe than Keck. We propose to use Robo-AO to conduct an investigatory study of the known sample of about 30 close late-M, L and T dwarf binaries to assess the presence of reference field stars that can be used as astrometric references for a dynamical mass study. The neighborhood of each star will be sampled with 4 dithered pointings of 180 seconds each to obtain a mosaiced window around the target star. Observations will be conducted at z' , with the future study to be conducted in the infrared bands with the proposed Robo-AO NIR camera²⁵, or with other AO systems. Separately, we would use the data to study the astrometric precision which can be achieved by mosaicing AO data. Robo-AO visible camera data is gathered through short, high frame rate images and is coadded later through a shift-and-add pipeline. By using this shift-scale-and-add pipeline, we will be able to reduce the tip-tilt anisoplanatism which dominates the AO errors in the field and allow us

²⁴Christoph Baranec: PI

²⁵Robo-AOs optics pass a 2 arcminute FoV, which make it attractive for AO studies (such as this one) that need large fields. Although the current IR camera cannot image this FoV, an upgrade to a 780×780 pixel (sub-region) H2RG camera is being planned in the future.

to reduce astrometric errors during mosaicing. This study, when published, would be a very useful metric for Robo-AOs performance in particular as well as AO mosaicing in general.

Based on the above, we have been awarded 7 hours of observations with the Robo-AO instrument on the Palomar 60" telescope, which will commence during the August and September 2012 Robo-AO runs.

8.2.2 Resolving the Radio Detected L Dwarf Tight Binary 2MASS J0746+20AB with Robo-AO

2M J0746AB is a tight L dwarf binary with a separation of ~ 2.7 AU, and is one of the two magnetically active ultracool dwarf binaries detected thus far (Phan-Bao et al., 2007; Osten et al., 2009). The spatial resolution of GUF1 ($0.35''\text{pixel}^{-1}$ or $0.2''\text{pxiel}^{-1}$ with no focal reducer) is not sufficient to resolve each component of the binary system, where 2M J0746AB has a separation of $\sim 0.35''$ (Konopacky et al., 2010). As outlined in the previous section, the Robo-AO system is capable of $\sim 0.1''$ resolution, with even greater resolutions expected with the advent of the NIR camera. Although not designed for high-precision photometry, the Robo-AO system could provide enough resolution to perform photometry on both binary components. The 2M J0746AB system remains a mystery in the context of the radio and optical variabilities - why do we not detect the optical component of the radio emissions from 2M J0746B, even though it has been observed for the other three pulsing dwarfs (Hallinan et al., 2007; Lane et al., 2007; Littlefair et al., 2008; Hallinan et al., 2008; Harding et al., 2012a). Perhaps the dynamics of a magnetically active binary system are such that the magnetic field orientation of 2M J0746A is misaligned with the member spin axis. This could explain the lack of radio emission from 2M J0746A, but not the lack of optical variability from 2M J0746B, especially since $H\alpha$ was also detected. These resolved photometric measurements, provided by the Robo-AO system, have the means of investigating the optical variable nature of 2M J0746B, and assess whether it is possible to detect even small levels of variability. If periodic variability is also detected to the same period as that reported by Berger et al. (2009), this would provide an answer to a strongly debated question by Harding et al. (2012a), and determine if a radio and optical link also exists for this binary system.

8.2.3 UV Ceti and BL Ceti

UV Ceti is a very active star, and is known for intense flaring and other such impulsive events. However, its binary companion, BL Ceti, is much less active. In observations by Benz et al. (1998), the radio corona of UV Ceti was resolved via VLBI observations, however they did not detect the corona of BL Ceti. Similarly, Audard et al. (2003) report a much lower X-ray flaring rate of BL Ceti as compared to UV Ceti, during Chandra X-ray observations. Furthermore, UV Ceti has much higher radio luminosities and has been observed to flare quite regularly. This behavior of the binary twins has provoked much discussion, since each binary has the same approximate mass of $\sim 0.1 M_{\odot}$, and rotation rates of $v \sin i_{\text{UV,Ceti}} = 29.5 \text{ km s}^{-1}$ and $v \sin i_{\text{BL,Ceti}} = 31.5 \text{ km s}^{-1}$, respectively (Jones et al., 2005). As discussed in earlier sections of this work, there have been both strong dipolar fields, as well as weaker non-axisymmetric dipolar and toroidal fields found for stars of $\leq 0.2 M_{\odot}$ (Donati et al., 2006; Morin et al., 2010). This came as a surprise since these stars occupy the same approximate position on the mass-rotation diagram, albeit with similar, or approximately identical stellar parameters, such as UV Ceti and BL Ceti. Therefore, we propose to observe the binary star, once again with the functionality of the Robo-AO system. We have already conducted high time resolution photometric monitoring of the system with GUFi in September 2010, and found a tentative period of either 4.45 or 5.45 hours for one component. The differential photometry in this case however, was carried out by fitting an aperture on both components of the system - since GUFi did not have the spatial resolution to sample each member to a high enough degree of accuracy, and required much higher cadence (and thus much lower SNR) to begin to identify the binarity. With a separation of $\sim 2''$, this would be a simple observation for Robo-AO. We would thus be capable of obtaining simultaneous photometric monitoring of each binary member. This would allow us to investigate the flaring rates of each star, thus assessing the coronal activity between UV Ceti and BL Ceti by comparing the flaring rates during the observation.

8.2.4 Period of Rotation Search for ZDI

It is possible to map the magnetic field topologies of stars via Zeeman Doppler Imaging (ZDI), which can distinguish between different types of magnetism, such as strong dipolar fields, with large-scale configurations, or weaker non-axisymmetric fields that evolve on much longer timescales than previously studies could detect (Morin et al., 2008, 2010). This ZDI technique has the ability to measure the broadening of magnetically sensitive

spectral lines in the stellar photosphere, regardless of their complexity e.g. (Donati et al., 2008). Based on the stellar rotation, i.e. - by sampling at least one rotation, it is possible to build a map of the large-scale component of the magnetic field on the surface. However, the rotation of stars $\geq M6$ or $M7$ become increasingly difficult to measure via the spectroscopic techniques outlined here, due to how dim the stars become. Therefore, GUFi is ideal for sampling the rotation periods of these stars. We are collaborating with Morin and co-workers in establishing the periods of rotation of the following M dwarf sample, during the quiescent stages of their observations: GJ 1111, GJ 1224, GJ 1245b, GJ 2069b, GL 51, LHS 3376, UV Ceti, VB 8 and VB 10. Rotation periods for these objects are expected to be of the order of days. Therefore, we decided to observe each target in 20 minute intervals, which was adequate to sample the periodic lightcurve, if present. Some of these targets have confirmed ZDI periods of rotation, with no photometric confirmation. This collaboration is purely based on GUFi's ability to provide the periods of rotation for these ZDI targets. The analyses and observations are on-going.

8.2.5 CHIMERA mk.II and the search for Kuiper Belt Objects

A second generation version of CHIMERA will be developed in 2013, in a collaborative project between Caltech and the JPL²⁶. CHIMERA mk.II* will offer the much larger field of view of 10 arcminutes at the prime focus of the 200-inch telescope, an upgrade that will require significant investment in custom designed optics. This system was originally considered during CHIMERA mk.I development. However, we concluded that either: 1) an extremely large sCMOS chip needed to be developed and placed in the prime focal plane, in order to sample the large beam size at the prime focus point. Or 2) custom optics were required to produce a seeing limited spot on the current Andor sCMOS chip. An example of such a system is shown in Appendix C. As well as continuing programs, such as PTF follow-up, this upgraded instrument will be used for a dedicated survey of dense star fields in the ecliptic to search for occultation of stars by Kuiper Belt Objects (KBOs). This proposed survey will use the instrument at 100 frames per second, full frame, for ~ 100 hours, yielding a data set that will be 50 times more sensitive than any previous such survey. The two colors offered by CHIMERA allow for easy confirmation of the occultation, due to the color dependent nature of the occultation diffraction pattern. The resulting data set will approach 1 Petabyte in size, untenable for storage and post-processing. A tailored

²⁶National Aeronautics and Space Administration (NASA): Jet Propulsion Laboratory (JPL)

*Gregg Hallinan: PI

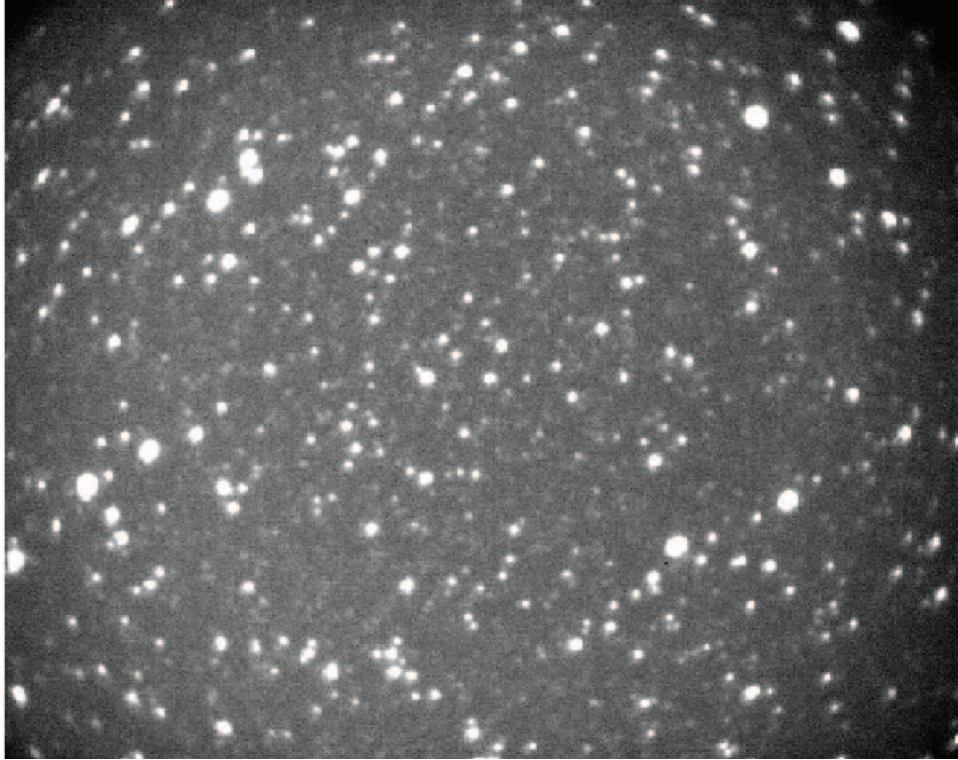


Figure 8.1: We show a Kuiper Belt Object field that was obtained with CHIMERA during the August 1 2012 UT commissioning. This frame was taken with a clear filter, with an exposure of 0.5 seconds. Here, with the native $\sim 3' \times 2.8'$ FOV of CHIMERA, we detect >1300 stars $\sim 3\sigma$ above the sky background.

pipeline for real-time identification of KBO occultations will be developed at Caltech and JPL. Such a campaign is extremely exciting, and could provide significant data in order to estimate the population of the KBO field in the solar system.

BIBLIOGRAPHY

- Abt, H. A., & Levy, S. G. (1976). Multiplicity among solar-type stars. *Astrophys. J.*, *30*, 273–306.
- Akerlof, C., Alcock, C., Allsman, R., Axelrod, T., Bennett, D. P., Cook, K. H., Freeman, K., Griest, K., Marshall, S., Park, H.-S., Perlmutter, S., Peterson, B., Quinn, P., Reimann, J., Rodgers, A., Stubbs, C. W., & Sutherland, W. (1994). Application of cubic splines to the spectral analysis of unequally spaced data. *Astrophys. J.*, *436*, 787–794.
- Alard, C. (2000). Image subtraction using a space-varying kernel. *Astron. & Astrophys. Suppl. Ser.*, *144*, 363–370.
- Alard, C., & Lupton, R. H. (1998). A Method for Optimal Image Subtraction. *Astrophys. J.*, *503*, 325.
- Albrecht, S., Reffert, S., Snellen, I. A. G., & Winn, J. N. (2009). Misaligned spin and orbital axes cause the anomalous precession of DI Herculis. *Nature*, *461*, 373–376.
- Albrecht, S., Winn, J. N., Carter, J. A., Snellen, I. A. G., & de Mooij, E. J. W. (2011). The Banana Project. III. Spin-Orbit Alignment in the Long-period Eclipsing Binary NY Cephei. *Astrophys. J.*, *726*, 68.
- Allard, F., Hauschildt, P. H., Alexander, D. R., Tamanai, A., & Schweitzer, A. (2001). The Limiting Effects of Dust in Brown Dwarf Model Atmospheres. *Astrophys. J.*, *556*, 357–372.
- Allard, F., Hauschildt, P. H., Baraffe, I., & Chabrier, G. (1996). Synthetic Spectra and Mass Determination of the Brown Dwarf GI 229B. *Astrophys. J.*, *465*, L123.
- Allen, C. W. (1973). *Astrophysical quantities*. London: University of London, Athlone Press, c1973, 3rd ed.
- Allred, J. C., Hawley, S. L., Abbett, W. P., & Carlsson, M. (2006). Radiative Hydrodynamic Models of Optical and Ultraviolet Emission from M Dwarf Flares. *Astrophys. J.*, *644*, 484–496.

- Antonova, A., Doyle, J. G., Hallinan, G., Bourke, S., & Golden, A. (2008). A mini-survey of ultracool dwarfs at 4.9 GHz. *Astron. & Astrophys.*, 487, 317–322.
- Antonova, A., Doyle, J. G., Hallinan, G., Golden, A., & Koen, C. (2007). Sporadic long-term variability in radio activity from a brown dwarf. *Astron. & Astrophys.*, 472, 257–260.
- Artigau, É., Bouchard, S., Doyon, R., & Lafrenière, D. (2009). Photometric Variability of the T2.5 Brown Dwarf SIMP J013656.5+093347: Evidence for Evolving Weather Patterns. *Astrophys. J.*, 701, 1534–1539.
- Audard, M., Güdel, M., & Skinner, S. L. (2003). Separating the X-Ray Emissions of UV Ceti A and B with Chandra. *Astrophys. J.*, 589, 983–987.
- Bailer-Jones, C. A. L. (2002). Dust clouds or magnetic spots? Exploring the atmospheres of L dwarfs with time-resolved spectrophotometry. *Astron. & Astrophys.*, 389, 963–976.
- Bailer-Jones, C. A. L. (2004). Spectroscopic rotation velocities of L dwarfs from VLT/UVES and their comparison with periods from photometric monitoring. *Astron. & Astrophys.*, 419, 703–712.
- Bailer-Jones, C. A. L. (2008). Correlated spectral variability in brown dwarfs. *Mon. Not. R. Astron. Soc.*, 384, 1145–1157.
- Bailer-Jones, C. A. L., & Lamm, M. (2003). Limits on the infrared photometric monitoring of brown dwarfs. *Mon. Not. R. Astron. Soc.*, 339, 477–485.
- Bailer-Jones, C. A. L., & Mundt, R. (1999). A search for variability in brown dwarfs and L dwarfs. *Astron. & Astrophys.*, 348, 800–804.
- Bailer-Jones, C. A. L., & Mundt, R. (2001). Variability in ultra cool dwarfs: Evidence for the evolution of surface features. *Astron. & Astrophys.*, 367, 218–235.
- Ballerini, P., Micela, G., Lanza, A. F., & Pagano, I. (2012). Multiwavelength flux variations induced by stellar magnetic activity: effects on planetary transits. *aap*, 539, A140.
- Barsony, M., Schombert, J. M., & Kis-Halas, K. (1991). The LkH-alpha 101 infrared cluster. *Astrophys. J.*, 379, 221–231.
- Basden, A. G., Haniff, C. A., & Mackay, C. D. (2003). Photon counting strategies with low-light-level CCDs. *Mon. Not. R. Astron. Soc.*, 345, 985–991.

- Basri, G. (2000). Observations of Brown Dwarfs. *Ann. Rev. Astron. Astrophys.*, 38, 485–519.
- Basri, G. (2001). Rotation and H α Emission Above and Below the Substellar Boundary (CD-ROM Directory: contribs/basri). In R. J. Garcia Lopez, R. Rebolo, & M. R. Zapatero Osorio (Eds.) *11th Cambridge Workshop on Cool Stars, Stellar Systems and the Sun*, vol. 223 of *Astronomical Society of the Pacific Conference Series*, (p. 261).
- Basri, G., & Marcy, G. W. (1995). A surprise at the bottom of the main sequence: Rapid rotation and NO H-alpha emission. *Astron. J.*, 109, 762–773.
- Basri, G., Marcy, G. W., & Graham, J. R. (1996). Lithium in Brown Dwarf Candidates: The Mass and Age of the Faintest Pleiades Stars. *Astrophys. J.*, 458, 600.
- Basri, G., & Martín, E. L. (1999). PPL 15: The First Brown Dwarf Spectroscopic Binary. *Astron. J.*, 118, 2460–2465.
- Bate, M. R. (2009). Stellar, brown dwarf and multiple star properties from hydrodynamical simulations of star cluster formation. *Mon. Not. R. Astron. Soc.*, 392, 590–616.
- Bate, M. R. (2012). Stellar, brown dwarf and multiple star properties from a radiation hydrodynamical simulation of star cluster formation. *Mon. Not. R. Astron. Soc.*, 419, 3115–3146.
- Becklin, E. E., & Zuckerman, B. (1988). A low-temperature companion to a white dwarf star. *Nature*, 336, 656–658.
- Beichman, C. A. (1987). The IRAS view of the Galaxy and the solar system. *Ann. Rev. Astron. Astrophys.*, 25, 521–563.
- Benz, A. O., Conway, J., & Gudel, M. (1998). First VLBI images of a main-sequence star. *Astron. & Astrophys.*, 331, 596–600.
- Benz, A. O., & Güdel, M. (1994). X-ray/microwave ratio of flares and coronae. *Astron. & Astrophys.*, 285, 621–630.
- Berdyugina, S. V. (2005). Starspots: A Key to the Stellar Dynamo. *Living Reviews in Solar Physics*, 2, 8.
- Berger, E. (2002). Flaring up All Over-Radio Activity in Rapidly Rotating Late M and L Dwarfs. *Astrophys. J.*, 572, 503–513.

- Berger, E. (2006). Radio Observations of a Large Sample of Late M, L, and T Dwarfs: The Distribution of Magnetic Field Strengths. *Astrophys. J.*, 648, 629–636.
- Berger, E., Ball, S., Becker, K. M., Clarke, M., Frail, D. A., Fukuda, T. A., Hoffman, I. M., Mellon, R., Momjian, E., Murphy, N. W., Teng, S. H., Woodruff, T., Zauderer, B. A., & Zavala, R. T. (2001). Discovery of radio emission from the brown dwarf LP944-20. *Nature*, 410, 338–340.
- Berger, E., Basri, G., Fleming, T. A., Giampapa, M. S., Gizis, J. E., Liebert, J., Martín, E., Phan-Bao, N., & Rutledge, R. E. (2010). Simultaneous Multi-Wavelength Observations of Magnetic Activity in Ultracool Dwarfs. III. X-ray, Radio, and H α Activity Trends in M and L dwarfs. *Astrophys. J.*, 709, 332–341.
- Berger, E., Gizis, J. E., Giampapa, M. S., Rutledge, R. E., Liebert, J., Martín, E., Basri, G., Fleming, T. A., Johns-Krull, C. M., Phan-Bao, N., & Sherry, W. H. (2008a). Simultaneous Multiwavelength Observations of Magnetic Activity in Ultracool Dwarfs. I. The Complex Behavior of the M8.5 Dwarf TVLM 513-46546. *Astrophys. J.*, 673, 1080–1087.
- Berger, E., Rutledge, R. E., Phan-Bao, N., Basri, G., Giampapa, M. S., Gizis, J. E., Liebert, J., Martín, E., & Fleming, T. A. (2009). Periodic Radio and H α Emission from the L Dwarf Binary 2MASSW J0746425+200032: Exploring the Magnetic Field Topology and Radius Of An L Dwarf. *Astrophys. J.*, 695, 310–316.
- Berger, E., Rutledge, R. E., Reid, I. N., Bildsten, L., Gizis, J. E., Liebert, J., Martín, E., Basri, G., Jayawardhana, R., Brandeker, A., Fleming, T. A., Johns-Krull, C. M., Giampapa, M. S., Hawley, S. L., & Schmitt, J. H. M. M. (2005). The Magnetic Properties of an L Dwarf Derived from Simultaneous Radio, X-Ray, and H α Observations. *Astrophys. J.*, 627, 960–973.
- Bodenheimer, P. (1978). Evolution of rotating interstellar clouds. III - On the formation of multiple star systems. *Astrophys. J.*, 224, 488–496.
- Boeshaar, P. C., Tyson, J. A., & Seitzer, P. (1986). Numbers of Low Mass Stars Found in a CTIO Deep CCD Survey. In *Bulletin of the American Astronomical Society*, vol. 18 of *Bulletin of the American Astronomical Society*, (p. 1039).

- Bookbinder, J. A., Walter, F. M., & Brown, A. (1992). HST Observations of AD Leo. In M. S. Giampapa, & J. A. Bookbinder (Eds.) *Cool Stars, Stellar Systems, and the Sun*, vol. 26 of *Astronomical Society of the Pacific Conference Series*, (p. 27).
- Bouy, H., Duchêne, G., Köhler, R., Brandner, W., Bouvier, J., Martín, E. L., Ghez, A., Delfosse, X., Forveille, T., Allard, F., Baraffe, I., Basri, G., Close, L., & McCabe, C. E. (2004). First determination of the dynamical mass of a binary L dwarf. *Astron. & Astrophys.*, 423, 341–352.
- Bryja, C., Humphreys, R. M., & Jones, T. J. (1994). The lowest mass stars in the Hyades. *Astron. J.*, 107, 246–253.
- Burgasser, A. J., Geballe, T. R., Leggett, S. K., Kirkpatrick, J. D., & Golimowski, D. A. (2006). A Unified Near-Infrared Spectral Classification Scheme for T Dwarfs. *Astrophys. J.*, 637, 1067–1093.
- Burgasser, A. J., Kirkpatrick, J. D., Brown, M. E., Reid, I. N., Burrows, A., Liebert, J., Matthews, K., Gizis, J. E., Dahn, C. C., Monet, D. G., Cutri, R. M., & Skrutskie, M. F. (2002). The Spectra of T Dwarfs. I. Near-Infrared Data and Spectral Classification. *Astrophys. J.*, 564, 421–451.
- Burgasser, A. J., & Putman, M. E. (2005). Quiescent Radio Emission from Southern Late-Type M Dwarfs and a Spectacular Radio Flare from the M8 Dwarf DENIS 1048-3956. *Astrophys. J.*, 626, 486–497.
- Burgasser, A. J., Reid, I. N., Siegler, N., Close, L., Allen, P., Lowrance, P., & Gizis, J. (2007). Not Alone: Tracing the Origins of Very-Low-Mass Stars and Brown Dwarfs Through Multiplicity Studies. *Protostars and Planets V*, (pp. 427–441).
- Burrows, A., Hubbard, W. B., Lunine, J. I., & Liebert, J. (2001). The theory of brown dwarfs and extrasolar giant planets. *Rev. Mod. Phys.*, 73, 719–765.
- Burrows, A., Hubbard, W. B., Saumon, D., & Lunine, J. I. (1993). An expanded set of brown dwarf and very low mass star models. *Astrophys. J.*, 406, 158–171.
- Burrows, A., Marley, M., Hubbard, W. B., Lunine, J. I., Guillot, T., Saumon, D., Freedman, R., Sudarsky, D., & Sharp, C. (1997). A Nongray Theory of Extrasolar Giant Planets and Brown Dwarfs. *Astrophys. J.*, 491, 856.

- Burrows, A., Sudarsky, D., & Lunine, J. I. (2003). Beyond the T Dwarfs: Theoretical Spectra, Colors, and Detectability of the Coolest Brown Dwarfs. *Astrophys. J.*, 596, 587–596.
- Carr, T. D., Desch, M. D., & Alexander, J. K. (1983). *BOOK: Phenomenology of magnetospheric radio emissions*, (pp. 226–284). Publisher: Dessler, A. J.
- Chabrier, G., & Baraffe, I. (1997). Structure and evolution of low-mass stars. *Astron. & Astrophys.*, 327, 1039–1053.
- Chabrier, G., & Baraffe, I. (2000). Theory of Low-Mass Stars and Substellar Objects. *Ann. Rev. Astron. Astrophys.*, 38, 337–377.
- Chabrier, G., Gallardo, J., & Baraffe, I. (2007). Evolution of low-mass star and brown dwarf eclipsing binaries. *Astron. & Astrophys.*, 472, L17–L20.
- Chabrier, G., & Küker, M. (2006). Large-scale α^2 -dynamo in low-mass stars and brown dwarfs. *Astron. & Astrophys.*, 446, 1027–1037.
- Chapman, G. A., & McGuire, T. E. (1977). The wavelength dependence of the facular excess brightness. *Astrophys. J.*, 217, 657–660.
- Clarke, F. J., Hodgkin, S. T., Oppenheimer, B. R., Robertson, J., & Haubois, X. (2008). A search for J-band variability from late-L and T brown dwarfs. *Mon. Not. R. Astron. Soc.*, 386, 2009–2014.
- Clarke, F. J., Oppenheimer, B. R., & Tinney, C. G. (2002b). A mini-survey for variability in early L dwarfs. *Mon. Not. R. Astron. Soc.*, 335, 1158–1162.
- Clarke, F. J., Tinney, C. G., & Covey, K. R. (2002). Periodic photometric variability of the brown dwarf Kelu-1. *Mon. Not. R. Astron. Soc.*, 332, 361–366.
- Close, L. M., Siegler, N., Freed, M., & Biller, B. (2003). Detection of Nine M8.0-L0.5 Binaries: The Very Low Mass Binary Population and Its Implications for Brown Dwarf and Very Low Mass Star Formation. *Astrophys. J.*, 587, 407–422.
- Cully, S. L., Fisher, G. H., Hawley, S. L., & Simon, T. (1997). Extreme Ultraviolet Explorer Spectra of the 1993 March Flares on AD Leonis: The Differential Emission Measure and Implications for Coronal Structure. *Astrophys. J.*, 491, 910.

- Cushing, M. C., Kirkpatrick, J. D., Gelino, C. R., Griffith, R. L., Skrutskie, M. F., Mainzer, A., Marsh, K. A., Beichman, C. A., Burgasser, A. J., Prato, L. A., Simcoe, R. A., Marley, M. S., Saumon, D., Freedman, R. S., Eisenhardt, P. R., & Wright, E. L. (2011). The Discovery of Y Dwarfs using Data from the Wide-field Infrared Survey Explorer (WISE). *Astrophys. J.*, 743, 50.
- Dahn, C. C., Harris, H. C., Vrba, F. J., Guetter, H. H., Canzian, B., Henden, A. A., Levine, S. E., Luginbuhl, C. B., Monet, A. K. B., Monet, D. G., Pier, J. R., Stone, R. C., Walker, R. L., Burgasser, A. J., Gizis, J. E., Kirkpatrick, J. D., Liebert, J., & Reid, I. N. (2002). Astrometry and Photometry for Cool Dwarfs and Brown Dwarfs. *Astron. J.*, 124, 1170–1189.
- Dantona, F., & Mazzitelli, I. (1985). Evolution of very low mass stars and brown dwarfs. I - The minimum main-sequence mass and luminosity. *Astrophys. J.*, 296, 502–513.
- Donati, J.-F., Forveille, T., Collier Cameron, A., Barnes, J. R., Delfosse, X., Jardine, M. M., & Valenti, J. A. (2006). The Large-Scale Axisymmetric Magnetic Topology of a Very-Low-Mass Fully Convective Star. *Science*, 311, 633–635.
- Donati, J.-F., Morin, J., Petit, P., Delfosse, X., Forveille, T., Aurière, M., Cabanac, R., Dintrans, B., Fares, R., Gastine, T., Jardine, M. M., Lignières, F., Paletou, F., Ramirez Velez, J. C., & Théado, S. (2008). Large-scale magnetic topologies of early M dwarfs. *Mon. Not. R. Astron. Soc.*, 390, 545–560.
- Dulk, G. A. (1985). Radio emission from the sun and stars. *Ann. Rev. Astron. Astrophys.*, 23, 169–224.
- Dulk, G. A., & Marsh, K. A. (1982). Simplified expressions for the gyrosynchrotron radiation from mildly relativistic, nonthermal and thermal electrons. *Astrophys. J.*, 259, 350–358.
- Dupuy, T. J., & Liu, M. C. (2011). On the Distribution of Orbital Eccentricities for Very Low-mass Binaries. *Astrophys. J.*, 733, 122.
- Dupuy, T. J., Liu, M. C., Bowler, B. P., Cushing, M. C., Helling, C., Witte, S., & Hauschildt, P. (2010). Studying the Physical Diversity of Late-M Dwarfs with Dynamical Masses. *Astrophys. J.*, 721, 1725–1747.
- Edelson, R. A., & Krolik, J. H. (1988). The discrete correlation function - A new method for analyzing unevenly sampled variability data. *Astrophys. J.*, 333, 646–659.

- Enoch, M. L., Brown, M. E., & Burgasser, A. J. (2003). Photometric Variability at the L/T Dwarf Boundary. *Astron. J.*, 126, 1006–1016.
- Ergun, R. E., Carlson, C. W., McFadden, J. P., Delory, G. T., Strangeway, R. J., & Pritchett, P. L. (2000). Electron-Cyclotron Maser Driven by Charged-Particle Acceleration from Magnetic Field-aligned Electric Fields. *Astrophys. J.*, 538, 456–466.
- Fegley, B., Jr., & Lodders, K. (1996). Atmospheric Chemistry of the Brown Dwarf Gliese 229B: Thermochemical Equilibrium Predictions. *Astrophys. J.*, 472, L37.
- Fekel, F. C., Jr. (1981). The properties of close multiple stars. *Astrophys. J.*, 246, 879–898.
- Forrest, W. J., Barnett, J. D., Ninkov, Z., Skrutskie, M., & Shure, M. (1989). Discovery of Low-Mass Brown Dwarfs in Taurus. *Pub. Astron. Soc. Pac.*, 101, 877.
- Forveille, T., Beuzit, J.-L., Delorme, P., Ségransan, D., Delfosse, X., Chauvin, G., Fusco, T., Lagrange, A.-M., Mayor, M., Montagnier, G., Mouillet, D., Perrier, C., Udry, S., Charton, J., Gigan, P., Conan, J.-M., Kern, P., & Michet, G. (2005). LP 349-25: A new tight M8V binary. *aap*, 435, L5–L8.
- Freedman, R. S., Marley, M. S., & Lodders, K. (2008). Line and Mean Opacities for Ultracool Dwarfs and Extrasolar Planets. *Astrophys. J.*, 174, 504–513.
- Fröhlich, C., & Lean, J. (2004). Solar radiative output and its variability: evidence and mechanisms. *aapr*, 12, 273–320.
- Fuhrmeister, B., & Schmitt, J. H. M. M. (2004). Detection and high-resolution spectroscopy of a huge flare on the old M 9 dwarf DENIS 104814.7-395606.1. *Astron. & Astrophys.*, 420, 1079–1085.
- Fukugita, M., Ichikawa, T., Gunn, J. E., Doi, M., Shimasaku, K., & Schneider, D. P. (1996). The Sloan Digital Sky Survey Photometric System. *Astron. J.*, 111, 1748.
- Gatewood, G., & Coban, L. (2009). Allegheny Observatory Parallaxes for Late M Dwarfs and White Dwarfs. *Astron. J.*, 137, 402–405.
- Gelino, C. R., Marley, M. S., Holtzman, J. A., Ackerman, A. S., & Lodders, K. (2002). L Dwarf Variability: I-Band Observations. *Astrophys. J.*, 577, 433–446.

- Gizis, J. E., Monet, D. G., Reid, I. N., Kirkpatrick, J. D., Liebert, J., & Williams, R. J. (2000). New Neighbors from 2MASS: Activity and Kinematics at the Bottom of the Main Sequence. *Astron. J.*, *120*, 1085–1099.
- Gizis, J. E., & Reid, I. N. (2006). 2MASSW J0746425+200322: Is the Secondary a Star or Brown Dwarf? *Astron. J.*, *131*, 638–639.
- Goldman, B., Cushing, M. C., Marley, M. S., Artigau, É., Baliyan, K. S., Béjar, V. J. S., Caballero, J. A., Chanover, N., Connelley, M., Doyon, R., Forveille, T., Ganesh, S., Gelino, C. R., Hammel, H. B., Holtzman, J., Joshi, S., Joshi, U. C., Leggett, S. K., Liu, M. C., Martín, E. L., Mohan, V., Nadeau, D., Sagar, R., & Stephens, D. (2008). CLOUDS search for variability in brown dwarf atmospheres. Infrared spectroscopic time series of L/T transition brown dwarfs. *Astron. & Astrophys.*, *487*, 277–292.
- Golimowski, D. A., Leggett, S. K., Marley, M. S., Fan, X., Geballe, T. R., Knapp, G. R., Vrba, F. J., Henden, A. A., Luginbuhl, C. B., Guetter, H. H., Munn, J. A., Canzian, B., Zheng, W., Tsvetanov, Z. I., Chiu, K., Glazebrook, K., Hoversten, E. A., Schneider, D. P., & Brinkmann, J. (2004). L' and M' Photometry of Ultracool Dwarfs. *Astron. J.*, *127*, 3516–3536.
- Güdel, M., & Benz, A. O. (1993). X-ray/microwave relation of different types of active stars. *Astrophys. J.*, *405*, L63–L66.
- Hale, A. (1994). Orbital coplanarity in solar-type binary systems: Implications for planetary system formation and detection. *Astron. J.*, *107*, 306–332.
- Hallinan, G., Antonova, A., Doyle, J. G., Bourke, S., Briskin, W. F., & Golden, A. (2006). Rotational Modulation of the Radio Emission from the M9 Dwarf TVLM 513-46546: Broadband Coherent Emission at the Substellar Boundary? *Astrophys. J.*, *653*, 690–699.
- Hallinan, G., Antonova, A., Doyle, J. G., Bourke, S., Lane, C., & Golden, A. (2008). Confirmation of the Electron Cyclotron Maser Instability as the Dominant Source of Radio Emission from Very Low Mass Stars and Brown Dwarfs. *Astrophys. J.*, *684*, 644–653.
- Hallinan, G., Bourke, S., Lane, C., Antonova, A., Zavala, R. T., Briskin, W. F., Boyle, R. P., Vrba, F. J., Doyle, J. G., & Golden, A. (2007). Periodic Bursts of Coherent Radio Emission from an Ultracool Dwarf. *Astrophys. J.*, *663*, L25–L28.

- Hallinan et al., G. (2012). *Under embargo*.
- Harding, L. K., Hallinan, G., Boyle, R. P., Golden, A., Sheehan, B., Zavala, R. T., & Butler, R. F. (2012a). Periodic Optical Variability of Radio Detected Ultracool Dwarfs. *Astrophys. J.*
- Harding, L. K., Hallinan, G., Konopacky, Q., Boyle, R. P., Butler, R. F., & Golden, A. (2012b). On the Orbital Coplanarity of the L Tight Binary Dwarf 2MASSW J0746425+200032. *Astrophys. J.*
- Harding, L. K., Hallinan, G., Kyne, G., Gardner, P., Baranec, C., Konidaris, N., & Kulikarni, S. (2012c). CHIMERA - a Prime Focus PTF Follow-up Instrument on the 200". *SPIE*.
- Harding, L. K., Kowalski, A. F., Hilton, E. J., Hawley, S. L., Hallinan, G., Boyle, R. P., Golden, A., & Butler, R. F. (2012d). An Investigation to Characterize the White Light Flare Emission of YZ CMi using High-Speed Photometry. *Astrophys. J.*
- Hawley, S. L., Allred, J. C., Johns-Krull, C. M., Fisher, G. H., Abbett, W. P., Alekseev, I., Avgoloupis, S. I., Deustua, S. E., Gunn, A., Seiradakis, J. H., Sirk, M. M., & Valenti, J. A. (2003). Multiwavelength Observations of Flares on AD Leonis. *Astrophys. J.*, 597, 535–554.
- Hawley, S. L., & Fisher, G. H. (1992). X-ray-heated models of stellar flare atmospheres - Theory and comparison with observations. *apjs*, 78, 565–598.
- Hawley, S. L., Fisher, G. H., Simon, T., Cully, S. L., Deustua, S. E., Jablonski, M., Johns-Krull, C. M., Pettersen, B. R., Smith, V., Spiesman, W. J., & Valenti, J. (1995). Simultaneous Extreme-Ultraviolet Explorer and Optical Observations of AD Leonis: Evidence for Large Coronal Loops and the Neupert Effect in Stellar Flares. *Astrophys. J.*, 453, 464.
- Hawley, S. L., & Pettersen, B. R. (1991). The great flare of 1985 April 12 on AD Leonis. *Astrophys. J.*, 378, 725–741.
- Hawley, S. L., Walkowicz, L. M., Allred, J. C., & Valenti, J. A. (2007). Near-Ultraviolet Spectra of Flares on YZ CMi. *Pub. Astron. Soc. Pac.*, 119, 67–81.
- Henry, T. J., & McCarthy, D. W., Jr. (1990). A systematic search for brown dwarfs orbiting nearby stars. *Astrophys. J.*, 350, 334–347.

- Hewitt, R. G., Melrose, D. B., & Ruennmark, K. G. (1981). A cyclotron theory for the beaming pattern of Jupiter's decametric radio emission. *Proceedings of the Astronomical Society of Australia*, 4, 221–226.
- Hilton, E. J., West, A. A., Hawley, S. L., & Kowalski, A. F. (2010). M Dwarf Flares from Time-resolved Sloan Digital Sky Survey Spectra. *Astron. J.*, 140, 1402–1413.
- Høg, E., Fabricius, C., Makarov, V. V., Urban, S., Corbin, T., Wycoff, G., Bastian, U., Schwekendiek, P., & Wicenec, A. (2000). The Tycho-2 catalogue of the 2.5 million brightest stars. *Astron. & Astrophys.*, 355, L27–L30.
- Horne, J. H., & Baliunas, S. L. (1986). A prescription for period analysis of unevenly sampled time series. *Astrophys. J.*, 302, 757–763.
- Hoxie, D. T. (1970). The Structure and Evolution of Stars of Very Low Mass. *Astrophys. J.*, 161, 1083.
- Janesick, J. R. (2001). Scientific Charge Coupled Devices. *SPIE*, 906, 83.
- Jenkins, J. S., Ramsey, L. W., Jones, H. R. A., Pavlenko, Y., Gallardo, J., Barnes, J. R., & Pinfield, D. J. (2009). Rotational Velocities for M Dwarfs. *Astrophys. J.*, 704, 975–988.
- Jensen, E. L. N., Mathieu, R. D., Donar, A. X., & Dullighan, A. (2004). Testing Protoplanetary Disk Alignment in Young Binaries. *Astrophys. J.*, 600, 789–803.
- Johns-Krull, C. M., & Valenti, J. A. (1996). Detection of Strong Magnetic Fields on M Dwarfs. *Astrophys. J.*, 459, L95.
- Jones, H. R. A., Pavlenko, Y., Viti, S., Barber, R. J., Yakovina, L. A., Pinfield, D., & Tennyson, J. (2005). Carbon monoxide in low-mass dwarf stars. *Mon. Not. R. Astron. Soc.*, 358, 105–112.
- Jumper, P. H., & Fisher, R. T. (2012). Shaping the Brown Dwarf Desert: Predicting the Primordial Brown Dwarf Binary Distributions from Turbulent Fragmentation. *ArXiv e-prints [arXiv1206.1045J]*.
- Kahler, S., Golub, L., Harnden, F. R., Liller, W., Seward, F., Vaiana, G., Lovell, B., Davis, R. J., Spencer, R. E., Whitehouse, D. R., Feldman, P. A., Viner, M. R., Leslie, B., Kahn, S. M., Mason, K. O., Davis, M. M., Crannell, C. J., Hobbs, R. W., Schneeberger, T. J., Worden, S. P., Schommer, R. A., Vogt, S. S., Pettersen, B. R., Coleman, G. D., Karpen,

- J. T., Giampapa, M. S., Hege, E. K., Pazzani, V., Rodono, M., Romeo, G., & Chugainov, P. F. (1982). Coordinated X-ray, optical, and radio observations of flaring activity on YZ Canis Minoris. *Astrophys. J.*, 252, 239–249.
- Kane, S. R., Kai, K., Kosugi, T., Enome, S., Landecker, P. B., & McKenzie, D. L. (1983). Acceleration and confinement of energetic particles in the 1980 June 7 solar flare. *Astrophys. J.*, 271, 376–387.
- Kirkpatrick, J. D. (2005). New Spectral Types L and T. *Ann. Rev. Astron. Astrophys.*, 43, 195–245.
- Kirkpatrick, J. D. (2008). Outstanding Issues in Our Understanding of L, T, and Y Dwarfs. In G. van Belle (Ed.) *14th Cambridge Workshop on Cool Stars, Stellar Systems, and the Sun*, vol. 384 of *Astronomical Society of the Pacific Conference Series*, (p. 85).
- Kirkpatrick, J. D., Henry, T. J., & Irwin, M. J. (1997). Ultra-Cool M Dwarfs Discovered by QSO Surveys.I: The APM Objects. *Astron. J.*, 113, 1421–1428.
- Kirkpatrick, J. D., Henry, T. J., & Liebert, J. (1993). The unique spectrum of the brown dwarf candidate GD 165B and comparison to the spectra of other low-luminosity objects. *Astrophys. J.*, 406, 701–707.
- Kirkpatrick, J. D., Henry, T. J., & McCarthy, D. W., Jr. (1991). A standard stellar spectral sequence in the red/near-infrared - Classes K5 to M9. *Astrophys. J.*, 77, 417–440.
- Kirkpatrick, J. D., Reid, I. N., Liebert, J., Cutri, R. M., Nelson, B., Beichman, C. A., Dahn, C. C., Monet, D. G., Gizis, J. E., & Skrutskie, M. F. (1999). Dwarfs Cooler than “M”: The Definition of Spectral Type “L” Using Discoveries from the 2 Micron All-Sky Survey (2MASS). *Astrophys. J.*, 519, 802–833.
- Kirkpatrick, J. D., Reid, I. N., Liebert, J., Gizis, J. E., Burgasser, A. J., Monet, D. G., Dahn, C. C., Nelson, B., & Williams, R. J. (2000). 67 Additional L Dwarfs Discovered by the Two Micron All Sky Survey. *Astron. J.*, 120, 447–472.
- Koen, C. (2003). A search for short time-scale I-band variability in ultracool dwarfs. *Mon. Not. R. Astron. Soc.*, 346, 473–482.
- Koen, C. (2006). Evidence for rapid evolution of periodic variations in an ultracool dwarf. *Mon. Not. R. Astron. Soc.*, 367, 1735–1738.

- Koen, C., Kilkenney, D., van Wyk, F., & Marang, F. (2010). UBVR(I)_C JHK observations of Hipparcos-selected nearby stars. *Mon. Not. R. Astron. Soc.*, *403*, 1949–1968.
- Koen, C., Matsunaga, N., & Menzies, J. (2004). A search for short time-scale JHK variability in ultracool dwarfs. *Mon. Not. R. Astron. Soc.*, *354*, 466–476.
- Konopacky, Q. M., Ghez, A. M., Barman, T. S., Rice, E. L., Bailey, J. I., III, White, R. J., McLean, I. S., & Duchêne, G. (2010). High-precision Dynamical Masses of Very Low Mass Binaries. *Astrophys. J.*, *711*, 1087–1122.
- Konopacky, Q. M., Ghez, A. M., Fabrycky, D. C., Macintosh, B. A., White, R. J., Barman, T. S., Rice, E. L., Hallinan, G., & Duchêne, G. (2012). Rotational Velocities of Individual Components in Very Low Mass Binaries. *Astrophys. J.*, *750*, 79.
- Kowalski, A. F., Hawley, S. L., Holtzman, J. A., Wisniewski, J. P., & Hilton, E. J. (2010). A White Light Megaflare on the dM4.5e Star YZ CMi. *Astrophys. J.*, *714*, L98–L102.
- Kratter, K. M. (2011). The Formation of Close Binaries. In L. Schmidtbreick, M. R. Schreiber, & C. Tappert (Eds.) *Evolution of Compact Binaries*, vol. 447 of *Astronomical Society of the Pacific Conference Series*, (p. 47).
- Kratter, K. M., Matzner, C. D., & Krumholz, M. R. (2008). Global Models for the Evolution of Embedded, Accreting Protostellar Disks. *Astrophys. J.*, *681*, 375–390.
- Kratter, K. M., Matzner, C. D., Krumholz, M. R., & Klein, R. I. (2010). On the Role of Disks in the Formation of Stellar Systems: A Numerical Parameter Study of Rapid Accretion. *Astrophys. J.*, *708*, 1585–1597.
- Krishna Kumar, C. (1985). Brief search for low-mass objects. *Pub. Astron. Soc. Pac.*, *97*, 294–296.
- Krishna Kumar, C. (1987). Search for low-mass objects. II. *Astron. J.*, *94*, 158–160.
- Kumar, S. S. (1963). The Structure of Stars of Very Low Mass. *Astrophys. J.*, *137*, 1121.
- Kurtz, D. W., Cunha, M. S., Saio, H., Bigot, L., Balona, L. A., Elkin, V. G., Shibahashi, H., Brandão, I. M., Uytterhoeven, K., Frandsen, S., Frimann, S., Hatzes, A., Lueftinger, T., Gruberbauer, M., Kjeldsen, H., Christensen-Dalsgaard, J., & Kawaler, S. D. (2011). The first evidence for multiple pulsation axes: a new rapidly oscillating Ap star in the Kepler field, KIC 10195926. *Mon. Not. R. Astron. Soc.*, *414*, 2550–2566.

- Lane, C., Hallinan, G., Zavala, R. T., Butler, R. F., Boyle, R. P., Bourke, S., Antonova, A., Doyle, J. G., Vrba, F. J., & Golden, A. (2007). Rotational Modulation of M/L Dwarfs due to Magnetic Spots. *Astrophys. J.*, 668, L163–L166.
- Latham, D. W., Stefanik, R. P., Mazeh, T., Mayor, M., & Burki, G. (1989). The unseen companion of HD114762 - A probable brown dwarf. *Nature*, 339, 38–40.
- Lee, K.-G., Berger, E., & Knapp, G. R. (2010). Short-term H α Variability in M Dwarfs. *Astrophys. J.*, 708, 1482–1491.
- Leggett, S. K., Allard, F., Geballe, T. R., Hauschildt, P. H., & Schweitzer, A. (2001). Infrared Spectra and Spectral Energy Distributions of Late M and L Dwarfs. *Astrophys. J.*, 548, 908–918.
- Leggett, S. K., & Hawkins, M. R. S. (1989). Low mass stars in the region of the Hyades cluster. *Mon. Not. R. Astron. Soc.*, 238, 145–153.
- Li, P. S., Norman, M. L., Mac Low, M.-M., & Heitsch, F. (2004). The Formation of Self-Gravitating Cores in Turbulent Magnetized Clouds. *Astrophys. J.*, 605, 800–818.
- Liebert, J., Kirkpatrick, J. D., Cruz, K. L., Reid, I. N., Burgasser, A., Tinney, C. G., & Gizis, J. E. (2003). A Flaring L5 Dwarf: The Nature of H α Emission in Very Low Mass (Sub)Stellar Objects. *Astron. J.*, 125, 343–347.
- Littlefair, S. P., Dhillon, V. S., Marsh, T. R., Shahbaz, T., Martín, E. L., & Copperwheat, C. (2008). Optical variability of the ultracool dwarf TVLM 513-46546: evidence for inhomogeneous dust clouds. *Mon. Not. R. Astron. Soc.*, 391, L88–L92.
- Lomb, N. R. (1976). Least-squares frequency analysis of unequally spaced data. *Astrophys. Space Sci.*, 39, 447–462.
- Lubow, S. H., & Ogilvie, G. I. (2000). On the Tilting of Protostellar Disks by Resonant Tidal Effects. *Astrophys. J.*, 538, 326–340.
- Maiti, M. (2007). Observational Evidence of Optical Variability in L Dwarfs. *Astron. J.*, 133, 1633–1644.
- Maiti, M., Sengupta, S., Parihar, P. S., & Anupama, G. C. (2005). Observation of R-Band Variability of L Dwarfs. *Astrophys. J.*, 619, L183–L186.

- Mangeney, A., & Veltri, P. (1976). On the theory of type I solar radio bursts. I - Beam plasma instabilities in a turbulent magnetized plasma. II - A model for the source. *Astron. & Astrophys.*, *47*, 165–192.
- Marcy, G. W., Basri, G., & Graham, J. R. (1994). A search for lithium in Pleiades brown dwarf candidates using the Keck HIRES echelle. *Astrophys. J.*, *428*, L57–L60.
- Marley, M. S., Saumon, D., Guillot, T., Freedman, R. S., Hubbard, W. B., Burrows, A., & Lunine, J. I. (1996). Atmospheric, Evolutionary, and Spectral Models of the Brown Dwarf Gliese 229 B. *Science*, *272*, 1919–1921.
- Martín, E. L., Delfosse, X., Basri, G., Goldman, B., Forveille, T., & Zapatero Osorio, M. R. (1999). Spectroscopic Classification of Late-M and L Field Dwarfs. *Astron. J.*, *118*, 2466–2482.
- Martín, E. L., Rebolo, R., & Magazzu, A. (1994). Constraints to the masses of brown dwarf candidates from the lithium test. *Astrophys. J.*, *436*, 262–269.
- Martín, E. L., Zapatero Osorio, M. R., & Lehto, H. J. (2001). Photometric Variability in the Ultracool Dwarf BRI 0021-0214: Possible Evidence for Dust Clouds. *Astrophys. J.*, *557*, 822–830.
- Mathioudakis, M., Bloomfield, D. S., Jess, D. B., Dhillon, V. S., & Marsh, T. R. (2006). The periodic variations of a white-light flare observed with ULTRACAM. *Astron. & Astrophys.*, *456*, 323–327.
- Mathioudakis, M., Seiradakis, J. H., Williams, D. R., Avgoloupis, S., Bloomfield, D. S., & McAteer, R. T. J. (2003). White-light oscillations during a flare on II Peg. *Astron. & Astrophys.*, *403*, 1101–1104.
- Matsumoto, T., & Hanawa, T. (2003). Fragmentation of a Molecular Cloud Core versus Fragmentation of the Massive Protoplanetary Disk in the Main Accretion Phase. *Astrophys. J.*, *595*, 913–934.
- Mauas, P. J. D., & Falchi, A. (1996). Atmospheric models of flare stars: the flaring state of AD Leonis. *Astron. & Astrophys.*, *310*, 245–258.
- McCarthy, D. W., Jr., Probst, R. G., & Low, F. J. (1985). Infrared detection of a close cool companion to Van Biesbroeck 8. *Astrophys. J.*, *290*, L9–L13.

- McKenzie, D. E., & Mullan, D. J. (1997). Periodic Modulation of X-Ray Intensity from Coronal Loops - Heating by Resonant Absorption? *Sol. Phys.*, 176, 127–145.
- McLean, M., Berger, E., & Reiners, A. (2012). The Radio Activity-Rotation Relation of Ultracool Dwarfs. *Astrophys. J.*, 746, 23.
- Melrose, D. B. (1976). An interpretation of Jupiter's decametric radiation and the terrestrial kilometric radiation as direct amplified gyroemission. *Astrophys. J.*, 207, 651–662.
- Mestel, L. (1977). Theoretical processes in star formation. In T. de Jong, & A. Maeder (Eds.) *Star Formation*, vol. 75 of *IAU Symposium*, (pp. 213–232).
- Mitra-Kraev, U., Harra, L. K., Williams, D. R., & Kraev, E. (2005). The first observed stellar X-ray flare oscillation: Constraints on the flare loop length and the magnetic field. *Astron. & Astrophys.*, 436, 1041–1047.
- Moffett, T. J. (1974). UV Ceti flare stars - Observational data. *Astrophys. J.*, 29, 1–42.
- Mohanty, S., & Basri, G. (2003). Rotation and Activity in Mid-M to L Field Dwarfs. *Astrophys. J.*, 583, 451–472.
- Mohanty, S., Basri, G., Shu, F., Allard, F., & Chabrier, G. (2002). Activity in Very Cool Stars: Magnetic Dissipation in Late M and L Dwarf Atmospheres. *Astrophys. J.*, 571, 469–486.
- Monin, J.-L., Ménard, F., & Peretto, N. (2006). Disc orientations in pre-main-sequence multiple systems. A study in southern star formation regions. *Astron. & Astrophys.*, 446, 201–210.
- Montes, D., López-Santiago, J., Gálvez, M. C., Fernández-Figueroa, M. J., De Castro, E., & Cornide, M. (2001). Late-type members of young stellar kinematic groups - I. Single stars. *Mon. Not. R. Astron. Soc.*, 328, 45–63.
- Morales-Calderón, M., Stauffer, J. R., Kirkpatrick, J. D., Carey, S., Gelino, C. R., Barrado y Navascués, D., Rebull, L., Lowrance, P., Marley, M. S., Charbonneau, D., Patten, B. M., Megeath, S. T., & Buzasi, D. (2006). A Sensitive Search for Variability in Late L Dwarfs: The Quest for Weather. *Astrophys. J.*, 653, 1454–1463.
- Morin, J., Donati, J.-F., Petit, P., Delfosse, X., Forveille, T., Albert, L., Aurière, M., Cabanac, R., Dintrans, B., Fares, R., Gastine, T., Jardine, M. M., Lignières, F., Paletou, F.,

- Ramirez Velez, J. C., & Théado, S. (2008). Large-scale magnetic topologies of mid M dwarfs. *Mon. Not. R. Astron. Soc.*, 390, 567–581.
- Morin, J., Donati, J.-F., Petit, P., Delfosse, X., Forveille, T., & Jardine, M. M. (2010). Large-scale magnetic topologies of late M dwarfs. *Mon. Not. R. Astron. Soc.*, 407, 2269–2286.
- Mullan, D. J., Herr, R. B., & Bhattacharyya, S. (1992). Transient periodicities in X-ray-active red dwarfs - First results from Mount Cuba and interpretation with an oscillating loop model. *Astrophys. J.*, 391, 265–275.
- Murdin, P. (2001). *Encyclopedia of astronomy and astrophysics*. Nature Publishing Group 2001, Brunel Road, Houndmills, Basingstoke, Hampshire, RG21 6XS, UK Registered No. 785998, and Institute of Physics Publishing 2001, Dirac House, Temple Back, Bristol, BS1 6BE, UK.
- Nakajima, T., Oppenheimer, B. R., Kulkarni, S. R., Golimowski, D. A., Matthews, K., & Durrance, S. T. (1995). Discovery of a cool brown dwarf. *Nature*, 378, 463–465.
- Neuhäuser, R., Briceño, C., Comerón, F., Hearty, T., Martín, E. L., Schmitt, J. H. M. M., Stelzer, B., Supper, R., Voges, W., & Zinnecker, H. (1999). Search for X-ray emission from bona-fide and candidate brown dwarfs. *Astron. & Astrophys.*, 343, 883–893.
- Offner, S. S. R., Kratter, K. M., Matzner, C. D., Krumholz, M. R., & Klein, R. I. (2010). The Formation of Low-mass Binary Star Systems Via Turbulent Fragmentation. *Astrophys. J.*, 725, 1485–1494.
- Oppenheimer, B. R., Kulkarni, S. R., Matthews, K., & Nakajima, T. (1995). Infrared Spectrum of the Cool Brown Dwarf Gl 229B. *Science*, 270, 1478–1479.
- Oppenheimer, B. R., Kulkarni, S. R., & Stauffer, J. R. (2000). Brown Dwarfs. *Protostars and Planets IV (Book - Tucson: University of Arizona Press; eds Mannings, V., Boss, A.P., Russell, S. S.)*, (p. 1313).
- Osten, R. A., Hawley, S. L., Bastian, T. S., & Reid, I. N. (2006). The Radio Spectrum of TVLM 513-46546: Constraints on the Coronal Properties of a Late M Dwarf. *Astrophys. J.*, 637, 518–521.
- Osten, R. A., Phan-Bao, N., Hawley, S. L., Reid, I. N., & Ojha, R. (2009). Steady and Transient Radio Emission from Ultracool Dwarfs. *Astrophys. J.*, 700, 1750–1758.

- Parker, E. N. (1975). The generation of magnetic fields in astrophysical bodies. X - Magnetic buoyancy and the solar dynamo. *Astrophys. J.*, 198, 205–209.
- Pavlenko, Y., Zapatero Osorio, M. R., & Rebolo, R. (2000). On the interpretation of the optical spectra of L-type dwarfs. *Astron. & Astrophys.*, 355, 245–255.
- Perrier, C., & Mariotti, J.-M. (1987). On the binary nature of Van Biesbroeck 8. *Astrophys. J.*, 312, L27–L30.
- Perryman, M. A. C., Lindegren, L., Kovalevsky, J., Hoeg, E., Bastian, U., Bernacca, P. L., Cr    , M., Donati, F., Grenon, M., Grewing, M., van Leeuwen, F., van der Marel, H., Mignard, F., Murray, C. A., Le Poole, R. S., Schrijver, H., Turon, C., Arenou, F., Froeschl  , M., & Petersen, C. S. (1997). The HIPPARCOS Catalogue. *Astron. & Astrophys.*, 323, L49–L52.
- Phan-Bao, N., Lim, J., Donati, J.-F., Johns-Krull, C. M., & Mart    n, E. L. (2009). Magnetic Field Topology in Low-Mass Stars: Spectropolarimetric Observations of M Dwarfs. *Astrophys. J.*, 704, 1721–1729.
- Phan-Bao, N., Osten, R. A., Lim, J., Mart    n, E. L., & Ho, P. T. P. (2007). Discovery of Radio Emission from the Tight M8 Binary LP 349-25. *Astrophys. J.*, 658, 553–556.
- Press, W. H., Teukolsky, S. A., Vetterling, W. T., & Flannery, B. P. (1992). *Numerical recipes in C. The art of scientific computing*. Cambridge: University Press, —c1992, 2nd ed.
- Radigan, J., Jayawardhana, R., Lafreni    , D., Artigau,     ., Marley, M., & Saumon, D. (2012). Large-amplitude Variations of an L/T Transition Brown Dwarf: Multi-wavelength Observations of Patchy, High-contrast Cloud Features. *Astrophys. J.*, 750, 105.
- Rebolo, R., Martin, E. L., & Magazzu, A. (1992). Spectroscopy of a brown dwarf candidate in the Alpha Persei open cluster. *Astrophys. J.*, 389, L83–L86.
- Reid, I. N., Burgasser, A. J., Cruz, K. L., Kirkpatrick, J. D., & Gizis, J. E. (2001). Near-Infrared Spectral Classification of Late M and L Dwarfs. *Astron. J.*, 121, 1710–1721.
- Reid, I. N., Cruz, K. L., Laurie, S. P., Liebert, J., Dahn, C. C., Harris, H. C., Guetter, H. H., Stone, R. C., Canzian, B., Luginbuhl, C. B., Levine, S. E., Monet, A. K. B., & Monet,

- D. G. (2003). Meeting the Cool Neighbors. IV. 2MASS 1835+32, a Newly Discovered M8.5 Dwarf within 6 Parsecs of the Sun. *Astron. J.*, 125, 354–358.
- Reid, I. N., Kirkpatrick, J. D., Gizis, J. E., Dahn, C. C., Monet, D. G., Williams, R. J., Liebert, J., & Burgasser, A. J. (2000). Four Nearby L Dwarfs. *Astron. J.*, 119, 369–377.
- Reid, I. N., Kirkpatrick, J. D., Gizis, J. E., & Liebert, J. (1999). BRI 0021-0214: Another Surprise at the Bottom of the Main Sequence. *Astrophys. J.*, 527, L105–L107.
- Reid, I. N., Kirkpatrick, J. D., Liebert, J., Gizis, J. E., Dahn, C. C., & Monet, D. G. (2002). High-Resolution Spectroscopy of Ultracool M Dwarfs. *Astron. J.*, 124, 519–540.
- Reiners, A., & Basri, G. (2007). The First Direct Measurements of Surface Magnetic Fields on Very Low Mass Stars. *Astrophys. J.*, 656, 1121–1135.
- Reiners, A., & Basri, G. (2008). Chromospheric Activity, Rotation, and Rotational Braking in M and L Dwarfs. *Astrophys. J.*, 684, 1390–1403.
- Reiners, A., & Basri, G. (2009). A Volume-Limited Sample of 63 M7-M9.5 Dwarfs. I. Space Motion, Kinematic Age, and Lithium. *Astrophys. J.*, 705, 1416–1424.
- Rieke, G. H., & Rieke, M. J. (1990). Possible substellar objects in the Rho Ophiuchi cloud. *Astrophys. J.*, 362, L21–L24.
- Robbins, M. S., & Hadwen, B. J. (2003). The noise performance of electron multiplying charge coupled devices. vol. 50 of *IEEE*, (pp. 1227–1232).
- Rockenfeller, B., Bailer-Jones, C. A. L., & Mundt, R. (2006a). Variability and periodicity of field M dwarfs revealed by multichannel monitoring. *Astron. & Astrophys.*, 448, 1111–1124.
- Rockenfeller, B., Bailer-Jones, C. A. L., Mundt, R., & Ibrahimov, M. A. (2006b). Multiband photometric detection of a huge flare on the M9 dwarf 2MASSW J1707183+643933. *Mon. Not. R. Astron. Soc.*, 367, 407–411.
- Rodonò, M. (1976). Double-Peaked Flare Events on Red Dwarf Stars and Solar 'sympathetic' Flares. In V. Bumba, & J. Kleczek (Eds.) *Basic Mechanisms of Solar Activity*, vol. 71 of *IAU Symposium*, (p. 475).

- Rodono', M., Houdebine, E. R., Catalano, S., Foing, B., Butler, C. J., Scaltriti, F., Cutispoto, G., Gary, D. E., Gibson, D. M., & Haisch, B. M. (1989). Simultaneous multi-wavelength observations of an intense flare on AD Leonis. In *Solar and Stellar Flares. Poster Papers*, (p. 53P).
- Ross, F. E. (1933). Astrometry with Mirrors and Lenses. *Astrophys. J.*, 77, 243.
- Ross, F. E. (1935). Lens Systems for Correcting Coma of Mirrors. *Astrophys. J.*, 81, 156.
- Route, M., & Wolszczan, A. (2012). The Arecibo Detection of the Coolest Radio-flaring Brown Dwarf. *Astrophys. J.*, 747, L22.
- Rutledge, R. E., Basri, G., Martín, E. L., & Bildsten, L. (2000). Chandra Detection of an X-Ray Flare from the Brown Dwarf LP 944-20. *Astrophys. J.*, 538, L141–L144.
- Saar, S. H., & Linsky, J. L. (1985). The photospheric magnetic field of the dM3.5e flare star AD Leonis. *Astrophys. J.*, 299, L47–L50.
- Scargle, J. D. (1982). Studies in astronomical time series analysis. II - Statistical aspects of spectral analysis of unevenly spaced data. *Astrophys. J.*, 263, 835–853.
- Schneider, J. (1959). *Phys. Rev. Lett.*, 2, 504.
- Scholz, A., Eisloffel, J., & Mundt, R. (2009). Long-term monitoring in IC4665: fast rotation and weak variability in very low mass objects. *Mon. Not. R. Astron. Soc.*, 400, 1548–1562.
- Schwabe, M. (1845). Sonnenflecken Von Herrn Hofrath Schwabe in Dessau. *Astronomische Nachrichten*, 22, 365.
- Schwarzenberg-Czerny, A. (1991). Accuracy of period determination. *Mon. Not. R. Astron. Soc.*, 253, 198–206.
- Schweitzer, A., Gizis, J. E., Hauschildt, P. H., Allard, F., & Reid, I. N. (2001). Analysis of Keck HIRES Spectra of Early L-Type Dwarfs. *Astrophys. J.*, 555, 368–379.
- Sheehan, B. (2008). *Development and Implementation of an L3CCD High Cadence Imaging System for Optical Astronomy*. Ph.D. thesis, School of Physics, Centre for Astronomy, National University of Ireland, Galway.

- Sheehan, B. J., & Butler, R. F. (2008). Development and use of an L3CCD high-cadence imaging system for Optical Astronomy. In D. Phelan, O. Ryan, & A. Shearer (Eds.) *High Time Resolution Astrophysics: The Universe at Sub-Second Timescales*, vol. 984 of *American Institute of Physics Conference Series*, (pp. 162–167).
- Shipman, H. L. (1986). An unsuccessful search for brown dwarf companions to white dwarf stars. In M. C. Kafatos, R. S. Harrington, & S. P. Maran (Eds.) *Astrophysics of Brown Dwarfs*, (pp. 71–75).
- Shu, F. H., Adams, F. C., & Lizano, S. (1987). Star formation in molecular clouds - Observation and theory. *Ann. Rev. Astron. Astrophys.*, 25, 23–81.
- Skrutskie, M. F., Dutkevitch, D., Strom, S. E., Edwards, S., Strom, K. M., & Shure, M. A. (1990). A sensitive 10-micron search for emission arising from circumstellar dust associated with solar-type pre-main-sequence stars. *Astron. J.*, 99, 1187–1195.
- Skrutskie, M. F., Forrest, W. J., & Shure, M. (1989). An infrared search for low-mass companions of stars near the sun. *Astron. J.*, 98, 1409–1417.
- Skrutskie, M. F., Forrest, W. J., & Shure, M. A. (1987). Direct infrared imaging of VB 8. *Astrophys. J.*, 312, L55–L58.
- Solanki, S. K., & Unruh, Y. C. (1998). A model of the wavelength dependence of solar irradiance variations. *aap*, 329, 747–753.
- Stamatellos, D., & Whitworth, A. P. (2009). The properties of brown dwarfs and low-mass hydrogen-burning stars formed by disc fragmentation. *Mon. Not. R. Astron. Soc.*, 392, 413–427.
- Stellingwerf, R. F. (1978). Period determination using phase dispersion minimization. *Astrophys. J.*, 224, 953–960.
- Stephens, D. C., Leggett, S. K., Cushing, M. C., Marley, M. S., Saumon, D., Geballe, T. R., Golimowski, D. A., Fan, X., & Noll, K. S. (2009). The 0.8–14.5 μm Spectra of Mid-L to Mid-T Dwarfs: Diagnostics of Effective Temperature, Grain Sedimentation, Gas Transport, and Surface Gravity. *Astrophys. J.*, 702, 154–170.
- Stephens, D. C., Marley, M. S., Noll, K. S., & Chanover, N. (2001). L-Band Photometry of L and T Dwarfs. *Astrophys. J.*, 556, L97–L101.

- Tian, H. (2000). *Noise Analysis in CMOS Image Sensors*. Ph.D. thesis, Department of Applied Sciences, Stanford University.
- Tinney, C. G., Mould, J. R., & Reid, I. N. (1993). The faintest stars - Infrared photometry, spectra, and bolometric magnitude. *Astron. J.*, *105*, 1045–1059.
- Tinney, C. G., & Reid, I. N. (1998). High-resolution spectra of very low-mass stars. *Mon. Not. R. Astron. Soc.*, *301*, 1031–1048.
- Tinney, C. G., Reid, I. N., Gizis, J., & Mould, J. R. (1995). Trigonometric Parallaxes and the HR Diagram at the Bottom of the Main Sequence. *Astron. J.*, *110*, 3014.
- Tinney, C. G., & Tolley, A. J. (1999). Searching for weather in brown dwarfs. *Mon. Not. R. Astron. Soc.*, *304*, 119–126.
- Twiss, R. Q. (1958). Radiation Transfer and the Possibility of Negative Absorption in Radio Astronomy. *Aust. Journ. Phys.*, *11*, 564.
- Twiss, R. Q., & Roberts, J. A. (1958). Electromagnetic Radiation from Electrons Rotating in an Ionized Medium under the Action of a Uniform Magnetic Field. *Aust. Journ. Phys.*, *11*, 424.
- Ushomirsky, G., Matzner, C. D., Brown, E. F., Bildsten, L., Hilliard, V. G., & Schroeder, P. C. (1998). Light-Element Depletion in Contracting Brown Dwarfs and Pre-Main-Sequence Stars. *Astrophys. J.*, *497*, 253–266.
- van den Oord, G. H. J., Doyle, J. G., Rodono, M., Gary, D. E., Henry, G. W., Byrne, P. B., Linsky, J. L., Haisch, B. M., Pagano, I., & Leto, G. (1996). Flare energetics: analysis of a large flare on YZ Canis Minoris observed simultaneously in the ultraviolet, optical and radio. *Astron. & Astrophys.*, *310*, 908–922.
- Vasavada, A. R., & Showman, A. P. (2005). Jovian atmospheric dynamics: an update after Galileo and Cassini. *Reports on Progress in Physics*, *68*, 1935–1996.
- Vrba, F. J., Henden, A. A., Luginbuhl, C. B., Guetter, H. H., Munn, J. A., Canzian, B., Burgasser, A. J., Kirkpatrick, J. D., Fan, X., Geballe, T. R., Golimowski, D. A., Knapp, G. R., Leggett, S. K., Schneider, D. P., & Brinkmann, J. (2004). Preliminary Parallaxes of 40 L and T Dwarfs from the US Naval Observatory Infrared Astrometry Program. *Astron. J.*, *127*, 2948–2968.

- Weis, E. W. (1974). On the inclination of rotation axes in visual binaries. *Astrophys. J.*, 190, 331–337.
- West, A. A., & Basri, G. (2009). A First Look at Rotation in Inactive Late-Type M Dwarfs. *Astrophys. J.*, 693, 1283–1289.
- West, A. A., Hawley, S. L., Walkowicz, L. M., Covey, K. R., Silvestri, N. M., Raymond, S. N., Harris, H. C., Munn, J. A., McGehee, P. M., Ivezić, Ž., & Brinkmann, J. (2004). Spectroscopic Properties of Cool Stars in the Sloan Digital Sky Survey: An Analysis of Magnetic Activity and a Search for Subdwarfs. *Astron. J.*, 128, 426–436.
- Wheelwright, H. E., Vink, J. S., Oudmaijer, R. D., & Drew, J. E. (2011). On the alignment between the circumstellar disks and orbital planes of Herbig Ae/Be binary systems. *aap*, 532, A28.
- Winglee, R. M., Dulk, G. A., & Bastian, T. S. (1986). A search for cyclotron maser radiation from substellar and planet-like companions of nearby stars. *Astrophys. J.*, 309, L59–L62.
- Worden, S. P., Schneeberger, T. J., Giampapa, M. S., Deluca, E. E., & Cram, L. E. (1984). The response of chromospheric emission lines to flares on YZ Canis Minoris. *Astrophys. J.*, 276, 270–280.
- Wu, C. S., & Lee, L. C. (1979). A theory of the terrestrial kilometric radiation. *Astrophys. J.*, 230, 621–626.
- Wynne, C. G. (1949). *Proc. Phys. Soc. (London)*, 62, 772.
- Wynne, C. G. (1965). Field correctors for large telescopes. *Appl. Opt.*, 4, 1185.
- Wynne, C. G. (1967). *Appl. Opt.*, 6, 1227.
- Wynne, C. G. (1972). Improved three-lens field correctors for paraboloids. *Mon. Not. R. Astron. Soc.*, 160, 13P.
- Yurchenko, S. N., Barber, R. J., & Tennyson, J. (2011). A variationally computed line list for hot NH₃. *Mon. Not. R. Astron. Soc.*, 413, 1828–1834.
- Zapatero Osorio, M. R., Martín, E. L., Bouy, H., Tata, R., Deshpande, R., & Wainscoat, R. J. (2006). Spectroscopic Rotational Velocities of Brown Dwarfs. *Astrophys. J.*, 647, 1405–1412.

- Zarka, P. (1998). Auroral radio emissions at the outer planets: Observations and theories. *J. Geophys. Res.*, *103*, 20159–20194.

LIST OF FIGURES

1.1	Plot of mass ($\log(M/M_{\odot})$) vs. central temperature (T_c ,K) from Chabrier & Baraffe (2000).	16
1.2	Plot of evolution of effective temperature (T_{eff}), versus time ($\log \tau$, years) from Chabrier & Baraffe (2000).	18
1.3	Plot of evolution of luminosity (L_{\odot}) of M dwarfs and substellar objects, with solar-metallicity $Z = Z_{\odot}$, as a function of time, t ($\log \tau$, years) (Burrows et al., 1997).	19
1.4	Plot of radius (R) vs. effective temperature (T_{eff}), for dwarfs from $0.0003 M_{\odot}$ (i.e. mass of Saturn) to $0.07 M_{\odot}$ (HBMM) (Burrows et al., 1997). . .	20
1.5	Plot of gravity (g , cm s^{-2}) versus effective temperature (T_{eff} , in K) for brown dwarfs and planets, for a range of masses ($0.0003 - 0.075 M_{\odot}$), over a range of ages from 300 Myr - 3 Gyr ($\log 6.5 - 9.5$ years) (Burrows et al., 1997).	21
1.6	Plot of spectra of a late-M, early to mid-L and late-L dwarf, taken from Kirkpatrick et al. (1999).	22
1.7	Plot of NIR spectra from a mid-L, a late-L and a T dwarf (Gliese 229B), taken from Kirkpatrick et al. (1999).	23
1.8	Plots from Cushing et al. (2011), who show a H -band spectrum of five ultracool dwarfs, spanning the T4 - Y0 spectral range.	24
1.9	Plots from Cushing et al. (2011), that show the spectral standards of a T6, T7 and T8 dwarf Burgasser et al. (2006), as well as a T9 and Y0 dwarf newly discovered by WISE.	25
1.10	Radio lightcurves of TVLM 513-46546 from Hallinan et al. (2007). . . .	31
1.11	Plot showing Jupiter's magnetospheric regions (Murdin, 2001).	33
2.1	(a) Andor iXon camera. (b) GUFi QE curve.	44
2.2	Plot of CCD vs. EM-CCD SNR (Sheehan, 2008).	46
2.3	GUFi instrument box, and adapter plates/mounts for Cassegrain focus at VATT.	49
2.4	(a) GUFi during assembly. (b) GUFi mounted at Cassegrain focus. . . .	50
2.5	(a) Andor NEO sCMOS detector. (b) QE curve of the sCMOS chip. . . .	54

2.6	Zemax drawing of CHIMERA optical design layout.	57
2.7	(a) Zemax RMS spot radius assessment. (b) Zemax plot of RMS spot radius vs. field position.	59
2.8	Solidworks drawing of CHIMERA instrument.	61
2.9	(a) CHIMERA components on the optical breadboard. (b) CHIMERA fully assembled.	62
2.10	CHIMERA optical system showing the dichroic beam splitter and custom g' mount held in the focusing tube of the collimating element.	62
2.11	CHIMERA proof of concept data: August 1, 2012.	66
3.1	Flow-chart of data management, data calibration/reduction, and pre-photometry steps, of the L3 pipeline.	72
3.2	Example of an I-band frame containing fringing (left), and after fringing was removed (right).	75
3.3	Schematic of the data management, data calibration/reduction, de-fringing and final reduced, de-fringed, science frame production.	76
3.4	Plot of optimum aperture assessment.	81
3.5	Plots showing the four main steps in the “quality control” MATLAB routines.	84
3.6	(a) Periodogram showing an example of the spectral leakage feature. (b) Plot showing aliased periods.	90
3.7	(a) Plot showing phase folded lightcurves to a correct an incorrect period. (b) Plot showing the PDM minimum theta (Θ) statistic for these folded lightcurves.	93
3.8	Least Squares Fit to a raw lightcurve from the M9 dwarf TVLM 513-46546, where the mean amplitude variability is assessed.	96
3.9	Plot of LP 349-25 October 2010 epoch with model sinusoid overplotted, investigating the presence of a second period.	98
3.10	(a) Plot of model sinusoidal signal (black) with a random noise component added (green). (b) Lomb Scargle periodogram identifying period error.	100
4.1	Filter transmission curves with over-plotted spectra of an M8 dwarf (A), an L0.5 dwarf (B) and an L3.5 dwarf (C) - the spectral range which encompasses our study.	116
4.2	LP 349-25 photometric results.	121
4.3	LP 349-25 statistical analysis.	122
4.4	The unusual behavior of LP 349-25.	124

4.5	2MASS J0746+2000 photometric results.	127
4.6	2MASS J0746+2000 statistical analysis.	128
4.7	LSR J1835+3259 photometric results.	130
4.8	LSR J1835+3259 statistical analysis.	131
4.9	TVLM 513-46546 photometric results.	133
4.10	TVLM 513-46546 statistical analysis.	134
4.11	BRI 0021-0214 photometric results.	135
4.12	2MASS J0036+18: (a) Photometric results. (b) Lomb Scargle periodogram and PDM analysis.	136
4.13	Summary of statistics for all targets.	137
5.1	Plot of the phase stability of TVLM 513-46546 over a ~ 5 year baseline. .	147
5.2	Plot of the correlated behavior of TVLM 513-46546 over a ~ 5 year base- line with models with <i>fixed</i> phase included.	148
5.3	Plots of Amplitude Analysis of TVLM 513-46546.	149
5.4	(a) Example of XCF applied to May 7 and May 8 2011 UT. (b) May 7 and May 8 2011 UT lightcurves phase agreement.	151
5.5	Plots of auroral emissions from TVLM 513-46546 showing the level of agreement between the spectroscopic and photometric measurements from Gemini, NTT, VLT and VATT.	153
5.6	Gemini archival data of the spectrum from TVLM 513-46546.	154
6.1	Constraining the system properties of 2MASS J0746+2000AB via the mod- els of Chabrier & Baraffe (2000).	166
6.2	On the orbital coplanarity of LP 349-25AB.	168
6.3	A sketch of the alignment planes of LP 349-25AB.	169
6.4	Plot of evolutionary model estimated radii for 2MASS J0746+2000A and 2MASS J0746+2000B.	172
6.5	On the orbital coplanarity of 2MASS J0746+2000A.	173
6.6	On the orbital coplanarity of 2MASS J0746+2000B.	174
6.7	A sketch of the alignment planes of 2MASS J0746+2000AB.	175
7.1	Impulsive flaring events from the dM4.5e flare star YZ CMi, February 25 2011 UT.	185
7.2	Flaring events in B-band from YZCMi on February 26 2011 UT, including the largest detected flare in our sample.	186

7.3	Simultaneous observations of YZ CMi by ARCSAT using u' , g' and r' , and GUFi using B-band.	187
7.4	Flaring events from the M3.5Ve flare star AD Leo.	189
7.5	Simultaneous observations of AD Leo by ARCSAT using $u' - g'$, and GUFi using V-band.	190
7.6	A V-band and r' flare from AD Leo, as detected by VATT (GUFi) and by ARCSAT.	191
7.7	Periodic loop oscillations events from the flare star YZ CMi.	192
7.8	The simultaneous observations of VATT (GUFi) and ARCSAT covering UV and optical wavelengths which detect loop oscillations.	193
8.1	Kuiper Belt Object field as obtained by CHIMERA.	206
A.1	Flaring events from the M4 flare star GJ 1243T.	236
B.1	Flaring events from GL 51 (raw).	240
B.2	Flaring events from GL 51 (binned).	241
B.3	Flaring events from GJ 2069a and GJ 2069b.	242
B.4	Flaring events from GL 1111.	243
C.1	Offner relay Zemax designs (3D system) I.	245
C.2	Offner relay Zemax designs (3D system) II.	246

LIST OF TABLES

1.1	Studies of Optical Variability in Ultracool Dwarfs.	38
2.1	GUPI mk.II Photometer Overview (System Characteristics).	43
2.2	Measured Sensitivity ($e^- \text{ ADU}^{-1}$) and Readnoise ($e^- \text{ pixel}^{-1} \text{ readout}^{-1}$).	47
2.3	CHIMERA Photometer Overview (System Characteristics).	53
2.4	CHIMERA Optical System Image Quality Assessment.	60
4.1	Summary of Campaign Sample Properties.	104
4.2	Observation Details.	114
4.3	Observation Details (cont.).	115
4.4	Confirmed Optical Periodic Variability in Radio Detected Ultracool Dwarf Sample.	118
4.5	Amplitude variability analysis.	119
4.6	Amplitude variability analysis (cont.).	120
6.1	Properties of the Binary 2MASS J0746+2000AB.	171
7.1	Flare Star Observation Details.	182
A.1	Flare Star Observation Details of GJ 1243.	237
B.1	Flare Star Observation Details of GL 51, GJ 2069ab and GL 1111.	239



Observations of GJ 1243

In this appendix we include details of observations of the M4 flare star GJ 1243, which was also observed as part of the flare star campaign as outlined in Chapter 7. The star was observed in the Johnson B-band and $H\alpha$ filters, with exposure times of <0.15 seconds. We detected 5 flares from there data on observations during the April epoch, which encompassed ~ 227000 frames. Again, these data were originally proposed as simultaneous observations to spectroscopy from the 3.5 m telescope, at APO. However, due to poor weather we did not obtain the spectroscopic component. The lightcurves from the campaign are shown in Figure A.1, and observation details are shown in Table A.1.

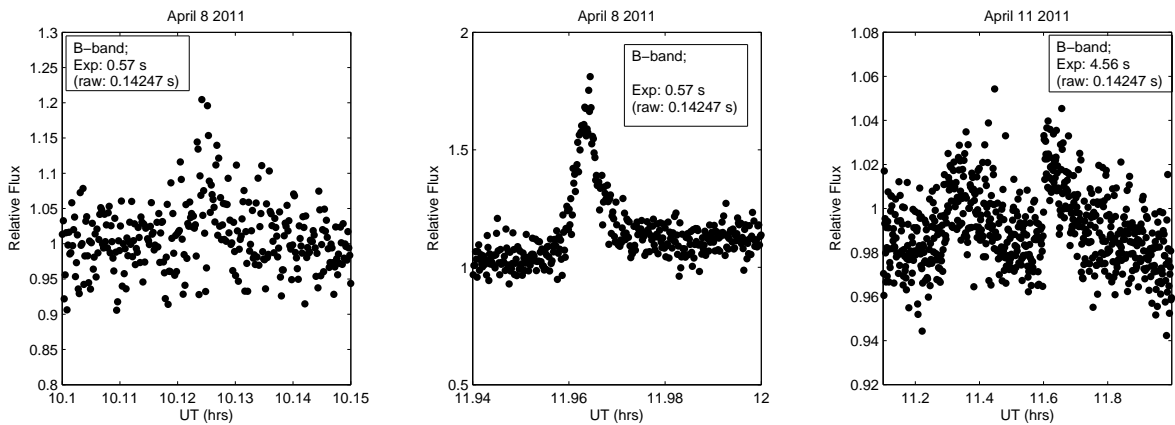


Figure A.1: Flaring from GJ 1243 on April 8, 11 and 13 2011 UT. Data were taken in the Johnson B-band and in the $H\alpha$ narrowband filter. We show binned lightcurves where the raw frames of 0.14247 seconds were summed to 0.57 second frames, to increase SNR. We detect no $H\alpha$ flaring in the data.

Source	Total Time (~hrs)	Date of Obs. (UT)	Length of Obs./# frames (~hrs/#)	Exp. Time (s)	Flares #
GJ 1243	10	2011 Apr 08	2.75/67175	0.14247	2
		2011 Apr 11	3.25/80000	0.14247	3
		2011 Apr 13	3.25/79542	0.14247	0
Source	Band	Readout Rate (MHz)	Amplifier	Window (pixels)	Instruments
GJ 1243	B	1	Conv.	80×200	GUFI/NMSU/ARCSAT
	B	1	Conv.	80×200	GUFI/NMSU/ARCSAT
	H α	1	Conv.	80×200	GUFI/NMSU/ARCSAT

Table A.1: Flare Star Observation Details of GJ 1243.

Here we show the observation details of the M4 flare star GJ 1243, that was carried out using the GUFI photometer on VATT. These were taken simultaneously to the NMSU 1 m telescope and 0.5 m ARCSAT telescopes at APO, which provided Sloan u' - g' photometry, albeit at much slower cadence than GUFI.

B

Observations of GL 51, GJ 2069a, GJ 2069b and GL 1111

In this appendix we include details of observations of the M type flare star GL 51, GJ 2069a, GJ 2069b and GL 1111. These data were obtained during the October - December 2010 VATT observation run, and were initially part of a ZDI campaign (refer to Chapter 8, § 8.2.4). Data were taken in 20 minute intervals, and were sampled between ~ 0.1 - 1 second. The purpose of these observations was not to detect flaring, but instead to establish the period of rotation of each object. This was part of a larger collaboration, where we sought to provide rotation periods for Zeeman Doppler Imaging parameters. As explained in previous sections, it becomes increasingly more difficult to establish a rotation period via spectroscopy due to how dim the stars become at cooler temperatures. Many of these stars were thus inaccessible to the instruments being used, and so GUFi was utilized for this purpose. Because the rotation periods of these objects are of the order of days, the 20 minute interval observations were effective in that many parts of the rotation could be sampled over a number of observations per given epoch, for each object. The rotation periods for some of these stars has already been found, and in this case we are providing a photometric confirmation. We do not discuss the rotation period analysis here since the values we obtained are still tentative and work is on-going in this respect. We used redder wavebands to try and avoid large flaring so we could sample the quiescent part of the lightcurve. However we still detect flaring in the data for each source. We include details of the observations in Table B.1 and examples of some of the events in the following appendix.

Source	Total Time (~hrs)	Date of Obs. (UT)	Length of Obs. (~hrs)	Exp. Time (s)	Flares #
GL 51	15	2010 Nov 16	5	1	1
		2009 Sept 26	5	0.14247	3
		2009 Sept 25	5	0.14247	0
GJ 2069ab	8	2010 Nov 15	2	1	1
		2010 Nov 16	2	1	1
		2010 Nov 17	2	1	2
		2010 Nov 27	2	1	3
		2011 Apr 08	2	1	1
GL 1111	6	2011 Apr 11	2	1	1
		2011 Apr 13	2	1	2
Source	Band	Readout Rate (MHz)	Amplifier	Window (pixels)	Instruments
GL 51	V	1	Conv.	512×512	GUF1
	I	1	Conv.	512×512	GUF1
	I	1	Conv.	512×512	GUF1
GJ 2069ab	V	1	Conv.	512×512	GUF1
	V	1	Conv.	512×512	GUF1
	V	1	Conv.	512×512	GUF1
GL 1111	V	1	Conv.	512×512	GUF1
	V	1	Conv.	512×512	GUF1
	V	1	Conv.	512×512	GUF1

Table B.1: Flare Star Observation Details of GL 51, GJ 2069ab and GL 1111.

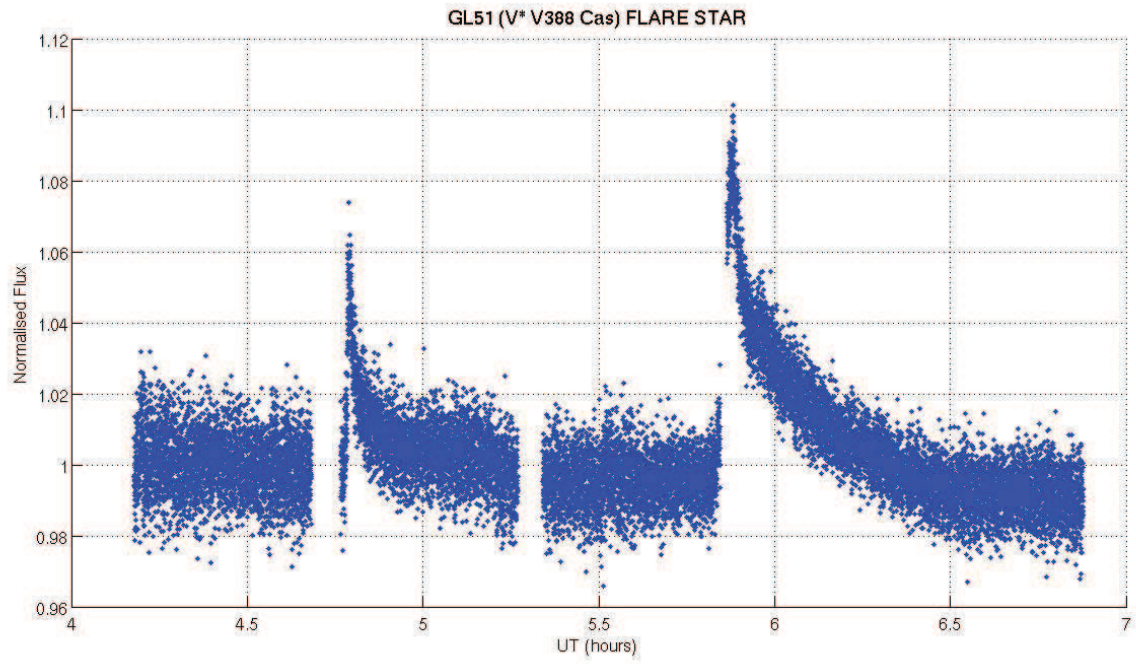


Figure B.1: Flaring from GL 51 on September 26 2009 UT. Data were taken in the Johnson I-band in this observation, and were originally taken to establish the dwarf's period of rotation.

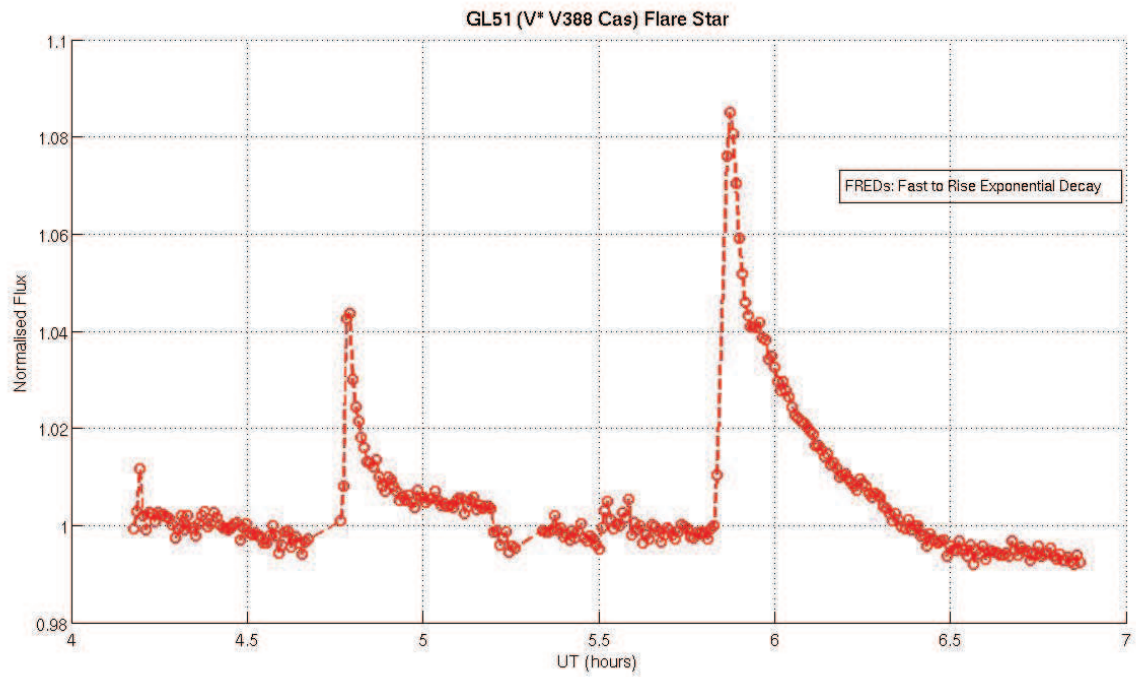


Figure B.2: Flaring from GL 51 as shown in the previous figure We have binned this data by a factor of 8 to increase the SNR and assess any substructure in the different phases of the event.

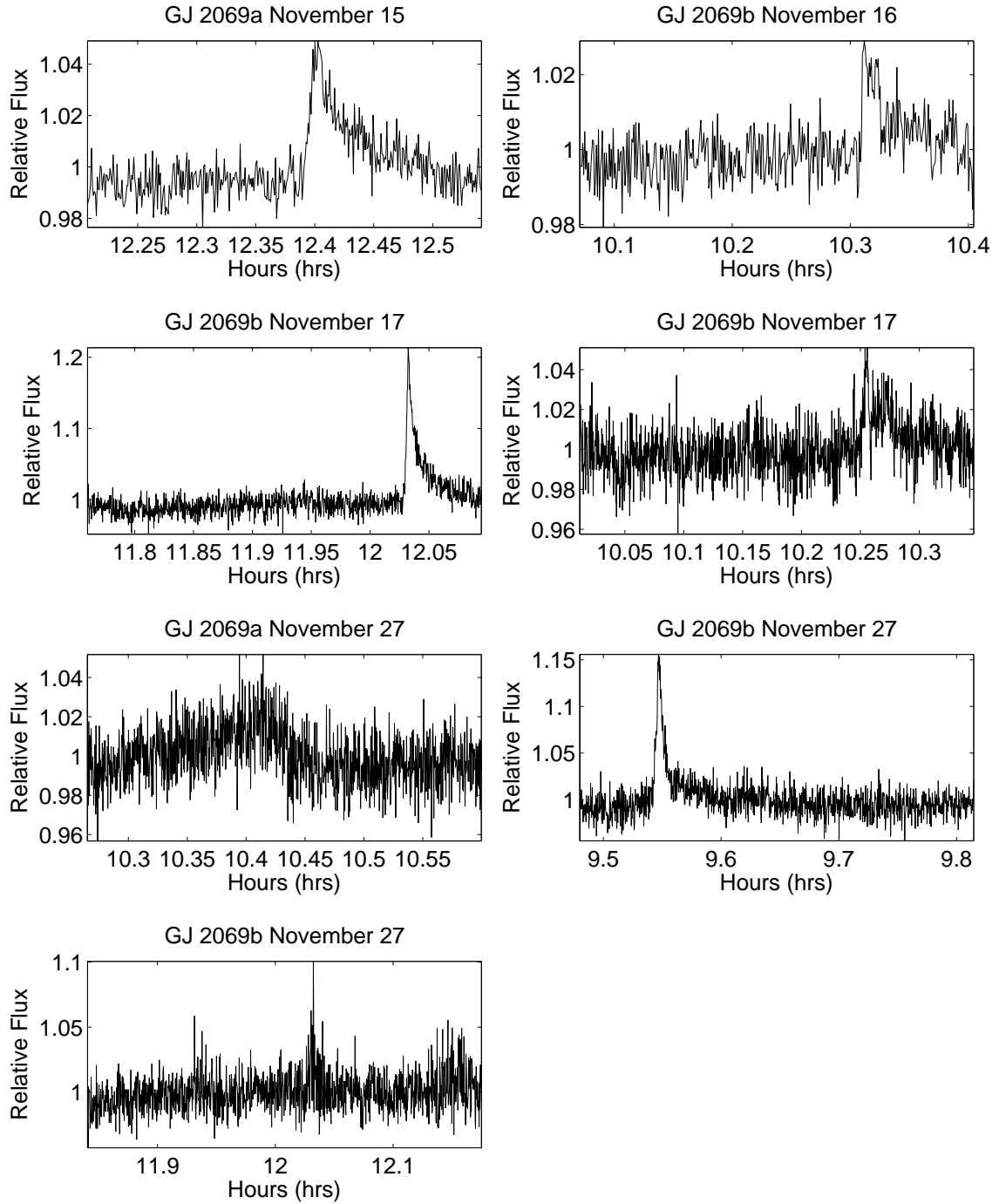


Figure B.3: Here we show the detected flaring from GJ 2069a and GJ 2069b, obtained during the brown dwarf observation campaign (October - December 2010 epochs). We detect flaring from both components of the GJ 2069 system, as indicated above, where GJ 2069b exhibits more flaring activity.

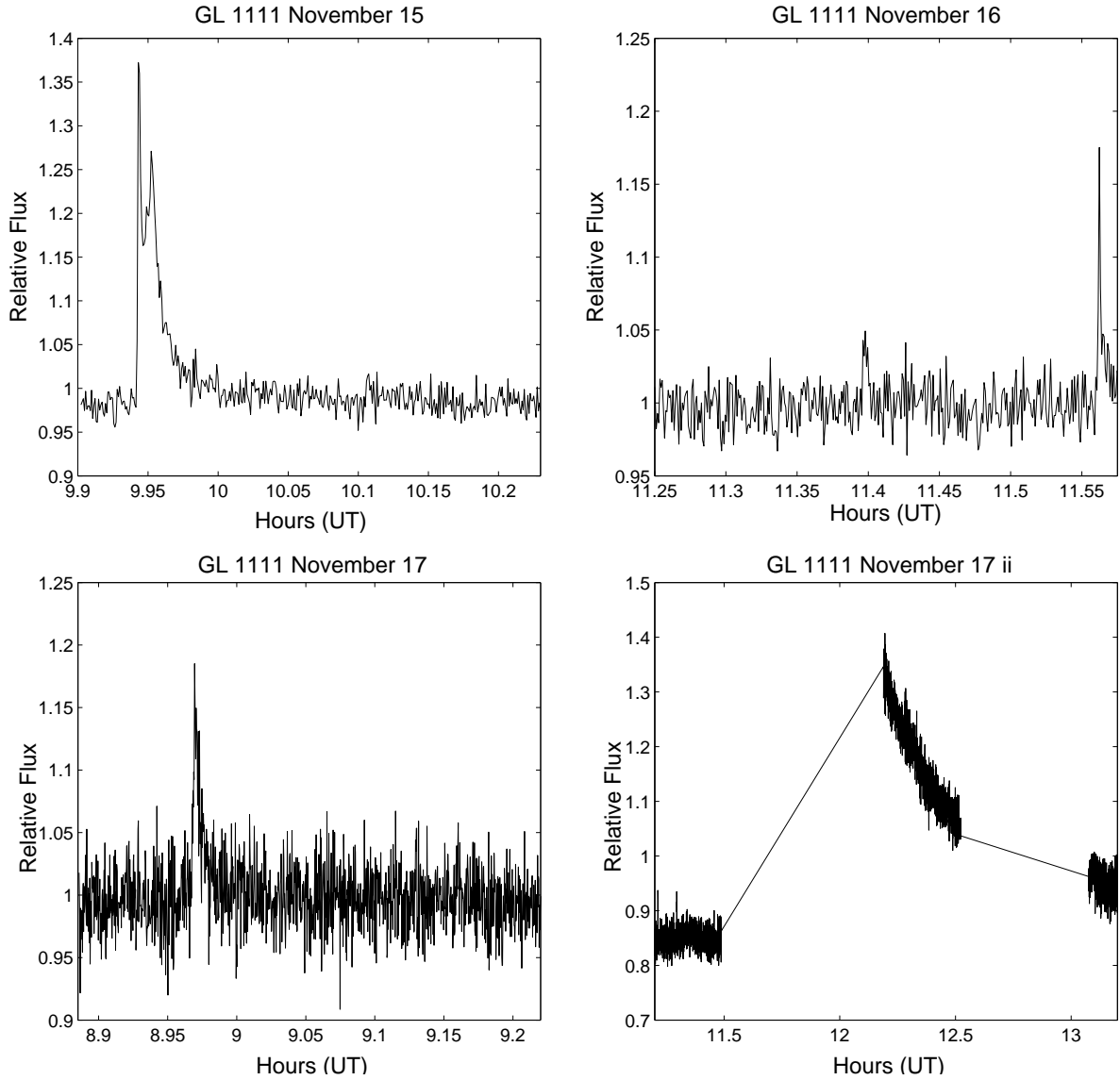


Figure B.4: Here we show the detected flaring from GL 1111, obtained during the same brown dwarf observation campaign as GJ 2069 (October - December 2010 epochs). We highlight the figure in the bottom right corner above, where three of the 20 minute observation intervals are shown. We clearly detect a flare, shown by the second data segment, however we did not sample the full event since we had moved to a different target from $\sim 11.5 - 12.3$ UT. Note the increase in quiescent flux levels after the event at ~ 13.3 UT, as compared to flux levels < 11 UT.



CHIMERA mk.II Conceptual Designs

As discussed in Chapter 8, CHIMERA mk.II* will offer the much larger field of view of 10 arcminutes at the prime focus of the 200-inch telescope, an upgrade that will require significant investment in custom designed optics. Here we show conceptual designs of an Offner relay system[†], that were considered during the optical evaluation of CHIMERA mk.I. The purpose of this design format, was to increase the ray path length, such that a full 10 minute field of view could fit on to the 16.6×14 mm Andor NEO sCMOS chip. Such a design requires custom optics, and very large elements. In the following figures, C.1 and C.2, we show a system of spherical mirrors, designed to maintain spot quality throughout the optical system, with minimal transmission loss. We have labelled the elements in these designs and have highlighted the corresponding element in the figure captions. As well as continuing programs, such as PTF follow-up, this upgraded instrument will be used for a dedicated survey of dense star fields in the ecliptic to search for occultation of stars by Kuiper Belt Objects. Since the upgrade will still utilize the Andor NEO, the instrument will obtain data at >100 frames for second, full frame, and ~ 1600 frames per second sub-frame.

We note that the conceptual designs that are shown in the following pages, are one example of many optical systems that must be considered in order to achieve a seeing-limited large field (>10 arcminutes) at prime of the 200-inch. Indeed, by placing an sCMOS chip who's dimensions are large enough to sample the full beam size at this point, would also be a viable option. However this would involve the development of this technology and thus require a considerable amount of resources. Furthermore, this design would neglect the two-color simultaneous system. CHIMERA is due to be re-designed as a second generation version in early 2013, in a collaborative project between Caltech and the JPL.

*Prof. Gregg Hallinan: PI

[†]Original optical design provided by Dr. Richard Dekaney of Caltech Optical Observatories; this is a conceptual design for another instrument and was slightly modified by the author for the purpose of a CHIMERA mk.II concept drawing. Private communication.

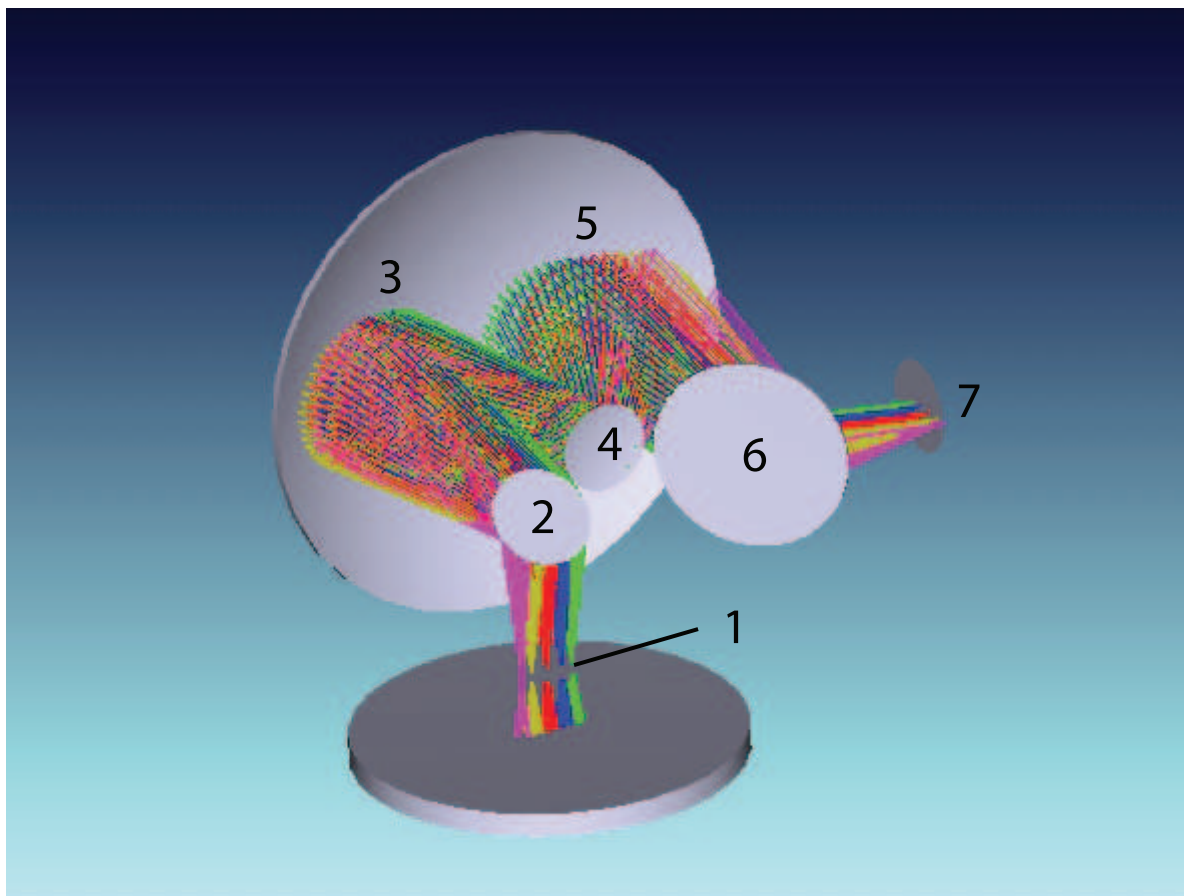


Figure C.1: Here we show an Offner relay setup, via the Zemax design software (3D system). The elements are labelled as follows: (1) Prime focus point. (2) Pick-off mirror at 45 degrees. (3) Reflection point 1 one side of large spherical mirror. (4) Reflection point 2 on to other side of large mirror. (5) Reflection point 3 from large mirror. (6) Dichroic beam splitter. (7) Focus point. We note that we only show one path from the dichroic mirror, labelled (6).

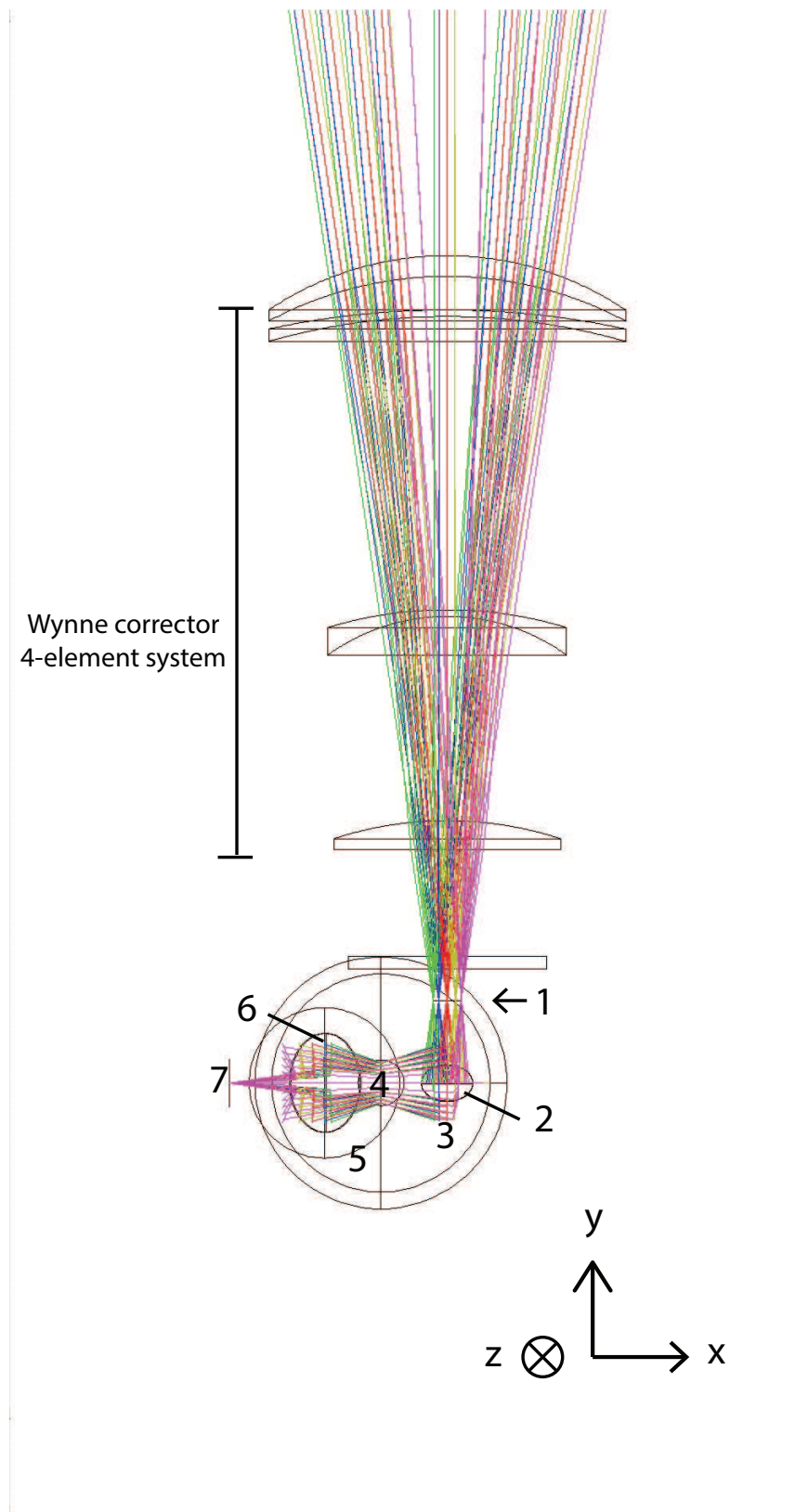


Figure C.2: We show the same setup as in Figure C.1, but also include the Wynne corrector system for reference. The element labelling is identical to that of the previous figure. We note that the negative Z axis is pointing in to the page.

SCIENCE

“Perfect as the wing of a bird may be, it will never enable the bird to fly if unsupported by the air. Facts are the air of science. Without them a man of science can never rise” ... -

Ivan Pavlov

“There is a single light of science, and to brighten it anywhere is to brighten it everywhere” ... - Isaac Asimov